ISSN 2074-272X

науково-практичний журнал

2022/6

Електротехніка і Електромеханіка

Electrical Engineering & Electromechanics

Електричні машини та апарати
Електротехнічні комплекси та системи
Промислова електроніка
Електричні станції, мережі і системи

Журнал включено до найвищої категорії «А» Переліку фахових видань України

З 2021 р. журнал індексується у Scopus

З 2015 р. журнал індексується у Web of Science Core Collection: Emerging Sources Citation Index

Electrical Engineering & Electromechanics

Scientific Journal was founded in 2002
Founder – National Technical University «Kharkiv Polytechnic Institute» (Kharkiv, Ukraine)

From no. 1 2021 Journal «Electrical Engineering & Electromechanics» is indexing in **Scopus** and from no. 1 2015 Journal is indexing in **Web of Science Core Collection: Emerging Sources Citation Index (ESCI)**.

Also included in DOAJ (Directory of Open Access Journals), in EBSCO's database, in ProQuest's databases – Advanced Technologies & Aerospace Database and Materials Science & Engineering Database, in Gale/Cengage Learning databases.

Editorial office address:
National Technical University «Kharkiv Polytechnic Institute», Kyrpychova Str., 2, Kharkiv, 61002, Ukraine
phones: +380 57 7076281, +380 67 3594696, **e-mail:** a.m.grechko@gmail.com (**Grechko O.M.)**

ISSN (print) 2074-272X
ISSN (online) 2309-3404

Printed 06 November 2022. Format 60 × 90 ⅛. Paper – offset. Laser printing. Edition 200 copies.
Printed by Printing house «Madrid Ltd» (18, Gudanova Str., Kharkiv, 61024, Ukraine)

Electrical Engineering & Electromechanics
Scientific Journal

no. 6, 2022

Table of Contents

Electrical Machines and Apparatus

Electrotechnical Complexes and Systems

Industrial Electronics

Power Stations, Grids and Systems

UDC 621.313 https://doi.org/10.20998/2074-272X.2022.6.01

H. Miloudi, M. Miloudi, A. Gourbi, M.H. Bermaki, A. Bendaoud, A. Zeghoudi

A high-frequency modeling of AC motor in a frequency range from 40 Hz to 110 MHz

Introduction. *Most electromagnetic compatibility models developed for the study of three-phase induction machines are generally valid for low and medium frequencies (<< 1 MHz). This frequency limit seems to be too restrictive for the overall study of conducted electromagnetic interference. In this paper, the model is using the proposed model and compared with experimental results in low and medium frequency. And then, the high-frequency modeling of induction motor is presented new method based on transfer function model. The proposed methodology is verified on an experimental and simulation, it's suitable for prediction of the terminal overvoltage analysis and electromagnetic interference problems and common-mode and differential-mode currents. The* ***novelty*** *of the work consists to develop an improved high-frequency motor model based on transfer function to represent the motor high-frequency behavior for frequency-domain analyses in the frequency range from 40 Hz up to 110 MHz .The* ***purpose*** *of this work is to study the common-mode impedance and the differential-mode impedance of AC motor. The determination of these impedances is done for firstly both common and differential modes at low and medium frequency, and then common-mode and differential-mode characteristics at high frequency.* ***Methods.*** *For the study of the path of common-mode and differential-mode currents in typical AC motor (0.25 kW, 50 Hz) an identification method in high frequency for induction motor has been proposed based on the transfer function in differential-mode and common-mode configuration. The low and medium frequency model were presented in the first time based on equivalent circuit of electrical motor. Then, the common-mode and differential-mode impedances were defined in high frequency using asymptotic approach. This motor was studied by MATLAB Software for simulation and also experimental measurements.* ***Results.*** *All the simulations were performed using the mathematical model and the results obtained are validated by experimental measurements performed in the University of the Federal Armed Forces Hamburg in Germany. The obtained results of common-mode and differential-mode at low frequency, medium and high frequency are compared between simulation and experiment.* References 34, table 2, figures 14.

Key words: **AC motor, differential-mode, common-mode, electromagnetic interference, high frequency.**

Вступ. *Більшість моделей електромагнітної сумісності, розроблених для дослідження трифазних асинхронних машин, загалом застосовні для низьких та середніх частот (<<1 МГц). Ця частотна межа здається надто суворою для загального вивчення кондуктивних електромагнітних перешкод. У цій статті запропонована модель використовується і порівнюється з експериментальними результатами за низької та середньої частоти. Потім представлений новий метод високочастотного моделювання асинхронного двигуна, що базується на моделі передавальної функції. Запропонована методологія перевірена експериментально та за допомогою моделювання, вона придатна для прогнозування аналізу перенапруг на клемах та проблем електромагнітних перешкод, а також синфазних та диференціальних струмів.* ***Новизна*** *запропонованої роботи полягає у розробці вдосконаленої моделі високочастотного двигуна на основі передавальної функції для представлення високочастотної поведінки двигуна для аналізу частотної області в діапазоні частот від 40 Гц до 110 МГц.* ***Мета*** *роботи полягає у вивченні синфазного імпедансу та диференціального імпедансу двигуна змінного струму. Визначення цих імпедансів виконується спочатку для синфазних та диференціальних мод на низькій та середній частоті, а потім для синфазних та диференціальних характеристик на високій частоті.* ***Методи***. *Для дослідження шляху синфазних та диференціальних струмів у типовому двигуні змінного струму (0,25 кВт, 50 Гц) було запропоновано метод ідентифікації на високій частоті для асинхронного двигуна, заснований на передавальній функції у конфігураціях диференціального та синфазного режимів. Вперше представлена низько- та середньочастотна модель на основі схеми заміщення електродвигуна. Потім синфазний та диференціальний імпеданси визначені на високій частоті з використанням асимптотичного підходу. Цей двигун був вивчений програмним забезпеченням MATLAB для моделювання та експериментальних вимірювань.* ***Результати***. *Все моделювання виконано з використанням математичної моделі, а отримані результати підтверджені експериментальними вимірами, проведеними в Університеті федеральних збройних сил у Гамбурзі, Німеччина. Отримані результати синфазного та диференціального режиму на низькій частоті, середній та високій частоті порівнюються між моделюванням та експериментом.* Бібл. 34, табл. 2, рис. 14.

Ключові слова: **двигун змінного струму, диференціальний режим, синфазний режим, електромагнітні завади, висока частота.**

Introduction. The evaluation impedance characteristic of the induction machine in high-frequency can help study and analyze the electromagnetic interference (EMI) in adjustable drives system, so accurate modeling of induction motors in high-frequency range plays an important role in overvoltage and EMI problems [1, 2].

In association with the inverter-fed-AC motor, the motor constitutes one of the main propagation paths of common-mode (CM) and differential-mode (DM) currents [3-5]. The proposed model based on the transfer function description of the main parasitic couplings in the induction machine can be used to evaluate the high-frequency leakage currents, which are the cause of electromagnetic interference to electronic, electric equipment, and electrical networks. We developed a behavioral model allowing a better representation of impedances of the machine.

In this paper the two models are presented, the first one is shown in Fig. 1, which is valid for low and medium frequencies (<< 1 MHz), this model was reported in [6-8]. After, we develop a new model for the high-frequency that is based on the asymptotical method using DM and CM impedance measurements of the induction machine.

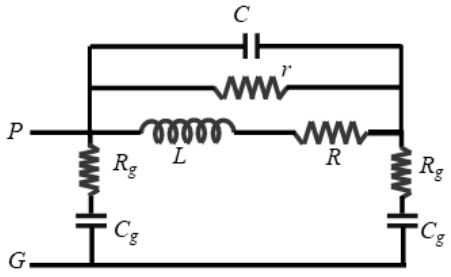

Fig. 1. Single-phase CM impedance proposed of AC motor [6, 9, 21]. Here r is stator and rotor phase resistance; L is phase leakage inductance; C is capacitance representing the turn to turn distributed capacitive coupling; R is resistance representing eddy currents inside the magnetic core and the frame; R_g is resistance representing winding-to-ground distributed resistances; C_g is capacitance representing the winding to ground distributed capacitive coupling

The proposed approach needs only the magnitude plot in the CM measurement configuration to descript the CM impedance of the AC motor, and the magnitude plot in the DM measurement configuration to descript the DM

impedance of the AC motor, and after we can verify the transfer function parameters of the motor by the second curve. So in this experimental setup, the motor is considered as a black box, and with frequency response, we can find the transfer function of CM and DM impedances of AC motor in a frequency range from 40 Hz up to 110 MHz.

A high-frequency induction machine model. The most frequency models of three-phase induction machines are generally constituted of a limited number of elements such as that presented in [2, 7, 9]. These models have been proposed in the literature for overvoltage and electromagnetic interference (EMI) analysis.

Many investigations into high-frequency induction motor modeling were recently reported in [6-8, 10-19]. The model presented in this work as well as those found in the literature requires the hypothesis of linearity of the machine. This assumes that the machine is never saturated. The elements depend solely on the frequency, which makes it possible to use the notion of impedance.

In [20] the influence of saturation is proved to be smaller than 2 % of the impedance's absolute value with a 5.5 kW induction machine. With frequencies higher than 80 kHz, the influence of the saturation disappears completely.

The studies in [16] have shown that the state of electromagnetic compatibility in motors, synchronous or induction, is not dependent on operating point, the high frequency (HF) model motor has the same characteristic with low speed or high speed. This enables us to restrict ourselves to identifying the machine in an off state.

The initial development of the equivalent models (Fig. 1) is generally based on an interpretation of the physical phenomena in the machine. The simplicity of this equivalent circuit gives them the advantage of being able to determine the various elements that make up them with a minimum number of measurements.

The impedance is a complex quantity, hence the magnitude and phase information are included in the impedance [22].

The magnitude Z_{DM} and phase angle $\varphi_{Z_{DM}}$ of the DM impedance of the induction machine can be evaluated respectively as:

$$Z_{DM} = \frac{K\left(\frac{1}{\omega_{n1}}\cdot s+1\right)}{\left[\left(\frac{1}{\omega_{n2}^2}\right)s^2+\frac{2\cdot\xi_2}{\omega_{n2}}s+1\right]}, \quad (1)$$

$$\varphi_{Z_{DM}} = \text{arctg}\left(\frac{\omega}{\omega_1}\right)-\text{arctg}\left(\frac{2\cdot\xi_2\cdot\frac{\omega}{\omega_2}}{1-\left(\frac{\omega}{\omega_2^2}\right)^2}\right). \quad (2)$$

The magnitude Z_{CM} and phase angle $\varphi_{Z_{CM}}$ of the CM impedance corresponding to the circuit of Fig. 1 can be evaluated as:

$$Z_{CM} = \frac{K\cdot\left[\left(\frac{1}{\omega_{n1}^2}\right)s^2+\frac{2\cdot\xi_1}{\omega_{n1}}s+1\right]}{s\cdot\left[\left(\frac{1}{\omega_{n2}^2}\right)s^2+\frac{2\cdot\xi_2}{\omega_{n2}}s+1\right]}, \quad (3)$$

$$\varphi_{Z_{CM}} = -90+\text{arctg}\left(\frac{2\cdot\xi_1\cdot\frac{\omega}{\omega_1}}{1-\left(\frac{\omega}{\omega_1^2}\right)^2}\right)-\text{arctg}\left(\frac{2\cdot\xi_2\cdot\frac{\omega}{\omega_2}}{1-\left(\frac{\omega}{\omega_2^2}\right)^2}\right), \quad (4)$$

where ω is the pulsation ($\omega = 2\cdot\pi f$, where f is the frequency); s is the variable from a Laplace transform ($s = j\cdot\omega$); rest of symbols are described in Tables 1, 2.

Experimental results. The impedance Analyzer Agilent 4294A was used to measure the impedance and phase angle of the motor ranging from small size (0.25 kW – 50 Hz) in the frequency range from 40 Hz to 110 MHz.

There are two measurements conducted with the induction machine.

Differential-mode configuration. Measuring the impedance between the three-phase terminals connected and the motor neutral using the setup shown in Fig. 2 provides the DM characteristics of the induction machine under test [11, 20, 21, 23-25].

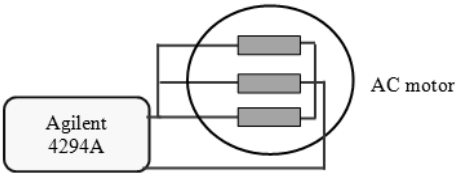

Fig. 2. DM test configuration

Fig. 3, 4 show respectively the magnitude and the phase of the measured DM characteristics as a function of frequency for 40 Hz to 110 MHz.

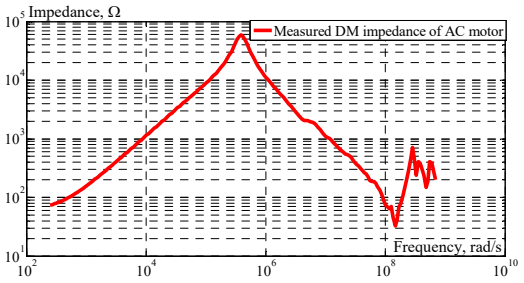

Fig. 3. DM impedance magnitude measurement

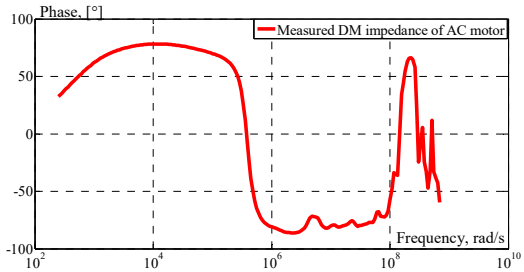

Fig. 4. DM impedance phase measurement

Common-mode configuration. Measuring three shortened phases against ground using the setup [1, 21, 23-26] shown in Fig. 5 provides the CM characteristics.

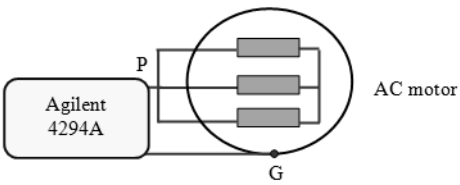

Fig. 5. CM test configuration

The evolution of the CM impedance of the motor as a function of the frequency obtained experimentally is represented in Fig. 6 (magnitude) and Fig. 7 (phase).

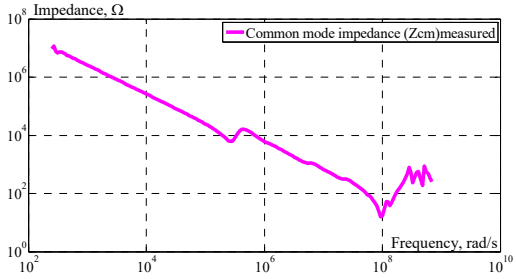

Fig. 6. CM impedance magnitude measurement

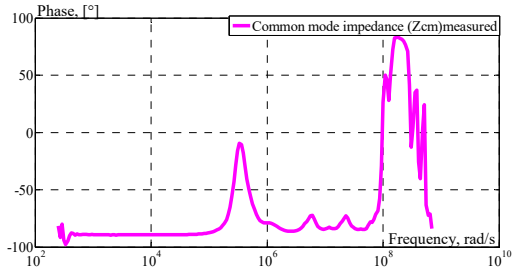

Fig. 7. CM impedance phase measurement

A high-frequency model for AC motor. In [2] and as illustrated in Fig. 3, 6, the model has been validated by DM and CM test measurements in both magnitude and phase within the frequency range from 40 Hz to 110 MHz.

The measurement impedance phase-motor neutral (Fig. 8, 9) provides the DM characteristics of the induction machine under test compared with the first proposed model shown respectively in (1) and (3).

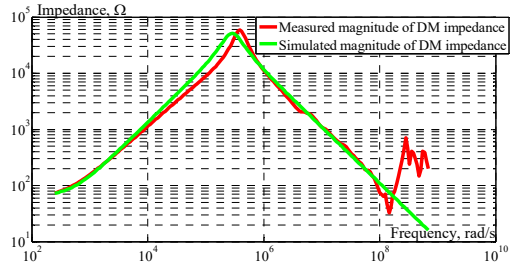

Fig. 8. Magnitude of the DM impedance

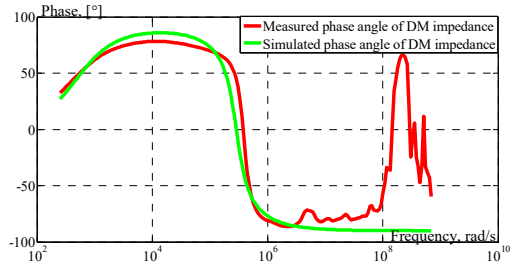

Fig. 9. Phase of the DM impedance

The values of transfer function parameters are listed in Table 1.

Table 1

Transfer functions parameters of DM impedance of AC motor

Constant terms K	65
The first natural frequency ω_{n1}	487
Value of zero	–487
The second natural frequency ω_{n2}	$2.88 \cdot 10^5$
Damped natural frequency ω_{p2}	$2.6713 \cdot 10^5$
Value of the first pole	$-1.07 \cdot 10^5 - j2.67 \cdot 10^5$
Value of the second pole	$-1.07 \cdot 10^5 + j2.67 \cdot 10^5$
The damping ratio ξ_2	0.371

Figures 10, 11 show the measurement CM impedance is plotted and compared with the mathematical model.

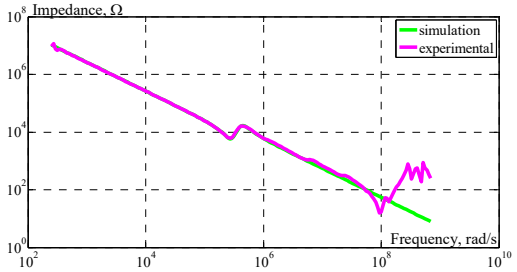

Fig. 10. Magnitude of the CM impedance

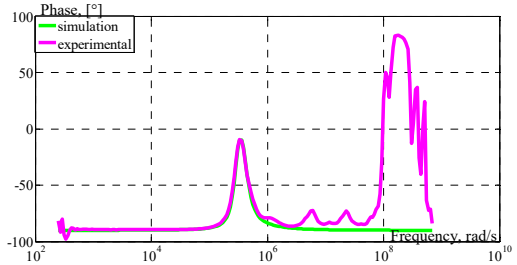

Fig. 11. Phase of the CM impedance

The values of transfer function parameters of the CM impedance are listed in Table 2.

Table 2

Transfer functions parameters of the CM impedance of AC motor

Constant terms K	$2.62005719 \cdot 10^9$
The first natural frequency ω_{n1}	$2.87688758 \cdot 10^5$
Damped natural frequency ω_{p1}	$2.81876265 \cdot 10^5$
The second natural frequency ω_{n2}	$4.16779364 \cdot 10^5$
Damped natural frequency ω_{p2}	$4.04598107 \cdot 10^5$
The first damping ratio ξ_1	0.2
The second damping ratio ξ_2	0.24

As shown in Fig. 8–11, superimposing the experimental results and simulation results of the proposed model, we verified that there is very good accordance between them in both magnitude and phase for low and medium frequencies (<< 1 MHz), and frequency components higher than 1 MHz are not able to deeply penetrate in the motor windings. For this reason, it's necessary to develop a new model in high-frequency.

A high-frequency model development for AC motor. The EMI interference levels produced by power switching converters in motor drive depend on several factors as:

- the switching frequency of the converter;
- the slope of the current and voltage at switching;
- the impedance of the main power supply;
- the length of cables from the converter to the motor.

The good evaluation of the input impedance of the system motor is key in the future evaluation of the level of the electromagnetic field around this system [27].

The most effective method in researching high-frequency characters of motor windings is multi-conductor and multi-element conducting mode [28-31] adopted lumped parameter model, this method is simplified and got the acceptable result. We proposed an approach applied to prediction the transfer function of three-phase AC motor in high-frequency, deal with the problem of building mathematical models of dynamic systems based on observed data from the motor in two configurations, CM and DM, and is thus an experimental modeling method. The proposed approach is valid for all physical models.

The system identification method base on the asymptote approach [32-34], this method is based on finding

the resonance frequencies, slopes of the asymptotes, and the terms of transfer functions corresponding to each straight line, to construct the entire transfer function of impedance in two configurations, CM and DM.

To validate the second proposed model described in this paper, two measurements were carried out on the 0.25 kW induction motor by using a Network Analyzer Agilent 4294 A in the frequency domain.

The model has been validated by DM (Fig. 12) and CM (Fig. 13) test measurements within the frequency range from 40 Hz to 110 MHz.

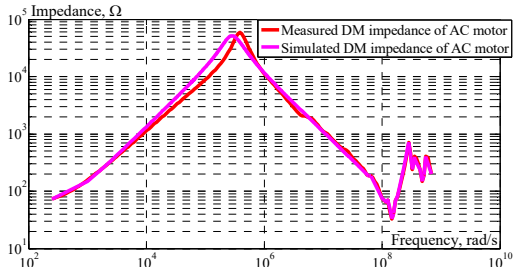

Fig. 12. Magnitude of DM impedance

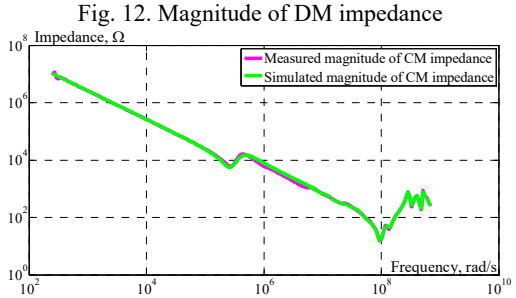

Fig. 13. Magnitude of CM impedance

The second model developed in this section is plotted with the measured results to verify that the model is an accurate representation of the machine in low, medium, and high frequencies. The plot in Fig. 12, 13 verifies that the model developed fits the measured impedance in the frequency range from 40 Hz to 110 MHz.

Analysis of HF model. HF impedances of the CM and the DM are shown in Fig. 14.

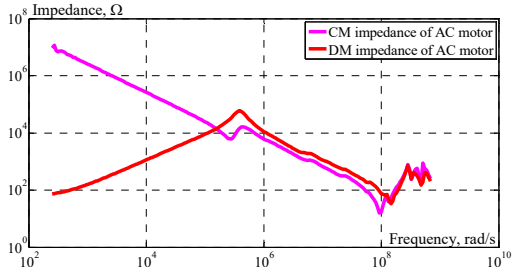

Fig. 14. Magnitude of CM impedance

The corresponding plot shown in Fig. 14 indicates that at DC the CM impedance of the induction machine behaves as an open circuit. As we increase the frequency, the impedance of the capacitor C_g dominates and decreases linearly with the frequency of slope –1. At the first resonant frequency, the impedance of the inductor equals that of the capacitor. Above the first resonance frequency, the magnitude of the impedance of the inductor L dominates and increases of slope +1 until the second resonance frequency, after the impedance of the capacitor contributes and the impedance magnitude decreases with the slope of –1. As the frequency is further increased, the CM impedance has series resonance phenomena until 110 MHz.

For the DM impedance, we can see that at low frequencies the inductor L dominates until the first resonance frequency. As the frequency increases, the capacitor C begins to dominate at the DM resonance frequency and the impedance decreases of slope –1. As the frequency is further increased, the DM impedance has the same series of resonance phenomena as the CM impedance.

Conclusions.

1. For the analysis of conducted EMI, it is necessary to build a satisfactory model of all parts of common-mode and differential-mode coupling paths between source and target of electromagnetic interference. Particularly for the adjustable speed drive system, the AC motor constitutes one of the main propagation paths of conducted electromagnetic perturbation.

2. In this paper, we investigated high-frequency modeling of the common-mode and differential-mode impedances of AC motors. The simulations are carried out using the proposed model in literature and compared with experimental results, making it possible to validate the first model in low and medium frequency.

3. An improved high-frequency motor model is developed to represent the motor high frequency; this model based on transfer function gives satisfactory results behavior for frequency-domain analyses in the frequency range from 40 Hz up to 110 MHz.

Acknowledgments. This research was supported by «La Direction Générale de la Recherche Scientifique et du Développement Technologique (DGRSDT)».

We would also like to show our gratitude to Stefan Dickmann, Professor, University of the Federal Armed Forces Hamburg in Germany for making measurement with us during the course of this research.

Conflict of interest. The authors declare no conflict of interest.

REFERENCES

1. Karakasli V., Ye Q., Griepentrog G., Wei J. A Parameterization of 6-Port High-Frequency Delta- and Star-Connected Induction Motor Model. *2020 International Symposium on Electromagnetic Compatibility - EMC EUROPE*, 2020, pp. 1-6. doi: https://doi.org/10.1109/EMCEUROPE48519.2020.9245646.

2. Wang L., Ngai-Man Ho C., Canales F., Jatskevich J. High-Frequency Modeling of the Long-Cable-Fed Induction Motor Drive System Using TLM Approach for Predicting Overvoltage Transients. *IEEE Transactions on Power Electronics*, 2010, vol. 25, no. 10, pp. 2653-2664. doi: https://doi.org/10.1109/tpel.2010.2047027.

3. Karimi S., Farjah E., Ghanbari T. Common and Differential Modes of Conducted Electromagnetic Interference in Electric Vehicle equipped with Supercapacitor. *2019 10th International Power Electronics, Drive Systems and Technologies Conference (PEDSTC)*, 2019. doi: https://doi.org/10.1109/pedstc.2019.8697677.

4. Wu Y., Yin S., Liu Z., Li H., See K.Y. Experimental Investigation on Electromagnetic Interference (EMI) in Motor Drive Using Silicon Carbide (SiC) MOSFET. *2020 International Symposium on Electromagnetic Compatibility - EMC EUROPE*, 2020, pp. 1-6. doi: https://doi.org/10.1109/EMCEUROPE48519.2020.9245674.

5. Guo Y., Penugonda S., Kim M., Lee J., Ha J., Yun S., Fan J., Kim H. Ground Bridge Effect on Reduction of Conducted Emission from Three-Phase Motor Drive System. *2019 International Symposium on Electromagnetic Compatibility - EMC EUROPE*, 2019, pp. 854-859. doi: https://doi.org/10.1109/emceurope.2019.8871992.

6. Miloudi H., Bendaoud A., Miloudi M., Dickmann S., Schenke S. Common mode and differential mode characteristics of AC motor for EMC analysis. *2016 International Symposium on Electromagnetic Compatibility - EMC EUROPE*, 2016, pp. 765-769. doi: https://doi.org/10.1109/EMCEurope.2016.7739260.

7. Revol B., Roudet J., Schanen J.-L., Loizelet P. EMI Study of Three-Phase Inverter-Fed Motor Drives. *IEEE Transactions on Industry Applications*, 2011, vol. 47, no. 1, pp. 223-231. doi: https://doi.org/10.1109/TIA.2010.2091193.

8. Degano M., Zanchetta P., Clare J., Empringham L. HF induction motor modeling using genetic algorithms and experimental impedance measurement. *2010 IEEE International Symposium on Industrial Electronics*, 2010, pp. 1296-1301. doi: https://doi.org/10.1109/ISIE.2010.5637052.

9. Ganjavi A., Rathnayake H., Zare F., Kumar D., Yaghoobi J., Davari P., Abbosh A. Common-Mode Current Prediction and Analysis in Motor Drive Systems for the New Frequency Range of 2–150 kHz. *IEEE Journal of Emerging and Selected Topics in Power Electronics*, 2022, vol. 10, no. 1, pp. 74-90. doi: https://doi.org/10.1109/JESTPE.2020.3006878.
10. Zhang Y., Li Q., Jiang D. A Motor CM Impedance Based Transformerless Active EMI Filter for DC-Side Common-Mode EMI Suppression in Motor Drive System. *IEEE Transactions on Power Electronics*, 2020, vol. 35, no. 10, pp. 10238-10248. doi: https://doi.org/10.1109/TPEL.2020.2980881.
11. Moreno Y., Almandoz G., Egea A., Arribas B., Urdangarin A. Analysis of Permanent Magnet Motors in High Frequency – A Review. *Applied Sciences*, 2021, vol. 11, no. 14, art. no. 6334. doi: https://doi.org/10.3390/app11146334.
12. Ryu Y., Han K.J. Improved transmission line model of the stator winding structure of an AC motor considering high-frequency conductor and dielectric effects. *2017 IEEE International Electric Machines and Drives Conference (IEMDC)*, 2017, pp. 1-6, doi: https://doi.org/10.1109/IEMDC.2017.8002140.
13. Zare F. Modeling of Electric Motors for Electromagnetic Compatibility Analysis. *Proceedings of the 2006 Australasian Universities Power Engineering Conference*, Melbourne Austria, 2006, pp. 1-5.
14. Ryu Y., Park B.-R., Han K.J. Estimation of High-Frequency Parameters of AC Machine From Transmission Line Model. *IEEE Transactions on Magnetics*, 2015, vol. 51, no. 3, pp. 1-4, art no. 8101404. doi: https://doi.org/10.1109/TMAG.2014.2355718.
15. Hasnaoui O. Electromagnetic interferences and common mode voltage generated by variable speed AC motors. *2014 International Conference on Electrical Sciences and Technologies in Maghreb (CISTEM)*, 2014, pp. 1-5. doi: https://doi.org/10.1109/CISTEM.2014.7076990.
16. Maki K., Funato H., Shao L. Motor modeling for EMC simulation by 3-D electromagnetic field analysis. *2009 IEEE International Electric Machines and Drives Conference*, 2009, pp. 103-108. doi: https://doi.org/10.1109/IEMDC.2009.5075190.
17. Boucenna N., Costa F., Hlioui S., Revol B. Strategy for Predictive Modeling of the Common-Mode Impedance of the Stator Coils in AC Machines. *IEEE Transactions on Industrial Electronics*, 2016, vol. 63, no. 12, pp. 7360-7371. doi: https://doi.org/10.1109/TIE.2016.2594052.
18. Chen H., Yan Y., Zhao H. Extraction of Common-Mode Impedance of an Inverter-Fed Induction Motor. *IEEE Transactions on Electromagnetic Compatibility*, 2016, vol. 58, no. 2, pp. 599-606. doi: https://doi.org/10.1109/TEMC.2016.2519543.
19. Weber S.-P., Hoene E., Guttowski S., John W., Reichl H. Modeling induction machines for EMC-Analysis. *2004 IEEE 35th Annual Power Electronics Specialists Conference*, 2004, vol. 1, pp. 94-98. doi: https://doi.org/10.1109/PESC.2004.1355720.
20. Boglietti A., Cavagnino A., Lazzari M. Experimental High-Frequency Parameter Identification of AC Electrical Motors. *IEEE Transactions on Industry Applications*, 2007, vol. 43, no. 1, pp. 23-29. doi: https://doi.org/10.1109/TIA.2006.887313.
21. Kahoul R., Marchal P., Azzouz Y., Mazari B. HF model of DC motor impedance EMC problems in automotive applications. *2008 IEEE International Symposium on Electromagnetic Compatibility*, 2008, pp. 1-5. doi: https://doi.org/10.1109/ISEMC.2008.4652143.
22. Jia K., Bohlin G., Enohnyaket M., Thottappillil R. Modelling an AC motor with high accuracy in a wide frequency range. *IET Electric Power Applications*, 2013, vol. 7, no. 2, pp. 116-122. doi: https://doi.org/10.1049/iet-epa.2012.0127.
23. Toulabi M.S., Wang L., Bieber L., Filizadeh S., Jatskevich J. A Universal High-Frequency Induction Machine Model and Characterization Method for Arbitrary Stator Winding Connections. *IEEE Transactions on Energy Conversion*, 2019, vol. 34, no. 3, pp. 1164-1177. doi: https://doi.org/10.1109/TEC.2019.2891349.
24. Hoffmann A., Ponick B. Statistical Deviation of High-Frequency Lumped Model Parameters for Stator Windings in Three-Phase Electrical Machines. *2020 International Symposium on Power Electronics, Electrical Drives, Automation and Motion (SPEEDAM)*, 2020, pp. 85-90. doi: https://doi.org/10.1109/SPEEDAM48782.2020.9161915.
25. Lu X., Zhang S., Liu C., Xie P., Chen H. Modeling of common-mode current in motor cable of inverter-fed motor drive system. *2016 Asia-Pacific International Symposium on Electromagnetic Compatibility (APEMC)*, 2016, pp. 511-514. doi: https://doi.org/10.1109/APEMC.2016.7522783.
26. Weens Y., Idir N., Franchaud J.-J., Bausiere R. Comparaison de deux méthodes de modélisation haute fréquence d'un moteur asynchrone. *Colloque International de Compatibilité Electromagnétique (CEM'06)*, Saint Malo, France, 2006, pp. 187-189. (Fra).
27. Roc'h A., Leferink F. Experimental investigation of the input common mode impedance of a motor and its cable up to 1 GHz. *2014 International Symposium on Electromagnetic Compatibility*, 2014, pp. 631-636, doi: https://doi.org/10.1109/EMCEurope.2014.6930982.
28. Liu J., Wang X., Jiang N. Application of ant colony algorithm to the analysis of high frequency equivalent circuit of DC motor. *WSEAS Transactions on Power Systems*, 2012, vol. 7, no. 1, pp. 1-11.
29. Liu J., Wang X., Jiang N. Study of Making Model and Simulating for DC Motor Windings Based on ACA. *2010 International Conference on Computational Intelligence and Software Engineering*, 2010, pp. 1-4. doi: https://doi.org/10.1109/cise.2010.5676972.
30. Benecke J., Dickmann S. Inductive and capacitive couplings in DC motors with built-in damping chokes. *2006 17th International Zurich Symposium on Electromagnetic Compatibility*, 2006, pp. 69-72. doi: https://doi.org/10.1109/EMCZUR.2006.214871.
31. Benecke J., Linde A., Dickmann S. Automatic HF model generation and impedance optimization for low voltage DC motors. *2008 18th International Conference on Electrical Machines*, 2008, pp. 1-6, doi: https://doi.org/10.1109/ICELMACH.2008.4800131.
32. Hrigua S., Costa F., Gautier C., Revol B. New modeling method based on transfer functions for EMI analysis in power electronic converters. *International Symposium on Electromagnetic Compatibility - EMC EUROPE*, 2012, pp. 1-6. doi: https://doi.org/10.1109/EMCEurope.2012.6396839.
33. Wu Y., Bi C., Jia K., Jin D., Li H., Yao W., Liu G. High-frequency modelling of permanent magnet synchronous motor with star connection. *IET Electric Power Applications*, 2018, vol. 12, no. 4, pp. 539-546. doi: https://doi.org/10.1049/iet-epa.2017.0593.
34. Miloudi H., Bendaoud A., Miloudi M., Dickmann S., Schenke S. A novel method of transfer-function identification for modeling DM impedance of AC motor. *2017 International Symposium on Electromagnetic Compatibility - EMC EUROPE*, 2017, pp. 1-5. doi: https://doi.org/10.1109/emceurope.2017.8094770.

Received 05.05.2022
Accepted 24.07.2022
Published 06.11.2022

Houcine Miloudi [1], *Lecturer,*
Mohamed Miloudi [1,2], *Lecturer,*
Abdelkader Gourbi [3,4], *Lecturer,*
Mohammed Hamza Bermaki [1], *Lecturer,*
Abdelber Bendaoud [1], *Professor,*
Abdelhakim Zeghoudi [1], *PhD,*
[1] Laboratory of Applications of Plasma, Electrostatics and Electromagnetic Compatibility (APELEC),
Djillali Liabes University Sidi-Bel-Abbes, Algeria,
e-mail: el.houcine@yahoo.fr (Corresponding Author);
bermaki.hamza@gmail.com; babdelber@gmail.com;
hakooumzeghoudi@gmail.com
[2] University of Relizane, Algeria,
e-mail: mohamed.miloudi@univ-relizane.dz
[3] Laboratory of Intelligent Control and Electrical Power Systems,
Djillali Liabes University Sidi-Bel-Abbes, Algeria,
e-mail: aekett@yahoo.fr
[4] Institute of Science and Applied Techniques,
Ahmed Ben Bella University, Oran, Algeria

How to cite this article:
Miloudi H., Miloudi M., Gourbi A., Bermaki M.H., Bendaoud A., Zeghoudi A. A high-frequency modeling of AC motor in a frequency range from 40 Hz to 110 MHz. *Electrical Engineering & Electromechanics*, 2022, no. 6, pp. 3-7. doi: https://doi.org/10.20998/2074-272X.2022.6.01

UDC 621.313 https://doi.org/10.20998/2074-272X.2022.6.02

Yu.V. Shurub, V.Ye. Vasilenkov, Yu.L. Tsitsyurskiy

Method of calculation of electromagnetic torque and energy losses of three-phase induction motors when powered by a regulated single-phase voltage

Introduction. *Single-phase power supply of induction motors is used in public utilities, in microclimate control systems for remote agricultural consumers, in water supply and pipeline transport systems, etc. In practice, there is the use of induction motors with three-phase stator winding in the conditions of single-phase power supply. Starting and operating capacitors are used to enable their operation when powered by a single-phase network.* ***Problem.*** *There are many fairly accurate methods for calculating the characteristics of an induction motor in asymmetric, including single-phase, modes of operation, but they are based on differential equations, which does not allow to obtain analytical expressions for preliminary analysis and synthesis of such systems.* ***Goal.*** *The purpose of this article is to develop the analytical method of definition of electromagnetic torque and energy losses of voltage-regulated three-phase induction motors working according to the scheme of single-phase inclusion with the phase-shifting capacitor.* ***Methodology.*** *The method is based on the theory of symmetric components and analysis of replacement schemes of induction machine in motor and generator modes.* ***Results.*** *The analysis of the obtained data shows that at a constant value of the phase-shifting capacitor capacity induction motor working according to the scheme of single-phase inclusion has a minimum of losses at one value of slip at different values of supply voltage. Therefore, if you keep this slip constant when the load changes, you can achieve a mode of minimizing losses at a constant value of the capacity, optimal for this slip. This shows that the thyristor voltage regulator can be used as an energy-saving element under variable load, while the capacitance of the phase-shifting capacitor can remain constant when changing the load in a wide range provided that this slip is stabilized.* ***Originality.*** *The developed method allows to obtain analytical expressions for comparative analysis of electromagnetic torque and energy losses of three-phase induction motors powered by a single-phase network at different values of the capacity of the phase-shifting capacitor, supply voltage for different variants of schemes for including three-phase induction motors in a single-phase network.* ***Practical value.*** *Based on the developed analytical method, the optimal parameters of phase-shifting capacitors and rational schemes for including three-phase induction motors in a single-phase network can be determined.* References 25, figures 3.

Key words: **induction motor, single-phase supply, voltage regulator, method of symmetric components, phase-shifting capacitor.**

Розроблено аналітичну методику розрахунку електромагнітного моменту та втрат енергії регульованих за напругою трифазних асинхронних двигунів при живленні від однофазної мережі за схемою з фазозсуваючим конденсатором. В основу методики покладено метод симетричних складових та аналіз схем заміщення асинхронної машини у двигунному та генераторному режимах роботи. На основі цієї методики можуть бути визначені оптимальні параметри фазозсуваючих конденсаторів та вибрані раціональні схеми включення трифазних асинхронних двигунів в однофазну мережу з регульованою напругою. Показано, що регулятор напруги може бути використаний як енергозберігаючий елемент при однофазному живленні трифазних асинхронних двигунів та його застосування дозволяє використовувати постійну ємність фазозсуваючого конденсатора при зміні навантаження у широких межах. Бібл. 25, рис. 3.

Ключові слова: **асинхронний двигун, однофазне живлення, регулятор напруги, метод симетричних складових, фазозсуваючий конденсатор.**

Introduction. Single-phase power supply of induction motors (IMs) is used in household and communal economy [1], in microclimate regulation systems of agricultural consumers [2], in water supply and pipeline transport systems [3]. In practice, the use of induction motors with a three-phase stator winding is observed under conditions of single-phase power supply [4, 5]. For the possibility of their operation when powered from a single-phase network, starting and working capacitors are used [6, 7]. The use of voltage-regulated electric drives based on three-phase induction motors makes it possible to meet the technological and energy-saving requirements of many consumers [8, 9], to facilitate start-up conditions [10], and to increase the energy efficiency of technological units by taking into account the nature of load changes in the algorithm for regulating closed-loop electric drive systems [11].

There are many fairly accurate methods for calculating [4-7, 12, 13] the characteristics of an induction motor in asymmetric, including single-phase, modes of operation, but they are based on differential equations, which does not allow obtaining analytical expressions for the preliminary selection of the capacity of the phase-shifting capacitor and comparative analysis of possible variants of connection schemes.

The goal of the article is to develop an analytical method for determining the electromagnetic torque and energy losses of voltage-regulated three-phase induction motors operating according to the single-phase circuit with a phase-shifting capacitor.

Object of study. Analytical expressions for calculating the electromagnetic torque and energy losses of a voltage-regulated three-phase induction motor with single-phase power supply will be considered using the example of the Steinmetz scheme (Fig. 1).

Regulation of the motor according to the voltage in this scheme takes place with the help of a thyristor voltage regulator (TVR). Let's note that the method developed in this article is based on the assumption that only the first harmonic component of the voltage is present at the output of the TVR, therefore it can be applied to any type of voltage regulator [14, 15]. Moreover, the voltage regulator can be considered similarly to three-phase systems as an energy-saving element [8]. Here, it should be taken into account that the

used technique does not take into account losses from higher harmonics of the current generated by the thyristor regulator, therefore the effective effect of energy saving will be smaller at low loads [16].

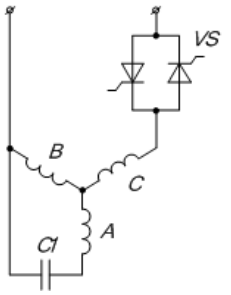

Fig. 1. Scheme of connection of a voltage-regulated three-phase motor in a single-phase network

This technique is proposed for a preliminary search analysis of electromagnetic torque values and energy losses of an induction motor powered by a single-phase network according to a scheme with a thyristor voltage regulator and a phase-shifting capacitor. For more accurate studies, it is necessary to use models that take into account the influence of non-sinusoidal and asymmetric on the motor parameters [17-20].

General relationships in the induction motor in single-phase mode of operation. To analyze the operation of an induction motor in single-phase mode, we will use the method of symmetrical components. The basis of the calculation will be the characteristics of IM in the symmetrical three-phase mode of operation. Here, we introduce the notation: M_1, I_1, Z_1, φ_1 are respectively, the dependence on the torque slip, current, module, and argument of the total resistance of the IM replacement circuit in the symmetrical motor mode, and M_2, I_2, Z_2, φ_2 are the same dependencies in the symmetrical generator mode.

The Kirchhoff equations for the circuit in Fig. 1 will be the following:

$$\underline{U}_C - \underline{U}_B = \underline{U}; \quad (1)$$

$$\underline{U}_A - \underline{U}_B = jX_{C1}\underline{I}_A, \quad (2)$$

where $\underline{U}$ is the complex value of the IM supply voltage, which is the output voltage of the TVR; $\underline{U}_A, \underline{U}_B, \underline{U}_C$ are the complex values of stator phase voltages; $jX_{C1}\underline{I}_A$ is the complex value of the voltage on the phase-shifting capacitor, where $X_{C1} = 1/(\omega \cdot C1)$.

Let's introduce the components of voltages and currents of forward (marked by index p), reverse (n) and zero (0) sequences:

$$\underline{U}_A = \underline{U}_p + \underline{U}_n + \underline{U}_0; \quad (3)$$

$$\underline{U}_B = \underline{U}_p a + \underline{U}_n a^2 + \underline{U}_0; \quad (4)$$

$$\underline{U}_C = \underline{U}_p a^2 + \underline{U}_n a + \underline{U}_0; \quad (5)$$

$$\underline{I}_A = \underline{I}_p + \underline{I}_n + \underline{I}_0, \quad (6)$$

where $\underline{U}_p, \underline{U}_n, \underline{U}_0$ are the complex values of forward, reverse and zero sequence voltages; $a = e^{-j\frac{2\pi}{3}}$ is the rotary multiplier; $\underline{I}_p = \frac{\underline{U}_p}{\underline{Z}_1}, \underline{I}_n = \frac{\underline{U}_n}{\underline{Z}_2}, \underline{I}_0 = \frac{\underline{U}_0}{\underline{Z}_0}$ are the complex values of currents of direct and reverse sequences.

Note that for the scheme in Fig. 1 zero sequence is absent due to the absence of a neutral wire.

Here $\underline{Z}_1, \underline{Z}_2$ are the complex resistances according to the parameters of the substitution schemes, respectively, of the forward and reverse sequences:

$$\underline{Z}_1 = Z_1(\cos\varphi_1 + j\sin\varphi_1); \quad (7)$$

$$\underline{Z}_2 = Z_2(\cos\varphi_2 + j\sin\varphi_2), \quad (8)$$

where $Z_1, Z_2, \varphi_1, \varphi_2$ are the modules and phases of complex resistances of forward and reverse sequences

Substituting (3)–(6) into (1), (2), we obtain:

$$(\underline{U}_p - \underline{U}_n)(a^2 - a) = \underline{U}; \quad (9)$$

$$\underline{U}_p\left(1 - a - \frac{jX_{C1}}{\underline{Z}_1}\right) + \underline{U}_n\left(1 - a^2 - \frac{jX_{C1}}{\underline{Z}_2}\right) = 0. \quad (10)$$

Let's introduce the basic values X_{C_0} for capacitive resistance:

$$X_{C_0} = \frac{\sqrt{3}U}{I_1} = \sqrt{3}Z_1, \quad (11)$$

where U and I_1 are the phase values of voltage and current in symmetrical motor mode.

Also we introduce the relative value of the capacity:

$$x = \frac{X_{C_0}}{X_{C1}} = \frac{1/\omega C_0}{1/\omega C_1} = \frac{C1}{C_0} \quad (12)$$

and the coefficient equal to the ratio of the currents of the anti-switching and motor modes with symmetrical power supply:

$$k_i = \frac{U/Z_2}{U/Z_1} = \frac{Z_1}{Z_2}. \quad (13)$$

After carrying out a series of transformations, we obtain expressions for the forward and reverse sequence voltages:

$$\underline{U}_p = \frac{\underline{U}\left[\frac{\sqrt{3}}{2}x - k_i\sin\varphi_2 - j\left(\frac{1}{2}x + k_i\cos\varphi_2\right)\right]}{\sqrt{3}\left\{\cos\varphi_1 + k_i\cos\varphi_2 + j[\sqrt{3}x - (\sin\varphi_1 + k_i\sin\varphi_2)]\right\}}; \quad (14)$$

$$\underline{U}_n = \frac{-\underline{U}\left[\frac{\sqrt{3}}{2}x - \sin\varphi_1 + j\left(\frac{1}{2}x - \cos\varphi_1\right)\right]}{\sqrt{3}\left\{\cos\varphi_1 + k_i\cos\varphi_2 + j[\sqrt{3}x - (\sin\varphi_1 + k_i\sin\varphi_2)]\right\}}. \quad (15)$$

Let's introduce the parameters characterizing the direct sequence voltage level

$$\alpha = U_p/U, \quad (16)$$

reverse sequence voltage level

$$\beta = U_n/U \quad (17)$$

and asymmetry coefficient

$$\gamma = U_n/U_p. \quad (18)$$

In (16) – (18) U_p, U_n, U are the modules, respectively, of voltages of direct, reverse sequences and supply voltage.

Moving to the modules in (14), (15), we find these parameters:

$$\alpha = \sqrt{\frac{x^2 - \theta_2 k_i x + k_i^2}{\left(\sqrt{3}x - \phi_2\right)^2 + \phi_1^2}}; \quad (19)$$

$$\beta = \sqrt{\frac{x^2 - \theta_1 x + 1}{\left(\sqrt{3}x - \phi_2\right)^2 + \phi_1^2}}; \quad (20)$$

$$\gamma = \sqrt{\frac{x^2 - \theta_1 x + 1}{x^2 - \theta_2 k_i x + k_i^2}}, \quad (21)$$

where $\theta_1 = \sqrt{3}\sin\varphi_1 + \cos\varphi_1$, $\theta_2 = \sqrt{3}\sin\varphi_2 - \cos\varphi_2$, $\phi_1 = \cos\varphi_1 + k_i\cos\varphi_2$, $\phi_2 = \sin\varphi_1 + k_i\sin\varphi_2$.

According to the described method, these asymmetry parameters can also be determined for other schemes of connection a three-phase motor in a single-phase network, for example, for a series-parallel scheme [3] or for a «star with a zero wire» scheme with self-excitation of the capacitor phase through a rotating rotor [21]. To do this, it is necessary to write down the Kirchhoff equations (1), (2) corresponding to each scheme and perform the following analytical transformations (3) – (15). Then parameters (16) – (18) can be used in further calculations for these schemes. Therefore, the proposed method can be generalized also to other possible schemes for connection a three-phase motor with a phase-shifting capacitor in a single-phase network.

Calculation of the electromagnetic torque of an induction machine in single-phase mode of operation. The electromagnetic torque in the symmetrical motor mode in the case of three-phase power supply M_1 can be determined from the expressions of the electromagnetic power P_{em}. On the one hand, it is equal

$$P_{em} = M_1 \cdot \omega_0, \quad (22)$$

where ω_0 is the angular frequency of idling.

On the other hand

$$P_{em} = 3I_{r1}^2 \frac{R_2}{s}, \quad (23)$$

where $I_{r1} = U/Z_{1r}$ is the effective value of the reduced rotor current in symmetrical mode; s is the slip; R_2 is the active resistance of the rotor reduced to the stator winding.

Equating these two expressions, we obtain:

$$M_1 = \frac{3}{\omega_0}\left(I_{r1}^2 \frac{R_2}{s}\right). \quad (24)$$

The electromagnetic torque in single-phase mode is defined as the difference between the torques of forward and reverse sequences:

$$M = M_p - M_n = \frac{3}{\omega_0}\left(I_{rp}^2 \frac{R_2}{s} - I_{rn}^2 \frac{R_2}{2-s}\right), \quad (25)$$

where $I_{rp} = U_p/Z_{1r}$, $I_{rn} = U_n/Z_{2r}$ are the modules of reduced rotor currents of forward and reverse sequences; Z_{1r}, Z_{2r} are the respectively, the modules of the equivalent resistances of the load branch of the L-shaped schemes of substitution of forward and reverse sequences.

Let's introduce the coefficient μ, which is equal to the ratio of torques for single-phase mode and motor three-phase symmetrical mode $\mu = M/M_1$:

$$\mu = \alpha^2 + k_\mu \beta^2 = \alpha^2\left(1 + k_\mu \gamma^2\right), \quad (26)$$

where $k_\mu = M_2/M_1$ is the coefficient equal to the ratio of generator M_2 and motor M_1 torques in three-phase symmetrical mode:

$$k_\mu = -\frac{Z_{1r}^2}{Z_{2r}^2} \cdot \frac{s}{2-s}. \quad (27)$$

Since the single-phase mode and the three-phase motor mode are considered with the same slips, the coefficient μ also determines the ratio of electromagnetic powers of AD when operating in these modes.

Using the obtained coefficients α, β, γ, μ, it is possible to analyze the IM characteristics using formulas valid for the three-phase symmetrical mode of operation obtained from the substitution scheme.

According to (24), the electromagnetic torque in the three-phase symmetrical mode is determined by:

$$M_1 = \frac{3U^2 R_2}{\omega_0 s\left[\left(R_1 + \frac{R_2}{s}\right)^2 + \left(X_1 + X_2\right)^2\right]}. \quad (28)$$

where R_1, R_2, X_1, X_2 are the parameters of the IM substitution scheme.

The electromagnetic torque of IM in single-phase mode is determined by the expression:

$$M = \mu M_1 = \frac{\alpha^2\left(1 + k_\mu \gamma^2\right)3U^2 R_2}{\omega_0 s\left[\left(R_1 + \frac{R_2}{s}\right)^2 + \left(X_1 + X_2\right)^2\right]}. \quad (29)$$

As can be seen from (29), the torque of a single-phase induction motor with regulated voltage at a given slip depends on the supply voltage, the direct sequence voltage level and the asymmetry coefficient, which in turn depend on the relative value of the capacity of the phase-shifting capacitor $x = X_{C_0}/X_{C1}$.

Calculation of losses in an induction motor in single-phase mode of operation. When operating with constant voltage, losses in IM in a symmetrical three-phase mode are divided into constant losses (consisting of losses in the stator copper from the magnetizing current and losses in steel), which do not depend on the load, and variable losses (consisting of losses in the stator copper and the rotor from the load current), which depend on the electromagnetic torque when operating with constant voltage [8]:

$$\Delta P_3 = \left(\frac{M}{M_N}\right)^2 \Delta P_{\text{var}.N} + \Delta P_{const.N}, \quad (30)$$

where $\Delta P_{\text{var}.N}, \Delta P_{const.N}$ are the nominal variable and constant losses; M_N is the nominal torque.

In an induction motor, when operating with alternating voltage, both mentioned components of losses become variable, and variable losses depend on slip and torque, and constant losses – on the voltage of the stator windings. The loss power in the rotor (slip losses):

$$\Delta P_r = M\omega_0 s, \quad (31)$$

where ω_0 is the idling rotation speed.

The loss power in the stator from the load current is recalculated through the loss power in the rotor and the ratio of the active resistances of the stator and rotor:

$$\Delta P_s = \Delta P_r \frac{R_1}{R_2}, \quad (32)$$

where R_1, R_2 are the active resistances of the IM substitution scheme.

Thus, the expression of variable losses has the form:

$$\Delta P_{\text{var}} = M\omega_0 s\left(1+\frac{R_1}{R_2}\right). \quad (33)$$

The second component of losses in IM, ΔP_{const}, depends on the voltage of the stator windings, which is indirectly equivalent to the dependence on the torque. Thus, when assuming the linearity of the parameters of the magnetic circuit and taking into account only the first harmonic component of currents and voltages, constant losses are proportional to the square of the voltage, which, in turn, is proportional to the electromagnetic torque:

$$\frac{\Delta P_{const}}{\Delta P_{const.N}} = \left(\frac{U}{U_N}\right)^2 = \frac{M}{M_{nat}}, \quad (34)$$

where ΔP_{const}, U, M are the current values of constant losses, voltage and torque; $\Delta P_{const.N}$, U_N, M_{nat} are the constant losses in the nominal mode, nominal voltage and torque on the natural mechanical characteristic at the nominal voltage and corresponding slip. Therefore, permanent losses can be expressed as:

$$\Delta P_{const} = \left(\frac{U}{U_N}\right)^2 \Delta P_{const.N}. \quad (35)$$

The basic values of the main types of losses are determined in the nominal mode and are presented in the form of two components. Let's express them through the parameters of the substitution scheme. The first component is variable losses (losses in the copper of the rotor and stator from the load current) in the nominal mode:

$$\Delta P_{\text{var}.N} = M_N\omega_0 s_N\left(1+\frac{R_1}{R_2}\right). \quad (36)$$

where s_N is the nominal slip.

Then from (33), (36):

$$\Delta P_{\text{var}} = \frac{M}{M_N}\frac{s}{s_N}\Delta P_{\text{var}.N}. \quad (37)$$

The second component is constant losses (losses in the stator copper from the magnetizing current and losses in the steel) in the nominal mode:

$$\Delta P_{const.N} = \frac{M_N\omega_0}{s_N}\left(\frac{R_1R_2}{X_0^2}+\frac{R_2}{R_0}\right), \quad (38)$$

where R_0, X_0 are the parameters of the magnetization branch of the IM substitution scheme.

When IM operates in single-phase mode, total electrical losses are equal to the sum of losses from direct and reverse sequence currents:

$$\Delta P_1 = \Delta P_{\text{var}.p} + \Delta P_{const.p} + \Delta P_{\text{var}.n} + \Delta P_{const.n}. \quad (39)$$

In the general case, constant and variable losses are calculated by (33), (35) separately for forward and reverse sequences. In the first case, the torque, slip and voltage values for the direct sequence are substituted into them: M_p, s and U_p. In the second one – M_n, $2–s$, and U_n.

In the further analysis, we will use the coefficients α, β, γ, k_μ, μ obtained earlier. When adjusting the IM voltage, the variable losses are expressed by dependencies:

- for the direct sequence:

$$\Delta P_{\text{var}.p} = \frac{M_p}{M_N}\frac{s}{s_N}\Delta P_{\text{var}.N}, \quad (40)$$

- for the reverse sequence:

$$\Delta P_{\text{var}.n} = \frac{M_n}{M_N}\frac{2-s}{s_N}\Delta P_{\text{var}.N}. \quad (41)$$

Let's express the torques from the currents of the forward and reverse sequences in terms of motor M_1 and the generator (anti-switching) M_2 torques in the symmetrical mode:

$$M_p = M_1\left(\frac{U_p}{U}\right)^2 = \alpha^2 M_1, \quad (42)$$

$$M_n = M_2\left(\frac{U_n}{U}\right)^2 = \beta^2 M_2. \quad (43)$$

Taking into account that

$$M_2/M_1 = k_\mu, \quad (44)$$

we obtain:

$$M_n = k_\mu\beta^2 M_1. \quad (45)$$

Then the total variable losses:

$$\Delta P_{\text{var}} = \Delta P_{\text{var}.p} + \Delta P_{\text{var}.n} = \\ = \alpha^2\frac{M_1}{M_N}\frac{s}{s_N}\Delta P_{\text{var}.N} + k_\mu\beta^2\frac{M_1}{M_N}\frac{2-s}{s_N}\Delta P_{\text{var}.N}. \quad (46)$$

Let's express ΔP_{var} through the coefficient of asymmetry $\gamma = \beta/\alpha$:

$$\Delta P_{\text{var}} = \alpha^2 M_1 A\left(s + k_\mu\gamma^2[2-s]\right), \quad (47)$$

where $A = \frac{\Delta P_{\text{var}.N}}{M_N s_N}$ is the constant coefficient.

Constant losses during voltage regulation are expressed by dependencies:

- for the direct sequence:

$$\Delta P_{const.p} = \left(\frac{U_p}{U_N}\right)^2 \Delta P_{const.N} = \alpha^2\left(\frac{U}{U_N}\right)^2 \Delta P_{const.N}, \quad (48)$$

- for the reverse sequence:

$$\Delta P_{const.n} = \left(\frac{U_n}{U_N}\right)^2 \Delta P_{const.N} = \beta^2\left(\frac{U}{U_N}\right)^2 \Delta P_{const.N}. \quad (49)$$

Taking into account the dependence

$$\left(\frac{U}{U_N}\right)^2 = \frac{M_1}{M_{nat}}, \quad (50)$$

where M_{nat} is the torque on the natural mechanical characteristic in motor mode with three-phase symmetrical power supply with slip, equal to slip in single-phase mode, we obtain:

$$\Delta P_{const.p} = \alpha^2 \frac{M_1}{M_{nat}} \Delta P_{const.N}, \quad (51)$$

$$\Delta P_{const.n} = \beta^2 \frac{M_1}{M_{nat}} \Delta P_{const.N}. \quad (52)$$

For linearized mechanical characteristics of IM, $M_{nat}/s = M_N/s_N$ is a fair relationship, which allows expressing M_{nat} through s. Then the total variable losses of IM can be given by the expression

$$\Delta P_{const} = \Delta P_{const.p} + \Delta P_{const.n} = \alpha^2 M_1 B \frac{1}{s}\left(1+\gamma^2\right), \quad (53)$$

where $B = \dfrac{\Delta P_{const.N} s_N}{M_N}$ is the constant coefficient.

The electromagnetic torque in the asymmetric mode M and the torque in the motor symmetric mode M_1 are related by the coefficient μ:

$$\mu = \frac{M}{M_1} = \alpha^2\left(1 + k_\mu \gamma^2\right). \quad (54)$$

Then the total electrical losses in IM from currents of direct and reverse sequences:

$$\Delta P_1 = \frac{M}{1+k_\mu\gamma^2}\left(A\left[s + k_\mu\gamma^2(2-s)\right] + B\frac{1}{s}\left[1+\gamma^2\right]\right). \quad (55)$$

The proposed technique allows for preliminary search analysis of this system.

Calculation results. We analyze the energy characteristics of IM 4A71B2U3 with a phase-shifting capacitor when connected according to the Steinmetz scheme (Fig. 1), calculated according to the above method. Figure 2 shows graphs of the dependencies of the relative losses of the single-phase mode ΔP_1 to the losses of the three-phase symmetrical mode ΔP_3 on slip at different values of the capacity of the phase-shifting capacitor and a constant nominal voltage. From these graphs, it can be seen that when the load changes, so that the losses do not exceed by more than 20 % of the symmetrical mode loss, it is necessary to change the capacity of the capacitor.

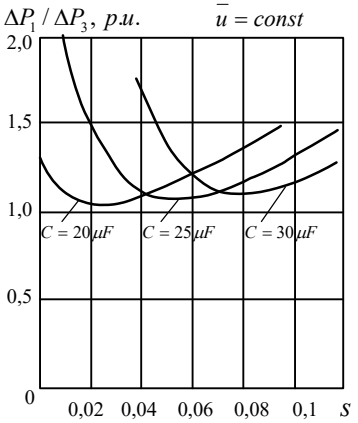

Fig. 2. Dependencies of relative losses on slip at different capacity values

At the same time, if the supply voltage is changed when the load changes, it is possible to achieve an energy-saving mode, as in the case of a symmetrical three-phase supply [8]. For example, Fig. 3 shows graphs of the dependencies of the relative losses $\Delta P_1/\Delta P_3$ on slip at different values of the relative voltage of the single-phase power supply $\bar{u} = U/U_N$ and constant value of the capacity of the phase-shifting capacitor C = 20 μF. From these characteristics, it can be seen that with constant value of the capacity, IM has a minimum of relative losses with approximately constant value of slip at different values of the supply voltage.

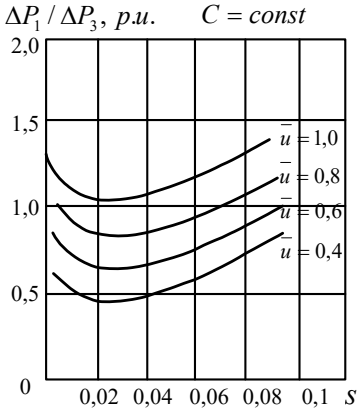

Fig. 3. Dependencies of relative losses on slip at different supply voltage values

Therefore, if this slip is kept constant when the load changes, it is possible to achieve a mode of loss minimization with constant optimal value of the capacity according to the criterion of the minimum ratio of single-phase mode losses to three-phase mode losses determined by the curves in Fig. 3, for some slip, which can be specified, for example, according to the recommendations [8], provided that electrical losses do not exceed the nominal value. This shows that the thyristor voltage regulator can be used as an energy-saving element under a variable load, while the capacity of the capacitor can remain constant over a wide range of load changes.

A comparison of the values calculated by the proposed method with those obtained by the model [20], which takes into account the influence of non-sinusoidity and asymmetry and is based on the differential equations of the electric machine, showed deviations of 3–15 % when determining torques and 5–20 % when determining losses. Smaller values correspond to modes with slips close to nominal. However, the analytical technique presented in the article allows for a comparative analysis of the characteristics of the motor with different capacities of the phase-shifting capacitor under different schemes of connection in a single-phase network and in the symmetrical mode under the same assumptions, such as the invariance of the parameters of the substitution schemes and the neglect of mechanical and additional losses. This makes it possible to see the influence of the capacity of the phase-shifting capacitor and the switching circuit [3, 21] on energy losses due to the asymmetric mode of operation.

Influence of higher harmonics. Functional capabilities of voltage-regulated induction electric drives are implemented in two main directions. The first one is related to speed regulation in a small (up to 30 %) range with a predominantly valve-like nature of the load and

ensuring a soft start [8]. With power supply from TVR, the power consumption is higher than with sinusoidal power supply due to increased losses from higher harmonics, with the same torque and slip reaching at α = 90–110 electrical degrees an excess of 20–30 % [16]. Moreover, the specified speed change range is provided by changing the control angle of thyristors α<60 electrical degrees [3]. If it is necessary to increase the adjustment range, it is possible to use a combined scheme with switching the connection scheme of the Steinmetz power part to a series-parallel one, which has a better harmonic composition [16].

The same scheme can provide a higher starting torque with a working capacity compared to the Steinmetz scheme [3]. While for schemes with a constant structure of the power part, the use of a working capacity may not provide the necessary starting properties, and requires the use of a separate starting capacitor, which worsens the weight and dimensions of the unit.

The second direction of the development of these electric drives is related to the minimization of power losses when the load changes, which, in the case of the assumption of a sinusoidal voltage at the output of the voltage regulator, is achieved by stabilizing the slip [8]. With the practical implementation of the law of energy consumption optimization, due to the influence of higher harmonics, the range of load torque change, during which energy saving is possible, decreases. To increase this range is also possible by using a combined scheme with the switching of the Steinmetz scheme to the «star with zero wire» scheme at low loads [21].

Also, the method proposed in the article, which takes into account only the first harmonic, can be applied to voltage regulators with modern means of power quality correction [22-25].

Conclusions.

Using the example of the Steinmetz scheme, an analytical method for calculating the electromagnetic torque and energy losses of a three-phase induction motor based on the scheme of connection in a single-phase network with a phase-shifting capacitor has been developed, which allows, under certain assumptions, to carry out a preliminary search analysis of voltage-regulated single-phase induction electric drives and to choose the optimal parameters of the capacitor. The proposed technique can also be applied to other possible schemes for connection a three-phase motor in a single-phase network when applying the Kirchhoff equations corresponding to these schemes. It is shown that the voltage regulator can be used as an energy-saving device, and its use allows the use of a constant capacity of the phase-shifting capacitor, optimal for one slip value, when the load changes over a wide range, provided that this slip is stabilized.

Conflict of interest. The authors declare no conflict of interest.

REFERENCES

1. Popovych O.M., Bibik O.V. Search and evaluation of ways to increase the energy efficiency of a monoblock pump in the application of complex design. *Bulletin of the NTU «KhPI». Series: Electric machines and electromechanical energy conversion*, 2018, no. 5, pp. 79-82. (Ukr). Available at: http://emepe.khpi.edu.ua/article/view/135209 (accessed 16 March 2022).

2. Khizhniak T.A., Husev O.O., Lipinskyi I.S. Remote control of electromechanical devices in the climate control system. *Technical Electrodynamics*, 2016, no. 5, pp. 32-34. (Ukr). doi: https://doi.org/10.15407/techned2016.05.032.

3. Shurub Yu.V, Vasilenkov V.Ye., Tsitsyurskiy Yu.L. Investigation of properties of combined scheme of single-phase switching of induction electric drive of pumping plants. *Technical Electrodynamics*, 2018, no. 6, pp. 50-53. (Ukr). doi: https://doi.org/10.15407/techned2018.06.050.

4. Malyar V.S., Malyar A.V. Established modes and static characteristics of three phase asynchronous motor powered with single phase network. *Energetika. Proceedings of CIS Higher Education Institutions and Power Engineering Associations*, 2016, vol. 59, no. 6, pp. 536-548. (Rus). doi: https://doi.org/10.21122/1029-7448-2016-59-6-536-548.

5. Malyar S.V., Malyar A.V. Mechanical characteristics of three-phase induction motors with single-phase power supply. *Electrical Engineering & Electromechanics*, 2016, no. 3, pp. 21-24. doi: https://doi.org/10.20998/2074-272X.2016.3.03.

6. da Silveira E.P., Pires R.C., de Almeida A.T.L., Jose A., Rezek J. Direct on line starting induction motor with Thyristor Switched Capacitor based voltage regulation. *2009 Brazilian Power Electronics Conference*, 2009, pp. 1124-1129. doi: https://doi.org/10.1109/COBEP.2009.5347707.

7. Malyar V., Hamola O., Maday V. Calculation of capacitors for starting up a three-phase asynchronous motor fed by single-phase power supply. *2016 17th International Conference Computational Problems of Electrical Engineering (CPEE)*, 2016, pp. 1-4. doi: https://doi.org/10.1109/CPEE.2016.7738735.

8. Andryushchenko O.A. Requirements for asynchronous electric motor and thyristor converter in electric drive ТПН-АД. *Elektromashynobuduvannia ta elektroobladnannia*, 1998, no. 50, pp. 10-16. (Rus). Available at: https://eltecs.op.edu.ua/index.php/journal/article/view/2820 (accessed 16 March 2022).

9. Shurub Yu.V. Statistical optimization of voltage regulated induction electric drives. *Technical Electrodynamics*, 2014, no. 5, pp. 116-118. (Ukr).

10. Rajaji L., Kumar C. Adaptive Neuro Fuzzy based soft starting of voltage-controlled induction motor drive. *IEEE SoutheastCon 2008*, pp. 448-453. doi: https://doi.org/10.1109/SECON.2008.4494337.

11. Shurub Y., Dudnyk A., Vasilenkov V., Tsitsyurskiy Y. Simulation of Random Loads Applied to Statistical Optimal Synthesis of Electric Drives. *2019 IEEE International Conference on Modern Electrical and Energy Systems (MEES)*, 2019, pp. 354-357. doi: https://doi.org/10.1109/MEES.2019.8896464.

12. Beshta A., Syomin A. Parameters estimation of induction motor equivalent circuit using asymmetrical stator supply. *Electromechanical and Energy Saving Systems*, 2014, no. 2, pp. 10-16. (Rus). Available at: http://ees.kdu.edu.ua/en/22014-26 (accessed 16 March 2022).

13. Savchenko V., Synyavskiy O., Dudnyk A., Nesvidomin A. Influence of Voltage Deviation and Asymmetry on Transitional Processes in Asynchronous Electric Drive. *2021 IEEE International Conference on Modern Electrical and Energy Systems (MEES)*, 2021, pp. 1-6. doi: https://doi.org/10.1109/MEES52427.2021.9598660.

14. Zigirkas G., Kalomiros J. Voltage control of single-phase induction motors using asymmetrical PWM and fuzzy logic. *2016 5th International Conference on Modern Circuits and Systems Technologies (MOCAST)*, 2016, pp. 1-4. doi: https://doi.org/10.1109/MOCAST.2016.7495119.

15. Sowmmiya U., Jamuna V. Voltage control scheme for three phase SVM inverter fed induction motor drive systems. *2011 1st*

International Conference on Electrical Energy Systems, 2011, pp. 207-211. doi: https://doi.org/10.1109/ICEES.2011.5725329.
16. Shurub Y.V., Tsitsyurskiy Y.L. Harmonic analysis of the combined circuit of single-phase switching of induction electric drive with thyristor control. *Electrical Engineering & Electromechanics*, 2020, no. 1, pp. 25-28. doi: https://doi.org/10.20998/2074-272X.2020.1.04.
17. Milykh V.I. Numerically-field analysis of the adequacy of the design data of three-phase induction motors and the method of their refinement on this basis. *Technical Electrodynamics*, 2018, no. 1, pp. 47-55. (Rus). doi: https://doi.org/10.15407/techned2018.01.047.
18. Milykh V.I. The system of automated formation of electrical machines computational models for the FEMM software environment. *Technical Electrodynamics*, 2018, no. 4, pp. 74-78. doi: https://doi.org/10.15407/techned2018.04.074.
19. Popovych O., Golovan I. Currents System for Efficient Mathematical Modeling of an Induction Motor Using the Field Analysis. *2019 IEEE International Conference on Modern Electrical and Energy Systems (MEES)*, 2019, pp. 142-145. doi: https://doi.org/10.1109/MEES.2019.8896624.
20. Popovych O.M., Golovan I.V. Study of changed main flux reactance of squirrel-cage induction motors using field analysis of their starting characteristics. *Technical Electrodynamics*, 2018, no. 5, pp. 69-72. doi: https://doi.org/10.15407/techned2018.05.069.
21. Shurub Y.V., Tsitsyurskiy Y.L., Rudenko Y.M. Improving the efficiency of an induction capacitor motor at partial load modes. *Bulletin of the NTU «KhPI». Series: Electric machines and electromechanical energy conversion*, 2019, no. 4, pp. 107-110. (Ukr). doi: https://doi.org/10.20998/2409-9295.2019.4.16.
22. Artemenko M.Y., Kaplun V.V., Bobrovnyk V.M., Polishchuk S.Y. Active filters application for energy losses reduction in three-phase power supply systems. *Technical Electrodynamics*, 2018, no. 4, pp. 53-56. doi: https://doi.org/10.15407/techned2018.04.053.
23. Chyzhenko O.I., Rybina O.B., Trach I.V. Semiconductive regulator for managing the network modes running in direct start of the asynchronal machine of the comparable capacity. *Proceedings of the Institute of Electrodynamics of the National Academy of Sciences of Ukraine*, 2019, no. 54, pp. 95-102. (Ukr). doi: https://doi.org/10.15407/publishing2019.54.095.
24. Butkevych O.F., Chyzhenko O.I., Popovych O.M., Trach I.V. An influence of the facts upon an electrical network's mode during direct start-up of an asynchronous machine in the complex load's composition. *Technical Electrodynamics*, 2018, no. 6, pp. 62-68. doi: https://doi.org/10.15407/techned2018.06.062.
25. Butkevych O., Chyzhenko O., Popovych O., Trach I., Golovan I. A Study of Transitional Modes of the Electric Network with the Powerful Electromechanical Load and FACTS. *2019 IEEE 6th International Conference on Energy Smart Systems (ESS)*, 2019, pp. 261-266. doi: https://doi.org/10.1109/ESS.2019.8764223.

Received 10.02.2022
Accepted 23.06.2022
Published 06.11.2022

Yu.V. Shurub[1], *PhD, Senior Research Scientist,*
V.Ye. Vasilenkov[2], *PhD, Assistant Professor,*
Yu.L. Tsitsyurskiy[2],
[1] Institute of Electrodynamics of NAS Ukraine,
56, Peremogy Avenue, Kyiv, 03680, Ukraine,
e-mail: yvshur@ukr.net (Corresponding Author)
[2] National University of Life and Environmental Sciences of Ukraine,
11, Heroiv Oborony Str., Kyiv, 03041, Ukraine,
e-mail: wasil14@ukr.net; geosfera@nubip.edu.ua

How to cite this article:
Shurub Yu.V., Vasilenkov V.Ye., Tsitsyurskiy Yu.L. Method of calculation of electromagnetic torque and energy losses of three-phase induction motors when powered by a regulated single-phase voltage. *Electrical Engineering & Electromechanics*, 2022, no. 6, pp. 8-14. doi: https://doi.org/10.20998/2074-272X.2022.6.02

UDC 621.3.013 https://doi.org/10.20998/2074-272X.2022.6.03

B.I. Kuznetsov, T.B. Nikitina, I.V. Bovdui, O.V. Voloshko, V.V. Kolomiets, B.B. Kobylianskyi

Synthesis of an effective system of active shielding of the magnetic field of a power transmission line with a horizontal arrangement of wires using a single compensation winding

Aim. *The theoretical and experimental studies of the effectiveness of reducing the level of the magnetic field in two-storey cottage of the old building of a power transmission line with a horizontal arrangement of wires by means of active shielding with single compensation winding.* ***Methodology*** *Spatial location coordinates of the compensating winding and the current in the shielding winding were determined during the design of systems of active screening based on solution of the vector game, in whith the vector payoffs is calculated based on Biot-Savart's law. The solution of this vector game calculated based on algorithms of multi-swarm multi-agent optimization.* ***Results*** *The results of theoretical and experimental studies of the effectiveness of reducing the level of the magnetic field in two-storey cottage of the old building of a power transmission line with a horizontal arrangement of wires by means of active shielding with single compensation winding are presented.* ***Originality.*** *For the first time, the theoretical and experimental studies of the effectiveness of reducing the level of the magnetic field in two-storey cottage of the old building of a power transmission line with a horizontal arrangement of wires by means of active shielding with single compensation winding are considered.* ***Practical value****. From the point of view of the practical implementation it is shown the possibility to reduce the level of magnetic field in two-storey cottage of the old building from power transmission line with a horizontal arrangement of wires by means of active shielding with single compensation winding to the sanitary standards of Ukraine.* References 48, figures 14.
Key words: **power transmission line, horizontal arrangement of wires, magnetic field, system of active screening, computer simulation, experimental research**.

Мета. *Проведено теоретичні та експериментальні дослідження ефективності зниження рівня магнітного поля в двоповерховому котеджі старої будівлі ЛЕП з горизонтальним розташуванням проводів за допомогою активного екранування з однією компенсаційною обмоткою.* ***Методика***. *Просторові координати розташування компенсуючої обмоти і струму в обмотці визначено при проектуванні системи активного екранування на основі рішення векторної гри, в якій вектор ціни розраховуються за законом Біо-Савара. Рішення цієї векторної гри розраховано на основі алгоритмів багаторойової багатоагентної оптимізації.* ***Результати.*** *Наведено результати теоретичних та експериментальних досліджень ефективності зниження рівня магнітного поля в двоповерховому котеджі старої будівлі ЛЕП з горизонтальним розташуванням проводів за допомогою активного екранування з однією компенсаційною обмоткою.* ***Оригінальність***. *Вперше проведено теоретичні та експериментальні дослідження ефективності зниження рівня магнітного поля в двоповерховому котеджі старої будівлі ЛЕП з горизонтальним розташуванням проводів за допомогою активного екранування з однією компенсаційною обмоткою.* ***Практична цінність***. *З точки зору практичної реалізації показана можливість зниження рівня магнітного поля в двоповерховому котеджі старої будівлі від ЛЕП з горизонтальним розташуванням проводів за допомогою активного екранування з однією компенсаційною обмоткою дорівня санітарних норм України.* Бібл. 48, рис. 14.
Ключові слова: **повітряна лінія електропередачі, горизонтальне розташування проводів, магнітне поле, система активного екранування, комп'ютерне моделювання, експериментальні дослідження.**

Introduction. The most dangerous source of technogenic magnetic field of power frequency for the population are high-voltage power lines. Without taking special measures, they create an intensive magnetic field (MF), which has carcinogenic properties at distances up to 100 m from the transmission line. Therefore, the world is tightening sanitary standards for the maximum allowable level of MF induction 50–60 Hz (less than 1 μT) and intensive work is being done to ensure them for the population. Currently, strict sanitary norms on the induction of MF (0.5 μT) are introduced in the regulations of the Ministry of Energy of Ukraine. However, at present in Ukraine these norms are often exceeded, which poses a threat to the health of millions of people living closer than 100 m from high-voltage power lines.

Comprehensive experimental studies of 10–330 kV overhead transmission lines conducted by the A. Pidhornyi Institute of Mechanical Engineering Problems of the National Academy of Sciences of Ukraine showed [1-4], that their MF are 3-5 times higher than the normative level at the border of previously formed sanitary zones by electric field.

This situation requires urgent measures to reduce by 3-5 times the MF of existing transmission lines within the cities of Ukraine. A similar situation is typical for most industrialized countries of the world, but in these countries have already created and widely used technologies for normalization of existing transmission lines.

The most effective technology is the reconstruction of power lines by removing them to a safe distance from residential buildings, or replacing overhead power lines with a cable line. However, such reconstruction requires huge financial resources. Therefore, less expensive for Ukraine are less expensive methods of shielding MF operating power lines, of which the required efficiency is provided by methods of active contour shielding of the magnetic field [5-10].

The technology of active contour shielding of magnetic field power lines has been developed [11-18] and used in developed countries for more than 10 years, such as the United States and Israel. In Ukraine at present, both such technology and the scientific basis for its creation are absent [19]. This does not allow relatively inexpensive methods to protect the population from man-made industrial frequency industrial power generated by transmission lines. Therefore, the creation of scientific bases of domestic technology of active shielding of industrial frequency magnetic field in buildings to a safe level is an urgent scientific and technical problem.

Many residential buildings and structures are located in close proximity to high-voltage power lines so that the level of induction of the MF inside them exceeds modern sanitary standards. In addition, due to the constant rise in land prices, the construction of residential, administrative

and other public buildings and structures in the areas of the existing high-voltage power lines continues. One of the possible ways to operate such buildings is the use of active shielding systems.

At present, various systems of active shielding of the technogenic magnetic field of power frequency are being intensively researched and implemented all over the world. In such systems, special windings are used as the executive body of the active shielding system – active winding, the number of which is determined by the specifics of the problem to be solved.

The simplest system is one that uses only one single compensating winding.

The aim of the work is to synthesize and study the effectiveness of the simplest system of active shielding of the magnetic field of a single-circuit power line with a horizontal arrangement of wires using only one compensation winding to reduce the magnetic field to a safe level.

Problem statement. As a source of technogenic magnetic field in the development of a power transmission line layout, we will take a single-circuit three-phase power transmission line 110 kV with a horizontal arrangement of current conductors, the dimensions of the supports of which are shown in Fig. 1.

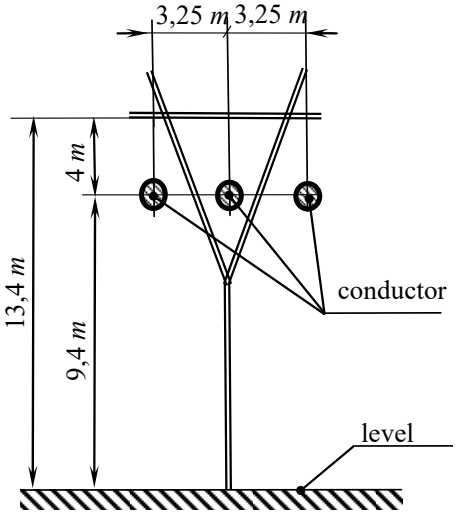

Fig. 1. Dimensions of the power transmission line with horizontal arrangement of wires

The choice of the dimensions of the suspension of current conductors on the supports of the power transmission line is carried out based on the condition for creating the maximum external magnetic field created by the current conductors of the power transmission line along the passage of the power transmission line route, namely, for the option with a minimum height of the location of the current conductors and the maximum distance between them. Based on the stated conditions, as the calculated dimensions of the power transmission line support, we select the dimensions of the anchor cable support (Fig. 1), while taking into account the height of the insulators (1 m) and the amount of sag of the conductors in the middle part between the supports (3 m).

The calculated dimensions of the anchor cable support of the «glass» type, taking into account the sag of the current conductors and the height of the insulators, are shown in Fig. 1. We do not take into account the «dance» of current conductors under the action of wind load, assuming the projection of current conductors in a vertical plane perpendicular to the base of the power transmission line support.

On Fig. 2 are shown the layout of the power transmission line, compensating winding and protected area.

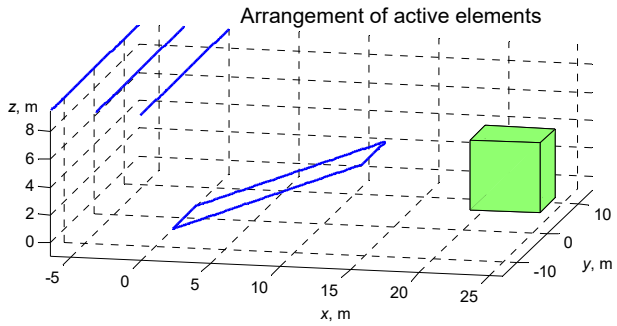

Fig. 2. Layout of the power transmission line, compensating winding and protected area

On Fig. 3 are shown lines of equal level of the induction module of the initial magnetic field of a three-phase single-circuit overhead power line. This induction is computed at a power line current of 1000 A. The induction of initial magnetic field in the considered space is 1.8 μT, which is 3.6 times higher than sanitary norms.

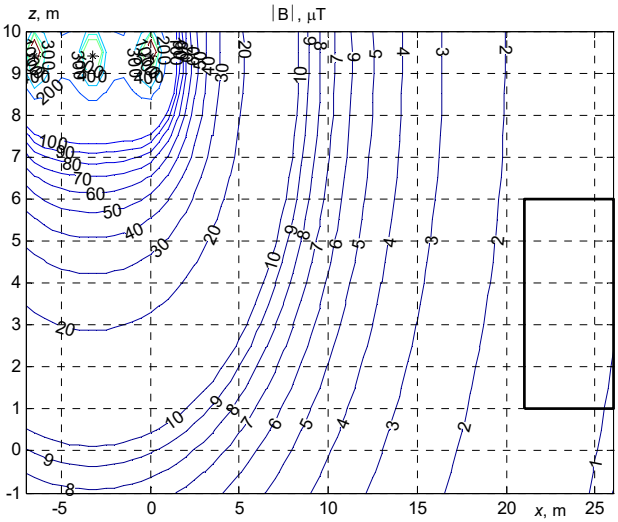

Fig. 3. Lines of equal level of the induction module of the initial magnetic field of a three-phase single-circuit overhead power line

To reduce the level of the magnetic field around the world, systems of active shielding of the magnetic field are used with the help of a system of special controlled magnetic field sources – windings with adjustable current, installed in the area where it is necessary to maintain internal magnetic field parameters [11-14].

For a given shielding space, in particular an two-storey cottage of the old building located in the immediate vicinity of an overhead power line, it is necessary to create a magnetic field by means of active shielding, which would compensate for the original magnetic field.

Consider a system of active shielding of magnetic field using a system of special controlled sources of magnetic field – windings with adjustable current, installed in the area where it is necessary to maintain the parameters of the internal magnetic field within specified limits.

Computational method. We introduce the vector of the required parameters of systems of active shielding, the components of which are vector of coordinates of the spatial location of the compensation windings and regulators parameters [20-24]. Also we introduce vector of the parameter of uncertainty of external magnetic field model [23, 24]. Then the problem of synthesis of systems of active shielding is associated with computation of such vector of the required parameters of systems of active shielding which assumes a minimum value from maximum value of the magnetic flux density at selected points of the shielding space [25-29]. However, in this case, it is necessary to simultaneously determine such a value of vector of the parameter uncertainty, at which the maximum value of the same magnetic flux density is maximum. This is the worst-case approach when robust systems synthesis [30-33].

This problem is the multi-criteria two-player zero-sum antagonistic game [40, 41]. The vector payoffs are the magnetic flux density in points of the shielding space. The vector payoff is the vector nonlinear functions of vector of the required parameters of systems of active shielding and vector of the parameter of uncertainty of external magnetic field model and calculated based on Biot-Savart's law [1]. In this game the first player is the parameters of systems of active shielding and its strategy is the minimization of vector payoff. The second player is the vector of parameter uncertainty and its strategy is maximization of the same vector payoff. The decision of this game is calculated on based of multi-swarm stochastic multi-agent optimization algorithm [42-48]. This decision is choose from systems of Pareto-optimal decisions [42].

Simulation results. Let us study the efficiency of the synthesized system of active shielding for this power transmission lines. To compensate for this technogenic magnetic field in the space under consideration, only one single compensation winding is used, the spatial arrangement of which is shown in Fig. 2. The distribution of the resulting magnetic field with the active screening system turned on is shown in Fig. 4.

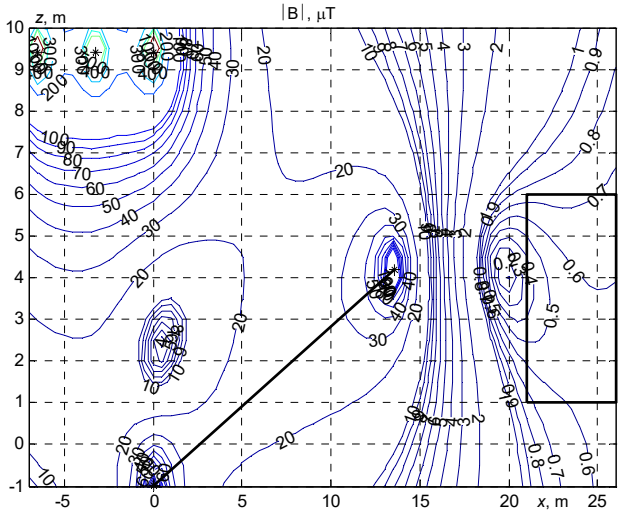

Fig. 4. Lines of equal level of the magnetic field induction module of a three-phase single-circuit overhead power line with active shielding system enabled with one winding of the magnetic actuator

As can be seen from this figure, using the active screening system, it was possible to reduce the induction level of the initial magnetic field to the level of 0.6 μT in the space under consideration. In this case, the efficiency of the active shielding system is more than 2.

On Fig. 5 are shown the dependences of the induction value of the initial magnetic field and the magnetic field with the active shielding system turned on as a function of the distance from the extreme current conductor of the power line.

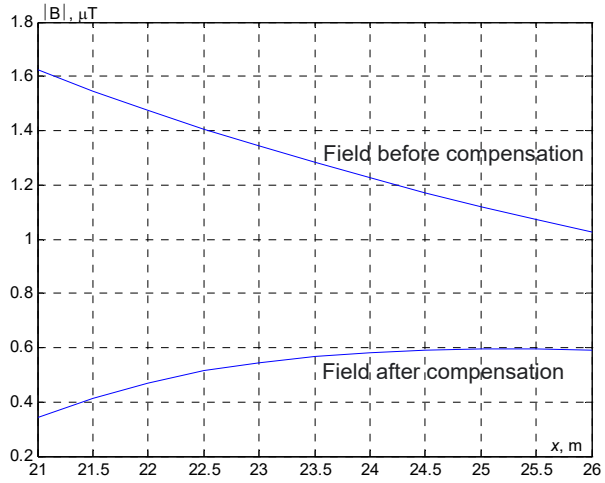

Fig. 5. Dependences of the induction value of the initial magnetic field and the magnetic field with the active shielding system turned on as a function of the distance from the extreme current conductor of the power line

On Fig. 6 are shown the space time characteristics of the magnetic field created by: *1*) power lines; *2*) compensating winding; *3*) the total magnetic field with the system turned on.

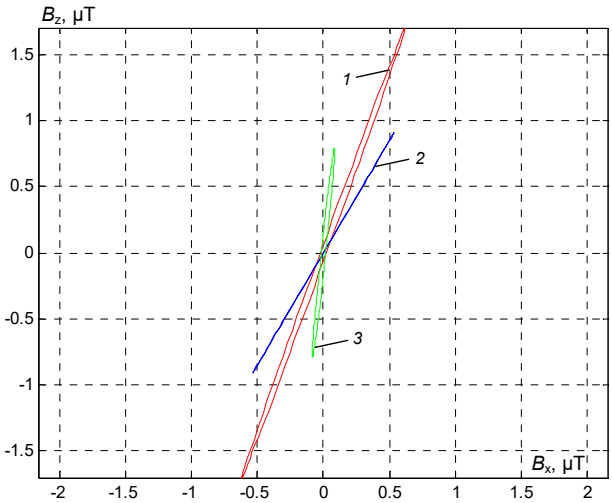

Fig. 6. The space time characteristics of the magnetic field created by: *1* – power lines; *2* – compensating winding; *3* – the total magnetic field with the system turned on

Experimental studies. To conduct experimental studies of the efficiency of the synthesized system, models of power transmission lines and systems have been developed. Using the geometric dimensions of the power transmission line (Fig. 1), the relative position and dimensions of the protected area, we calculate the dimensions of the overhead line layout. The obtained dimensions for placing the windings and installing three-

phase wires for modeling the field of an overhead line are shown in Fig. 7.

An example of the developed layout of the current conductors of the power transmission line, the compensating winding and the protected area is shown in Fig. 7. The area in which it is necessary to shield the magnetic field also is shown by a rectangle located on the right side of the Fig. 7.

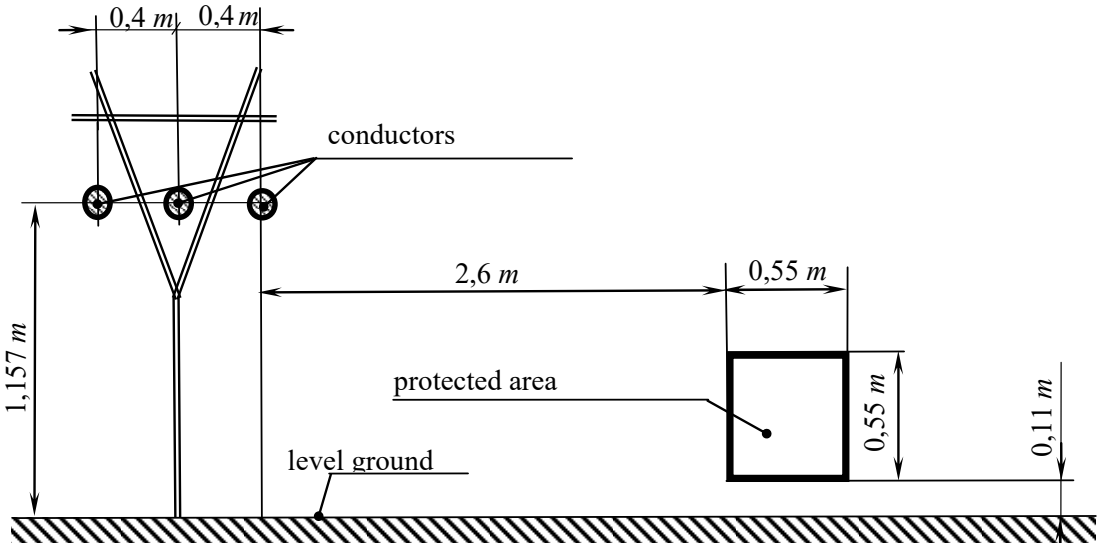

Fig. 7. Estimated dimensions of models of anchor cable support and shielding area

Simulation of model of system of active shielding. Let us study the efficiency of the synthesized model of system of active shielding for this power transmission lines. In Fig. 8 are shown the calculation scheme for the layout of power transmission lines, compensating winding and protected area.

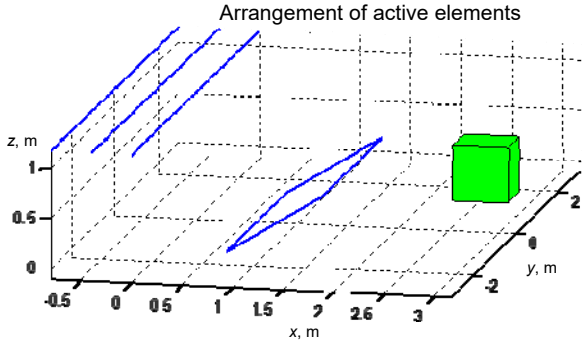

Fig. 8. The calculation scheme for the layout of power transmission lines, compensating winding and protected area

The distribution of the resulting magnetic field with the active screening system turned on is shown in Fig. 4. As can be seen from this figure, using the active screening system, it was possible to reduce the induction level of the initial magnetic field to the level of 0.6 μT in the space under consideration. In this case, the efficiency of the active shielding system is more than 2.

On Fig. 9 are shown the lines of equal level of the induction module of the initial magnetic field of the model of three-phase single-circuit overhead power line. This induction is computed at the model power line current of 100 A. The induction of initial magnetic field of model in the considered space is 1.6 μT.

The distribution of the resulting magnetic field with the model of active screening system turned on is shown in Fig. 10. As can be seen from this figure, using the active screening system, it was possible to reduce the induction level of the initial magnetic field to the level of 0.4 μT in the space under consideration. In this case, the efficiency of the active shielding system is 4.

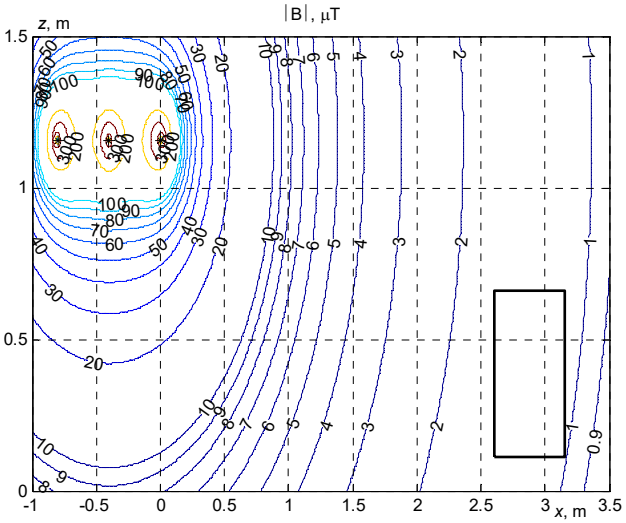

Fig. 9. The lines of equal level of the induction module of the initial magnetic field of the model of three-phase single-circuit overhead power line

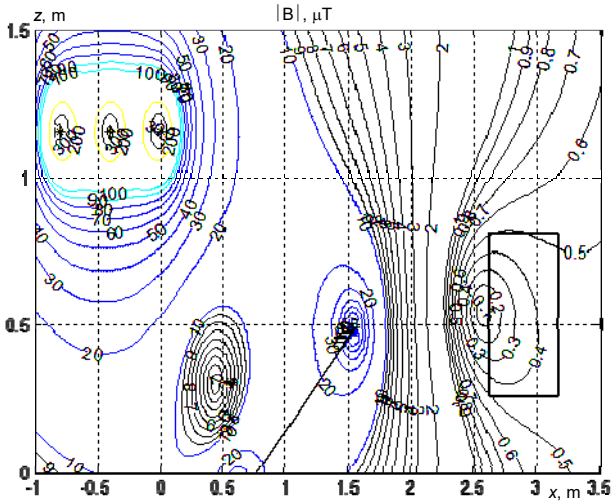

Fig. 10. The distribution of the resulting magnetic field with the model of active screening system turned on

On Fig. 11 are shown the dependences of the induction value of the initial magnetic field and the magnetic field with the active shielding system turned on as a function of the distance from the extreme current conductor of the power line.

Note that as follows from the comparison of Fig. 5 and Fig. 11, the shielding factor of the system layout is 4, which is greater than the shielding factor of the original system.

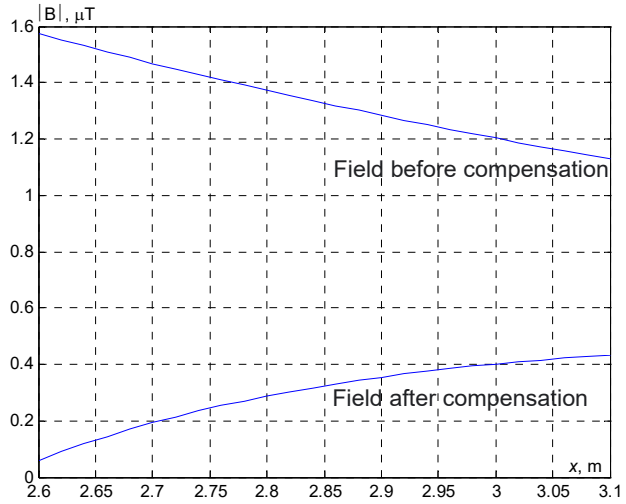

Fig. 11. Dependences of the induction value of the initial magnetic field and the magnetic field with the active shielding system turned on as a function of the distance from the extreme current conductor of the power line

On Fig. 12 are shown the space time characteristics of the magnetic field created by: *1*) power lines; *2*) compensating winding; *3*) the total magnetic field with the system turned on.

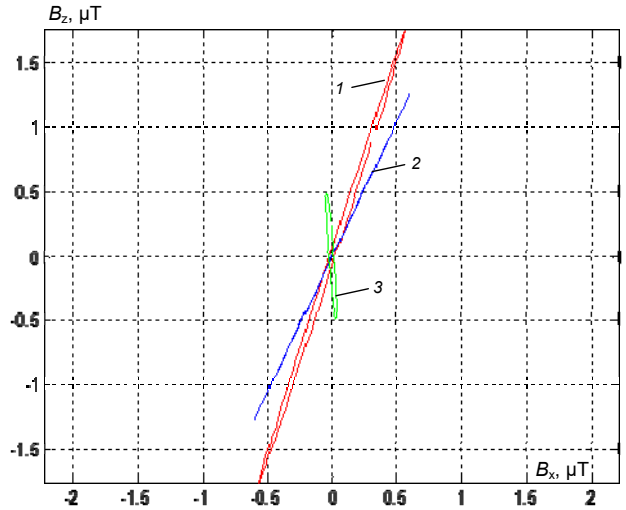

Fig. 12. The space time characteristics of the magnetic field created by: *1* – power; *2* – compensating winding; *3* – the total magnetic field with the system turned on

Results of experimental studies of model of system of active screening. Let us now consider the results of experimental studies of model of system of active screening.

The layout of the models of power transmission lines, compensating winding and protected area are shown in Fig. 13.

Fig. 13. The layout of the models of power transmission lines, compensating winding and protected area

On Fig. 14 are shown the experimental dependences of the induction of the initial magnetic field of the layout *1*) and the magnetic field when the layout of the active shielding system is turned on *2*)–*4*) as a function of the distance from the extreme current conductor of the power transmission line.

It has been experimentally established that the system with the open control circuit has the greatest shielding factor – more than 3, as it is shown curve *2* in Fig. 14. The screening factor with a closed control loop (curves *3*) and (curves *4*) depends on the position of the sensor, with which the resulting magnetic field is measured.

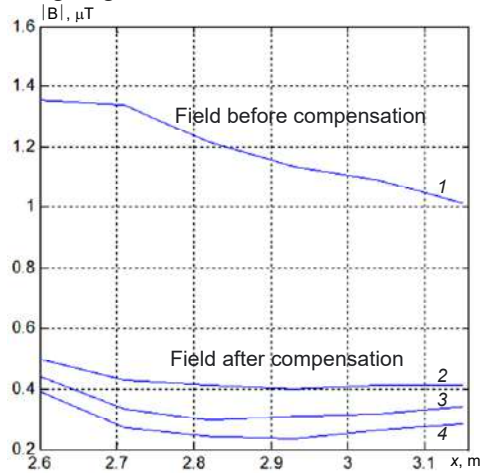

Fig. 14. The experimental dependences of the induction of the initial magnetic field of the layout and the magnetic field when the layout of the system of active shielding is turned on

Conclusions.

1. For the first time, the theoretical and experimental studies of the effectiveness of reducing the level of the magnetic field in two-storey cottage of the old building of a power transmission line with a horizontal arrangement of wires by means of active shielding with single compensation winding.

2. The space-time characteristics of the magnetic field generated by a power transmission line with a horizontal arrangement of wires have been studied. It is shown that these characteristics have the shape of an elongated ellipse, which confirms the possibility of effective compensation of such a magnetic field using single compensation winding.

3. The synthesis of single-circuit systems of active shielding of the magnetic field created by single-circuit

overhead power lines 110 kV with a horizontal arrangement of wires in a two-story cottage of an old building was carried out. As a result of the synthesis, the coordinates of the location of single compensation winding, as well as the current and phase in these compensation winding, were determined to ensure high shielding efficiency.

4. For the synthesis of robust systems of active shielding, the vector game solution was calculated based on stochastic multi-agent optimization algorithms. The calculation of the game payoff vector and restrictions was carried out on the basis of the Biot–Savart law.

5. Theoretically and experimentally confirmed the possibility of reducing the magnetic field to a safe level of sanitary standards of Ukraine in a two-story cottage of an old building from power lines with a horizontal arrangement of wires using a synthesized simple system of active shielding with a single compensation winding.

Conflict of interest. The authors declare that they have no conflicts of interest.

REFERENCES

1. Rozov V.Yu., Grinchenko V.S., Yerisov A.V., Dobrodeyev P.N. Efficient shielding of three-phase cable line magnetic field by passive loop under limited thermal effect on power cables. *Electrical Engineering & Electromechanics*, 2019, no. 6, pp. 50-54. doi: https://doi.org/10.20998/2074-272x.2019.6.07.

2. Rozov V.Y., Pelevin D.Y., Pielievina K.D. External magnetic field of urban transformer substations and methods of its normalization. *Electrical Engineering & Electromechanics*, 2017, no. 5, pp. 60-66. doi: https://doi.org/10.20998/2074-272X.2017.5.10.

3. Yerisov A.V., Pielievina K.D., Pelevin D.Y.Calculation method of electric power lines magnetic field strength based on cylindrical spatial harmonics. *Electrical Engineering & Electromechanics*, 2016, no. 2, pp. 24-27. doi: https://doi.org/10.20998/2074-272X.2016.2.04.

4. Rozov V.Yu., Kundius K.D., Pelevin D.Ye. Active shielding of external magnetic field of built-in transformer substations. *Electrical Engineering & Electromechanics*, 2020, no. 3, pp. 24-30. doi: https://doi.org/10.20998/2074-272x.2020.3.04.

5. Salceanu A., Paulet M., Alistar B.D., Asiminicesei O. Upon the contribution of image currents on the magnetic fields generated by overhead power lines. *2019 International Conference on Electromechanical and Energy Systems (SIELMEN)*. 2019. doi: https://doi.org/10.1109/sielmen.2019.8905880.

6. Del Pino Lopez J.C., Romero P.C. Influence of different types of magnetic shields on the thermal behavior and ampacity of underground power cables. *IEEE Transactions on Power Delivery*, Oct. 2011, vol. 26, no. 4, pp. 2659-2667. doi: https://doi.org/10.1109/tpwrd.2011.2158593.

7. Ippolito L., Siano P. Using multi-objective optimal power flow for reducing magnetic fields from power lines. *Electric Power Systems Research*, 2004, vol. 68, no. 2, pp. 93-101. doi: https://doi.org/10.1016/S0378-7796(03)00151-2.

8. Barsali S., Giglioli R., Poli D. Active shielding of overhead line magnetic field: Design and applications. *Electric Power Systems Research*, May 2014, vol. 110, pp. 55-63. doi: https://doi.org/10.1016/j.epsr.2014.01.005.

9. Bavastro D., Canova A., Freschi F., Giaccone L., Manca M. Magnetic field mitigation at power frequency: design principles and case studies. *IEEE Transactions on Industry Applications*, May 2015, vol. 51, no. 3, pp. 2009-2016. doi: https://doi.org/10.1109/tia.2014.2369813.

10. Beltran H., Fuster V., García M. Magnetic field reduction screening system for a magnetic field source used in industrial applications. *9 Congreso Hispano Luso de Ingenieria Eléctrica (9 CHLIE)*, Marbella (Málaga, Spain), 2005, pp. 84-99. Available at: https://www.researchgate.net/publication/229020921_Magnetic_field_reduction_screening_system_for_a_magnetic_field_source_used_in_industrial_applications (Accessed 22.06.2021).

11. Bravo-Rodríguez J., Del-Pino-López J., Cruz-Romero P. A Survey on Optimization Techniques Applied to Magnetic Field Mitigation in Power Systems. *Energies*, 2019, vol. 12, no. 7, p. 1332. doi: https://doi.org/10.3390/en12071332.

12. Canova A., del-Pino-López J.C., Giaccone L., Manca M. Active Shielding System for ELF Magnetic Fields. *IEEE Transactions on Magnetics*, March 2015, vol. 51, no. 3, pp. 1-4. doi: https://doi.org/10.1109/tmag.2014.2354515.

13. Canova A., Giaccone L. Real-time optimization of active loops for the magnetic field minimization. *International Journal of Applied Electromagnetics and Mechanics*, Feb. 2018, vol. 56, pp. 97-106. doi: https://doi.org/10.3233/jae-172286.

14. Canova A., Giaccone L., Cirimele V. Active and passive shield for aerial power lines. *Proc. of the 25th International Conference on Electricity Distribution (CIRED 2019)*, 3-6 June 2019, Madrid, Spain. Paper no. 1096. Available at: https://www.cired-repository.org/handle/20.500.12455/290 (Accessed 28 May 2021).

15. Canova A., Giaccone L. High-performance magnetic shielding solution for extremely low frequency (ELF) sources. *CIRED - Open Access Proceedings Journal*, Oct. 2017, vol. 2017, no. 1, pp. 686-690. doi: https://doi.org/10.1049/oap-cired.2017.1029.

16. Celozzi S. Active compensation and partial shields for the power-frequency magnetic field reduction. *2002 IEEE International Symposium on Electromagnetic Compatibility*, Minneapolis, MN, USA, 2002, vol. 1, pp. 222-226. doi: https://doi.org/10.1109/isemc.2002.1032478.

17. Celozzi S., Garzia F. Active shielding for power-frequency magnetic field reduction using genetic algorithms optimization. *IEE Proceedings - Science, Measurement and Technology*, 2004, vol. 151, no. 1, pp. 2-7. doi: https://doi.org/10.1049/ip-smt:20040002.

18. Celozzi S., Garzia F. Magnetic field reduction by means of active shielding techniques. *WIT Transactions on Biomedicine and Health*, 2003, vol. 7, pp. 79-89. doi: https://doi.org/10.2495/ehr030091.

19. Kuznetsov B.I., Nikitina T.B., Bovdui I.V., Kolomiets V.V., Kobylianskiy B.B. Overhead power lines magnetic field reducing in multi-story building by active shielding means. *Electrical Engineering & Electromechanics*, 2021, no. 2, pp. 23-29. doi: https://doi.org/10.20998/2074-272X.2021.2.04.

20. Martynenko G. Practical application of the analytical method of electromagnetic circuit analysis for determining magnetic forces in active magnetic bearings. *2020 IEEE Problems of Automated Electrodrive. Theory and Practice (PAEP)*, 2020, pp. 1-4, doi: https://doi.org/10.1109/paep49887.2020.9240774.

21. Martynenko G., Martynenko V. Modeling of the dynamics of rotors of an energy gas turbine installation using an analytical method for analyzing active magnetic bearing circuits. *2020 IEEE KhPI Week on Advanced Technology (KhPIWeek)*, 2020, pp. 92-97. doi: https://doi.org/10.1109/KhPIWeek51551.2020.9250156.

22. Buriakovskyi S.G., Maslii A.S., Pasko O.V., Smirnov V.V. Mathematical modelling of transients in the electric drive of the switch – the main executive element of railway automation. *Electrical Engineering & Electromechanics*, 2020, no. 4, pp. 17-23. doi: https://doi.org/10.20998/2074-272X.2020.4.03.

23. Ostroverkhov M., Chumack V., Monakhov E., Ponomarev A. Hybrid Excited Synchronous Generator for Microhydropower Unit. *2019 IEEE 6th International Conference on Energy Smart Systems (ESS)*, Kyiv, Ukraine, 2019, pp. 219-222. doi: https://doi.org/10.1109/ess.2019.8764202.

24. Ostroverkhov M., Chumack V., Monakhov E. Ouput Voltage Stabilization Process Simulation in Generator with Hybrid Excitation at Variable Drive Speed. *2019 IEEE 2nd Ukraine Conference on Electrical and Computer Engineering (UKRCON)*, Lviv, Ukraine, 2019, pp. 310-313. doi: https://doi.org/10.1109/ukrcon.2019.8879781.

25. Tytiuk V., Chornyi O., Baranovskaya M., Serhiienko S., Zachepa I., Tsvirkun L., Kuznetsov V., Tryputen N. Synthesis of a fractional-order $PI^{\lambda}D^{\mu}$-controller for a closed system of switched reluctance motor control. *Eastern-European Journal of Enterprise Technologies*, 2019, no. 2 (98), pp. 35-42. doi: https://doi.org/10.15587/1729-4061.2019.160946.

26. Zagirnyak M., Chornyi O., Zachepa I. The autonomous sources of energy supply for the liquidation of technogenic accidents. *Przeglad Elektrotechniczny*, 2019, no. 5, pp. 47-50. doi: https://doi.org/10.15199/48.2019.05.12.

27. Chornyi O., Serhiienko S. A virtual complex with the parametric adjustment to electromechanical system parameters. *Technical Electrodynamics*, 2019, pp. 38-41. doi: https://doi.org/10.15407/techned2019.01.038.

28. Shchur I., Kasha L., Bukavyn M. Efficiency Evaluation of Single and Modular Cascade Machines Operation in Electric

Vehicle. *2020 IEEE 15th International Conference on Advanced Trends in Radioelectronics, Telecommunications and Computer Engineering (TCSET)*, Lviv-Slavske, Ukraine, 2020, pp. 156-161. doi: https://doi.org/10.1109/tcset49122.2020.235413.
29. Shchur I., Turkovskyi V. Comparative Study of Brushless DC Motor Drives with Different Configurations of Modular Multilevel Cascaded Converters. *2020 IEEE 15th International Conference on Advanced Trends in Radioelectronics, Telecommunications and Computer Engineering (TCSET)*, Lviv-Slavske, Ukraine, 2020, pp. 447-451. doi: https://doi.org/10.1109/tcset49122.2020.235473.
30. Ostroumov I., Kuzmenko N., Sushchenko O., Pavlikov V., Zhyla S., Solomentsev O., Zaliskyi M., Averyanova Y., Tserne E., Popov A., Volosyuk V., Ruzhentsev N., Dergachov K., Havrylenko O., Kuznetsov B., Nikitina T., Shmatko O. Modelling and simulation of DME navigation global service volume. *Advances in Space Research*, 2021, vol. 68, no. 8, pp. 3495-3507. doi: https://doi.org/10.1016/j.asr.2021.06.027.
31. Averyanova Y., Sushchenko O., Ostroumov I., Kuzmenko N., Zaliskyi M., Solomentsev O., Kuznetsov B., Nikitina T., Havrylenko O., Popov A., Volosyuk V., Shmatko O., Ruzhentsev N., Zhyla S., Pavlikov V., Dergachov K., Tserne E. UAS cyber security hazards analysis and approach to qualitative assessment. In: Shukla S., Unal A., Varghese Kureethara J., Mishra D.K., Han D.S. (eds) *Data Science and Security. Lecture Notes in Networks and Systems*, 2021, vol. 290, pp. 258-265. Springer, Singapore. doi: https://doi.org/10.1007/978-981-16-4486-3_28.
32. Zaliskyi M., Solomentsev O., Shcherbyna O., Ostroumov I., Sushchenko O., Averyanova Y., Kuzmenko N., Shmatko O., Ruzhentsev N., Popov A., Zhyla S., Volosyuk V., Havrylenko O., Pavlikov V., Dergachov K., Tserne E., Nikitina T., Kuznetsov B. Heteroskedasticity analysis during operational data processing of radio electronic systems. In: Shukla S., Unal A., Varghese Kureethara J., Mishra D.K., Han D.S. (eds) *Data Science and Security. Lecture Notes in Networks and Systems*, 2021, vol. 290, pp. 168-175. Springer, Singapore. doi: https://doi.org/10.1007/978-981-16-4486-3_18.
33. Shmatko O., Volosyuk V., Zhyla S., Pavlikov V., Ruzhentsev N., Tserne E., Popov A., Ostroumov I., Kuzmenko N., Dergachov K., Sushchenko O., Averyanova Y., Zaliskyi M., Solomentsev O., Havrylenko O., Kuznetsov B., Nikitina T. Synthesis of the optimal algorithm and structure of contactless optical device for estimating the parameters of statistically uneven surfaces. *Radioelectronic and Computer Systems*, 2021, no. 4, pp. 199-213. doi: https://doi.org/10.32620/reks.2021.4.16.
34. Volosyuk V., Zhyla S., Pavlikov V., Ruzhentsev N., Tserne E., Popov A., Shmatko O., Dergachov K., Havrylenko O., Ostroumov I., Kuzmenko N., Sushchenko O., Averyanova Yu., Zaliskyi M., Solomentsev O., Kuznetsov B., Nikitina T. Optimal Method for Polarization Selection of Stationary Objects Against the Background of the Earth's Surface. *International Journal of Electronics and Telecommunications*, 2022, vol. 68, no. 1, pp. 83-89. doi: https://doi.org/10.24425/ijet.2022.139852.
35. Gal'chenko V.Y., Vorob'ev M.A. Structural synthesis of attachable eddy-current probes with a given distribution of the probing field in the test zone. *Russian Journal of Nondestructive Testing*, Jan. 2005, vol. 41, no. 1, pp. 29-33. doi: https://doi.org/10.1007/s11181-005-0124-7.
36. Halchenko V.Y., Ostapushchenko D.L., Vorobyov M.A. Mathematical simulation of magnetization processes of arbitrarily shaped ferromagnetic test objects in fields of given spatial configurations. *Russian Journal of Nondestructive Testing*, Sep. 2008, vol. 44, no. 9, pp. 589-600. doi: https://doi.org/10.1134/S1061830908090015.
37. Ostroumov I., Kuzmenko N., Sushchenko O., Zaliskyi M., Solomentsev O., Averyanova Y., Zhyla S., Pavlikov V., Tserne E., Volosyuk V., Dergachov K., Havrylenko O., Shmatko O., Popov A., Ruzhentsev N., Kuznetsov B., Nikitina T. A probability estimation of aircraft departures and arrivals delays. In: Gervasi O. et al. (eds) *Computational Science and Its Applications – ICCSA 2021. ICCSA 2021. Lecture Notes in Computer Science*, vol. 12950, pp. 363-377. Springer, Cham. doi: https://doi.org/10.1007/978-3-030-86960-1_26.
38. Chystiakov P., Chornyi O., Zhautikov B., Sivyakova G. Remote control of electromechanical systems based on computer simulators. *2017 International Conference on Modern Electrical and Energy Systems (MEES)*, Kremenchuk, Ukraine, 2017, pp. 364-367. doi: https://doi.org/10.1109/mees.2017.8248934.
39. Zagirnyak M., Bisikalo O., Chorna O., Chornyi O. A Model of the Assessment of an Induction Motor Condition and Operation Life, Based on the Measurement of the External Magnetic Field. *2018 IEEE 3rd International Conference on Intelligent Energy and Power Systems (IEPS)*, Kharkiv, 2018, pp. 316-321. doi: https://doi.org/10.1109/ieps.2018.8559564.
40. Ummels M. *Stochastic Multiplayer Games Theory and Algorithms*. Amsterdam University Press, 2010. 174 p.
41. Shoham Y., Leyton-Brown K. *Multiagent Systems: Algorithmic, Game-Theoretic, and Logical Foundations.* Cambridge University Press, 2009. 504 p.
42. Ray T., Liew K.M. A Swarm Metaphor for Multiobjective Design Optimization. *Engineering Optimization*, 2002, vol. 34, no. 2, pp. 141-153. doi: https://doi.org/10.1080/03052150210915.
43. Zilzter Eckart. *Evolutionary algorithms for multiobjective optimizations: methods and applications*. PhD Thesis Swiss Federal Institute of Technology, Zurich, 1999. 114 p.
44. Xiaohui Hu, Eberhart R.C., Yuhui Shi. Particle swarm with extended memory for multiobjective optimization. *Proceedings of the 2003 IEEE Swarm Intelligence Symposium*. SIS'03 (Cat. No.03EX706), Indianapolis, IN, USA, 2003, pp. 193-197. doi: https://doi.org/10.1109/sis.2003.1202267.
45. Pulido G.T., Coello C.A.C. A constraint-handling mechanism for particle swarm optimization. *Proceedings of the 2004 Congress on Evolutionary Computation* (IEEE Cat. No.04TH8753), Portland, OR, USA, 2004, vol. 2, pp. 1396-1403. doi: https://doi.org/10.1109/cec.2004.1331060.
46. Michalewicz Z., Schoenauer M. Evolutionary Algorithms for Constrained Parameter Optimization Problems. *Evolutionary Computation*, 1996, vol. 4, no. 1, pp. 1-32. doi: https://doi.org/10.1162/evco.1996.4.1.1.
47. Zhyla S., Volosyuk V., Pavlikov V., Ruzhentsev N., Tserne E., Popov A., Shmatko O., Havrylenko O., Kuzmenko N., Dergachov K., Averyanova Y., Sushchenko O., Zaliskyi M., Solomentsev O., Ostroumov I., Kuznetsov B., Nikitina T. Statistical synthesis of aerospace radars structure with optimal spatio-temporal signal processing, extended observation area and high spatial resolution. *Radioelectronic and Computer Systems*, 2022, no. 1, pp. 178-194. doi: https://doi.org/10.32620/reks.2022.1.14.
48. Xin-She Yang, Zhihua Cui, Renbin Xiao, Amir Hossein Gandomi, Mehmet Karamanoglu. *Swarm Intelligence and Bio-Inspired Computation: Theory and Applications*, Elsevier Inc., 2013. 450 p.

Received 10.05.2022
Accepted 13.08.2022
Published 06.11.2022

B.I. Kuznetsov[1], *Doctor of Technical Science, Professor,*
T.B. Nikitina[2], *Doctor of Technical Science, Professor,*
I.V. Bovdui[1], *PhD, Senior Research Scientist,*
O.V. Voloshko[1], *PhD, Junior Research Scientist,*
V.V. Kolomiets[2], *PhD, Assistant Professor,*
B.B. Kobylianskyi[2], *PhD, Associate Professor,*
[1] A. Pidhornyi Institute of Mechanical Engineering Problems of the National Academy of Sciences of Ukraine,
2/10, Pozharskogo Str., Kharkiv, 61046, Ukraine,
e-mail: kuznetsov.boris.i@gmail.com (Corresponding Author)
[2] Educational scientific professional pedagogical Institute of Ukrainian Engineering Pedagogical Academy,
9a, Nosakov Str., Bakhmut, Donetsk Region, 84511, Ukraine,
e-mail: tatjana55555@gmail.com; nnppiuipa@ukr.net

How to cite this article:
Kuznetsov B.I., Nikitina T.B., Bovdui I.V., Voloshko O.V., Kolomiets V.V., Kobylianskyi B.B. Synthesis of an effective system of active shielding of the magnetic field of a power transmission line with a horizontal arrangement of wires using a single compensation winding. *Electrical Engineering & Electromechanics*, 2022, no. 6, pp. 15-21. doi: https://doi.org/10.20998/2074-272X.2022.6.03

UDC 621.3.01 https://doi.org/10.20998/2074-272X.2022.6.04

L. Moussaoui, S. Aouaouda, R. Rouaibia

Fault tolerant control of a permanent magnet synchronous machine using multiple constraints Takagi-Sugeno approach

Introduction. *Fault diagnosis, and fault tolerant control issues are becoming very important to ensure a good supervision of systems and guarantee the safety of human operators and equipments even if system complexity increases.* ***Problem.*** *In fact, the presence of faults in actuators, sensors and processes can lead to system performance degradation, system breakdown, economic loss, and even disastrous situations. Furthermore, Actuator saturation or control input saturation is probably the most usual nonlinearity encountered in control engineering because of the physical impossibility of applying unlimited control signals and/or safety constraints.* ***Purpose.*** *This article is dedicated to the problem of fault tolerant control for constrained nonlinear systems described by a Takagi-Sugeno model. One of the interests of this type of models is the possibility of extend some tools and methods from linear system case to the nonlinear one.* ***The novelty*** *of the work consists in developing a fault tolerant control algorithm for a nonlinear Permanent Magnet Synchronous Machine model using an observer based state-feedback control technique in order to enhance fault and state estimation despite actuator saturation and system disturbances.* ***Methods.*** *Indeed a sensor fault detection observer based residual generator is synthesized with a guaranteed L_2 performance to attenuate the external disturbances effect from one side and to maximize the residual sensitivity to faults from the other side. Based on Lyapunov function, design conditions are formulated in terms of Linear Matrix Inequalities to ensure stability of the global system.* ***Practical value.*** *A detailed study concerning nonlinear permanent magnet synchronous machine model, which is consolidated by simulation results, is conducted to show the used algorithm's effectiveness guarantying fault estimation and reconfiguration of the control law to maintain stable performance even in the presence of actuator faults, external perturbation and the phenomenon of actuator saturation.* References 19, tables 1, figures 5.

Key words: **Takagi-Sugeno models, actuator saturation, state estimation, actuator faults diagnosis, fault tolerant control, permanent magnet synchronous machine model, linear matrix inequalities.**

Вступ. *Діагностика несправностей і питання стійкості до відмови стають дуже важливими для забезпечення хорошого контролю систем і гарантії безпеки людей-операторів і обладнання, навіть якщо складність системи зростає.* ***Проблема***. *Насправді наявність несправностей у виконавчих механізмах, датчиках і процесах може призвести до зниження продуктивності системи, поломки системи, економічних втрат і навіть катастрофічних ситуацій. Крім того, насичення виконавчого механізму або насичення керуючого входу, ймовірно, є найбільш поширеною нелінійністю, що зустрічається в техніці керування через фізичну неможливість застосування необмежених керуючих сигналів та обмежень безпеки.* ***Мета***. *Ця стаття присвячена проблемі стійкості до відмови нелінійних систем з обмеженнями, що описуються моделлю Такагі-Сугено. Однією з переваг цього типу моделей є можливість поширення деяких інструментів та методів з випадку лінійної системи на нелінійну.* ***Новизна*** *роботи полягає у розробці алгоритму управління стійкості до відмови для моделі нелінійної синхронної машини з постійними магнітами з використанням методу управління зі зворотним зв'язком станом на основі спостерігача, щоб поліпшити оцінку помилок і станів, незважаючи на насичення приводу і збурення системи.* ***Методи***. *Дійсно, генератор нев'язки на основі спостерігача виявлення несправності датчика синтезується з гарантованою продуктивністю L_2, щоб послабити вплив зовнішніх перешкод з одного боку та максимізувати залишкову чутливість до несправностей з іншого боку. На основі функції Ляпунова умови проєктування формулюються в термінах лінійних матричних нерівностей для забезпечення стійкості глобальної системи.* ***Практична цінність***. *Детальне дослідження нелінійної моделі синхронної машини з постійними магнітами, об'єднане результатами моделювання, проводиться для демонстрації ефективності використовуваного алгоритму, що гарантує оцінку відмов та реконфігурацію закону управління для підтримки стабільної роботи навіть за наявності відмов приводу, зовнішніх збурень та явища насичення приводу.* Бібл. 19, табл. 1, рис. 5.

Ключові слова: **моделі Такагі-Сугено, насичення приводу, оцінка стану, діагностика несправностей приводу, стійкість до відмов, модель синхронної машини з постійними магнітами, лінійні матричні нерівності.**

Introduction. Faults detection and isolation (FDI) has been the subject of many research for linear and nonlinear systems. However, in practical cases used only the FDI block for the process is not enough to preserve desired performance, security and system stability. Hence, fault tolerance must be treated and controllers are synthesized to ensure system stability even in failed situations and degraded operations. We can classify the fault tolerant control (FTC) into passive FTC and active FTC [1, 2]. The first approach can be considered as a robust control, and it requires a priori knowledge of faults that can affect the system, the controller is then designed to compensate them, all possible faults are considered as uncertainties, and an adaptive observer is employed to estimate the fault and state signals. The second is called active FTC, we use in this approach a very robust FDI block to know with exactitude the information's about faults which constitutes its major disadvantage. Indeed, a false alarm or an undetected fault can lead to degradation of performance or even instability [3].

During the design of the FTC controller, we must take into account the saturation of the actuator to avoid the undesirable effects that can destabilize the closed-loop system, and degrade the desired performances [4, 5]. Therefore, much attention has been given to stability analysis and controller design for systems with actuator saturation [6]. More-over, several works propose a norm-bounded controller based on multi-model Takagi-Sugeno (T-S) fuzzy approach, due to the exceptional characteristics of T-S fuzzy models for control purposes to avoid control inputs limitations.

Many researches are developed around the T-S multimodel representation [7, 8]. Nonlinear systems described by T-S models have been considered actively and especially in the fields of control, state estimation and

diagnosis of nonlinear systems. This is related to the fact that T-S fuzzy model can approximate exactly any nonlinear system without loss of information. A T-S model can be obtained using the non-linearity sector approach by aggregating the local models using appropriate interpolation functions [9]. These models have a great ability to represent the complex dynamic system.

The stability analysis of a T-S system has been studied in most cases by using a quadratic Lyapunov function, and solutions are almost expressed as linear matrix inequalities (LMI) [10, 11].

Goal. This paper aims to develop a robust control approach subject to multiple system constraints, i.e. actuator faults, input saturation, external perturbation. The system is presented as a T-S fuzzy multi-model, and then an observer-based FTC design method is introduced to preserve the stability of the system with disturbance rejection. The observer and controller gains are obtained through an L_2 minimisation by solving LMI conditions.

The main contribution is to develop model-based FTC-scheme for nonlinear dynamic systems described by T-S models and subject to input constraints. Using the Lyapunov theory for T-S systems, the obtained results are less conservative and formulated in terms of LMI conditions. Consequently, the proposed procedure has also two advantages over the previous cited works. Firstly, it is able to estimate time variable fault types. Secondly, for the analysis of the fuzzy systems, to reduce the computational cost of double summation slack matrices has been introduced, which leads to a simple design procedure. Furthermore, compared to the approach presented in [12-16] the proposed FTC controller design method can be considered for a large class of nonlinear constrained systems.

Problem statement. Let consider the following constrained and disturbed T-S model:

$$\begin{cases} \dot{x} = \sum_{i=1}^{r} \mu_i(\xi(t))\left(A_i x + B_i sat(u + f_u(t))\right) + d(t) \\ y = \sum_{i=1}^{r} \mu_i(\xi(t)) C_i x \end{cases} \quad (1)$$

where $x \in R^n$ is the state vector; $u \in R^m$ is the control input; $y \in R^p$ is the system output; A_i, B_i, C_i are the constant matrices with appropriate dimensions; $d(t)$ is the external disturbance signal; $f_u(t)$ is the actuator failure; $\xi(t) = [\xi_1(t) \ \ldots \ \xi_r(t)]$ is the decision variables; $\mu_i(\xi(t))$ is the normalized activation function satisfying the sum convex propriety [17]:

$$\begin{cases} 0 \le \mu_i(\xi(t)) \le 1 \ \ \forall i \in \{1, 2, \cdots, r\} \\ \sum_{i=1}^{r} \mu_i(\xi(t)) = 1 \\ \mu_i(\xi(t)) = \dfrac{w_i(\xi(t))}{\sum_{i=1}^{r} w_i(\xi(t))} \\ w_i(\xi(t)) = \prod_{j=1}^{r} M_{ij}(\xi_j(t)) \end{cases} \quad (2)$$

where $w_i(\xi(t))$ are the weights; $M_{ij}(\xi_j(t))$ are the fuzzy set. The function sat$(u + f_u(t))$ represents the actuator failure saturation function.

The following lemmas and notations will be used in the rest of this paper:

Lemma 1 [2]: Let consider two matrices X and Y and a scalar σ such that the following inequality is verified:

$$X^T Y + Y^T X < \sigma X^T X + \sigma^{-1} Y^T Y, \sigma > 0. \quad (3)$$

Lemma 2 [18, 19]: Let E be an $m \times m$ diagonal matrix whose elements are 1 or 0. Suppose that $|v_i| \le \bar{u}_i$ for all $i \in I_m$ where v_i and u_i are the i^{th} element of $v \in R^m$ and $u \in R^m$ respectively. If $x \in \bigcap_{j=1}^{r} L(H_j)$ for $x \in R^n$, then

$$\begin{cases} sat(u, \bar{u}) = \sum_{s=1}^{2^m} \alpha_s (E_s u + \bar{E}_s v) \\ \sum_{s=1}^{2^m} \alpha_s = 1, \quad 0 \le \alpha_s \le 1 \\ v = -\sum_{j=1}^{r} \mu_j H_j x \end{cases} \quad (4)$$

$$L(H_j) = \left\{ x \in R^n, | \, h_i^j x | \le \bar{u}_i \right\}, \quad (5)$$

where E_s denotes all elements of E, $\bar{E}_S = 1 - E_S$; H_j is the $m \times n$ matrix and h_i^j is the i^{th} row of the matrix H_j; α_s is the weighting functions related to the polytopic representation of the saturation function.

Lemma 3 [18]: An ellipsoid $\varepsilon(P, \rho)$ is inside $\bigcap_{j=1}^{r} L(H_j)$ if and only if:

$$\forall i \in I_m : (h_i^j)^T (P / \rho) h_i^j \le \bar{u}_i^2, \quad (6)$$

where h_i^j is the i^{th} row of the matrix H_j.

Assumption 1 [3]: the faults are assumed to have a first time derivative bounded as:

$$\left\| \dot{f}(t) \right\| \le f_{1\max}, \quad 0 \le f_{1\max} \le \infty$$

Throughout the paper $H(Z)$ denotes the Hermitian of a matrix Z, i.e. $H(Z) = Z + Z^T$; and I denotes the identity matrix.

Fault tolerant control of T-S multi-model. The design of the controller is based on FTC bloc with multi-constraints (actuator fault, actuator saturation and external disturbance) as shown in Fig. 1, ensuring the convergence of the estimated states and the detection of the faults by the observer.

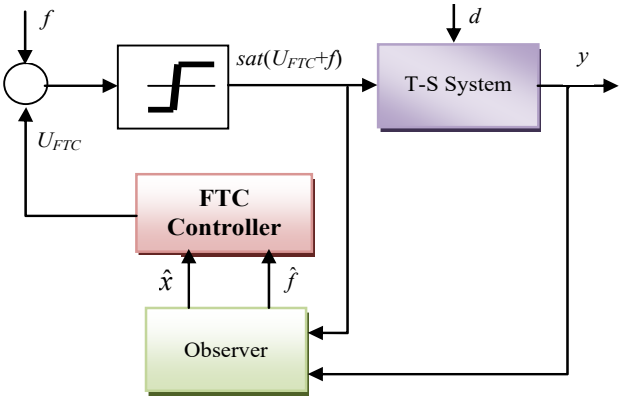

Fig. 1. Fault tolerant control scheme

The following observer is adopted to estimate both faults and system states as:

$$\begin{cases} \dot{\hat{x}} = \sum_{i=1}^{r} \mu_i \left(A_i \hat{x} + B_i sat(u + \hat{f}_u(t)) + L_i e_y \right) \\ \hat{y} = C\hat{x} \\ \dot{\hat{f}}_u = T \sum_{i=1}^{r} \mu_i F_i \left(\dot{e}_y + \delta e_y \right) \\ e_y = y - \hat{y} \end{cases} \quad (7)$$

where $\hat{f} \in R^n$ is the estimated state; $\hat{f}_u(t)$ is the estimated fault; L_i, T, F_i and δ are the observer gains to be determined.

The proposed FTC control law is given by:

$$U_{FTC} = -\sum_{i=1}^{r} \mu_i K_i \hat{x} - \hat{f}_u(t); \tag{8}$$

$$V_{FTC} = -\sum_{i=1}^{r} \mu_i H_i \hat{x}, \tag{9}$$

where K_i, H_i are the $m \times n$ gains matrices to be determined.

In this work, the saturation function can be written as polytopic representation defined by:

$$sat(u + \hat{f}_u(t)) = E_{\alpha s}\left(U_{FTC} + \hat{f}_u(t)\right) + \bar{E}_{\alpha s} V_{FTC} \tag{10}$$

with:

$$E_{\alpha s} = \sum_{s=1}^{2^m} \alpha_s E_s; \tag{11}$$

$$\bar{E}_{\alpha s} = \sum_{s=1}^{2^m} \alpha_s \bar{E}_s. \tag{12}$$

Using (10), the system (1) will be:

$$\dot{x} = \sum_{i=1}^{r} \mu_i \left(A_i x + B_i \left[E_{\alpha s}\left(U_{FTC} + f_u(t)\right) + \bar{E}_{\alpha s} V_{FTC} \right] \right) + d(t). \tag{13}$$

Using (8), (9) one can obtain:

$$\dot{x} = \sum_{i=1}^{r} \mu_i \begin{pmatrix} \left(A_i - B_i\left(E_{\alpha s} K_i + \bar{E}_{\alpha s} H_i\right)\right)x \\ + B_i\left(E_{\alpha s} K_i + \bar{E}_{\alpha s} H_i\right) e_x + B_i E_{\alpha s} e_f \end{pmatrix} + d(t) \tag{14}$$

with:

$$e_x = x - \hat{x}; \tag{15}$$

$$e_f = f_u - \hat{f}_u. \tag{16}$$

Theorem 1. The system that generate state error e_x, and fault error e_f is stable and asymptotically converge to zero and achieve a disturbance rejection level $\gamma > 0$ if there exist a symmetric positive definite matrix X, matrices $\bar{L}_i$, $\bar{K}_i$, Z_j, T, F_i and scalars δ, σ_{1i} ... σ_{3i}, solutions of the following LMI constraints:

$$\min_{X, \bar{L}_i, \bar{K}_i, Z_j, T, F_i, \delta, \sigma_{1i}, \ldots \sigma_{3i}} \gamma;$$

$$\begin{bmatrix} \bar{u}_i^2 & z_i^j \\ (z_i^j)^T & X \end{bmatrix} \geq 0, \quad \forall i \in I_m; \tag{17}$$

$$\begin{bmatrix}
D_{11}'' & * & * & * & * & * & * & * & * & * & * \\
D_{21}'' & D_{22}'' & * & * & * & * & * & * & * & * & * \\
D_{31}'' & D_{32}'' & D_{33}'' & * & * & * & * & * & * & * & * \\
I & I & -\frac{1}{\delta^T} C^T & -\gamma^2 I & * & * & * & * & * & * & * \\
X & 0 & 0 & 0 & I & * & * & * & * & * & * \\
0 & X & 0 & 0 & 0 & \sigma_{1i} I & * & * & * & * & * \\
0 & \bar{L}_i & 0 & 0 & 0 & 0 & \sigma_{2i} I & * & * & * & * \\
0 & X & 0 & 0 & 0 & 0 & 0 & \sigma_{3i} I & * & * & * \\
0 & 0 & \frac{1}{\delta} F_i C A_i & 0 & 0 & 0 & 0 & 0 & \sigma_{1i}^{-1} I & * & * \\
0 & 0 & \frac{1}{\delta} F_i C & 0 & 0 & 0 & 0 & 0 & 0 & \sigma_{2i}^{-1} I & * \\
0 & 0 & F_i C & 0 & 0 & 0 & 0 & 0 & 0 & 0 & \sigma_{3i}^{-1} I
\end{bmatrix} < 0; \tag{18}$$

with:

$$\begin{aligned}
D_{11}'' &= H\,(A_i X - B_i E_{\alpha s} \bar{K}_i - B_i \bar{E}_{\alpha s} Z_j); \\
D_{21}'' &= (\bar{K}_i^T E_{\alpha s}^T + Z_j^T \bar{E}_{\alpha s}^T) B_i^T; \\
D_{31}'' &= E_{\alpha s}^T B_i^T; \\
D_{22}'' &= A_i X + X A_i^T - \bar{L}_i - \bar{L}_i^T = H\,(A_i X - \bar{L}_i); \\
D_{32}'' &= E_{\alpha s}^T B_i^T; \\
D_{33}'' &= -H\,(\frac{1}{\delta} F_i C B_i E_{\alpha s}).
\end{aligned} \tag{19}$$

The controller gains are obtained by $K_i = \bar{K}_i \cdot X^{-1}$, $H_j = Z_j \cdot X^{-1}$ and the observer gains are derived by $L_i = \bar{L}_i \cdot (CX)^{-1}$.

Proof: let $X = (P_1/\rho)^{-1}$ and $Z_j = H_j \cdot X$ the inequality (6) can be written as:

$$\bar{u}_i^2 X - \left(z_i^j\right)^T z_i^j \geq 0, \tag{20}$$

where z_i^j is the i^{th} row of the matrix Z_j and by Schur complement, inequality (20) can be written as (17).

The goal is to determine the unknowns' parameters of the controller L_i, T, F_i and δ. Let us choose the following Lyapunov function:

$$V = x^T P_1 x + e_x^T P_1 e_x + \frac{1}{\delta} e_f^T T^{-1} e_f > 0, \tag{21}$$

where P_1 is the symmetric positive definite matrix.

The derivative of V with respect to time t is given by:

$$\begin{aligned}
\dot{V} = {} & \dot{x}^T P_1 x + x^T P_1 \dot{x} + \dot{e}_x^T P_1 e_x + e_x^T P_1 \dot{e}_x + \\
& + \frac{1}{\delta} \dot{e}_f^T T^{-1} e_f + \frac{1}{\delta} e_f^T T^{-1} \dot{e}_f \quad < 0
\end{aligned} \tag{22}$$

According to (14)–(16), $\dot{V}$ becomes:

$$\begin{aligned}
\dot{V} = {} & x^T \Psi_{ij}^T P_1 x + e_f^T E_{\alpha s}^T B_i^T P_1 x + e_x^T (K_i^T E_{\alpha s}^T + \\
& + H_i^T \bar{E}_{\alpha s}^T) B_i^T P_1 x + d^T P_1 x + x^T P_1 \Psi_{ij} x + x^T P_1 B_i E_{\alpha s} e_f + \\
& + x^T P_1 B_i (E_{\alpha s} K_i + \bar{E}_{\alpha s} H_i) e_x + x^T P_1 d + e_x^T \phi_i^T P_1 e_x + \\
& + e_f^T E_{\alpha s}^T B_i^T P_1 e_x + d^T P_1 e_x + e_x^T P_1 \phi_i e_x + e_x^T P_1 B_i E_{\alpha s} e_f + \\
& + e_x^T P_1 d + \frac{1}{\delta} \dot{f}_u^T T^{-1} e_f - \frac{1}{\delta}^T \dot{e}_y^T F_i^T e_f - e_y^T F_i^T e_f + \\
& + \frac{1}{\delta} e_f^T T^{-1} \dot{f}_u - \frac{1}{\delta} e_f^T F_i \dot{e}_y - e_f^T F_i e_y
\end{aligned} \tag{23}$$

with:

$$\Psi_{ij} = A_i - B_i\left(E_{\alpha s} K_i + \bar{E}_{\alpha s} H_i\right); \tag{24}$$

$$\phi_i = A_i - L_i C. \tag{25}$$

The dynamic of the state estimation error, output error and the fault estimation error are calculated by:

$$\dot{e}_x = \sum_{i=1}^{r} \mu_i \left(\phi_i e_x + B_i E_{\alpha s} e_f\right) + d(t); \tag{26}$$

$$\dot{e}_y = C\dot{e}_x = C\left(\sum_{i=1}^{r} \mu_i \left(\phi_i e_x + B_i E_{\alpha s} e_f\right) + d(t)\right); \tag{27}$$

$$\dot{e}_f = \dot{f}_u - \dot{\hat{f}}_u. \tag{28}$$

Now, using Lemma 1 and Assumption 1 we can write:

$$\begin{aligned}
\frac{1}{\delta} \dot{f}_u^T T^{-1} e_f + \frac{1}{\delta} e_f^T T^{-1} \dot{f}_u < {} & \frac{1}{\delta} e_f^T G e_f + \\
& + \frac{1}{\delta} f_{1\max}^2 \lambda_{\max}\left(T^{-1} G^{-1} T^{-1}\right)
\end{aligned} \tag{29}$$

Based on the dynamic errors defined by (26)–(28) and the inequality (29) the time derivative of the Lyapunov function (23) is rewritten as follows after some algebraic manipulation using Lemma 1:

$$\begin{bmatrix}
\delta_{11} & * & * & * \\
\delta_{21} & \delta_{22} & * & * \\
E_{\alpha s}^T B_i^T P_1 & \delta_{32} & \delta_{33} & * \\
P_1 & P_1 & -\frac{1}{\delta^T} C^T F_i^T & -\gamma^2
\end{bmatrix} < 0 \tag{30}$$

with:

$$\delta_{11} = \Psi_{ij}{}^T P_1 + P_1 \Psi_{ij} + I;$$
$$\delta_{21} = \left(K_i{}^T E_{\alpha s}{}^T + H_i{}^T \bar{E}_{\alpha s}{}^T\right) B_i{}^T P_1;$$
$$\delta_{22} = \phi_i{}^T P_1 + P_1 \phi_i;$$
$$\delta_{32} = E_{\alpha s}{}^T B_i{}^T P_1 - \frac{1}{\delta} F_i C \phi_i - F_i C; \quad (31)$$
$$\delta_{23} = P_1 B_i E_{\alpha s} - \frac{1}{\delta^T} \phi_i{}^T C^T F_i^T - C^T F_i^T;$$
$$\delta_{33} = -\frac{1}{\delta^T} E_{\alpha s}{}^T B_i{}^T C^T F_i^T - \frac{1}{\delta} F_i C B_i E_{\alpha s} + \frac{1}{\delta} G \cdot$$

Multiplying (30) left and right by diag(X X 1 1), where $P_1^{-1} = X$ the following inequality is derived:

$$\begin{bmatrix} D_{11} & * & * & * \\ \left(\bar{K}_i{}^T E_{\alpha s}{}^T + Z_j{}^T \bar{E}_{\alpha s}{}^T\right) B_i{}^T & D_{22} & * & * \\ E_{\alpha s}{}^T B_i{}^T & D_{32} & D_{33} & * \\ I & I & -\frac{1}{\delta^T} C^T F_i^T & -\gamma^2 \end{bmatrix} < 0 \quad (32)$$

with:

$$D_{11} = H\,(A_i X - B_i E_{\alpha s} \bar{K}_i - B_i \bar{E}_{\alpha s} Z_j) + XIX;$$
$$D_{22} = A_i X + X A_i{}^T - \bar{L}_i - \bar{L}_i{}^T = H\,(A_i X - \bar{L}_i);$$
$$D_{32} = E_{\alpha s}{}^T B_i{}^T - \frac{1}{\delta} F_i C A_i X + \frac{1}{\delta} F_i C L_i C X - F_i C X; \quad (33)$$
$$D_{33} = -H\,(\frac{1}{\delta} F_i C B_i E_{\alpha s}) \cdot$$

Applying Lemma 1 the inequality (32) becomes:

$$\begin{bmatrix} D'_{11} & * & * & * \\ D'_{21} & D'_{22} & * & * \\ D'_{31} & D'_{32} & D'_{33} & * \\ I & I & -\frac{1}{\delta^T} C^T F_i^T & -\gamma^2 \end{bmatrix} < 0 \quad (34)$$

with:

$$D'_{11} = H\,(A_i X - B_i E_{\alpha s} \bar{K}_i - B_i \bar{E}_{\alpha s} Z_j) + XIX;$$
$$D'_{21} = \left(\bar{K}_i{}^T E_{\alpha s}{}^T + Z_j{}^T \bar{E}_{\alpha s}{}^T\right) B_i{}^T;$$
$$D'_{31} = E_{\alpha s}{}^T B_i{}^T;$$
$$D'_{22} = H\,(A_i X - L_i C X) = A_i X + X A_i{}^T - \bar{L}_i - \bar{L}_i{}^T +;$$
$$+ \sigma_{1i}{}^{-1} XX + \sigma_{2i}{}^{-1} \bar{L}_i \bar{L}_i{}^T + \sigma_{3i}{}^{-1} XX \quad (35)$$
$$D'_{32} = E_{\alpha s}{}^T B_i{}^T;$$
$$D'_{33} = -H\,(\frac{1}{\delta} F_i C B_i E_{\alpha s}) + \sigma_{1i} \frac{1}{\delta} F_i C A_i A_i{}^T C^T F_i^T \frac{1}{\delta^T} + .$$
$$+ \sigma_{2i} \frac{1}{\delta} F_i C C^T F_i^T \frac{1}{\delta^T} + \sigma_{3i} F_i C C^T F_i^T$$

Now, applying Schur complement on terms D'_{11}, D'_{22} and D'_{33}, the theorem 1 is hold.

Simulation results. In order to show the effectiveness of the proposed FTC approach, a PMSM non linear model is considered. The nonlinear PMSM model is given by:

$$\frac{di_d}{dt} = \dot{x}_1 = f_1(x) + g_1 u_d$$
$$\frac{di_q}{dt} = \dot{x}_2 = f_2(x) + g_2 u_q \quad (36)$$
$$\frac{dw_r}{dt} = \dot{x}_3 = f_3(x)$$

with:

$$F(x) = \begin{pmatrix} f_1(x) \\ f_2(x) \\ f_3(x) \end{pmatrix} = \begin{pmatrix} a_1 x_1 + a_2 x_2 x_3 \\ b_1 x_2 + b_2 x_1 x_3 + b_3 x_3 \\ c_1 x_3 + c_2 x_1 x_2 + c_3 x_2 + c_4 C_r \end{pmatrix};$$
$$G = \begin{pmatrix} g_1 & 0 \\ 0 & g_2 \\ 0 & 0 \end{pmatrix};$$
$$a_1 = -R / L_d \;;\; a_2 = p L_q / L_d$$
$$b_1 = -R / L_q \;;\; b_2 = -pL_d / L_q \;;\; b_3 = -p\varphi_f / L_q$$
$$c_1 = -f / J \;;\; c_2 = k_1 / J \;;\; c_3 = k_2 / J \;;\; c_4 = -1 / J$$
$$g_1 = 1 / L_d \;;\; g_2 = 1 / L_q$$
$$\begin{pmatrix} \dot{x}_1 \\ \dot{x}_2 \\ \dot{x}_3 \end{pmatrix} = \begin{pmatrix} \frac{di_d}{dt} \\ \frac{di_q}{dt} \\ \frac{dw_r}{dt} \end{pmatrix} = \begin{pmatrix} f_1(x) \\ f_2(x) \\ f_3(x) \end{pmatrix} + \begin{pmatrix} g_1 & 0 \\ 0 & g_2 \\ 0 & 0 \end{pmatrix} \begin{pmatrix} u_d \\ u_q \end{pmatrix}.$$

The different parameters values are given in Table 1.

Table 1

PMSM parameters

Parameter	Description	Value
R	Stator resistance, Ω	1.4
L_d	Direct stator inductance, H	0.0066
L_q	Quadratic stator inductance, H	0.0058
f	Coefficient of friction, N·m/rad·s	0.00038
p	Number of pole pairs	3
J	Moment of inertia, kg·m^2	0.00176

Furthermore, to see the effectiveness of the proposed approach by applying the FTC law with the derived controller and observer gains, Fig. 2–4 show the estimated states and real ones obtained with the FTC law.

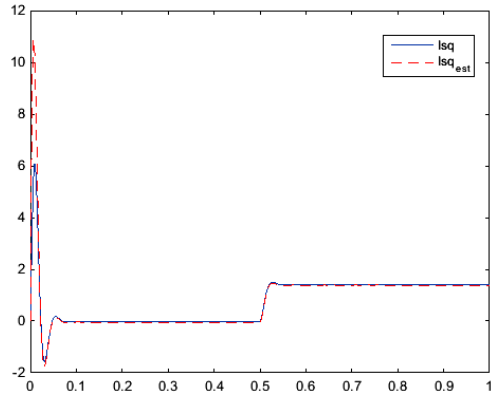

Fig. 2. Stator current I_q and their estimation

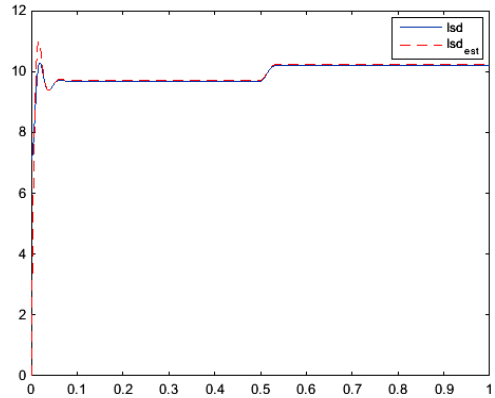

Fig. 3. Stator current I_d and their estimation

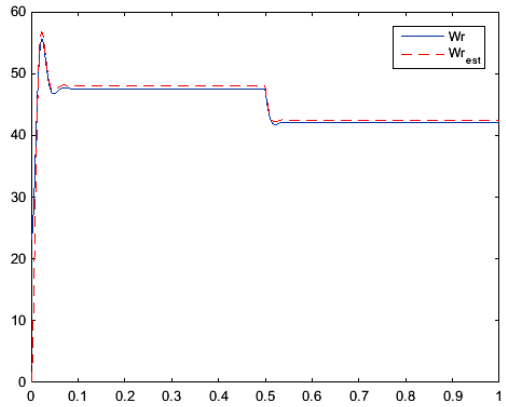

Fig. 4. Motor speed and their estimation

It should be highlighted that the proposed FTC design approach gives promising results while preserving the stability and guarantee the disturbance rejection. The fault has been estimated by the observer (5) as illustrated in Fig. 5.

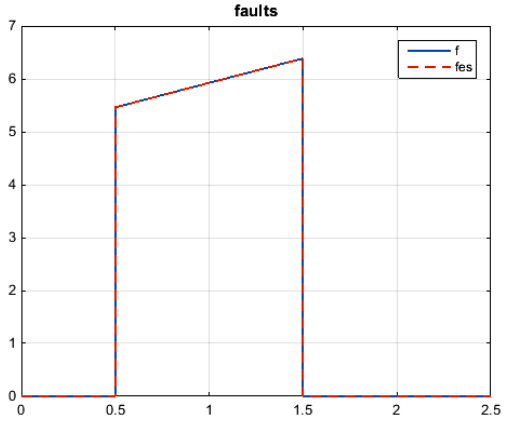

Fig. 5. Fault and their estimation

Conclusions.

This paper is dedicated to the design of fault tolerant control strategy for nonlinear systems described by Takagi-Sugeno models. The systematic procedure is presented to deal with the faulty actuator and input system saturation and applied into permanent magnet synchronous machine. The proposed fault tolerant control design approach is based on a robust observer to estimate both the actuator faults and the system states used to synthesize the controller law. The main advantage of the proposed approach is to synthesize the control law by taking into consideration the saturation limits. Using Lyapunov theory, sufficient conditions are derived by solving an linear matrix inequalities optimization problem by taking into account the saturation level. It can be noticed from the simulation results that the proposed fault tolerant control strategy is clearly approved on a permanent magnet synchronous machine model. It is clear that the values of the speed and currents estimated by the observers follow correctly the objectives even when changing the torque at 0.5 s, also estimated faults follow correctly generated fault between 0.5–1.5 s.

As future works, the proposed approach may be generalized to Takagi-Sugeno systems with unmeasurable decision variable and/or subject to sensor saturations.

Conflict of interest. The authors declare no conflict of interest.

REFERENCES

1. Ichalal D., Marx B., Ragot J., Mammar S., Maquin D. Sensor fault tolerant control of nonlinear Takagi-Sugeno systems. Application to vehicle lateral dynamics. *International Journal of Robust and Nonlinear Control*, 2016, vol. 26, no. 7, pp. 1376-1394. doi: https://doi.org/10.1002/rnc.3355.

2. Ichalal D., Marx B., Ragot J., Maquin D. Observer based actuator fault tolerant control for nonlinear Takagi-Sugeno systems : an LMI approach. *18th Mediterranean Conference on Control and Automation, MED'10*, 2010, pp. 1278-1283. doi: https://doi.org/10.1109/MED.2010.5547874.

3. Ichalal D., Marx B., Maquin D., Ragot J. New fault tolerant control strategy for nonlinear systems with multiple model approach. *2010 Conference on Control and Fault-Tolerant Systems (SysTol)*, 2010, pp. 606-611. doi: https://doi.org/10.1109/SYSTOL.2010.5675951.

4. Zuo Z., Ho D.W.C., Wang Y. Fault tolerant control for singular systems with actuator saturation and nonlinear perturbation. *Automatica*, 2010, vol. 46, no. 3, pp. 569-576. doi: https://doi.org/10.1016/j.automatica.2010.01.024.

5. Dang Q.V., Vermeiren L., Dequidt A., Dambrine M. LMI approach for robust stabilization of Takagi–Sugeno descriptor systems with input saturation. *IMA Journal of Mathematical Control and Information*, 2018, vol. 35, no. 4, pp. 1103-1114. doi: https://doi.org/10.1093/imamci/dnx019.

6. Bernstein D.S., Michel A.N. A chronological bibliography on saturating actuators. *International Journal of Robust and Nonlinear Control*, 1995, vol. 5, no. 5, pp. 375-380. doi: https://doi.org/10.1002/rnc.4590050502.

7. Takagi T., Sugeno M. Fuzzy identification of systems and its applications to modeling and control. *IEEE Transactions on Systems, Man, and Cybernetics*, 1985, vol. SMC-15, no. 1, pp. 116-132. doi: https://doi.org/10.1109/TSMC.1985.6313399.

8. Tanaka K., Wang H.O. *Fuzzy Control Systems Design and Analysis*. John Wiley & Sons, Inc. 2001. 302 p. doi: https://doi.org/10.1002/0471224596.

9. Tarbouriech S., Garcia G., Gomes da Silva J.M., Queinnec I. *Stability and Stabilization of Linear Systems with Saturating Actuators*. Springer London, 2011. 430 p. doi: https://doi.org/10.1007/978-0-85729-941-3.

10. Boyd S., El Ghaoui L., Feron E., Balakrishnan V. Linear Matrix Inequalities in System and Control Theory. *Society for Industrial and Applied Mathematics*, 1994. 185 p. doi: https://doi.org/10.1137/1.9781611970777.

11. Aouaouda S., Chadli M., Cocquempot V., Tarek Khadir M. Multi-objective H − / H ∞ fault detection observer design for Takagi-Sugeno fuzzy systems with unmeasurable premise variables: descriptor approach. *International Journal of Adaptive Control and Signal Processing*, 2013, vol. 27, no. 12, pp. 1031-1047. doi: https://doi.org/10.1002/acs.2374.

12. Bouarar T., Marx B., Maquin D., Ragot J. Trajectory tracking fault tolerant controller design for Takagi-Sugeno systems subject to actuator faults. *2011 International Conference on Communications, Computing and Control Applications (CCCA)*, 2011, pp. 1-6. doi: https://doi.org/10.1109/CCCA.2011.6031484.

13. Benzaouia A., El Hajjaji A., Hmamed A., Oubah R. Fault tolerant saturated control for T–S fuzzy discrete-time systems with delays. *Nonlinear Analysis: Hybrid Systems*, 2015, vol. 18, pp. 60-71. doi: https://doi.org/10.1016/j.nahs.2015.06.003.

14. Nguyen A., Dequidt A., Dambrine M. Anti-windup based dynamic output feedback controller design with performance consideration for constrained Takagi–Sugeno systems. *Engineering Applications of Artificial Intelligence*, 2015, vol. 40, pp. 76-83. doi: https://doi.org/10.1016/j.engappai.2015.01.005.

15. Nguyen A.-T., Laurain T., Palhares R., Lauber J., Sentouh C., Popieul J.-C. LMI-based control synthesis of constrained Takagi–Sugeno fuzzy systems subject to L2 or L∞ disturbances. *Neurocomputing*, 2016, vol. 207, pp. 793-804. doi: https://doi.org/10.1016/j.neucom.2016.05.063.

16. Nguyen A.-T., Sentouh C., Popieul J.-C. Fuzzy steering control for autonomous vehicles under actuator saturation: Design and experiments. *Journal of the Franklin Institute*, 2018, vol. 355, no. 18, pp. 9374-9395. doi: https://doi.org/10.1016/j.jfranklin.2017.11.027.

17. Bezzaoucha S., Marx B., Maquin D., Ragot J. State and output feedback control for Takagi-Sugeno systems with saturated actuators. *International Journal of Adaptive Control and Signal Processing*, 2016, vol. 30, no. 6, pp. 888-905. doi: https://doi.org/10.1002/acs.2649.

18. Saifia D., Chadli M., Karimi H.R., Labiod S. Fuzzy control for Electric Power Steering System with assist motor current input constraints. *Journal of the Franklin Institute*, 2015, vol. 352, no. 2, pp. 562-576. doi: https://doi.org/10.1016/j.jfranklin.2014.05.007.

19. Saifia D., Chadli M., Labiod S., Guerra T.M. Robust H ∞ static output feedback stabilization of T-S fuzzy systems subject to actuator saturation. *International Journal of Control, Automation and Systems*, 2012, vol. 10, no. 3, pp. 613-622. doi: https://doi.org/10.1007/s12555-012-0319-3.

Received 08.03.2022
Accepted 13.06.2022
Published 06.11.2022

Lotfi Moussaoui[1], *Doctor and Senior Lecturer in Automatic,*
Sabrina Aouaouda[1], *PhD, Professor,*
Reda Rouaibia[1], *Doctor and Senior Lecturer in Automatic,*
[1] Department of Electrical Engineering,
Faculty of Science and Technology,
Mohamed-Cherif Messaadia University Souk Ahras,
BP 1553, Souk Ahras, Algeria.
e-mail: l.moussaoui@univ-soukahras.dz (Corresponding Author),
sabrina.aouaouda@univ-soukahras.dz,
r.rouaibia@univ-soukahras.dz

How to cite this article:
Moussaoui L., Aouaouda S., Rouaibia R. Fault tolerant control of a permanent magnet synchronous machine using multiple constraints Takagi-Sugeno approach. *Electrical Engineering & Electromechanics*, 2022, no. 6, pp. 22-27. doi: https://doi.org/10.20998/2074-272X.2022.6.04

UDC 621.314 https://doi.org/10.20998/2074-272X.2022.6.05

E. Parimalasundar, N.M.G. Kumar, P. Geetha, K. Suresh

Performance investigation of modular multilevel inverter topologies for photovoltaic applications with minimal switches

Introduction. *In recent years, a growing variety of technical applications have necessitated the employment of more powerful equipment. Power electronics and megawatt power levels are required in far too many medium voltage motor drives and utility applications. It is challenging to incorporate a medium voltage grid with only one power semiconductor that has been extensively modified. As a result, in high power and medium voltage settings, multiple power converter structure has been offered as a solution. A multilevel converter has high power ratings while also allowing for the utilization of renewable energy sources. Renewable energy sources such as photovoltaic, wind, and fuel cells may be readily connected to a multilevel inverter topology for enhanced outcomes. The* ***novelty*** *of the proposed work consists of a novel modular inverter structure for solar applications that uses fewer switches.* ***Purpose.*** *The proposed architecture is to decrease the number of switches and Total Harmonic Distortions. There is no need for passive filters, and the proposed design enhances power quality by creating distortion-free sinusoidal output voltage as the level count grows while also lowering power losses.* ***Methods.*** *The proposed topology is implemented with MATLAB / Simulink, using gating pulses and various pulse width modulation methodologies. Moreover, the proposed model also has been validated and compared to the hardware system.* ***Results.*** *Total harmonic distortion, number of power switches, output voltage and number of DC sources are compared with conventional topologies.* ***Practical value.*** *The proposed topology has been very supportive for implementing photovoltaic based multilevel inverter, which is connected to large demand in grid.* References 12, table 5, figures 23.

Key words: **fast Fourier transform, multilevel inverter, photovoltaic, pulse width modulation techniques, total harmonic distortion.**

Вступ. *В останні роки зростаюча різноманітність технічних застосувань вимагає використання потужнішого обладнання. Силова електроніка і мегаватні рівні потужності потрібні в багатьох приводах двигунів середньої напруги і комунальних застосуваннях. Складно увімкнути мережу середньої напруги лише з одним сильно модифікованим напівпровідниковим приладом. В результаті, для установок високої потужності та середньої напруги як рішення було запропоновано структуру з кількома силовими перетворювачами. Багаторівневий перетворювач має високу номінальну потужність, а також дозволяє використовувати відновлювані джерела енергії. Відновлювані джерела енергії, такі як фотоелектричні, вітряні та паливні елементи можуть бути легко підключені до топології багаторівневого інвертора для покращення результатів.* ***Новизна*** *роботи полягає у новій модульній структурі інвертора для сонячних батарей, у якій використовується менше перемикачів.* ***Мета.*** *Пропонована архітектура призначена для зменшення кількості перемикачів та загальних гармонійних спотворень. Немає необхідності в пасивних фільтрах, а пропонована конструкція покращує якість електроенергії, створюючи синусоїдальну вихідну напругу без спотворень зі зростанням кількості рівнів, а також знижуючи втрати потужності.* ***Методи.*** *Пропонована топологія реалізована за допомогою MATLAB/Simulink з використанням стробуючих імпульсів та різних методологій широтно-імпульсної модуляції. Крім того, запропонована модель також була перевірена та порівняна з апаратною системою.* ***Результати.*** *Загальне гармонійне спотворення, кількість силових ключів, вихідна напруга та кількість джерел постійного струму порівнюються із звичайними топологіями.* ***Практична цінність.*** *Запропонована топологія дуже сприятлива для реалізації багаторівневого інвертора на основі фотоелектричних елементів, який пов'язаний із великим попитом у мережі.* Бібл. 12, табл. 5, рис. 23.

Ключові слова: **швидке перетворення Фур'є, багаторівневий інвертор, фотовольтаїка, широтно-імпульсна модуляція, повні гармонічні спотворення.**

1. Introduction. Multilevel inverter (MLI) topology has lately emerged as a critical option for high-power medium-voltage energy control. The most essential topologies, according to [1], are diode-clamped inverter (neutral-point clamped), capacitor-clamped (flying capacitor), and cascaded multi cell with distinct dc sources. Among the most significant controlling and modulation techniques developed for this series of inverters are asymmetric multilevel based sinusoidal pulse width modulation, multilevel selective harmonic elimination, and space-vector modulations [1].

The authors of [2] proposed a revolutionary multilevel pulse width modulation-based inverter design for the use of stand-alone solar systems. This system is made up of a pulse width modulation (PWM) inverter, a set of voltage level inverters, a staircase output voltage generator, and cascaded transformers. It creates higher voltage waves by generating a big voltage to the necessary levels using cascaded transformers with a franchise secondary. The engine's secondary turn-ratio has been set suitably [2].

According to [3], alternating phase opposed disposition PWM for diode-clamped inverters seems to have the same harmonic effectiveness as phase-shifted carrier PWM for cascaded inverters and composite PWM for hybrid inverters whenever the carrier frequencies have been chosen to achieve having similar number of inverter switch conversions within every cycle. Using knowledge, a PWM technique for cascaded and hybrid inverters are developed that provides the same harmonic advantages as phase disposition PWM for diode-clamped inverters [3].

2. Literature review. The most important and noteworthy applications of these converters, such as particular laminators, conveyors, and grid-connected photovoltaic regulators, are emphasized. The need for an effective front end on the input stage of inverters that feed regenerative applications, as well as the many circuit design options, is also discussed. Furthermore, fast growing industries also including high-voltage high-power devices and sensing applications, as well as some additional future development prospects, are being examined [4, 5].

The fundamental disadvantage of a traditional cascaded MLI is that when levels rise, additional semiconductor switches are required. This changes the size of the inverter and complicates the control strategy. The use of a MLI with fewer switches minimizes the size of the inverter and simplifies control [6]. The diode clamped, flying capacitor, and cascaded H-bridge inverters are the three principal MLI topologies used in commercial applications with different dc voltage sources.

Capacitor voltage balancing is an issue in flying capacitor and diode-clamped inverters, but it is handled in cascaded H-bridge inverters. The main problem of classic

cascaded is that additional semiconductor switches are required even as levels grow. As a result, many adjustments will be required to reduce the size and cost of the inverter [7]. The authors of [8] investigated a number of recent articles on problems such as the creation of inverted pulse width modulation method in cascaded H-bridged MLI systems.

According to [9], multilevel converters are essential in both moderate and high-power applications. Diode clamped, flying capacitor, and cascaded H-bridged are the three most common configurations for multi-level inverters. To accomplish medium voltage and high-performance characteristics, the modular design of cascaded-H bridged MLI characteristics and performance is adopted. Short and open circuit faults are two forms of power switching device failures that might occur in cascaded H-bridged multilevel inverter (CHB-MLI). Short circuit problems mostly damage, so protection from short circuit is required. Artificial neural network approaches for short circuit protection by using high potency fuses and de-saturation method.

The authors of [10] had analyzed open-circuit faults in power switches the device shutting down, and they can go undetected for a long time. This could cause secondary defects in the inverter or other drive components, culminating in the entire system being shut down and expensive repairs.

The authors of [11] had analyzed fault analysis in inverter and also faults an inverter device is used continuously under abnormal settings, further issues will arise, resulting in severe consequences. Furthermore, the MLI is composed of several switching devices and the entire system is complex in structure, and there are numerous nonlinear impacts. As a result, MLIs need some novel diagnostic strategies which could not deal with nonlinear detection issues but also diagnose and locate faults easily. The device voltage and current of a multilayer inverter might vary based on the part and location of the faults. Some research concentrates on the device output current or voltage to assess fault form and position more quickly and easily, and then used the sample to expand a number of fault diagnosis techniques. Owing to the dangerous effects of short circuit faults on converter circuits, this type of fault must be detected as soon as possible. It is necessary to remember that certain circuit drivers are already in a position to detect defective switches. Hence considering the value of medium voltage drives on the industry, robust detection mechanisms need to be discussed.

The authors of [12] had investigated green energy and helping in solving various challenges such as climate change and pollution, the implementation of renewable distributed energy resources in the operational distribution system has risen fast. Due to its qualities of rapid charging and discharging, regulating power quality, and meeting peak energy demand, integrating battery energy storage systems might be regarded one of several finest alternatives in providing answers to the listed difficulties.

The fundamental objectives of the proposed research effort are to develop a high-performance MLI which has less number of power semiconductor switches. By the reduction of number of switches, total harmonic distortion (THD) and power losses have been minimized. The proposed technique is validated with the help of experimental setup.

3. Multicarrier pulse width modulation techniques.

3.1 Alternate phase opposition disposition. This approach requires that one of those (m – 1) carrier frequency signal be phase distorted from one another by 180 degrees alternatively for an m-level sequence pattern, as illustrated in Fig. 1 for various modulating signals. There are no harmonics at f_c because the most important harmonics are focused as circuit distortion around the carrier frequency f_c.

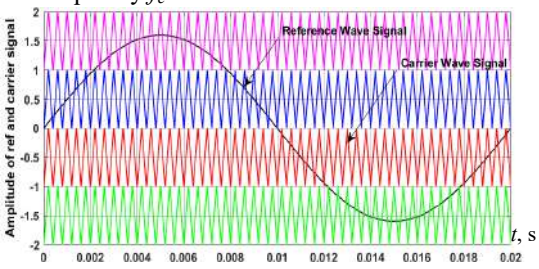

Fig. 1. Alternate phase opposition disposition multicarrier PWM

3.2 Phase opposition disposition. The carrier signal waveforms seem to be in phase around the outer minimal standard value, while the ones above and behind minimal have a 180 degree phase shift, as seen in Fig. 2 for different frequency components. In both the phase and line voltage waveforms, the highest harmonics are grouped around the carrier frequency signal f_c.

3.3 Phase disposition. As established in Fig. 3, when using the phase disposition modulation scheme, every one of the carrier signals is in phase.

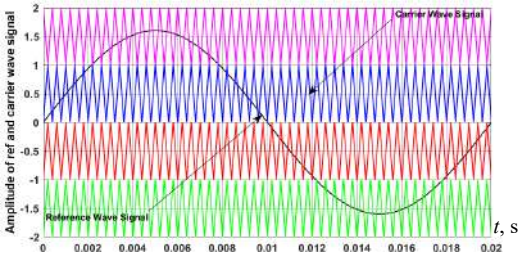

Fig. 2. Phase opposition disposition multicarrier PWM

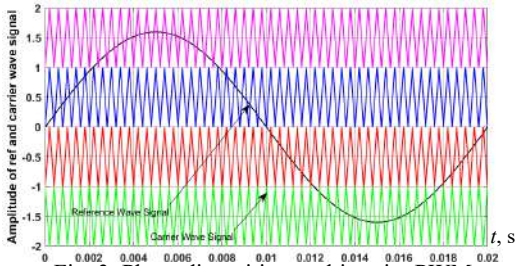

Fig. 3. Phase disposition multicarrier PWM

4. Proposed topologies. A three-phase low component power semiconductor switch based multilevel DC-link inverter scheme is used to address the limitations of standard topology. Simulation modelling and analysis are used to assess the dependability of a five-level inverter with an inductive load. H-bridge inverters link separated voltage levels and series switches to connect voltage sources to loads. As the number of levels increases, so does the circuit complexity. The proposed design operates in symmetrical mode to decrease the number of switches while maintaining the same number of output levels by maintaining the DC source amplitudes equal and the sinusoidal waveform. Figure 4 shows the photovoltaic (PV) connected modular recommended MLI I and II, with the configuration of the inverter being the focus of this whole study.

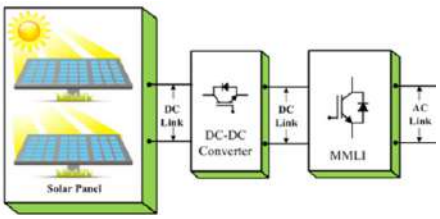

Fig. 4. Photovoltaic connected modular MLI

4.1 Proposed topology - **I.** The suggested five-level modular MLI, which provides a greater number of output voltage levels, is depicted in Fig. 5, $+2V_{dc}$, $+V_{dc}$, 0, $-V_{dc}$, and $-2V_{dc}$ are the five output levels. The PWM method is used in this inverter to generate high quality output. When four level shifted, triangular waveforms are compared to a single sine wave, four signals are created. The number of switches is decreased to 6(m–2) in this suggested architecture, where m is represents the number of output voltage levels. The switching patterns of the proposed modular MLI are shown in Table 1. Table 2 lists the parameters which are used in the simulation analysis.

4.2 Proposed topology - II. A modified MLI topology is presented for three-phase systems to minimise the number of switches and alleviate the disadvantages of standard design. The functioning of a five-level inverter with a resistive load is evaluated via simulation. Isolated DC voltage sources and switches are linked in series. Switches are used by H-bridge inverters to link voltage sources to loads. By retaining the amplitudes of the DC sources constant, the suggested topology operates in symmetrical mode, reducing the number of switches while maintaining the same number of voltage output levels. The circuit complexity grows as the proportion of levels increases, culminating in a sinusoidal waveform.

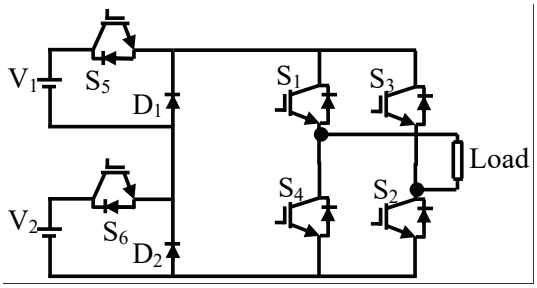

Fig. 5. Proposed modular MLI - I

Table 1

Switching patterns of proposed modular MLI - I

Vo	S1	S2	S3	S4	S5	S6
$+2V_{dc}$	1	1	0	0	1	1
$+V_{dc}$	1	1	0	0	1	0
0	0	0	0	0	0	0
$-V_{dc}$	0	0	1	1	0	1
$-2V_{dc}$	0	0	1	1	1	1

Table 2

Design parameters of proposed modular MLI - I

Parameters	Range
Input voltage (DC)	115 V
Output voltage(Peak)/Ph.	230 V
Output frequency	50 Hz
Inverter switching frequency	10 kHz
Modulation Index	1
Load resistance	100 Ω
Power Rating	1.587 kW

In this proposed (Fig. 6) architecture, the number of switches is reduced to 6 (m–2) where m is the number of levels. For MLI to work effectively, diodes are also required. The design and operation of this topology is more complicated than standard approaches. According to the generalization of configuration in symmetrical arrangement for N-level output, the principal switches used here are 6(m–2) for three phases, where 'm' is the number of levels. If m value is 5, the total number of switches in this topology is 18, and two DC sources are necessary. The switching patterns of the proposed modular MLI are shown in Table 3. The switching patterns of the proposed MLI are shown in Table 4 lists the parameters which are used in the simulation analysis.

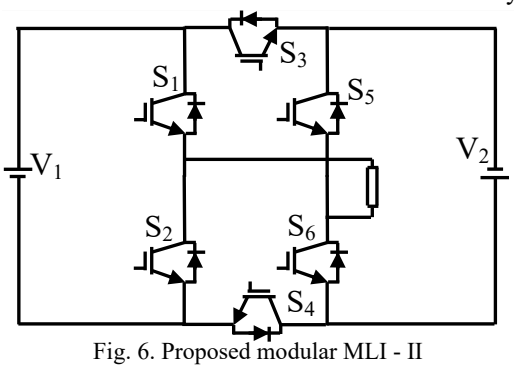

Fig. 6. Proposed modular MLI - II

Table 3

Switching patterns of proposed modular MLI - II

Vo	S1	S2	S3	S4	S5	S6
$+2V_{dc}$	1	0	0	1	1	0
$+V_{dc}$	0	1	0	1	1	0
0	0	0	0	0	0	0
$-V_{dc}$	0	1	1	0	1	0
$-2V_{dc}$	0	1	1	0	0	1

Table 4

Design parameters of proposed modular MLI – II

Parameters	Range
Input voltage (DC)	115 V
Output voltage(Peak)/Ph.	230 V
Output frequency	50 Hz
Inverter switching frequency	10 kHz
Modulation Index	1
Load resistance	100 Ω
Power Rating	1.2 kW

5. Results and discussion.

5.1 Proposed topology - I. Figure 7 illustrates the MATLAB / Simulink Model of proposed - I MLI. Figure 8 depicts the modular five level three phase voltage output configuration over the load. The waveform yields the input and output voltages of 115 V and 230 V, respectively. Fast Fourier transform (FFT) analysis of alternate phase opposition disposition (APOD), phase opposition disposition (POD), and phase disposition (PD) based pulse width modulation is shown in Fig. 9–11. The switching pulse turn device sequence, as well as the cascaded MLI level output voltage.

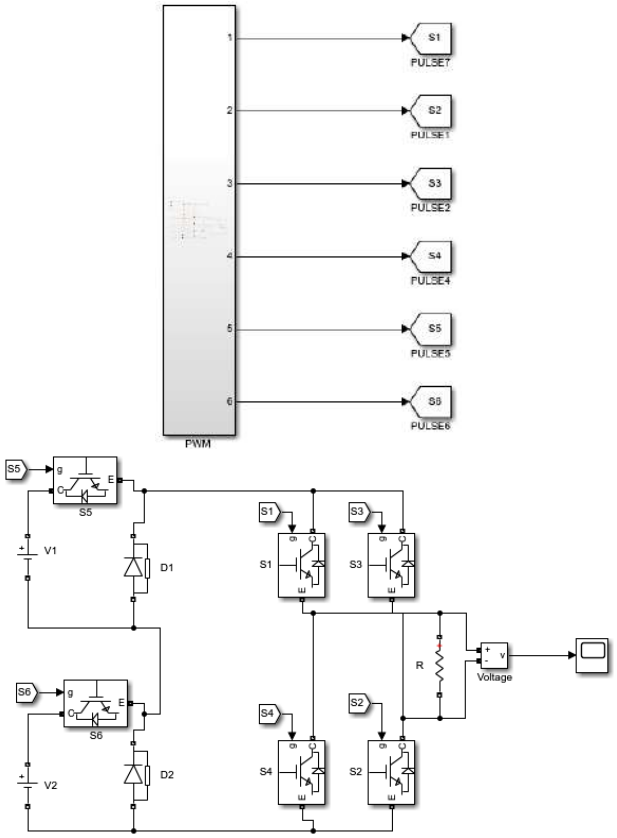

Fig. 7. MATLAB / Simulink model of proposed - I modular MLI

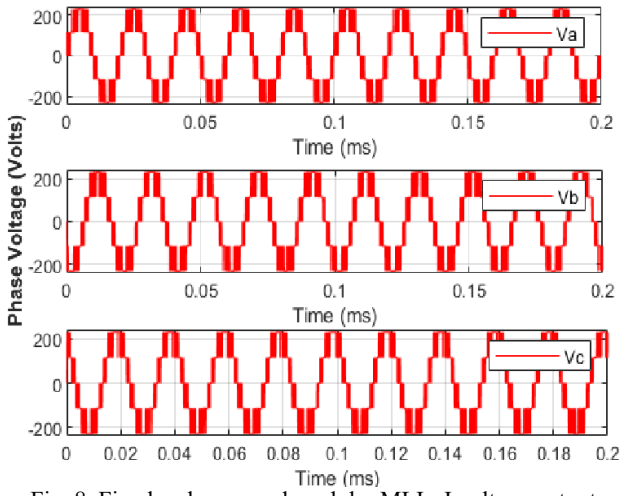

Fig. 8. Five level proposed modular MLI - I voltage output pattern for three phase system

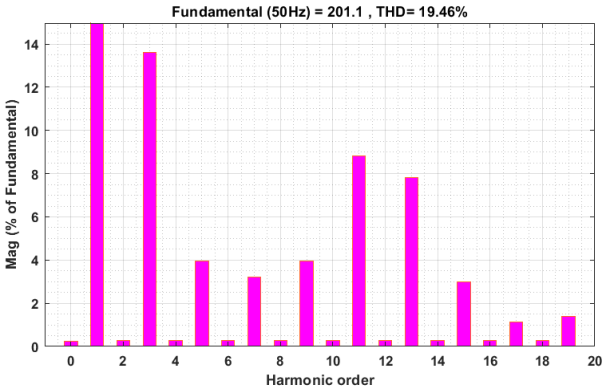

Fig. 9. FFT investigation of the proposed modular MLI - I with APOD

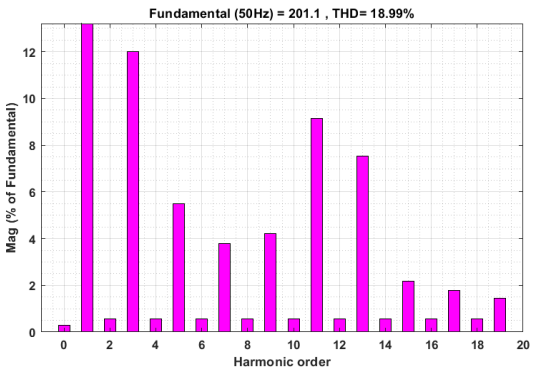

Fig. 10. FFT investigation of the proposed modular MLI - I with POD

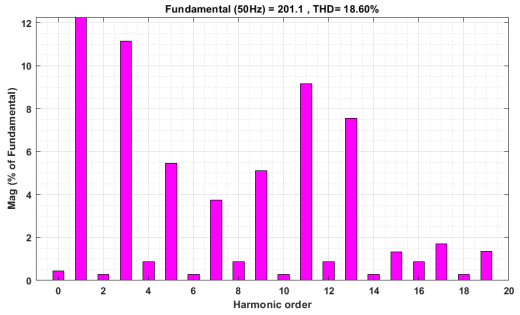

Fig. 11. FFT investigation of the proposed modular MLI - I with PD

5.2 Proposed topology - II. Figure 12 illustrates the MATLAB / Simulink model proposed - II MLI.

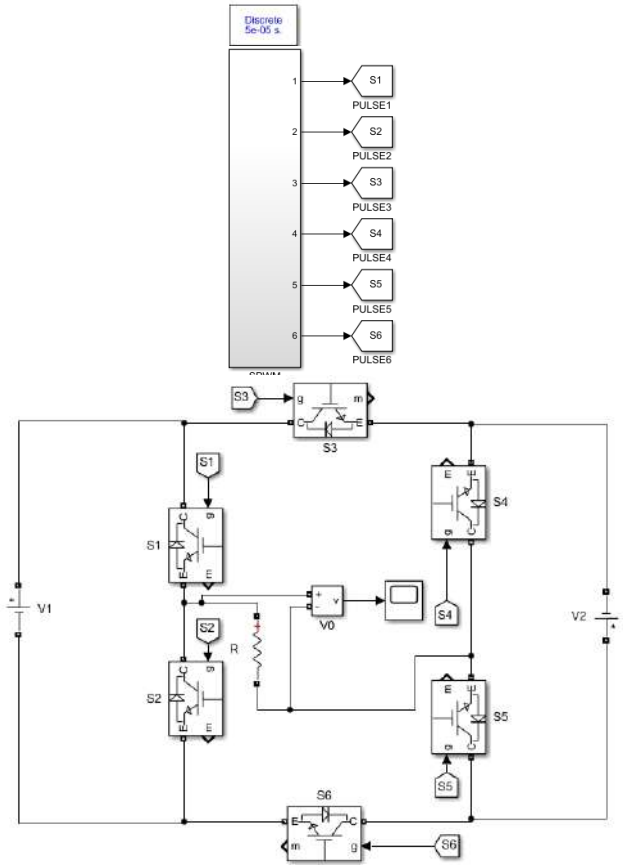

Fig. 12. MATLAB / Simulink model of proposed - II modular MLI

Figure 13 shows the switching pulses of modular MLI - I. Figure 14 illustrates the modular five and 230 V, respectively. FFT analysis of APOD, POD, and PD based pulse width modulation is shown in Fig. 15–17.

The switching pulse turn device sequence, as well as the cascaded MLI level output voltage. Figure 18 shows the switching pulses of modular MLI - II.

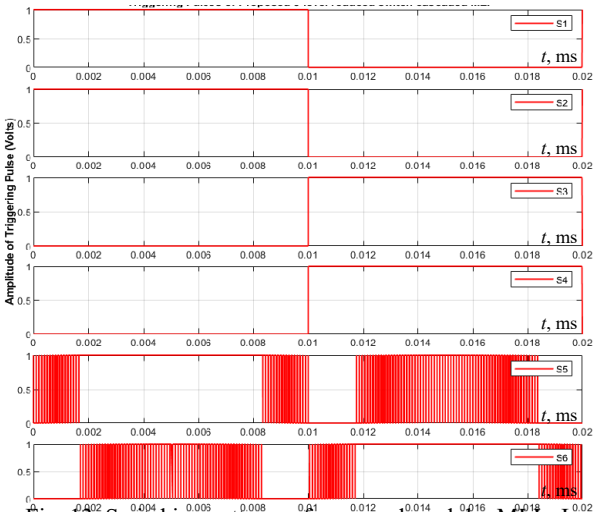

Fig. 13. Switching patterns of proposed modular MLI - I

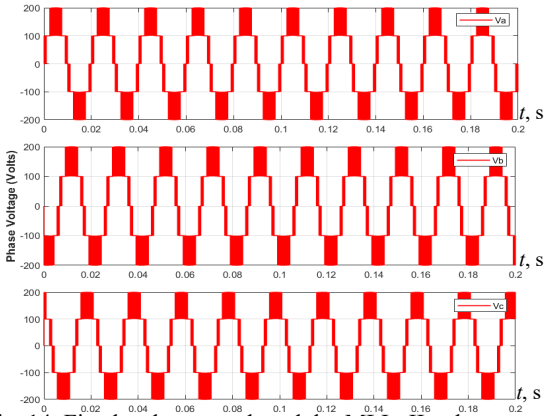

Fig. 14. Five level proposed modular MLI - II voltage output pattern for three phase system

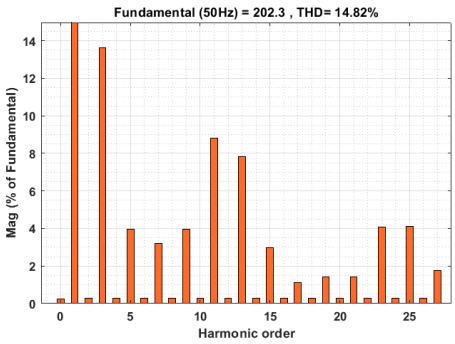

Fig. 15. FFT investigation of the proposed modular MLI - II with APOD

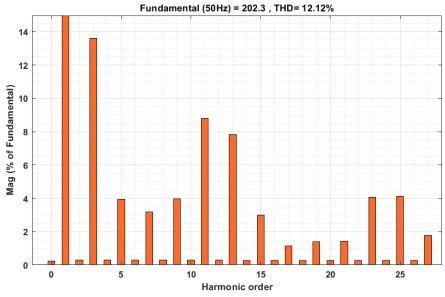

Fig. 16. FFT investigation of the proposed modular MLI - II with POD

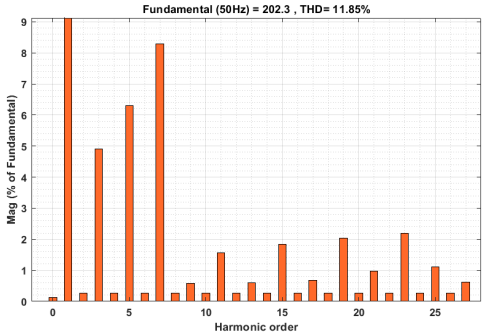

Fig. 17. FFT investigation of the proposed modular MLI - II with PD

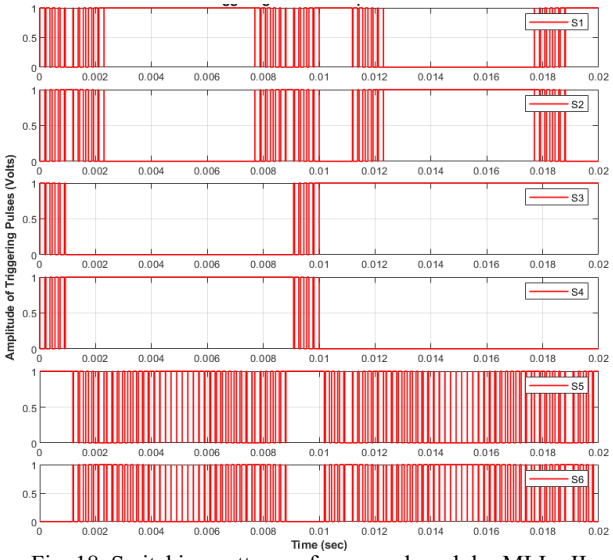

Fig. 18. Switching patterns of proposed modular MLI – II

Figures 19, 20 illustrate the detail of THD analysis of conventional and proposed modular MLI and switch count analysis of conventional and proposed modular MLI respectively which is calculated based on the mathematical expressions represented in Table 5.

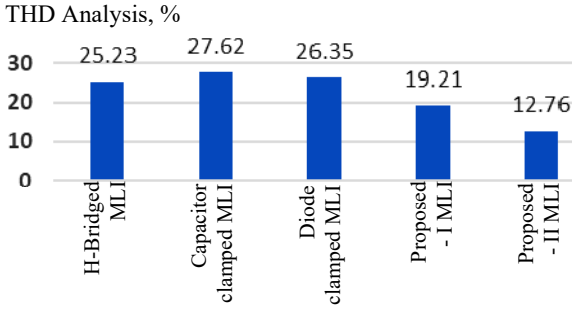

Fig. 19. THD analysis of conventional and proposed modular MLI

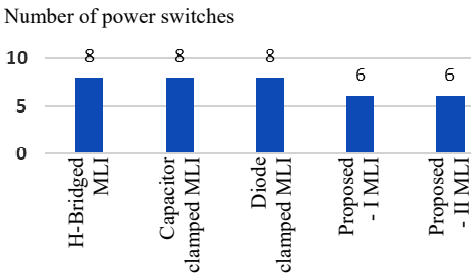

Fig. 20. Switch count analysis of conventional and proposed modular MLI

Table 5

Comparative properties of conventional and proposed MLIs

MLI structure	Cascaded H-bridge	Diode clamped	Flying capacitor	Proposed topology – I	Proposed topology – II
Power semiconductor switches	6(m–1)	6(m–1)	6(m–1)	6(m–2)	6(m–2)
Bridged diodes	6(m–1)	6(m–1)	6(m–1)	6(m–2)	6(m–2)
Diodes for clamping	–	3(m–2)	–	–	–
Splitting capacitors for DC	–	m–1	m–1	–	–
Clamping capacitors for DC	–	–	3m	–	–
Other diodes	–	–	–	m+1	m+1

6. Experimental results and discussion. In order to evaluate the performance of the proposed 5-level structure, IGBTs are employed as switching devices in the proposed 5-level MLI prototype. The experimental setup arrangement for the proposed 5-level single large multilevel power converter (SL-MLPC) is depicted in Fig. 21. The field-programmable gate array is used in this research to generate pulses for the power switches. In Xilinx software, the Verilog-language is utilised to program all of the switching states of the proposed topology. The switching pulses are eventually transported through optic-wires to the gate driver circuits, where they are employed to power the IGBTs in the proposed topology. Several experimental results predicated on a 620 W laboratory model are provided in this part to validate the results of the designed inverter. A PV simulator was employed as a power supply in this case, and the recommended point of common coupling was used to communicate the accuracy of the control system, which was controlled by a Texas instrument.

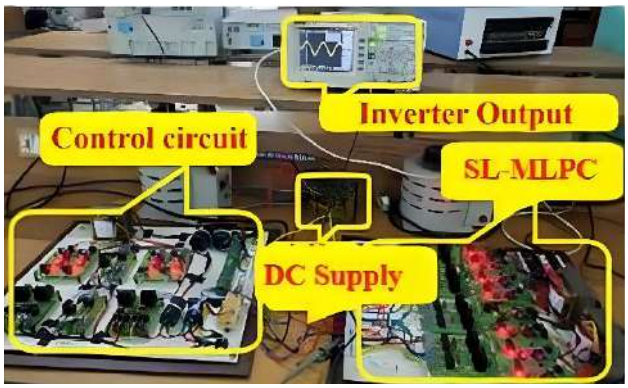

Fig. 21. Experimental prototype of the proposed inverter

Figures 22, 23 illustrate the inverter's five-level voltage waveform with a maximum value of 203 V, which would be required to inserting power into the transmission system, as well as the sinusoidal injected current with unity power factor, which provides the proposed topology output results. The supply current to the power network has a maximum amplitude of roughly 5 A, as seen in the graph. The 50 Hz network reference voltage and single phase five level of the proposed inverter are shown in Figures 22, 23.

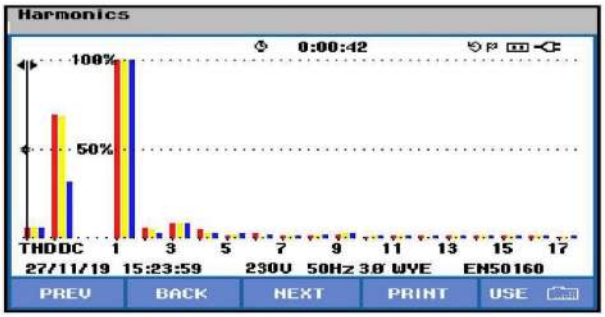

Fig. 22. Five level proposed – I MLI topology

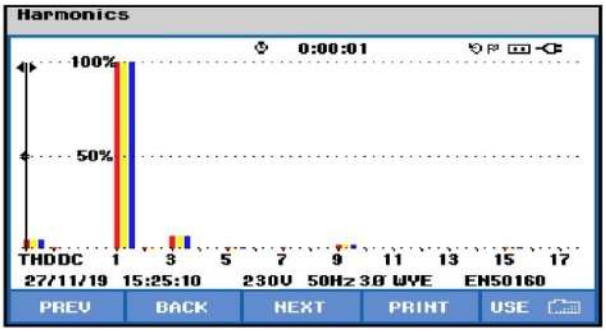

Fig. 23. Five level proposed – II MLI topology

7. Conclusions. The suggested multilevel inverter architecture may be a viable option for powering photovoltaic applications. A five-level inverter was explored and controlled using a multi-carrier approach, which required fewer switching states each cycle. The recommended new modular multilevel inverter with a system to obtain and the switching patterns of five-level multilevel inverter are generated based on the working pattern of power electronic switching devices, according to the MATLAB / Simulink and hardware results. When compared to earlier multilevel inverter topologies, the suggested topology achieves good results in terms of reducing power switching components, total harmonic distortion, driver circuits, device stress, and switching losses. In that approach the proposed – I and II multilevel inverter give the total harmonic distortion values are 19.21 % and 12.76 % respectively which is compared less than the value of conventional topologies. Due to the presence of completely power switches based proposed – II multilevel inverter topology give lesser harmonics than proposed – I multilevel inverter. The total harmonic distortion value is also minimized in this proposed model using different multicarrier pulse width modulation approaches.

Conflict of interest. The authors declare that they have no conflicts of interest.

REFERENCES

1. Khoun-Jahan H. Switched Capacitor Based Cascaded Half-Bridge Multilevel Inverter With Voltage Boosting Feature. *CPSS Transactions on Power Electronics and Applications*, 2021, vol. 6, no. 1, pp. 63-73. doi: https://doi.org/10.24295/CPSSTPEA.2021.00006.

2. Grandi G., Loncarski J., Dordevic O. Analysis and Comparison of Peak-to-Peak Current Ripple in Two-Level and Multilevel PWM Inverters. *IEEE Transactions on Industrial Electronics*, 2015, vol. 62, no. 5, pp. 2721-2730. doi: https://doi.org/10.1109/TIE.2014.2363624.

3. Lingom P.M., Song-Manguelle J., Mon-Nzongo D.L., Flesch R.C.C., Jin T. Analysis and Control of PV Cascaded H-Bridge Multilevel Inverter With Failed Cells and Changing Meteorological Conditions. *IEEE Transactions on Power*

Electronics, 2021, vol. 36, no. 2, pp. 1777-1789. doi: https://doi.org/10.1109/TPEL.2020.3009107.
4. Ezhilvannan P., Krishnan S. An Efficient Asymmetric Direct Current (DC) Source Configured Switched Capacitor Multi-level Inverter. *Journal Européen Des Systèmes Automatisés*, 2020, vol. 53, no. 6, pp. 853-859. doi: https://doi.org/10.18280/jesa.530611.
5. Siddique M.D., Mekhilef S., Rawa M., Wahyudie A., Chokaev B., Salamov I. Extended Multilevel Inverter Topology With Reduced Switch Count and Voltage Stress. *IEEE Access*, 2020, vol. 8, pp. 201835-201846. doi: https://doi.org/10.1109/ACCESS.2020.3026616.
6. Saeedian M., Adabi M.E., Hosseini S.M., Adabi J., Pouresmaeil E. A Novel Step-Up Single Source Multilevel Inverter: Topology, Operating Principle, and Modulation. *IEEE Transactions on Power Electronics*, 2019, vol. 34, no. 4, pp. 3269-3282. doi: https://doi.org/10.1109/TPEL.2018.2848359.
7. Sandeep N., Yaragatti U.R. Design and Implementation of a Sensorless Multilevel Inverter With Reduced Part Count. *IEEE Transactions on Power Electronics*, 2017, vol. 32, no. 9, pp. 6677-6683. doi: https://doi.org/10.1109/TPEL.2017.2681739.
8. Suresh K., Parimalasundar E. A Modified Multi Level Inverter With Inverted SPWM Control. *IEEE Canadian Journal of Electrical and Computer Engineering*, 2022, vol. 45, no. 2, pp. 99-104. doi: https://doi.org/10.1109/ICJECE.2022.3150367.
9. Jahan H.K., Panahandeh F., Abapour M., Tohidi S. Reconfigurable Multilevel Inverter With Fault-Tolerant Ability. *IEEE Transactions on Power Electronics*, 2018, vol. 33, no. 9, pp. 7880-7893. doi: https://doi.org/10.1109/TPEL.2017.2773611.
10. Haji-Esmaeili M.M., Naseri M., Khoun-Jahan H., Abapour M. Fault-Tolerant and Reliable Structure for a Cascaded Quasi-Z-Source DC–DC Converter. *IEEE Transactions on Power Electronics*, 2017, vol. 32, no. 8, pp. 6455-6467. doi: https://doi.org/10.1109/TPEL.2016.2621411.
11. Kiran Kumar G., Parimalasundar E., Elangovan D., Sanjeevikumar P., Lannuzzo F., Holm-Nielsen J.B. Fault Investigation in Cascaded H-Bridge Multilevel Inverter through Fast Fourier Transform and Artificial Neural Network Approach. *Energies*, 2020, vol. 13, no. 6, art. no. 1299. doi: https://doi.org/10.3390/en13061299.
12. Belbachir N., Zellagui M., Settoul S., El-Bayeh C.Z., Bekkouche B. Simultaneous optimal integration of photovoltaic distributed generation and battery energy storage system in active distribution network using chaotic grey wolf optimization. *Electrical Engineering & Electromechanics*, 2021, no. 3, pp. 52-61. doi: https://doi.org/10.20998/2074-272X.2021.3.09.

Received 11.04.2022
Accepted 26.06.2022
Published 06.11.2022

Ezhilvannan Parimalasundar [1], *Associate Professor*,
Nathella Munirathnam Giri Kumar [1], *Professor*,
Prahalathan Geetha [2], *Professor*,
Krishnan Suresh [3], *Associate Professor*,
[1] Department of Electrical & Electronics Engineering,
Sree Vidyanikethan Engineering College,
Tirupati, AP – 517102, India,
e-mail: parimalasundar.e@vidyanikethan.edu (Corresponding Author); nmgkumar@gmail.com
[2] Department of Electronics and Communication Engineering,
Sree Vidyanikethan Engineering College
Tirupati, AP – 517102, India,
e-mail: mailpgeetha2013@gmail.com
[3] Department of Electrical and Electronics Engineering,
Christ (Deemed to be University), Bangalore, India,
e-mail: sureshk340@gmail.com

How to cite this article:
Parimalasundar E., Kumar N.M.G., Geetha P., Suresh K. Performance investigation of modular multilevel inverter topologies for photovoltaic applications with minimal switches. *Electrical Engineering & Electromechanics*, 2022, no. 6, pp. 28-34. doi: https://doi.org/10.20998/2074-272X.2022.6.05

UDC 621.314 https://doi.org/10.20998/2074-272X.2022.6.06

B.V. Sai Thrinath, S. Prabhu, B. Meghya Nayak

Power quality improvement by using photovoltaic based shunt active harmonic filter with Z-source inverter converter

Introduction. *The major source of energy for a long time has been fossil fuels, however this has its drawbacks because of their scarcity, exhaustibility, and impossibility of reusing them. Presently, a shunt active harmonic filter-equipped two-stage solar photovoltaic system is showing off its performance shunt active harmonic filter. The global power system has been impacted by current harmonics during the most modern industrial revolution.* ***Novelty.*** *The proposed work is innovative, by adopting the hysteresis modulation mode with Z-source inverter to enhance the performance of the system. Furthermore, the shunt active harmonic filter also get assists in this system for better improvement in the quality of power.* ***Purpose.*** *By incorporating an impedance source inverter and a photovoltaic shunt active harmonic filter methods, harmonic issues are mitigated.* ***Methods.*** *Load compensation is one of the services that the shunt active harmonic filter offers, in addition to harmonic compensation, power factor correction, and many other functions. The current pulse width modulation voltage source inverter method is more expensive, requires two converters owing to its two-stage conversion, has significant switching losses, and has a low rate of the reaction. The new model, in which the voltage source inverter is substituted out for a Z-source inverter converter, has been developed in order to address the problems of the existing system.* ***Results.*** *Rather than using a hybrid of DC-DC and DC-AC converters, the suggested system uses a shunt active harmonic filter that is powered by a photovoltaic source using a Z-source inverter. Utilizing Z-source inverter helps to address the present issues with conventional configurations.* ***Practical value.*** *By using software MATLAB/Simulink, this photovoltaic shunt active harmonic filter technique is analyzed. Shunt active harmonic filter, which produces compensatory current from the reference current obtained as from main supply, is powered by the photovoltaic array.* References 18, table 2, figures 13.
Key words: **photovoltaic, shunt active harmonic filter, Z-source inverter, PI controller, pulse width modulation.**

Вступ. *Основним джерелом енергії довгий час були викопні види палива, проте це мало свої недоліки через їх дефіцит, вичерпність та неможливість їх повторного використання. В даний час двоступенева сонячна фотоелектрична система, обладнана активним шунтуючим фільтром гармонік, демонструє свої робочі характеристики шунтуючого активного фільтра гармонік. На глобальну енергетичну систему вплинули гармоніки струму під час найсучаснішої промислової революції.* ***Новизна***. *Пропонована робота є інноваційною, оскільки вона використовує режим гістерезисної модуляції з інвертором Z-джерела для підвищення продуктивності системи. Крім того, шунтуючий активний фільтр гармонік також допомагає в цій системі для покращення якості електроенергії.* ***Мета***. *Включення інвертора джерела імпедансу та методів активного фільтру гармонік із фотогальванічним шунтом знижує гармонійні проблеми.* ***Методи***. *Компенсація навантаження – це одна з функцій, які шунтуючий активний фільтр гармонік пропонує на додаток до компенсації гармонік, корекції коефіцієнта потужності та багатьох інших функцій. Інверторний метод широтно-імпульсної модуляції струму дорожчий, вимагає двох перетворювачів через його двокаскадного перетворення, має значні втрати комутації і має низьку швидкість реакції. Нова модель, в якій інвертор джерела напруги замінює перетворювач інвертора Z-джерела, була розроблена для вирішення проблем існуючої системи.* ***Результати***. *Замість використання гібрида перетворювачів постійного та змінного струму в запропонованій системі використовується активний шунтуючий фільтр гармонік, який живиться від фотоелектричного джерела з використанням інвертора Z-джерела. Використання інвертора з Z-джерелом допомагає вирішити проблеми з традиційними конфігураціями.* ***Практична цінність***. *За допомогою програмного забезпечення MATLAB/Simulink аналізується метод активного фільтру гармонік фотоелектричного шунта. Шунтуючий активний фільтр придушення гармонік, який виробляє компенсаційний струм із опорного струму, отриманого від мережі, живиться від фотоелектричної батареї.* Бібл. 18, табл. 2, рис. 13.
Ключові слова: **фотовольтаїка, шунтуючий активний фільтр придушення гармонік, інвертор Z-джерела, ПІ-регулятор, широтно-імпульсна модуляція.**

Introduction. The main issues with a practical photovoltaic (PV) system include power loss owing to variations in operating circumstances, such as temperature or irradiance, the significant computing burden imposed by contemporary maximum power point tracking (MPPT) techniques, and optimizing the PV array output during abrupt weather patterns. The perturb and observation (P&O) strategy is chosen for the majority of PV systems [1].

In [2] investigates a solar control system simulation model that can be applied to PV power plants or the construction of solar inverters. This approach combines a DC-DC boost converter utilizing the MPPT methods conductivity, iterative, and P&O. In [3] Nowadays, one of the key elements influencing an economic growth is power quality. In order to meet consumer demand, utilities must supply more electricity as the population increases. The difficulties and worries that occur from the addition of solar power to the grid are examined in this research. In grid-connected solar systems, the shunt active power filter (SAPF) with PI controller is aimed at enhancing power quality. In [4] presently, among the most popular power electronics topology is Z-source inverters (ZSI). This article gives a brief introduction to the ZSI and examines its many topologies in depth, as well as the use of ZSI in the industrial applications. In [5] comprised of two control operations, the first of which uses a fuzzy logic controller to extract the maximum energy point from a PV panel's DC-DC converter. The main objective of this study, as stated in [6], is to decrease network power loss while simultaneously enhancing the bus voltage stability. This paper presents the modeling and simulation outcomes of a static compensator premised on a ZSI. In [7] when the decoupled double synchronous reference frame theory may be used to extract the magnificent of currents and prevent double frequency oscillations induced by introducing positive and negative-sequence currents into unbalanced, nonlinear loads. A three-level voltage source converter design is used for SAPF implementation and will provide compensating at the point of common coupling (PCC). Shunt active harmonic filter (SAHF) is employed in [8] to reduce the current harmonics. The process utilized to derive the reference current affects the filter's performance and precision. A three-phase SAHF, phase locked loop, and hysteresis are used in this study. The IGBT-based SAHF is activated by hysteresis switching [9].

In [10] resents a two stage ZSI for a PV single phase application. Here, ZSI includes an additional mode called the shoot through state, which allows it to function in a single stage, or even as a boost converter with voltage source inverter (VSI). ZSI outperforms BC+VSI in terms of downsides. A solar PV source is linked to an interactively three-phase SAPF in [11] through some kind of ZSI.

The proposed resolution aims to reduce the total harmonic distortion (THD) of the source current [12]. In a solar system that is linked to the grid, the harmonics caused by non-linear loads cannot be efficiently compensated by ordinary LC filters. The SAHF is presented due to its qualities and abilities for harmonic mitigation. The filter control system's primary focus is on producing reference source current, and this paper is used to reduce the harmonic currents [13].

In [14-18] power systems are using non-linear loads more and more frequently. This includes equipment like UPSs, inverters, converters, and others of a similar nature. These loads result in harmonics, which are quasi and distorted currents, in the source current. The P&O method is used to track the rated maximum characteristics of the PV module. The harmonic injection techniques are investigated and analyzed for grid connected system. The OPAL-RT-5600 is implemented under many circumstances by multi-variable filter associated with synchronous reference frame controller to reduce harmonics and to inject active power to the grid.

Modeling of PV & SAHF with VSI.

A) PV module. A PV system is made up of solar panels that use the photoelectric effect to transform solar light directly into electricity. Figure 1,*a* shows the equivalent circuit diagram for a solar cell, where R_s and R_{sh} stand for series and shunt resistance, respectively. The properties of *I-V* and *P-V* are shown in Fig. 1,*b*.

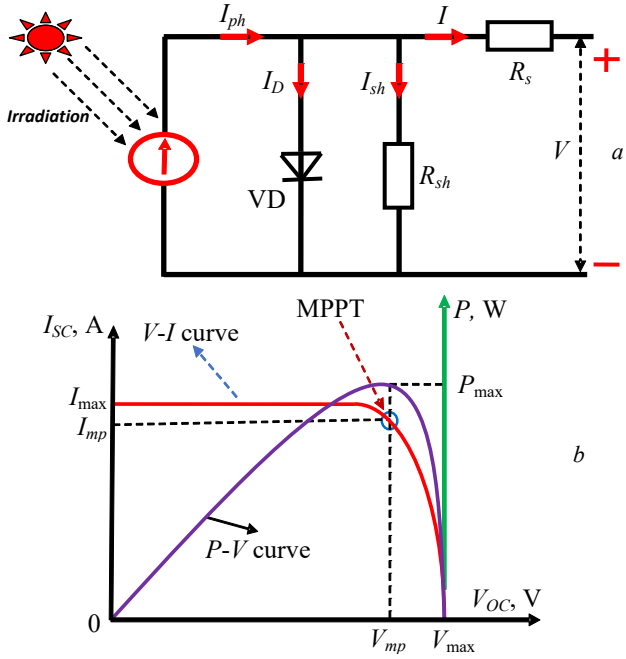

Fig. 1. *a* – simplified equivalent circuit diagram of PV cell; *b* – *I-V* and *P-V* characteristics of PV cell

According to the Shockley theory, the diode current is:

$$I_d = I_s\left[\exp\left(\frac{q\cdot V}{n\cdot K\cdot T}\right)-1\right], \qquad (1)$$

where I_s is the transistor saturate current; q is the electron charge; V is the voltage; K is the Boltzmann constant; n is the ideal factor; T is the cell temperature.

Since the two boundary elements of a PV module, namely V_{oc} and I_{sc}, are found by first reducing V=0 to produce I_{sc} and afterwards V_{oc} by setting cell current I=0, equation (1) results in:

$$V_{oc} = \frac{n\cdot K\cdot T}{q}\cdot\ln\left(\frac{I}{I_0}\right). \qquad (2)$$

The output of the PV cells changes with solar irradiation, hence the MPPT tracking algorithm is employed to make sure the PV system is operating as efficiently as possible. The formula $d(V\cdot I)/dt = 0$ provides the maximum voltage level. Then,

$$V_{oc} = V_{oc} - \frac{K\cdot T}{q}\cdot\ln\left[\left(\frac{V_{mp}\cdot q}{n\cdot K\cdot T}\right)+1\right]. \qquad (3)$$

Cell junction quality can be measured by the form factor, which is provided by:

$$FF = \left(\frac{V_{mp}\cdot I_{mp}}{V_{oc}\cdot I_{sc}}\right). \qquad (4)$$

The quality is greater the closer the level of form factor is near unity. Furthermore, the following factors are used to determine the PV module's efficiency:

$$\%\eta = \left(\frac{FF\cdot V_{oc}\cdot I_{sc}}{P_{in}}\right). \qquad (5)$$

B) Shunt active harmonic filter. SAPFs injected an equal but adverse harmonic compensation current to minimize current harmonics. The SAPF acts as a current source in this scenario, injecting the phase-shifted by 180° harmonic components produced by the loads. As a result, the active filter's impact wipes out harmonic current components present in the load current, keeping the source current continuous and in phase also with proper phase-to-neutral voltage. Any kind of load regarded as a harmonic source can be used in accordance with this concept. Additionally, the active power filter may correct the load power factor with the right control strategy. The active power filter and irregular load are viewed as the perfect resistor by the power distribution network in this way. Figure 2 displays the SAPF's compensating characteristic features.

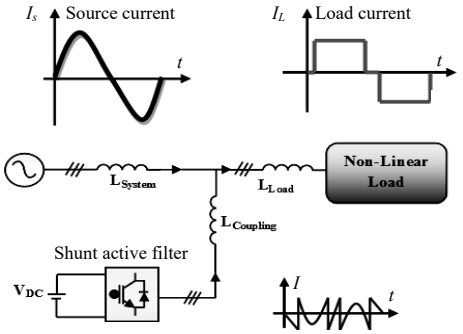

Fig. 2. Shunt active harmonic filter

A reference current is initially produced by the SAHF employing a PI controller. The advantage of this technique is that it eliminates the need for synchronizing with the phase voltage. The hysteresis controller design the switching pulse through pulse width modulation (PWM) from the reference current as well as the current needed to configure the DC link capacitor.

The voltage of the immediate supply is:

$$V_S(t) = V_{SM}\sin(\omega t). \quad (6)$$

At PCC, nodal analysis provides the source current:

$$I_s(t) = I_L(t) - I_H(t). \quad (7)$$

then $I_L(t)$ is indicated as:

$$I_L(t) = I_1\sin(\omega t + \Phi_1) + \sum_{h=0}^{\infty} I_h \sin(n\cdot\omega t + \Phi_h). \quad (8)$$

The harmonics element is the second terminology used here. The load current and supply voltage may be used to compute the instantaneous value of the load demand.

Calculating the total power demand is as follows:

$$P_L(t) = I_L(t)\cdot V_S(t). \quad (9)$$

As from load power, the true power may be calculated as follows:

$$P_f(t) = V_{SM}\cdot I_1\sin^2(\omega t)\cdot\cos\Phi_1 = V_S(t)\cdot I_S(t). \quad (10)$$

Following compensating, the source current would be:

$$I_S(t) = \frac{P_f(t)}{V_S(t)} = I_1\cdot\cos\Phi_1\cdot\sin(\omega t) = I_{SM}\cdot\sin(\omega t). \quad (11)$$

where I_{SM} is the maximum source current magnitude.

C) SAHF with VSI. The SAHF system, which is coupled in a parallel arrangement with a non linear load, is powered by a PV array system that is implemented with a P&O MPPT controller, as shown in Fig. 3.

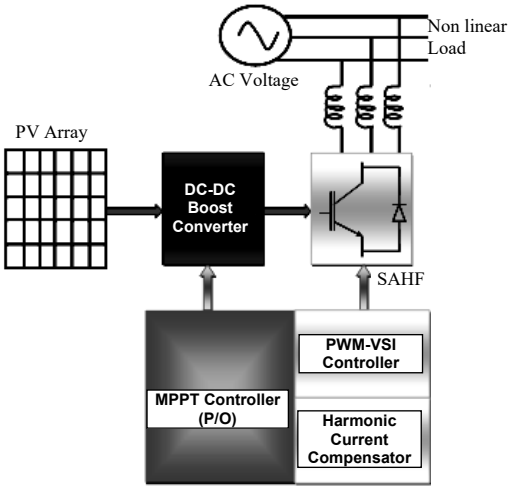

Fig. 3. SAHF with VSI

PWM-VSI controller is used to construct the SAHF. The switching pulse for VSI is produced using an adaptable hysteresis regulator. The reference current is extracted by the PI controller. To create switching pulses, the reference current that was extracted is then compared to the supply current. The source current's components are introduced by the nonlinear load. In order to diminish the harmonics present in the source current and make it sinusoidal and in phase with the input signal, the SAHF creates compensatory current that is the same size as the source current but also with a 180° phase shift. Sensing the baseline current taken from the power supply generates the compensatory current.

Proposed topology.

A) SAHF with impedance source inverter. In Fig. 4 by combining PV-based SAHF plus ZSI, the recommended method addresses issues with power quality. Researchers enhanced power quality in the prior method using PV-based SAHF with VSI. In this method, the maximum power is tracked by the P&O algorithm utilizing the MPPT methodology, a boost converter, a VSI, and other devices. The ZSI, SAHF, PV array, and other important building blocks are included in the recommended approach. We can reduce expenses, boost response rates, and just do deal with two-stage conversion thanks to this novel technique. Only one difference between the operation and the existing technique is the substitution of ZSI for BC+VSI.

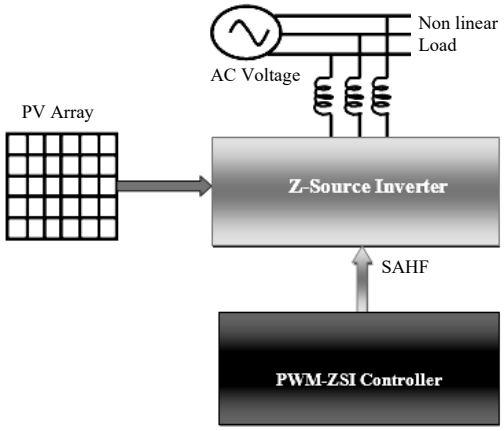

Fig. 4. SAHF with ZSI

Figure 5 illustrates the ZSI distinctive impedance network, which consists of 2 splitting inductors and 2 X-shaped capacitors. The three-phase ZSI bridge has nine switching states, as opposed to the normal VSI's eight. When the load connections are short circuited either via the bottom 3 switching devices or even the top 3 switching devices, accordingly, the ZSI has 6 original states when the DC link voltage is impressing across the three-phase loads and 2 zero states.

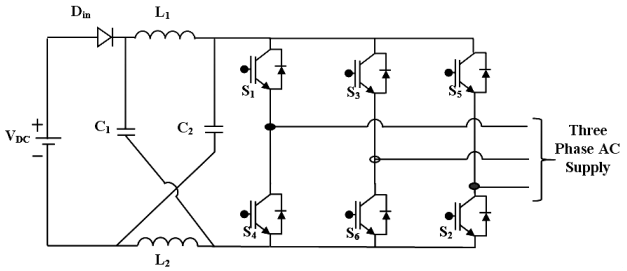

Fig. 5. Impedance source inverter

The Z-network is in charge of accelerating and monitoring the MPPT. The total power received by the inverters from the DC supply will determine the Shoot through switching frequency T_0/T (P&O technique). The MPPT tracking used in the conventional BC+VSI topology is the same as this. When combining it with ZSI, the switching frequency at MPPT uses the entire amount of electricity from the PV panel.

B) Operating modes. Depending on the inverter bridge's power switches, the ZSI can operate in one of three different ways, as seen below.

Mode 1. Null stator zero state. In this condition, an open circuit is analogous to an inverter bridge. Switches (S1, S3, S5) or (S2, S4, S6) are in the ON position in this condition.

Mode 2. Active stator non-shoot through state. Six states are currently operational. In the ON state are (S1, S3, S6), (S3, S5, S2), (S5, S1, S4), (S2, S4, S5), (S4, S6, S1), or (S6, S2, S3). As the load is shorted through either the upper

or lower 3 switching devices, the inverter bridging is from one of 2 zero states. In this state, as illustrated in Fig. 6, the bridge can be thought of as an open-circuit (current source with really no current flowing.

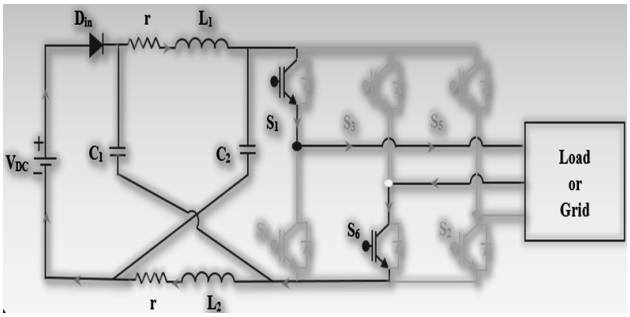

Fig. 6. Equivalent circuit of ZSI viewed from the DC link when the bridge is in an on-shoot through mode

Although there is no current flowing from the DC source to the load, the DC source's voltage may be seen between both the inductor as well as the capacitor. Switches on the identical leg of the 3 phase inverter are activated. It resembles a short circuit. S1 through S6 are in the ON position. One of the 7 shoot through (ST) modes is being used by the inverter bridge. The bridge is regarded as a fault current from the inverter's DC connection, as shown in Fig. 7. In contrast to zero governed by state, the capacitor's DC voltage is increased to the required amount depending on the ST duty cycle throughout this mode, not across the load as it would be in zero state operation.

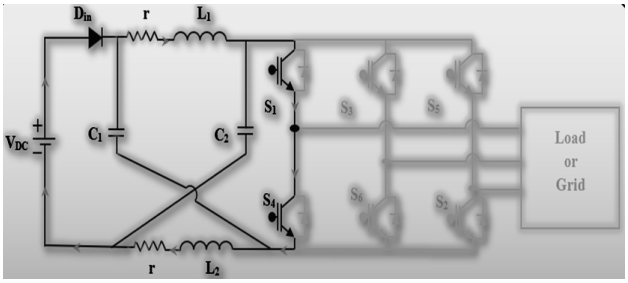

Fig. 7. Equivalent circuit of ZSI viewed from the DC link when the bridge is in a shoot through mode

C) Components design. During in the conventional operating mode, the voltage level is visible across the capacitor but not the inductor since there is no boost involved (only a pure DC current flows through the inductors). The inductor's responsibility is to control the current ripple when Z-source mode (in which boost is used) is active. A linear rise in inductor current occurs during ST, and the voltage across the inductor is much like the voltage across the capacitor. The inductor current drops linearly in non-ST mode (conventional 8 states), as well as the voltage across the inductor seems to be the difference between both the input voltage from the PV and the voltage across the capacitor.

The average current through the inductor is:

$$I_1 = P / P_V, \quad (12)$$

where P is the total power.

Highest ST occurs when there is the greatest current ripple across the inductors. Hence, it is necessary to determine the inductors peak-to-peak current ripple. According to a few applied in diverse studies, it has been discovered that as a general rule, for the majority of ZSI instances, roughly 30 % (or 60 % peak to peak) current ripples is selected for design.

Inductor max current:

$$I_L = I_L + 30\ \%, \quad (13)$$

Inductor min current:

$$I_L = I_L - 30\ \%. \quad (14)$$

Capacitor design. The capacitor reduces current swell and produces a relatively steady voltage that outputs a sinusoidal voltage. According to the mode 3 of Z-source operation and $I_L = I_C$, the capacitor charges the inductor throughout ST. The capacitor values may be roughly determined by limiting the capacitor voltage ripple to about 3 % at peak power, which is often employed in the majority of applications in various publications for ZSI:

$$C = I_l \cdot T_0 / \Delta V_C\ , \quad (15)$$

where in T_0 denotes the switch primary cycle ST time; I_L is the calculated average current either through the inductor:

$$\Delta V_C = V \cdot 3\ \%. \quad (16)$$

Table 1

Operation modes of ZSI

Mode / State	S1	S2	S3	S4	S5	S6
Zero state	ON	OFF	ON	OFF	ON	OFF
	OFF	ON	OFF	ON	OFF	ON
Active state	ON	OFF	ON	OFF	OFF	ON
	OFF	ON	ON	OFF	ON	OFF
	ON	OFF	OFF	ON	ON	OFF
	OFF	ON	OFF	ON	ON	OFF
	ON	OFF	OFF	ON	OFF	ON
	OFF	ON	ON	OFF	OFF	ON
Shoot through state	ON	ON	OFF	OFF	OFF	OFF
	OFF	OFF	ON	ON	OFF	OFF
	OFF	OFF	OFF	OFF	ON	ON

Simulation results and analysis.

A) VSI with SAHF. Using the software MATLAB / Simulink, the PV-SAHF system has been tested. SAHF, which produces compensatory current from reference current retrieved from the mains, is powered by the PV array. Figures 8,*a*,*b*, which depict the PV array's *P-V* and *I-V* characteristics at 25° and 45 °C cell temperatures, respectively and Fig. 8,*c* shows the V_{DC} of VSI. The resulting point on the graph corresponds to the PV array's peak power. At this stage, a P/O MPPT-based controller controls the PV array system for optimal efficiency. The characteristics show that while the open-circuit lowers as the temperature rises, the short-circuit current rises.

The input mains sources current of VSI with the inclusion of a harmonic filter in shunt mode is shown in Fig. 9,*a*. According to Fig. 9,*b*, the PWM-VSI creates the compensatory current to reduce the harmonic currents. Harmonics are cancelled by a compensatory current that has the same amplitude as harmonic components but a 180° phase shift.

Figure 9,*c*, which depicts the source current following SAHF integration, demonstrates how the source current changes to a sinusoidal shape after SAHF integration, becoming harmonic-free. The shunt SAHF system reduces harmonics while enhancing power factor. Figure 9,*c* shows that the source current improves in power factor and is harmonic-free when the SAHF system is connected to VSI .

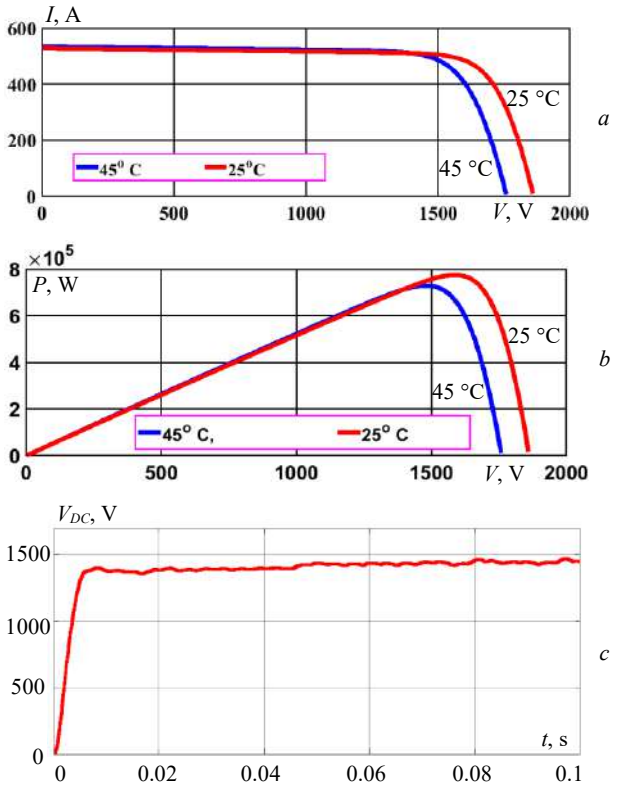

Fig. 8. *a*) *V-I* characteristics of PV array;
b) *P-V* characteristics of PV array; *c*) V_{DC} of VSI

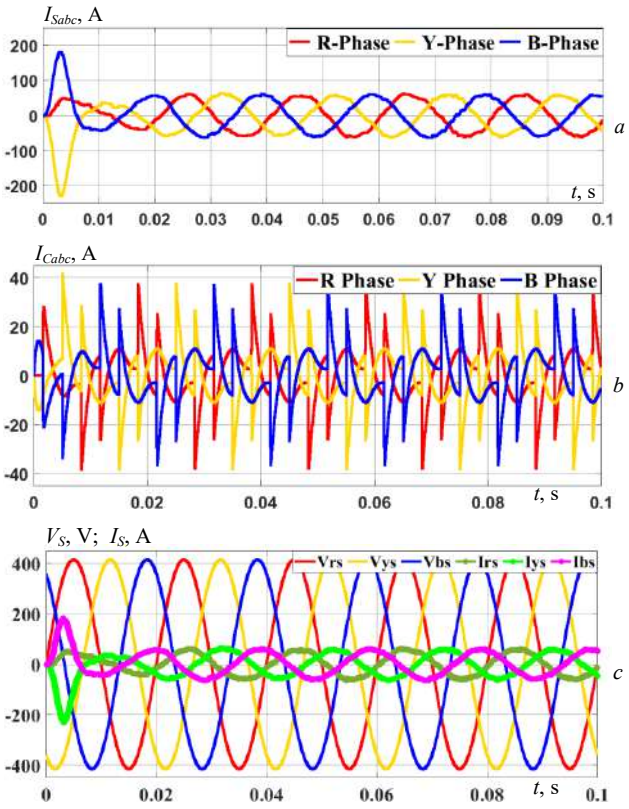

Fig. 9. *a*) Source current at supply mains of VSI with SAHF;
b) Compensating current of VSI with SAHF;
c) Power factor improvement of the supply mains by VSI with SAHF

From Fig. 10 shows that the THD is reduced to a satisfactory level when connecting with the SAHF by VSI at fundamental frequency of 50 Hz, THD attained is 7.31 %.

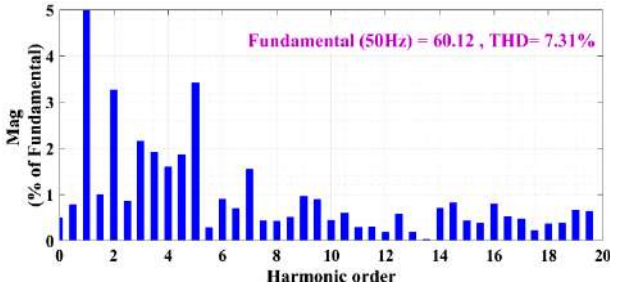

Fig. 10. THD present in source current by VSI with SAHF

B) ZSI with SAHF. MATLAB / Simulink program is being used to test the PV-SAHF system. The SAHF is powered by the PV array, which creates compensatory current using the reference current that was taken from the mains. Figures 11,*a*,*b*, respectively, demonstrate the *P-V* and *I-V* characteristics of the PV array at 25° and 45 °C cell temperature. The resultant graphed point represents the PV array's peak power point. For the PV array system to run as efficiently as possible, a P&O MPPT based controller is used at this stage. The characteristics indicate that when temperature rises, the short-circuit current increases while the open-circuit voltage falls. Figure 11,*c* shows the V_{DC} of the impedance source inverter in accord with all these results.

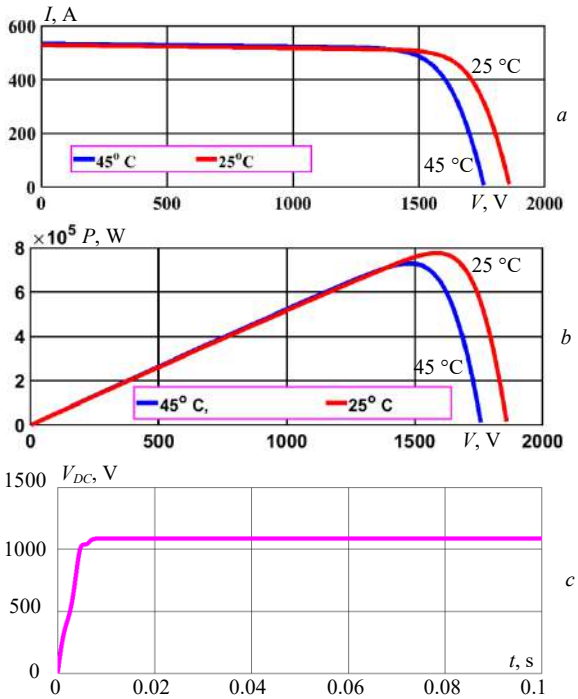

Fig. 11. a) *V-I* characteristics of PV array;
b) *P-V* characteristics of PV array;
c) V_{DC} of impedance source inverter

In Fig. 12,*a* the input power supplies source current of the VSI is displayed with the harmonic filter included in the shunt mode. Impedance source inverter produces compensating current to lessen harmonic currents, as seen in Fig. 12,*b*. A compensating current that has a 180° phase shift and the same magnitude as the harmonic components cancels the harmonics. Following SAHF integrations, the source current assumes a sinusoidal form and becomes harmonic-free, as seen in Fig. 12,*c*, which displays the source current during SAHF integration.

The SAHF system reduces harmonics while enhancing power factor. Figure 12,*c* shows that the source

current improves in power factor and is harmonic-free when the SAHF system is connected to ZSI.

The SAHF system improves power factor while reducing harmonics. When the SAHF system is linked to ZSI Fig. 12,*c* indicates that the source current has an improved power factor and therefore is harmonic-free.

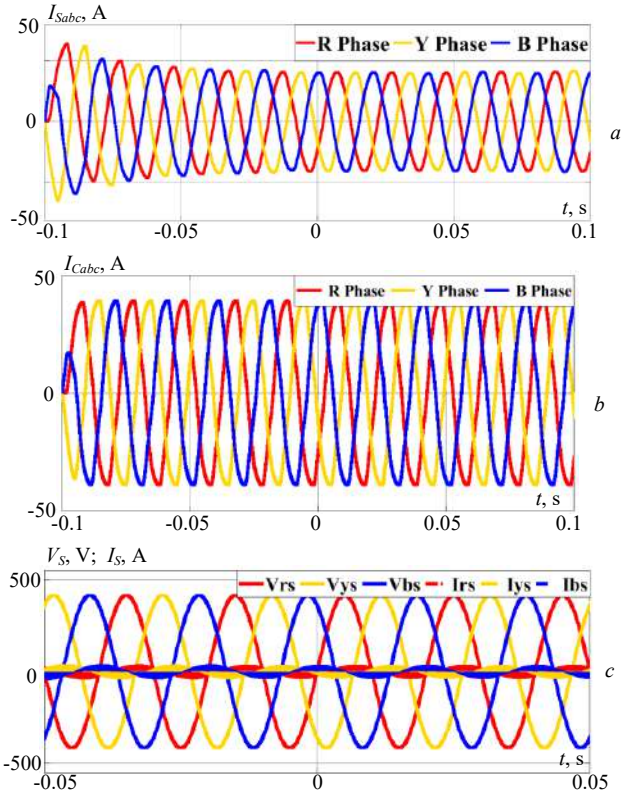

Fig. 12. *a*) Source current at supply mains of ZSI with SAHF; *b*) Compensating current of ZSI with SAHF; *c*) Power factor improvement of the supply mains by ZSI with SAHF

Figure 13 shows that the THD is 1.76 % at 6 kHz when connecting with the SAHF by ZSI at fundamental frequency of 50 Hz.

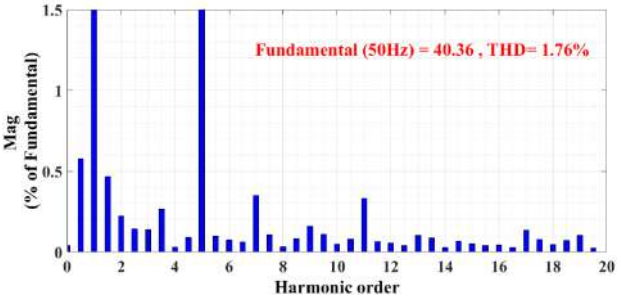

Fig. 13. THD present in source current by ZSI with SAHF

Table 2 shows the comparison between existing topology (VSI with SAHF) and proposed topology (ZSI with SAHF) infers the THD is less in the ZSI.

Table 2

Comparison of SAHF with VSI and ZSI

no.	Topology	Switching frequency, kHz	Parameters				%, THD
			Inductance, mH		Capacitance, mF		
			L_1	L_2	C_1	C_2	
1	VSI with SAHF	5	5	–	0.1	0.012	7.31
2	ZSI with SAHF	5	1.1	1.1	0.5	0.5	1.76

Conclusions.

The primary objectives of the proposed system are to utilize renewable energy sources and include the Z-source inverter architecture. The extra DC-DC converter makes the system more difficult, increases its price, and decreases its effectiveness. Instead of combining DC-DC and DC-AC converters, the suggested system in this setup is a shunt active harmonic filter powered by a photovoltaic source using a Z-source inverter. The use of Z-source inverter helps to overcome the difficulties that conventional topologies are now facing. Analysis of the photovoltaic shunt active harmonic filter system with Z-source inverter performance under various operating conditions in the MATLAB / Simulink environment reveals that the harmonic components are substantially below the stated IEEE norm, which is less than 5 %. Z-source inverter is employed in applications including electric motor drives, photovoltaic power production, and fuel cells because to its special ability to reduce dead time and boost system effectiveness.

Conflict of interest. The authors declare that they have no conflicts of interest.

REFERENCES

1. Manoharan P., Subramaniam U., Babu T.S., Padmanaban S., Holm-Nielsen J.B., Mitolo M., Ravichandran S. Improved Perturb and Observation Maximum Power Point Tracking Technique for Solar Photovoltaic Power Generation Systems. *IEEE Systems Journal*, 2021, vol. 15, no. 2, pp. 3024-3035. doi: https://doi.org/10.1109/JSYST.2020.3003255.

2. Verma N., Jain A., Nishi Ahuja H., Singh G. Maximum Power Point Tracking MPPT Methods for Photovoltaic Modules. *2021 International Conference on Advance Computing and Innovative Technologies in Engineering (ICACITE)*, 2021, pp. 223-227. doi: https://doi.org/10.1109/ICACITE51222.2021.9404571.

3. Shiva C., Bhavani R., Prabha N.R. Power quality improvement in a grid integrated solar PV system. *2017 IEEE International Conference on Intelligent Techniques in Control, Optimization and Signal Processing (INCOS)*, 2017, pp. 1-6. doi: https://doi.org/10.1109/ITCOSP.2017.8303144.

4. Saeed N., Ibrar A., Saeed A. A Review on Industrial Applications of Z-Source Inverter. *Journal of Power and Energy Engineering*, 2017, vol. 05, no. 09, pp. 14-31. doi: https://doi.org/10.4236/jpee.2017.59002.

5. Kumar A., Kumar P. Power Quality Improvement for Grid-connected PV System Based on Distribution Static Compensator with Fuzzy Logic Controller and UVT/ADALINE-based Least Mean Square Controller. *Journal of Modern Power Systems and Clean Energy*, 2021, vol. 9, no. 6, pp. 1289-1299. doi: https://doi.org/10.35833/MPCE.2021.000285.

6. Usha N., Vijaya Kumar M. Power Quality improvement using ZSI based STATCOM in Radial and weakly Meshed Distribution Systems. *International Journal of Advanced Research in Electrical, Electronics and Instrumentation Engineering,* 2013, vol. 2, no. 11, pp. 5365-5372. Available at: https://www.ijareeie.com/upload/2013/november/7_-Power.pdf (Accessed 20.12.2021).

7. Kumar S.K., Ranga J., Pradeep Kumar C.S.K.B., Jayalakshmi S. PV based Shunt Active Power Filter for harmonics mitigation using Decoupled DSRF theory. *2019 5th International Conference on Advanced Computing & Communication Systems (ICACCS)*, 2019, pp. 1108-1110. doi: https://doi.org/10.1109/ICACCS.2019.8728527.

8. Chavan U.M., Thorat A.R., Bhosale S.S. Shunt Active Filter for Harmonic Compensation Using Fuzzy Logic Technique. *2018 International Conference on Current Trends towards Converging Technologies (ICCTCT)*, 2018, pp. 1-6. doi: https://doi.org/10.1109/ICCTCT.2018.8550962.

9. SmitaSinghai S. Compensation of Harmonics of Fully Controlled Loads by Using SAHF. *IOSR Journal of Electrical and Electronics Engineering*, 2017, vol. 12, no. 02, pp. 01-10. doi: https://doi.org/10.9790/1676-1202010110.
10. Sharma K., Shanker S., Gidwani L., Palwalia D.K. An Investigation on Two Stage VSI and ZSI for PV based Single Phase Application. *2019 9th Annual Information Technology, Electromechanical Engineering and Microelectronics Conference (IEMECON)*, 2019, pp. 30-35. doi: https://doi.org/10.1109/IEMECONX.2019.8876978.
11. Teta A., Kouzou A., Rezaoui M.M., Abu-Rub H. Interactive PV-Shunt Active Power Filter based on Impedance Source Inverter Controlled by SRF-MVF. *2021 18th International Multi-Conference on Systems, Signals & Devices (SSD)*, 2021, pp. 306-311. doi: https://doi.org/10.1109/SSD52085.2021.9429460.
12. Rai R., Bhatia R.S., Nijhawan P. DC-DC conversion based on ZSI and boost rectifier using fuzzy logic control. *2016 7th India International Conference on Power Electronics (IICPE)*, 2016, pp. 1-5. doi: https://doi.org/10.1109/IICPE.2016.8079377.
13. Rasul M.J.M.A., Khang H.V., Kolhe M. Harmonic mitigation of a grid-connected photovoltaic system using shunt active filter. *2017 20th International Conference on Electrical Machines and Systems (ICEMS)*, 2017, pp. 1-5. doi: https://doi.org/10.1109/ICEMS.2017.8056401.
14. Jegadeeswari G. Performance analysis of power quality improvement using shunt active power filter. *International Journal of Recent Technology and Engineering*, 2019, vol. 7, no. 5, pp. 1-3. Available at: https://www.ijrte.org/wp-content/uploads/papers/v7i5s2/ES1995017519.pdf (Accessed 20.12.2021).
15. Shaik A.K., Prabhu S., Shaik J., Pathan M.K., Sai M.G. Modelling and Design of Three State Three Switch Buck Boost Inverter. *2020 International Conference on Smart Technologies in Computing, Electrical and Electronics (ICSTCEE)*, 2020, pp. 548-553. doi: https://doi.org/10.1109/ICSTCEE49637.2020.9277431.
16. Saremi Hasari S.A., Soori S., Salemnia A., Khosrogorji S. Z-source DG-active filter. *2016 7th Power Electronics and Drive Systems Technologies Conference (PEDSTC)*, 2016, pp. 248-252. doi: https://doi.org/10.1109/PEDSTC.2016.7556869.
17. Bourouis B., Djeghloud H., Benalla H. Energy efficiency of a 3-level shunt active power filter powered by a fuel-cell / battery DC bus with regulated duty cycles. *Electrical Engineering & Electromechanics*, 2021, no. 5, pp. 30-38. doi: https://doi.org/10.20998/2074-272X.2021.5.05.
18. Baazouzi K., Bensalah A.D., Drid S., Chrifi-Alaoui L. Passivity voltage based control of the boost power converter used in photovoltaic system. *Electrical Engineering & Electromechanics*, 2022, no. 2, pp. 11-17. doi: https://doi.org/10.20998/2074-272X.2022.2.02.

Received 01.06.2022
Accepted 25.07.2022
Published 06.11.2022

B.V. Sai Thrinath[1], *Assistant Professor*, *PhD*,
S. Prabhu [1], *Associate Professor*, *PhD*,
B. Meghya Nayak [2], *Associate Professor*, *PhD*,
[1] Sree Vidyanikethan Engineering College,
Tirupati, AP – 517102, India,
e-mail: connectbvst@gmail.com (Corresponding Author);
prabhutajmahal6@gmail.com
[2] Arvind Gavali College of Engineering,
Satara – 415015, Maharashtra, India,
e-mail: meghya29@gmail.com

How to cite this article:
Sai Thrinath B.V., Prabhu S., Meghya Nayak B. Power quality improvement by using photovoltaic based shunt active harmonic filter with Z-source inverter converter. *Electrical Engineering & Electromechanics*, 2022, no. 6, pp. 35-41. doi: https://doi.org/10.20998/2074-272X.2022.6.06

UDC 621.3 https://doi.org/10.20998/2074-272X.2022.6.07

A.A. Bengharbi, S. Laribi, T. Allaoui, A. Mimouni

Photovoltaic system faults diagnosis using discrete wavelet transform based artificial neural networks

Introduction. *This research work focuses on the design and experimental validation of fault detection techniques in grid-connected solar photovoltaic system operating under Maximum Power Point Tracking mode and subjected to various operating conditions.* ***Purpose.*** *Six fault scenarios are considered in this study including partial shading, open circuit in the photovoltaic array, complete failure of one of the six IGBTs of the inverter and some parametric faults that may appear in controller of the boost converter.* ***Methods.*** *The fault detection technique developed in this work is based on artificial neural networks and uses discrete wavelet transform to extract the features for the identification of the underlying faults. By applying discrete wavelet transform, the time domain inverter output current is decomposed into different frequency bands, and then the root mean square values at each frequency band are used to train the neural network.* ***Results.*** *The proposed fault diagnosis method has been extensively tested on the above faults scenarios and proved to be very effective and extremely accurate under large variations in the irradiance and temperature.* ***Practical significance.*** *The results obtained in the binary numerical system allow it to be used as a machine code and the simulation results has been validated by MATLAB / Simulink software.* References 21, tables 5, figures 7.

Key words: **artificial neural network, discrete wavelet transform, fault diagnosis, photovoltaic system.**

Вступ. *Ця дослідницька робота присвячена розробці та експериментальній перевірці методів виявлення несправностей у підключеній до мережі сонячній фотоелектричній системі, що працює в режимі відстеження точки максимальної потужності та піддається різним умовам експлуатації.* ***Мета***. *У цьому дослідженні розглядаються шість сценаріїв відмови, включаючи часткове затінення, обрив кола у фотогальванічній батареї, повна відмова одного з шести IGBT інвертора та деякі параметричні відмови, які можуть виникнути в контролері перетворювача, що підвищує.* ***Методи***. *Методика виявлення несправностей, розроблена у цій роботі, полягає в штучних нейронних мережах і використовує дискретне вейвлет-перетворення для отримання ознак для ідентифікації основних несправностей. Застосовуючи дискретне вейвлет-перетворення, вихідний струм інвертора в часовій області розкладається на різні смуги частот, а потім середньоквадратичні значення в кожній смузі частот використовуються для навчання нейронної мережі.* ***Результати***. *Запропонований метод діагностики несправностей був всебічно протестований на вказаних вище сценаріях несправностей і виявився дуже ефективним і надзвичайно точним при великих коливаннях освітленості і температури.* ***Практична значимість***. *Результати, отримані в двійковій системі числення, дозволяють використовувати її як машинний код, а результати моделювання були підтверджені програмним забезпеченням MATLAB/Simulink.* Бібл. 21, табл. 5, рис. 7.

Ключові слова: **штучна нейронна мережа, дискретне вейвлет-перетворення, діагностика несправностей, фотоелектрична система.**

Abbreviations

ANN	Artificial neural network	MPPT	Maximum power point tracking
CNN	Convolutional neural networks	PLL	Phase lock loop
CWT	Continuous wavelet transform	PSO	Particle swarm optimization
DWT	Discrete wavelet transform	PV	Photovoltaic
HF	High frequency	RMS	Root mean square
HPF	High-pass filter	SVPWM	Space vector pulse width modulation
LF	Low frequency	VOC	Vector oriented control
LPF	Low-pass filter	WT	Wavelet transform

Introduction. Global energy demand is rising at a fast pace and CO_2 emissions have reached their highest record in recent years; which has prompted the industrialized world to search for alternative energies resources to overcome the declining fossil fuel reserves. Solar PV energy is one of the most promising renewable energies sources [1]. Therefore, PV power generation has become so mainstream and usually is distributed in some distant and cruel environments, and because some faults are inevitable during the long-term operation of the PV system it has become clear that PV system require to be better protected against faults [2, 3]. Also the electrical faults and interconnected power system increases the cost and emission ratio very high [4].

Detecting faults of the PV components and fix it is necessary to avoid economic losses and big incidents that may established in this systems, thus ensuring secure and robust systems [5]. Moreover, more time and costs are suffered when malfunction is failed to be detected in a timely manner in the system. Therefore, to ensure a high-quality system for prolonged, it is essential to recognize the times and locations of faults and failures immediately [5].

Since diagnosing faults is essential to the PV systems, over the past few years researchers have become increasingly interested in diagnosing complex system faults. A large number of fault diagnostic methods and several approaches have been proposed by researchers. In [6] a new PV array fault diagnosis technique capable of automatically extracting features from raw data for PV array fault classification was proposed. That technique shows good fault diagnosis precision on both noisy and noiseless data. In [7], a technique for the rapid detection and isolation of faults in the DC micro-grids without deactivating the entire network has been introduced. The technique is based on sampling branch current measurements then using WT to capture the features from the network current signals. The authors in [8] presented a new approach to effectively classify and detect PV system faults using deep two-dimensional (2-D) CNN to extract features from 2-D scalograms generated from PV system data. In [9], the authors propose a recurrent neural network-based long short-term memory approach for the detection of high impedance fault in PV integrated power system. In [10], a CNN was combined with a chaotic system

and the DWT and applied to the diagnosis of insulation faults in cross-linked polyacetylene power cables. The method presented in [11] is based on the combination of an ANN with WT and leads to an accurate fault location strategy in bipolar current source converter based high voltage DC transmission system. In [12], a design of a monitoring system using a perceptron multilayer ANN for the detection of rolling element-bearings failure was proposed. The authors in [13] applied WT to extract the features of fault signals then used them for training an ANN that can classify and detect faults in DC microgrid.

Many techniques are used to detecting the faults in the PV systems, from the above we note that fault detection is directly dependent on signal current or voltage which is sensed using sensors and sampled for further process. Next, effective and different feature extraction techniques are used in the discussed fault detection methods to obtain the most versatile and effective features possible.

The objective of this work is to create an artificial neural network observer that can detect and classify faults in photovoltaic system. By using DWT on real data of PV system under different operating conditions with and without faults in order to extract the features then learn and train the ANN with these features.

Materials and methods. The experimental grid-connected PV system used in this study is depicted in Fig. 1 and its presentation with the proposed fault detection method – in Fig. 2.

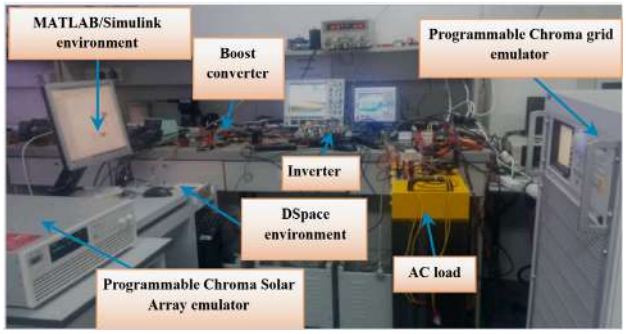

Fig. 1. Depict implemented grid-connected PV system [14]

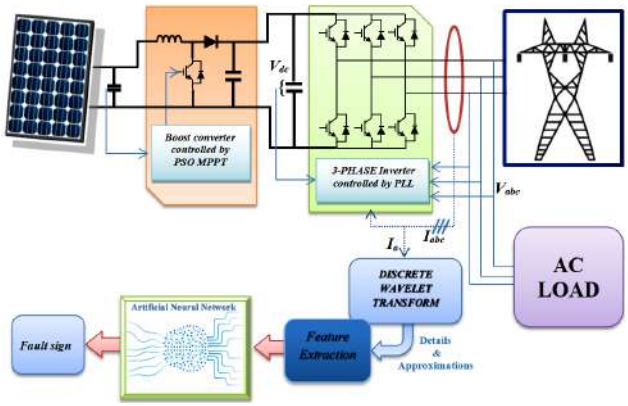

Fig. 2. Presentation of implemented grid-connected PV system with the proposed fault detection method

A typical grid-connected PV system implemented in the laboratory is used to verify the fault detection performance of data dependent methods against real faults in practical conditions and MPPT mode. The output of the PV array is created by the programmable Chroma 62150H-1000S Solar Array emulator which allows modifies the effects of peripheral conditions (irradiance G and temperature T), and as a grid emulator The programmable AC source Chroma 61,511. A DSpace 1104 environment implement the control algorithm and used also for data acquisition. Based on the grid-side signals, VOC based on SVPWM is used to control the active and reactive powers. The inverter output voltage is synchronized with the grid voltage through the PLL. For safety and protection purposes, the AC load is used when real faults are applied. To extract maximum power from the PV array, a MPPT controller based on PSO technique is used [14].

Therefore, this system was used to create and collect real faulty data for fault detection experimental validation; we refer interested readers to [15, 16] for more details on settings of this system. the PV array voltage V_{PV} and current I_{PV} and DC voltage V_{dc} as shown in Fig. 1, are real-time measured signals with a sampling time of $T_s = 100$ µs [14].

The minimum set of variables associated with faults is: $\{I_{PV}, V_{PV}, V_{dc}, |I|, f_I, |V|, f_V\}$, where f_I, f_V are current and voltage frequency. It used for observing the PV system.

The real-time measured and estimated signals form a data matrix Y of 7 columns:

$$Y = [I_{PV} \;\; V_{PV} \;\; V_{dc} \;\; |I| \;\; f_I \;\; |V| \;\; f_V]^T. \qquad (1)$$

This work considers the detection of the 6 factual faults listed in Table 1 that were injected into the PV system. The faults are of different types and locations and are injected manually in separate experiments to ensure an entire analysis. Each trial lasts about 10 to 15 s where in the fault is applied around the 7th to 9th s. Degradation faults are not considered in this work, as their detection requires long-term data at large sampling time intervals [14].

Table 1

Realistic injected fault in the PV system [14]

Fault	Type	Description
F1	Inverter fault	Complete failure in one of the six IGBTs
F2	Feedback sensor fault	One phase sensor fault 20%
F3	PV array mismatch	10 to 20% non homogeneous partial shading
F4	PV array mismatch	15% open circuit in PV array
F5	MPPT controller fault	–20% gain parameter of PI controller in MPPT controller of the boost converter
F6	Boost converter controller fault	+20% in time constant parameter of PI controller in MPPT controller of the boost converter

Proposed fault detection strategy. The proposed fault detection method is described by the flowchart of Fig. 3. The fault diagnosis algorithm uses the inverter output current signals for feature extraction approach based on the DWT. The aim of signal processing is to extract the features of the signal from several angles through several transform methods to aid in signal analysis and processing. The wavelet function is a new foundation for expressing signals and a good method for analyzing the signal from different resolutions [10].

Feature extraction using wavelet transform. Feature extraction is the most important part in the proposed fault detection and classification process.

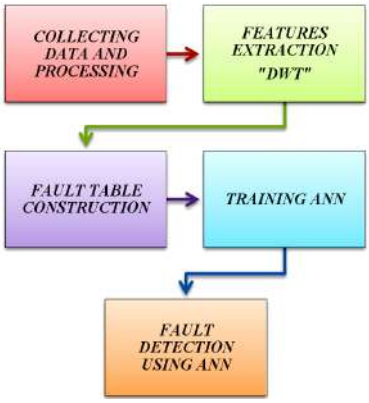

Fig. 3. Flowchart of the proposed fault detection system

Better features lead to improved system performance and reliability, because the accuracy of a system depends on the quality and robustness of the feature extraction process. Wavelet transform is a mathematical tool for temporal frequency analysis and has been used in several fault detection applications. It is based on the transformation of the temporal signal into a series of parameters called approximation and detail representing the slow and fast changes in the signal, respectively. The wavelets are defined as follows [17]:

$$\Psi_{ab}(t)=\frac{1}{\sqrt{a}}\cdot\Psi\left(\frac{t-b}{a}\right), \tag{2}$$

where a and b are the scale factor and position factor respectively.

Wavelet transform is divided into CWT and DWT [10]. The DWT algorithm translates and dilates the wavelet according to discrete values. Therefore, a and b will be discretized as follows [18]:

$$\begin{cases} a=a_0^m; \\ b=n\cdot b_0\cdot a_0^m, \end{cases} \tag{3}$$

where $a_0 > 1$, $b_0 > 0$; a_0 and $b_0 \in Z$; m and n are the integers permitting the control of the dilation and the translation of the original wavelet [17].

The DWT algorithm is used to eliminate noise in the original signal and also to decompose the time domain signal into different frequency groups. The original signal $f(t)$ passes through two complementary filters: a HPF and a LPF appear as two signals defined as the approximation signal ***A*** and the detail signal ***D*** as shown in Fig. 4.

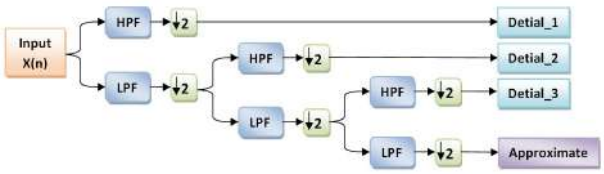

Fig. 4. DWT implementation procedure

The approximation is the large-scale and the low frequency part of the signal and the detail is the small-scale and high frequency part of the signal [18].

Through DWT, the input signals which consist of LF and HF components can be decomposed into frequency bands. Then, through down-sampling, the first level of wavelet transform can be obtained [10].

For a reliable and fast analysis, a prior knowledge of the signal levels N to be processed is necessary. The following equation gives this required parameter [17]:

$$N_{levels}=\text{int}\left(\frac{\log\left(f_e/f_s\right)}{\log 2}\right)+2\,, \tag{4}$$

where f_s is the supply frequency; f_e is the sampling frequency. Note that N_{levels} should be an integer.

The appropriate decompositions number can calculated based on the knowledge of f_s and f_e. In our case, considering a supply frequency of 50 Hz and a sampling frequency of 10 kHz, the number of decomposition levels required is [17]:

$$N_{levels}=n_{ls}+2=\text{int}\left(\frac{\log\left(10^4/50\right)}{\log 2}\right)+2=9 \text{ levels.} \tag{5}$$

Table 2 presents the different frequency bands acquired by the discrete wavelet decomposition. Figure 5 shows the DWT that implemented to decompose the current signal (i_a) in MATLAB/Simulink environment to obtained the Details.

Table 2

Frequency bands obtained by multi-level decomposition

Levels	Approximations		Details	
J=1	A1	0-5000	D1	5000-10000
J=2	A2	0-2500	D2	2500-5000
J=3	A3	0-1250	D3	1250-2500
J=4	A4	0-625	D4	625-1250
J=5	A5	0-312.5	D5	312.5-625
J=6	A6	0-156.25	D6	156.25-312.5
J=7	A7	0-78.125	D7	78.125-156.25
J=8	A8	0-39.0625	D8	39.0625-78.125
J=9	A9	0-19.5313	D9	19.5313-39.0625

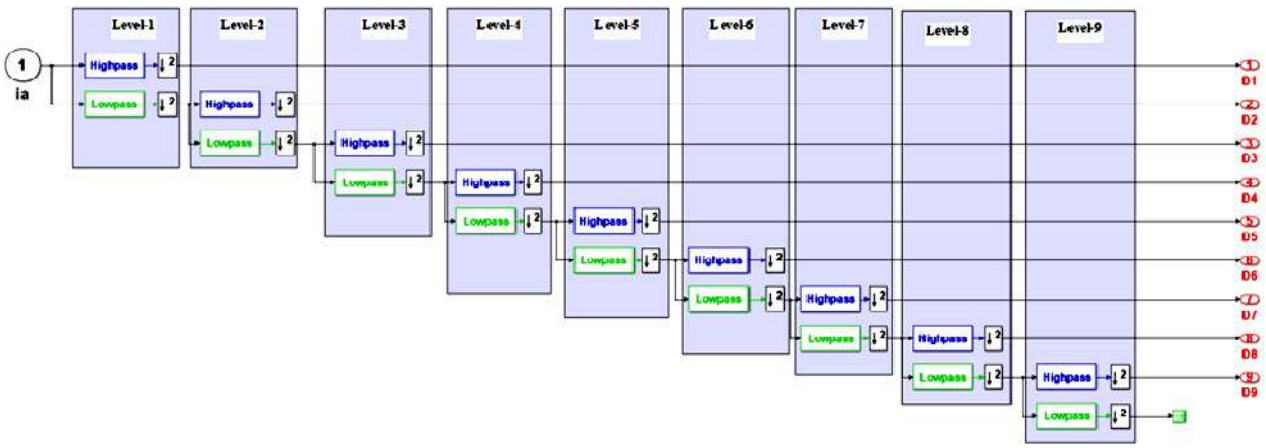

Fig. 5. DWT implemented in MATLAB / Simulink environment

Figure 6,*a* shows the inverter output current (i_a) in healthy case, and in Fig. 6,*c* in faulty case (F1).

Different details extracted from the obtained inverter output current signal by the DWT technique for the healthy case in Fig. 6,*b* and the faulty case in Fig. 6,*d* (F1) is displayed below. By comparing healthy case details and faulty case (F1) Details of the PV system state as depicted in Fig. 6,*b* and Fig. 6,*d* a remarkable variation in details amplitude is observed.

Note that these statements are valid for the other faulty cases when we compare it with the healthy case.

The variation in those details provides some useful information in the signal to extract and use it to train ANN.

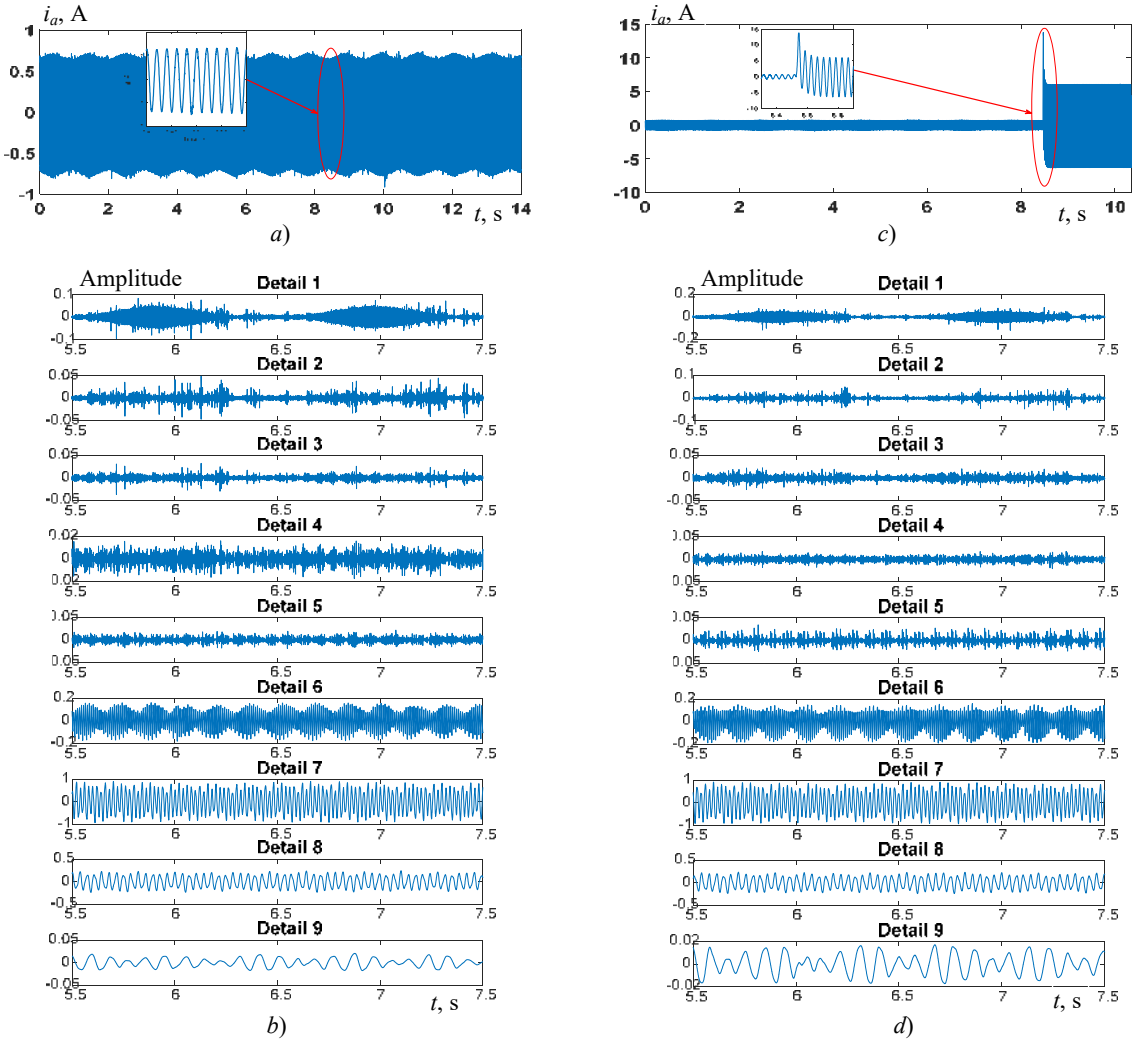

Fig. 6. Inverter output current (i_a) and its details in healthy and faulty cases

Fault table based on extracted features. The next process is to create a fault table according to feature values under each fault by using the RMS of each detail:

$$RMS = \sqrt{\frac{1}{n}\sum_i x_i^2}\ , \qquad (6)$$

where x_i denotes the measurements and n is the number of measurements.

We should carefully observed these feature values because these values will use for training. Using this fault Table 3, an ANN is trained and then used to identify the faults.

Table 3

Fault table based on extracted features

	$D1_{RMS}$	$D2_{RMS}$	$D3_{RMS}$	$D4_{RMS}$	$D5_{RMS}$	$D6_{RMS}$	$D7_{RMS}$	$D8_{RMS}$	$D9_{RMS}$
Healthy	0.0167	0.0040	0.0038	0.0042	0.0058	0.0798	0.4734	0.1243	0.0142
F1	0.0132	0.0034	0.0037	0.0092	0.0229	0.2653	1.5706	0.4442	0.1148
F2	0.0172	0.0042	0.0041	0.0044	0.0061	0.0808	0.4832	0.1268	0.0132
F3	0.0173	0.0053	0.0040	0.0042	0.0075	0.0624	0.3529	0.0925	0.0094
F4	0.0162	0.0042	0.0034	0.0037	0.0056	0.0637	0.3744	0.0981	0.0109
F5	0.0172	0.0045	0.0045	0.0049	0.0091	0.0869	0.4644	0.1219	0.0127
F6	0.0173	0.0045	0.0045	0.0048	0.0094	0.0900	0.4759	0.1250	0.0108

Artificial neural network. The Artificial neural network system has proven its capability in a variety of engineering applications such as estimation, process control and diagnostics [19].

ANN is modeled on the human brain and nervous system. It requires to train and calculate hidden layer weights according to the inputs and required outputs before using it in a specific system. It consists of the input layer, hidden layer or layers, and an output layer. Weights of hidden nodes are calculated during the training process to provide the exact output in case of same or nearly equal input combinations. Back-propagation technique is used for weight training of neural network; this method calculates the gradient of a loss function with respect to all weights in the network so that the gradient is fed to the optimization method which uses it to update weights in an attempt to minimize loss function [20].

The ANN architecture employed in this work is shown in Fig. 7. It consists of the input layer with 9 neurons, one for each RMS detail, a hidden layer with 10 neurons, and an output layer with 4 neurons referring to the sign of the fault we want to detect. The back-propagation technique used for training is based on Levenberg-Marquardt algorithm. The sigmoid activation function is used for hidden and output layers.

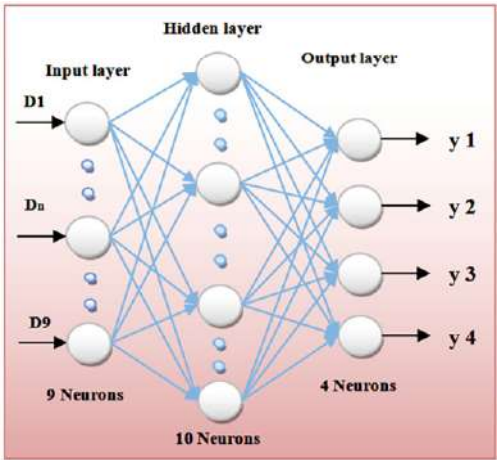

Fig. 7. ANN Structure

Table 4 represents the corresponding sign to each fault; the sign consist of 4 variables in binary numerical system which indicates to fault number ("***F***"*n*) in decimal numerical system. The objective of using the binary numerical system as target output is to use it as machine code.

Table 4

Fault sign

	y1	y2	y3	y4	Decimal N°
Healthy	0	0	0	0	0
F1	1	0	0	0	1
F2	0	1	0	0	2
F3	1	1	0	0	3
F4	0	0	1	0	4
F5	1	0	1	0	5
F6	0	1	1	0	6

Results and discussion. First of all, the ANN must be trained with healthy and faulty data. Then this trained neural network is used for fault detection system.

MATLAB/Simulink neural network toolbox is used to train the neural network according to the extracted features shown in Table 3 and the sign given in Table 4. The training process is simple and easy to perform using the MATLAB toolbox. The trained neural network can be easily converted to Simulink blocks or a MATLAB function which can be readily integrated in our designed system.

At the end of the training process, the model obtained consists of the optimal weight and the bias vector. The minimum performance gradient was set and training will stop when any one of conditions is met.

An automatic learning of the ANN is performed until a mean squared error of $2.1884 \cdot 10^{-22}$ is obtained at epoch 13.

Table 5 represents the obtained results in MATLAB/Simulink environment; it shows that the results are similar to the target output in Table 4.

Table 5

Tests results

Healthy	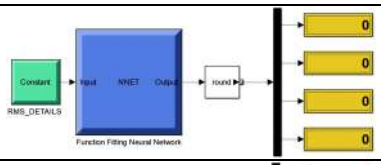	=▶	0
F1	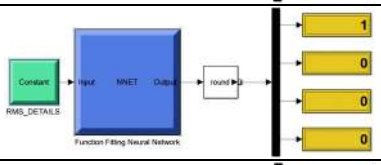	=▶	1
F2	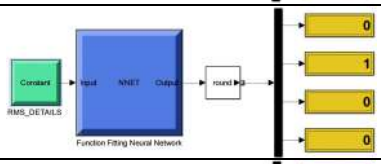	=▶	2
F3	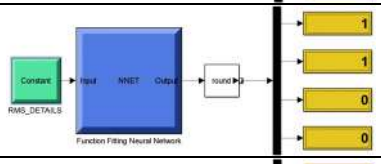	=▶	3
F4	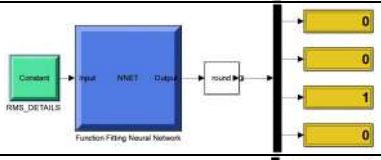	=▶	4
F5	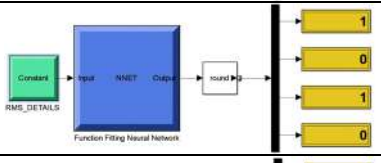	=▶	5
F6	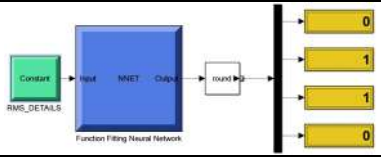	=▶	6

Conclusion. In this research work, we presenting a study of diagnostic technique for PV system based on real data, using wavelet transform and artificial neurons network. This study aims to find a solution to an effective and robust detection faults in the PV system such as partial shading, an open-circuit of the PV array of the system, a complete failure in one of the six IGBTs of the inverter and some parametric faults.

This technique shows a good performance. Furthermore, the simplicity of this proposed algorithm also shortens the response time, that's why it can detect the faults with high speed and accuracy.

Appendix. Reference [21] represents the grid-connected PV system faults data that are collected from lab experiments of faults in a PV microgrid system. There

are 16 data files in '.mat' form and also '.csv' form. Experimental data files are available in [21].

Acknowledgment. The authors would like to thank A. Bakdi, A. Guichi, S. Mekhilef and W. Bounoua for providing grid-connected PV system faults data from lab experiments which was part of this research work.

Conflict of interest. The authors declare no conflict of interest.

REFERENCES

1. Eltawil M.A., Zhao Z. MPPT techniques for photovoltaic applications. *Renewable and Sustainable Energy Reviews*, 2013, vol. 25, pp. 793-813. doi: https://doi.org/10.1016/j.rser.2013.05.022.

2. Albers M.J., Ball G. Comparative Evaluation of DC Fault-Mitigation Techniques in Large PV Systems. *IEEE Journal of Photovoltaics*, 2015, vol. 5, no. 4, pp. 1169-1174. doi: https://doi.org/10.1109/JPHOTOV.2015.2422142.

3. Liu S., Dong L., Liao X., Cao X., Wang X., Wang B. Application of the Variational Mode Decomposition-Based Time and Time–Frequency Domain Analysis on Series DC Arc Fault Detection of Photovoltaic Arrays. *IEEE Access*, 2019, vol. 7, pp. 126177-126190. doi: https://doi.org/10.1109/ACCESS.2019.2938979.

4. Akbar F., Mehmood T., Sadiq K., Ullah M.F. Optimization of accurate estimation of single diode solar photovoltaic parameters and extraction of maximum power point under different conditions. *Electrical Engineering & Electromechanics*, 2021, no. 6, pp. 46-53. doi: https://doi.org/10.20998/2074-272X.2021.6.07.

5. Kim G.G., Lee W., Bhang B.G., Choi J.H., Ahn H.-K. Fault Detection for Photovoltaic Systems Using Multivariate Analysis With Electrical and Environmental Variables. *IEEE Journal of Photovoltaics*, 2021, vol. 11, no. 1, pp. 202-212. doi: https://doi.org/10.1109/JPHOTOV.2020.3032974.

6. Appiah A.Y., Zhang X., Ayawli B.B.K., Kyeremeh F. Long Short-Term Memory Networks Based Automatic Feature Extraction for Photovoltaic Array Fault Diagnosis. *IEEE Access*, 2019, vol. 7, pp. 30089-30101. doi: https://doi.org/10.1109/ACCESS.2019.2902949.

7. Jayamaha D.K.J.S., Lidula N.W.A., Rajapakse A.D. Wavelet-Multi Resolution Analysis Based ANN Architecture for Fault Detection and Localization in DC Microgrids. *IEEE Access*, 2019, vol. 7, pp. 145371-145384. doi: https://doi.org/10.1109/ACCESS.2019.2945397.

8. Aziz F., Ul Haq A., Ahmad S., Mahmoud Y., Jalal M., Ali U. A Novel Convolutional Neural Network-Based Approach for Fault Classification in Photovoltaic Arrays. *IEEE Access*, 2020, vol. 8, pp. 41889-41904. doi: https://doi.org/10.1109/ACCESS.2020.2977116.

9. Veerasamy V., Wahab N.I.A., Othman M.L., Padmanaban S., Sekar K., Ramachandran R., Hizam H., Vinayagam A., Islam M.Z. LSTM Recurrent Neural Network Classifier for High Impedance Fault Detection in Solar PV Integrated Power System. *IEEE Access*, 2021, vol. 9, pp. 32672-32687. doi: https://doi.org/10.1109/ACCESS.2021.3060800.

10. Wang M.-H., Lu S.-D., Liao R.-M. Fault Diagnosis for Power Cables Based on Convolutional Neural Network With Chaotic System and Discrete Wavelet Transform. *IEEE Transactions on Power Delivery*, 2022, vol. 37, no. 1, pp. 582-590. doi: https://doi.org/10.1109/TPWRD.2021.3065342.

11. Ankar S., Sahu U., Yadav A. Wavelet-ANN Based Fault Location Scheme for Bipolar CSC-Based HVDC Transmission System. *2020 First International Conference on Power, Control and Computing Technologies (ICPC2T)*, 2020, pp. 85-90. doi: https://doi.org/10.1109/ICPC2T48082.2020.9071450.

12. Souad S.L., Azzedine B., Meradi S. Fault diagnosis of rolling element bearings using artificial neural network. *International Journal of Electrical and Computer Engineering (IJECE)*, 2020, vol. 10, no. 5, pp. 5288-5295. doi: https://doi.org/10.11591/ijece.v10i5.pp5288-5295.

13. Jayamaha D.K.J., Lidula N.W., Rajapakse A. Wavelet Based Artificial Neural Networks for Detection and Classification of DC Microgrid Faults. *2019 IEEE Power & Energy Society General Meeting (PESGM)*, 2019, pp. 1-5. doi: https://doi.org/10.1109/PESGM40551.2019.8974108.

14. Bakdi A., Bounoua W., Guichi A., Mekhilef S. Real-time fault detection in PV systems under MPPT using PMU and high-frequency multi-sensor data through online PCA-KDE-based multivariate KL divergence. *International Journal of Electrical Power & Energy Systems*, 2021, vol. 125, art. no. 106457. doi: https://doi.org/10.1016/j.ijepes.2020.106457.

15. Guichi A., Talha A., Berkouk E.M., Mekhilef S., Gassab S. A new method for intermediate power point tracking for PV generator under partially shaded conditions in hybrid system. *Solar Energy*, 2018, vol. 170, pp. 974-987. doi: https://doi.org/10.1016/j.solener.2018.06.027.

16. Bakdi A., Bounoua W., Mekhilef S., Halabi L.M. Nonparametric Kullback-divergence-PCA for intelligent mismatch detection and power quality monitoring in grid-connected rooftop PV. *Energy*, 2019, vol. 189, art. no. 116366. doi: https://doi.org/10.1016/j.energy.2019.116366.

17. Eddine C.B.D., Azzeddine B., Mokhtar B. Detection of a two-level inverter open-circuit fault using the discrete wavelet transforms technique. *2018 IEEE International Conference on Industrial Technology (ICIT)*, 2018, pp. 370-376. doi: https://doi.org/10.1109/ICIT.2018.8352206.

18. Souad L., Azzedine B., Eddine C.B.D., Boualem B., Samir M., Youcef M. Induction machine rotor and stator faults detection by applying the DTW and N-F network. *2018 IEEE International Conference on Industrial Technology (ICIT)*, 2018, pp. 431-436. doi: https://doi.org/10.1109/ICIT.2018.8352216.

19. Bouchaoui L., Hemsas K.E., Mellah H., Benlahneche S. Power transformer faults diagnosis using undestructive methods (Roger and IEC) and artificial neural network for dissolved gas analysis applied on the functional transformer in the Algerian north-eastern: a comparative study. *Electrical Engineering & Electromechanics*, 2021, no. 4, pp. 3-11. doi: https://doi.org/10.20998/2074-272X.2021.4.01.

20. Talha M., Asghar F., Kim S.H. A Novel Three-Phase Inverter Fault Diagnosis System Using Three-dimensional Feature Extraction and Neural Network. *Arabian Journal for Science and Engineering*, 2019, vol. 44, no. 3, pp. 1809-1822. doi: https://doi.org/10.1007/s13369-018-3156-8.

21. Bakdi A., Guichi A., Mekhilef S., Bounoua W. GPVS-Faults: Experimental Data for fault scenarios in grid-connected PV systems under MPPT and IPPT modes, *Mendeley Data*, 2020, V1. doi: https://dx.doi.org/http://dx.doi.org/10.17632/n76t439f65.1.

Received 15.05.2022
Accepted 25.07.2022
Published 06.11.2022

Abdelkader Azzeddine Bengharbi[1], *PhD Student,*
Saadi Souad Laribi[1], *Doctor of Electrical Engineering,*
Tayeb Allaoui[1], *Professor of Electrical Engineering,*
Amina Mimouni[1], *PhD Student,*
[1] Energy Engineering and Computer Engineering (L2GEGI) Laboratory, University of Tiaret,
BP P 78 Zaâroura, 14000, Tiaret, Algeria.
e-mail: bengharbi.aek.azz@univ-tiaret.dz (Corresponding Author);
souad.laribi@univ-tiaret.dz;
tayeb.allaoui@univ-tiaret.dz;
amina.mimouni@univ-tiaret.dz

How to cite this article:
Bengharbi A.A., Laribi S., Allaoui T., Mimouni A. Photovoltaic system faults diagnosis using discrete wavelet transform based artificial neural networks. *Electrical Engineering & Electromechanics*, 2022, no. 6, pp. 42-47. doi: https://doi.org/10.20998/2074-272X.2022.6.07

UDC 621.3 https://doi.org/10.20998/2074-272X.2022.6.08

R. Hamdi, A. Hadri Hamida, O. Bennis

On modeling and real-time simulation of a robust adaptive controller applied to a multicellular power converter

Introduction. *This paper describes the simulation and the robustness assessment of a DC-DC power converter designed to interface a dual-battery conversion system. The adopted converter is a Buck unidirectional and non-isolated converter, composed of three cells interconnected in parallel and operating in continuous conduction mode.* ***Purpose.*** *In order to address the growing challenges of high switching frequencies, a more stable, efficient, and fixed-frequency-operating power system is desired.* ***Originality.*** *Conventional sliding mode controller suffers from high-frequency oscillation caused by practical limitations of system components and switching frequency variation. So, we have explored a soft-switching technology to deal with interface problems and switching losses, and we developed a procedure to choose the high-pass filter parameters in a sliding mode-controlled multicell converter.* ***Methods.*** *We suggest that the sliding mode is controlled by hysteresis bands as the excesses of the band. This delay in state exchanges gives a signal to control the switching frequency of the converter, which, in turn, produces a controlled trajectory. We are seeking an adaptive current control solution to address this issue and adapt a variable-bandwidth of the hysteresis modulation to mitigate nonlinearity in conventional sliding mode control, which struggles to set the switching frequency. Chatter problems are therefore avoided. A boundary layer-based control scheme allows multicell converters to operate with a fixed-switching-frequency.* ***Practical value.*** *Simulation studies in the MATLAB / Simulink environment are performed to analyze system performance and assess its robustness and stability. Thus, our converter is more efficient and able to cope with parametric variation.* References 17, figures 6.
Key words: **multicellular converters, sliding mode control, high switching frequency, hysteresis modulation.**

Вступ. *У статті описується моделювання та оцінка надійності силового перетворювача постійного струму, призначеного для взаємодії із системою перетворення з двома батареями. Прийнятий перетворювач є односпрямованим і неізольованим перетворювачем Бака, що складається з трьох паралельно з'єднаних між собою осередків, що працюють в режимі безперервної провідності.* ***Мета***. *Для вирішення проблем, пов'язаних з високими частотами перемикання, потрібна більш стабільна, ефективна система живлення з фіксованою частотою.* ***Оригінальність***. *Звичайний регулятор ковзного режиму страждає від високочастотних коливань, викликаних практичними обмеженнями компонентів системи та зміною частоти перемикання. Отже, ми дослідили технологію м'якого перемикання для вирішення проблем інтерфейсу та комутаційних втрат, а також розробили процедуру вибору параметрів фільтра верхніх частот у багатоосередковому перетворювачі зі ковзним режимом.* ***Методи***. *Ми припускаємо, що ковзний режим управляється смугами гістерезису як надлишками смуги. Ця затримка обміну станами дає сигнал управління частотою перемикання перетворювача, який, своєю чергою, створює керовану траєкторію. Ми шукаємо рішення для адаптивного керування струмом, щоб вирішити цю проблему і адаптувати гістерезисну модуляцію зі змінною смугою пропускання для пом'якшення нелінійності у звичайному ковзному режимі керування, яке щосили намагається встановити частоту перемикання. Таким чином вдається уникнути проблем із деренчанням. Схема керування на основі прикордонного шару дозволяє перетворювачам з кількома осередками працювати з фіксованою частотою перемикання.* ***Практична цінність***. *Імітаційне моделювання у середовищі MATLAB/Simulink виконується для аналізу продуктивності системи та оцінки її надійності та стабільності. Таким чином, наш перетворювач ефективніший і здатний справлятися зі зміною параметрів.* Бібл. 17, рис. 6.
Ключові слова: **багатоосередкові перетворювачі, ковзне управління, висока частота перемикання, гістерезисна модуляція.**

Introduction. Designing a dual-battery 12/48 V conversion system is challenging because it requires careful management of power transfer from the 48 V rail to its 12 V rail [1, 2]. One option is to use a buck unidirectional DC-DC converter located between the 12 V and 48 V batteries. This converter can be used to step down the voltage and transfer power between batteries. The introduction of unidirectional DC-DC converters, simplifies design, reduces cost and encourages adoption in low-cost cars [3]. The power distribution network also has the ability to detect faults in auxiliary loads as well as turn these loads on and off. The power distribution network is implemented with two main systems: the auxiliary power system, which consists of a 2.4 W buck converter with current limiting control circuits at 12 V. The other system is the control system, which is developed using microcontrollers and autonomous controllers [4].

In addition, DC-DC power converters are ideal candidates in many applications such as electric vehicles, fuel cells and others. They have been the subject of much research over three decades [5-9]. The control of these converters has often been implemented using pulse width modulation and discrete component and integrated circuit techniques in different anterior research work that have reached its limits [10, 11]. Besides, nonlinear sliding mode controllers represent a very promising strategy for parallel multi-channel converters integrate control techniques with numerous sliding surfaces and an intrinsic variable. They are simple to develop, robust, and respond well in transient and steady conditions. Furthermore, they limit switching frequency variation, reduce inappropriate transient response, and achieve a proper balance of transient and stationary performance [12-14]. This drives us to propose a sliding mode controller implementation based on the hysteresis function. The technology is simple to use and does not necessitate the use of any additional auxiliary circuits or sophisticated computations. Previous research indicates that the main barriers to using sliding mode control are two interrelated factors: chatter and excessive activity of control actions [15-17]. The amplitude of chattering is clearly acknowledged to be linked to the magnitude of a discontinuous controller. These two issues can be dealt with concurrently, if the magnitude is limited to a minimal recommended levels determined by the sliding mode's existence criteria. In such a highly interesting context, we developed an adaptive sliding mode controller. It can be used to decrease chatter, with the purpose of ensuring an adaptive

and dynamic control. The main concept behind the adaptive control technique is to create systems that display the same dynamic features under relevant uncertainty situations and adequate to overcome uncertainties and disturbances. This method will be thoroughly discussed in the remainder of our study. The body of the paper is structured as follows:

In the converter topology and mathematical model section, we will explain and model the adopted system. In the controller design section, we will examine the hysteresis modulation-based sliding mode controller. In the simulation results and stability analyses section, we will discuss the simulation findings and analyze the effectiveness of the control measures. And we will end with a conclusion.

Converter topology and mathematical model. Figure 1 depicts the multicell DC-DC buck converter under investigation. It consists of three identical modules coupled via a resistive load R and a filter capacitor C to a continuous DC input voltage source V_I. Each module is built around a power MOSFET S, an antiparallel diode D, and a filter inductor L. It's important to note that the parallel switching buck converter works in continuous conduction mode. In other words, the 3 cells are identical, each cell have the same value of the inductor L. The converter may be described by an equation system based on a mathematical model with mean values, and the system dynamics of the examined converter can be defined as follows:

$$L \cdot \frac{\mathrm{d}I_{Lj}}{\mathrm{d}t} = V_I \cdot D - V_O; \quad (1)$$

$$C \cdot \frac{\mathrm{d}V_O}{\mathrm{d}t} = I_L + \frac{V_O}{R}, \quad (2)$$

where I_{Lj} is the current that flows via inductance j = 1, 2, 3; I_L is the current at the converter's output; V_I is the input voltage; V_O is the converter's output voltage; D is the duty cycle.

The condition of space is expressed as follow:

$$x_1 = V_{ref} - V_O;$$

$$x_2 = \dot{x}_1 = -\frac{\mathrm{d}V_O}{\mathrm{d}t} = \frac{1}{C \cdot \left(\frac{V_O}{R} - \int \left(\frac{u \cdot V_I - V_O}{L} \right) \mathrm{d}t \right)}, \quad (3)$$

where V_{ref} is the required output value.

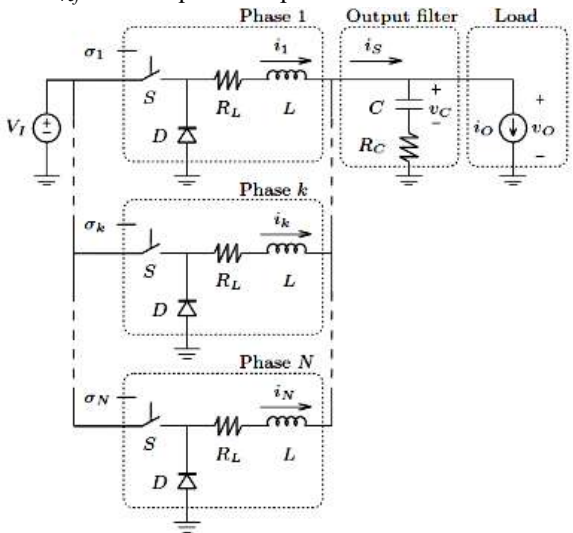

Fig. 1. Paralleled-multicellular converter

Controller design. We develop a robust control strategy in a way that our multicell buck converter become more stable, more efficient and able to cope with parametric variation.

At this level, our interest is to explore an adaptive feedback current control approach to tackle this difficulty, by using a variable-bandwidth hysteresis modulation to limit the nonlinearity phenomena in traditional sliding mode control to fix the switching frequency. The reconfiguration of the (3) helps us to design the sliding mode voltage controller:

$$\begin{bmatrix} \dot{x}_1 \\ \dot{x}_2 \end{bmatrix} = \begin{bmatrix} 0 & 1 \\ -\frac{1}{LC} & -\frac{1}{RC} \end{bmatrix} \cdot \begin{bmatrix} x_1 \\ x_2 \end{bmatrix} + \begin{bmatrix} 0 \\ -\frac{V_I}{LC} \end{bmatrix} \cdot u + \begin{bmatrix} 0 \\ \frac{V_{ref}}{LC} \end{bmatrix}. \quad (4)$$

We can determine the switching function u, by taking into account the estimated state trajectory including the control parameters x_1 and x_2. Clearly, the basic principle of sliding mode control is to design a control law that will direct the trajectory of state variables to a desired operating point. In the case of the buck converter under study, it is appropriate to have a control law that adopts a switching function such that:

$$u = \frac{1}{2 \cdot (1 + \mathrm{sign}(S))}, \quad (5)$$

where u is the logic state of the power switch of the converter; S is the path of the instantaneous state.

The proposed control scheme shown in Fig. 2 requires that the instantaneous information on the two converter states x_1 and x_2 be fed into the controller to produce the control signal u as described in (5).

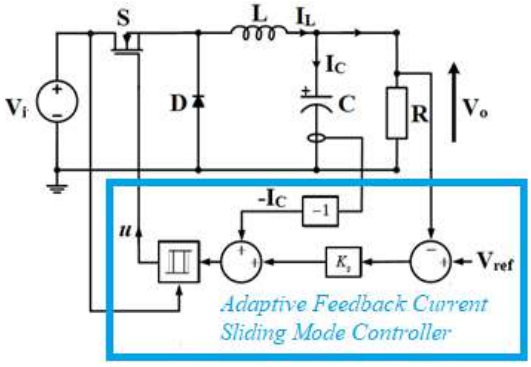

Fig. 2. Variable band-width hysteresis modulation-based sliding mode current controller

The method of implementing the sliding mode control is to use a relay of the sign function with the calculated trajectory S as shown in Fig. 3. This method is commonly used and known as the conventional strategy of the sliding mode, as illustrated in Fig. 4.

When u = 1, the phase trajectory for any arbitrary starting position on the phase plane will converge to the equilibrium point ($x_1 = V_{ref} - V_O$; $x_2 = 0$), after a finite time period. Similarly, when u = 0, all trajectories converge to the equilibrium point ($x_1 = V_{ref}$; $x_2 = 0$). Thus, the sliding surface is defined by:

$$S = K_{p1} \cdot (V_{ref} - V_O) + K_{p2} \cdot i_O; \quad (6)$$

$$K_{p1} = \frac{1}{r_C \cdot C}; \quad K_{p2} = -\frac{1}{C}. \quad (7)$$

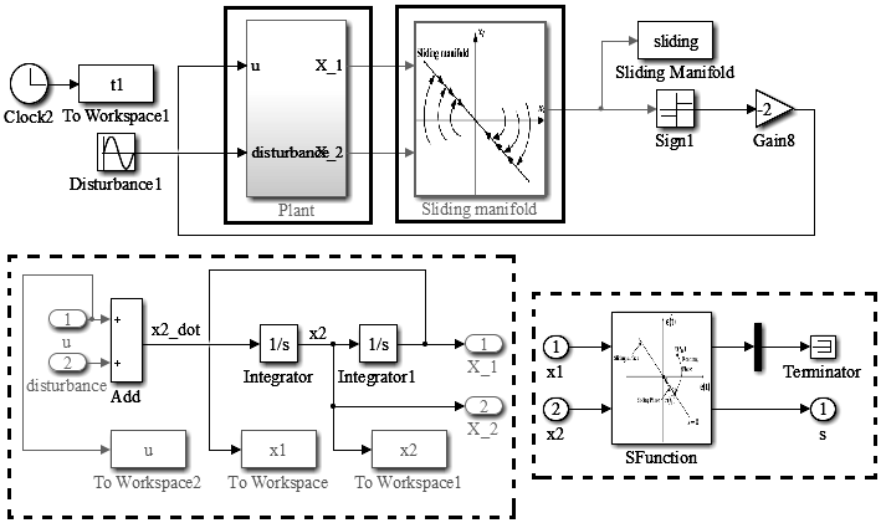

Fig. 3. Simulation of the sliding mode control in relation to the converter state variables

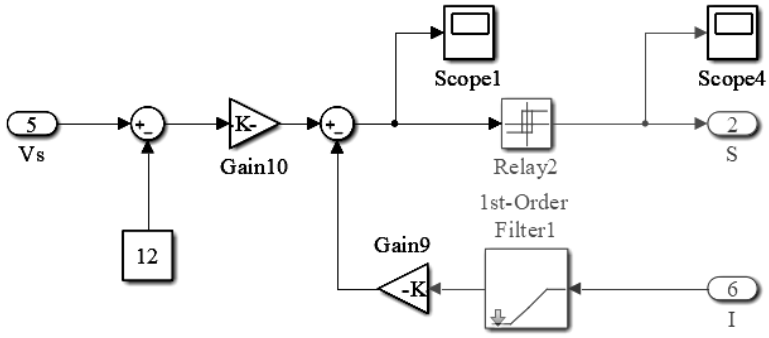

Fig. 4. Diagram of the controller in conventional sliding mode

Given this, it is simpler to reconfigure the switching function as described below:

$$S = \frac{1}{r_C \cdot \left(V_{ref} - V_O\right)} - i_O \,. \tag{8}$$

The control is applied simultaneously without phase shift to the three topologically identical cells of a non-isolated and asynchronous converter. The objective is to fix the switching frequency of the converter by referring to an adaptive feedback approach. For this purpose, we integrate a hysteresis modulator and develop a variable hysteresis band function to mitigate the non-linearity phenomenon of the conventional sliding mode. Then, we apply an adaptive feedback current control technique to overcome the dilemma of variable switching frequency. Still in order to ensure the fixed frequency operation of the proposed hysteresis modulator, a requirement is imposed, and that the hysteresis bandwidth must satisfy it, is:

$$B_{\text{var-width}} = \frac{\Delta i_O}{2} = \frac{\left(V_I - V_O\right)}{2 \cdot L \cdot fw} \cdot \left(\frac{V_O}{V_I}\right). \tag{9}$$

The converter control scheme has two modes of operation: one when the error paths are outside the boundary layer and the other when they are inside the boundary layer. The boundary layer, which varies in time, is formed by a frequency ramp signal ($fw = 1/T$). The boundaries of this layer correspond to the maximum and minimum values of the ramp. Figure 5 duplicates the control scheme of the variable band hysteresis model based on the sliding mode. At the beginning of each switching cycle, we determine whether the error paths are within the limits of the time-varying ramp and, based on this, we determine the operating mode.

Simulation results and stability analyses. In this section, and to properly study the behavior of the closed-loop multi-cell DC-DC buck converter and the evaluation of its performance under stable and dynamic conditions, several robustness tests have been performed to analyze the sensitivity of the implemented strategies to the variations of the converter parameters.

Figure 6 shows the response of the output voltage and the output current of the converter to parametric changes. It seems clear that the system operating with the sliding mode controller combined with a variable band hysteresis modulation obtains a better compromise from transient to steady state. Thus, its transition response is smoother, more stable, without overshoot and with less oscillations.

Figure 6,*a* shows the output voltage response and output load current response when the system undergoes a change in output reference from 8 V to 12 V. The switching from one value to another is almost similar is characterized by high precision with a relatively short transition time.

Figure 6,*b* shows that, during an increase/decrease in resistance every 0.2 s, the closed-loop output voltage response exhibits an undesirable transient drop that lasts a few seconds followed abruptly by a steady state.

Figure 6,*c* shows the output voltage response and the output load current response when the system undergoes a change in supply, every 0.2 s, it varies between 40 V and 60 V and the output voltage is regulated to 12 V. There is a slight increase in amplitude, however, the output voltage and output load current vary around the reference value.

The simulations performed show extremely encouraging results regarding the efficiency and robustness of reference tracking, the control law allows a faster rejection of the effect of load change. These results demonstrate the effectiveness of the sliding mode control for such a type of converter and mainly for a dual-battery conversion system. This finding highlights the key contribution of our work: we obtain a large reduction of the switching frequency variation thanks to the suggested technique.

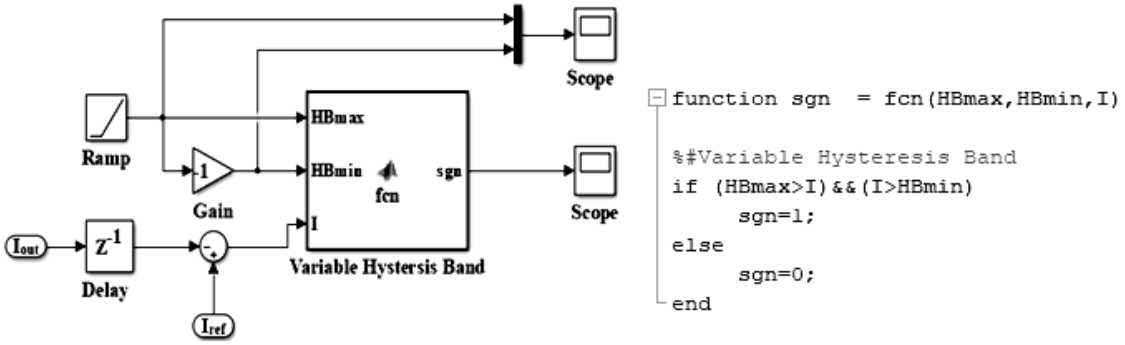

Fig. 5. The control scheme of the variable band hysteresis model based on the sliding mode

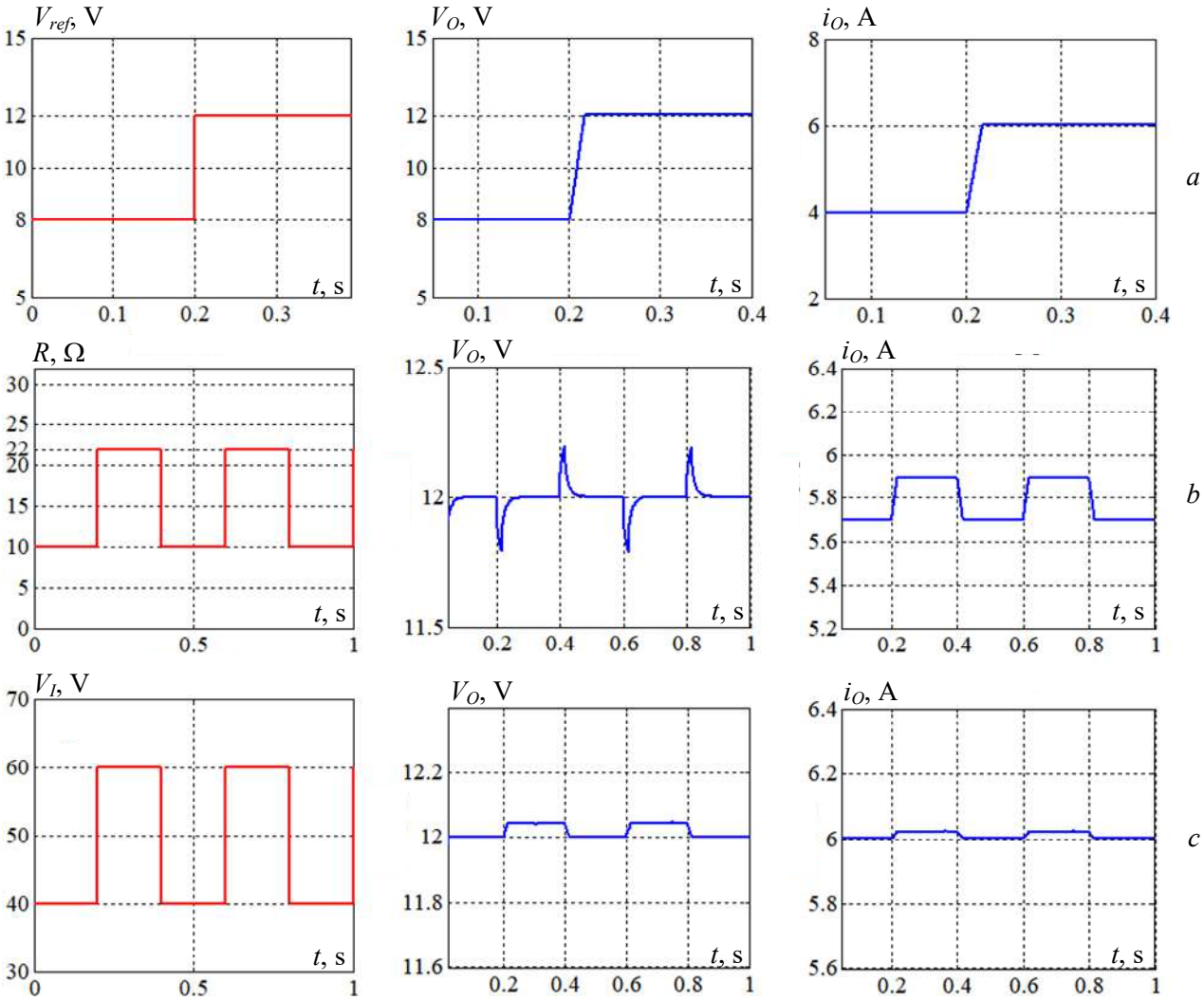

Fig. 6. Response of the output voltage V_O and output current i_O of the converter to parametric changes:
a) Variation of the reference voltage V_{ref} from 8 V to 12 V;
b) Increase/decrease of the load R from 10 Ω to 22 Ω;
c) Increase/decrease of the input voltage V_I from 40 V to 60 V

Conclusions.

It is found that the sliding mode based variable bandwidth hysteresis control is favored as it provides superior performance in both source voltage disturbance rejection and load transient response with greatly desired output voltage tracking and also provides high efficiency. This sort of control has been shown to be effective in both stability and trajectory tracking challenges. In addition, this controller is faster to the point that the response time at 5 % is mainly short. Its appropriate dynamic accuracy is characterized by zero overshoot during the transient of the output voltage response. Thus, it provided similar

performance, improved dynamic drive and could adapt to varieties of voltage and load. The use of variable bandwidth hysteresis modulation and switching frequency fixing leads to large-scale dynamics and allows the reduction of the magnitude of the control action to the smallest achievable value as well as finite-time convergence. The simulations performed show very promising results in terms of reference tracking performance and robustness. They prove the relevance of the sliding mode control for this type of system. Not to mention that paralleling switching cells favors the increase of the output current, with a reduction of its oscillations compared to the oscillations of the currents of each phase.

Conflict of interest. The authors declare no conflict of interest.

REFERENCES

1. Hamdi R., Hamida A.H., Bennis O., Babaa F. HM-Based SMVC with Adaptive Feedforward Controller Applied to DC-DC Converter. *2020 International Conference on Electrical and Information Technologies (ICEIT)*, 2020, pp. 1-6. doi: https://doi.org/10.1109/ICEIT48248.2020.9113220.

2. Do W., Eguchi K., Shibata A. An analytical approach for parallel switched capacitor converter. *Energy Reports*, 2020, vol. 6, pp. 338-342. doi: https://doi.org/10.1016/j.egyr.2020.11.233.

3. Li H., Jiang X., Zou Y., Liu C. A time-domain stability analysis method for paralleled LLC resonant converter system based on Floquet theory. *Microelectronics Reliability*, 2020, vol. 114, art. no. 113849. doi: https://doi.org/10.1016/j.microrel.2020.113849.

4. Ben Said S., Ben Saad K., Benrejeb M. HIL simulation approach for a multicellular converter controlled by sliding mode. *International Journal of Hydrogen Energy*, 2017, vol. 42, no. 17, pp. 12790-12796. doi: https://doi.org/10.1016/j.ijhydene.2017.01.198.

5. Djondiné P. Overview of Control Techniques for Multicellular Converter. *Journal of Engineering Sciences*, 2018, vol. 5, no. 1, pp. E10-E14. doi: https://doi.org/10.21272/jes.2018.5(1).e3.

6. Engelkemeir F., Gattozzi A., Hallock G., Hebner R. An improved topology for high power soft-switched power converters. *International Journal of Electrical Power & Energy Systems*, 2019, vol. 104, pp. 575-582. doi: https://doi.org/10.1016/j.ijepes.2018.07.049.

7. Romashko V.Y., Batrak L.M., Abakumova O.O. Step-up/step-down regulators in maximum power transmission mode. *Electrical Engineering & Electromechanics*, 2022, no. 2, pp. 18-22. doi: https://doi.org/10.20998/2074-272X.2022.2.03.

8. Merlin Suba G., Kumaresan M. Design of LLC resonant converter with silicon carbide MOSFET switches and nonlinear adaptive sliding controller for brushless DC motor system. *Electrical Engineering & Electromechanics*, 2022, no. 4, pp. 34-43. doi: https://doi.org/10.20998/2074-272X.2022.4.05.

9. Bouraghda S., Sebaa K., Bechouat M., Sedraoui M. An improved sliding mode control for reduction of harmonic currents in grid system connected with a wind turbine equipped by a doubly-fed induction generator. *Electrical Engineering & Electromechanics*, 2022, no. 2, pp. 47-55. doi: https://doi.org/10.20998/2074-272X.2022.2.08.

10. Patin N. *Power Electronics Applied to Industrial Systems and Transports*. Elsevier, 2016. 272 p. doi: https://doi.org/10.1016/C2015-0-04476-8.

11. Kolli A., Gaillard A., De Bernardinis A., Bethoux O., Hissel D., Khatir Z. A review on DC/DC converter architectures for power fuel cell applications. *Energy Conversion and Management*, 2015, vol. 105, pp. 716-730. doi: https://doi.org/10.1016/j.enconman.2015.07.060.

12. Al-Baidhani H., Kazimierczuk M.K., Salvatierra T., Reatti A., Corti F. Sliding-Mode Voltage Control of Dynamic Power Supply for CCM. *2019 IEEE International Symposium on Circuits and Systems (ISCAS)*, 2019, pp. 1-5. doi: https://doi.org/10.1109/ISCAS.2019.8702628.

13. Ma G., Wang B., Xu D., Zhang L. Switching control strategy based on non-singular terminal sliding mode for buck converter in auxiliary energy source. *Energy Procedia*, 2018, vol. 145, pp. 139-144. doi: https://doi.org/10.1016/j.egypro.2018.04.023.

14. Wu Y., Huangfu Y., Ma R., Ravey A., Chrenko D. A strong robust DC-DC converter of all-digital high-order sliding mode control for fuel cell power applications. *Journal of Power Sources*, 2019, vol. 413, pp. 222-232. doi: https://doi.org/10.1016/j.jpowsour.2018.12.049.

15. Das S., Salim Qureshi M., Swarnkar P. Design of integral sliding mode control for DC-DC converters. *Materials Today: Proceedings*, 2018, vol. 5, no. 2, pp. 4290-4298. doi: https://doi.org/10.1016/j.matpr.2017.11.694.

16. Pandey S.K., Patil S.L., Ginoya D., Chaskar U.M., Phadke S.B. Robust control of mismatched buck DC–DC converters by PWM-based sliding mode control schemes. *Control Engineering Practice*, 2019, vol. 84, pp. 183-193. doi: https://doi.org/10.1016/j.conengprac.2018.11.010.

17. Naik B.B., Mehta A.J. Sliding mode controller with modified sliding function for DC-DC Buck Converter. *ISA Transactions*, 2017, vol. 70, pp. 279-287. doi: https://doi.org/10.1016/j.isatra.2017.05.009.

Received 28.05.2022
Accepted 11.06.2022
Published 06.11.2022

Rihab Hamdi[1]*, PhD,*
Amel Hadri Hamida[1]*, Professor,*
Ouafae Bennis[2]*, Professor,*
[1] LMSE Laboratory,
University of Biskra, 07000 Biskra, Algeria,
e-mail: rihab.hamdi2012@gmail.com (Corresponding Author);
am_hadri@yahoo.fr;
[2] PRISME Institute,
University of Orleans, Chartres, 28000, France,
e-mail: ouafae.bennis@univ-orleans.fr

How to cite this article:
Hamdi R., Hadri Hamida A., Bennis O. On modeling and real-time simulation of a robust adaptive controller applied to a multicellular power converter. *Electrical Engineering & Electromechanics*, 2022, no. 6, pp. 48-52. doi: https://doi.org/10.20998/2074-272X.2022.6.08

UDC 621.3 https://doi.org/10.20998/2074-272X.2022.6.09

B. Mahdad, K. Srairi

Interactive artificial ecosystem algorithm for solving power management optimizations

Introduction. *Power planning and management of practical power systems considering the integration and coordination of various FACTS devices is a vital research area. Recently, several metaheuristic methods have been developed and applied to solve various optimization problems. Among these methods, an artificial ecosystem based optimization has been successfully proposed and applied to solve various industrial and planning problems.* ***The novelty*** *of the work consists in creating an interactive process search between diversification and intensification within the standard artificial ecosystem based optimization. The concept of the introduced variant is based on creating dynamic interaction between production operator and consumer operator during search process.* ***Purpose.*** *This paper introduces an interactive artificial ecosystem based optimization to solve with accuracy the multi objective power management optimization problems.* ***Methods.*** *The solution of the problem was carried out using MATLAB program and the developed package is based on combining the proposed metaheuristic method and the power flow tool based Newton-Raphson algorithm.* ***Results.*** *Obtained results confirmed that the proposed optimizer tool may be suitable to solve individually and simultaneously various objective functions such as the total fuel cost, the power losses and the voltage deviation.* ***Practical value.*** *The efficiency of the proposed variant in terms of solution quality and convergence behavior has been validated on two practical electric test systems: the IEEE-30-bus, and the IEEE-57-bus. A statistical comparative study with critical review is elaborated and intensively compared to various recent metaheuristic techniques confirm the competitive aspect and particularity of the proposed optimizer tool in solving with accuracy the power management considering various objective functions.* References 34, tables 11, figures 16.

Key words: **artificial ecosystem based optimization, power management, intensification and diversification, FACTS devices.**

Вступ. *Планування електроживлення та управління енергосистемами, що експлуатуються, з урахуванням інтеграції та координації різних пристроїв FACTS (гнучка система передачі змінного струму) є життєво важливою галуззю досліджень. Останнім часом було розроблено та застосовано кілька метаевристичних методів для вирішення різних задач оптимізації. Серед цих методів оптимізація на основі штучної екосистеми була успішно запропонована та застосована для вирішення різних промислових та планувальних завдань.* ***Новизна*** *роботи полягає у створенні інтерактивного процесу пошуку між диверсифікацією та інтенсифікацією в рамках стандартної оптимізації на основі штучної екосистеми. Концепція представленого варіанта заснована на створенні динамічної взаємодії між оператором-виробником та оператором-споживачем у процесі пошуку.* ***Мета***. *У статті представлено інтерактивну оптимізацію на основі штучної екосистеми для точного вирішення багатоцільових завдань оптимізації управління живленням.* ***Методи***. *Розв'язання задачі здійснювалося за допомогою програми MATLAB, а розроблений пакет заснований на об'єднанні запропонованого метаевристичного методу та інструменту Powerflow на основі алгоритму Ньютона-Рафсона.* ***Результати***. *Отримані результати підтвердили, що запропонований інструмент оптимізатора може бути придатний для індивідуального та одночасного розв'язання різних цільових функцій, таких як загальна вартість палива, втрати потужності та відхилення напруги.* ***Практична цінність***. *Ефективність запропонованого варіанта з точки зору якості рішення та поведінки збіжності була підтверджена на двох реальних електричних випробувальних системах: шині IEEE-30 та шині IEEE-57. Статистичне порівняльне дослідження з критичним оглядом розроблено та інтенсивно порівнюється з різними сучасними метаевристичними методами, що підтверджують конкурентний аспект та особливість запропонованого інструменту оптимізатора у точному розв'язанні управління живленням з урахуванням різних цільових функцій.* Бібл. 34, табл. 11, рис. 16.

Ключові слова: **оптимізація на основі штучної екосистеми, управління енергією, інтенсифікація та диверсифікація, пристрої FACTS (гнучка система передачі змінного струму).**

Introduction. As well demonstrated and stated in many research papers, that no a standard optimizer tool capable to solve various optimization tasks. For this reason, many optimizer tools based metaheuristic algorithms known also as global optimization methods have been developed. It is well proven that each developed method has its specific drawbacks and advantages, so, the majority of metaheuristic methods have special parameters to adjust designed to balance the search activity between intensification and diversification. The famous idea firstly introduced by Carpentier [1] namely economic dispatch which is a simplified and particular case of optimal power flow (OPF) becomes a vital tool for solving various power management optimization problems. The OPF planning strategy consists in improving the solution quality of a single or combined objective functions such as the total fuel cost (TFC), the total power loss (TPL), the total voltage deviation (TVD) and the voltage stability (VS) index while satisfying various security constraints. The concept of OPF tool becomes more attractive and vital for experts with the intensive installation of several types of flexible ac transmission system (FACTS) and the intense orientation towards integration of renewable sources. In the literature various determinist methods based mathematical formulation and several metaheuristic techniques have been proposed to solve many power management problems associated to modern electric systems. These methods have been designed and adapted to solve the conventional single or multi objective OPF considering several FACTS and various renewable sources energy such as wind and photovoltaic sources. In [2] a brief review is proposed on the famous metaheuristic methods applied to solve various power systems planning and control, among these methods: Genetic algorithm (GA), particle swarm optimization (PSO), differential evolution (DE), tabu search algorithm (TS), simulated annealing, etc. Continuously and to enhance the performances of the standard metaheuristic algorithms, many variants have been developed. The main idea introduced by these variants based metaheuristic methods such as in [3] are focused on how adjusting with efficacy the evolution of specific parameters and how to create flexible equilibrium during search process between diversification and intensification. Towards this pertinent

context, and to improve the solution of various practical configurations associated to the multi objective OPF, various recent optimization techniques have been designed and proposed. These recent optimization techniques characterized by low parameters to adjust, and their research mechanism is adaptive to create a flexible balance during search process between intensification and diversification. Among these methods, in [4] authors proposed a new interactive sine cosine algorithm (ISCA) to solve the security OPF considering critical state operations. In the same context, an interactive procedure named micro SCA is introduced and greatly improved the mechanism search of the standard SCA. In [5] a new variant named partitioning whale algorithm (PWOA) has been successfully applied to solve with accuracy the multi objective OPF. In [6] a new chaotic electromagnetic field algorithm based optimization is applied to improve the solution of the OPF. In [7] authors applied a moth swarm optimizer (MSO) to solve the OPF considering various operation and security constraints. In [8] an enhanced grasshopper variant is adapted and used to solve the multi objective OPF. In [9] authors suggested a variant based Jaya algorithm (AMTPG-Jaya) to enhance the solution of multi objective OPF. In [10] a new algorithm named tree seed algorithm (TSA) is proposed. In [11] a hybrid algorithm based on combing the PSO and gravitational search algorithm (GSA) is proposed to enhance the solution of the multi objective OPF. In [12] the lightning attachment optimization (LAO) technique is used for solving the security OPF. In [13] a combined technique based on PSO and pattern search (PS) algorithm is adapted to solve the OPF considering the integration of FACTS controllers. In [14] a variant based on teaching-learning algorithm is applied to solve the multi objective OPF. In [15] a chaotic bat algorithm (CBA) is adapted and applied to solve the reactive power management (RPM) problems. In [16] a new variant based social spider optimization (SSO) algorithm is used to improve the performances of the standard algorithm in solving the OPF by considering various goal functions. In [17] the PSO, GA and evolutionary algorithm (EA) are applied to solve the multi objective OPF problems. In [18] a new adaptive partitioning flower pollination algorithm (APFPA) is introduced and successfully applied to improve the OPF solution considering various objective functions at normal condition and under load growth. In [19] a modified salp swarm algorithm (MSSA) is successfully adapted and applied to solve the reactive power management optimization of the Algerian electric power system. In [20], a chaotic salp swarm algorithm (CSSA) is applied to solve various objective functions based OPF. In [21] a new stud krill herd algorithm (SKH) is adapted and used to solve the OPF with various objective functions. In [22] an improved adaptive differential evolution is suggested to solve various objectives based OPF problems. In [23] a novel variant based salp swarm algorithm is successfully applied to improve the solution quality of the multi objective OPF. In [24] a squirrel search algorithm is applied to solve the economic dispatch considering practical constraints such as the valve loading effect and multiple fuels. In [25] a novel variant based grey wolf optimizer (GWO) namely, crisscross search based GWO (CS-GWO) is proposed to solve the OPF considering several objective functions. In [26] the whale optimizer is adapted and applied to solve the dynamic economic emission dispatch. In [27] a slime mould algorithm is proposed to solve the stochastic optimal power flow based wind energy and considering static VAR compensators. In [28] a hybrid algorithm based on combing the genetic algorithm and the salp swarm algorithm to solve the simultaneous allocation of multiple distribution generation and shunt compensators to improve the performances of radial distribution systems.

Recently, a new optimizer tool based metaheuristic concept namely artificial ecosystem optimizer (AEO) has been proposed by in [29]. AEO is inspired from the interactive flow of energy in an ecosystem on the earth. The robustness of the proposed mechanism search based AEO has been validated on many categories of test benchmark functions and practical engineering problems [29]. In the literature the standard AEO algorithm and a limited number of proposed variants based AEO have been applied to solve various practical optimization problems, however, a very limited number of variants based AEO have been proposed and applied to solve the active and reactive power management optimization problems without considering the integration of FACTS devices. Among these variants based AEO, in [30] the standard AEO is adapted to solve the reactive power management of many electric test systems such as the IEEE 30-Bus, the IEEE 118-Bus, the 300-Bus and the Algerian electric network 114-Bus, in this study, the bank compensators are the main compensator devices investigated to improve the performances of the reactive power management. In [31] the standard AEO is successfully investigated to solve the reconfiguration of radial distribution systems considering the integration of multi distributed generations (DGs) and multi bank capacitors. In [32] the AEO is designed and applied to solve the combined problem based optimal locations of photovoltaic (PV) and wind sources based DGs and compensator devices, and in [33] an enhanced AEO is designed and adapted to solve the optimal location of DGs to minimize the TPL in radial distribution systems. In this study an interactive variant based AEO is proposed to solve various multi objective power management problems considering the integration of multi SVC devices based FACTS technology. The main contributions achieved in this paper compared to the standard AEO and to other metaheuristic techniques are summarized in four points:

- a new variant named interactive AEO is proposed to solve the multi objective power management optimization problems;
- a dynamic interaction between production operator and consumer operator during search process is introduced to right balance between diversification and intensification;
- the proposed interactive artificial ecosystem optimizer (IAEO) is characterized by a flexible equilibrium during search process between intensification and diversification;
- the TFC, the TPL and the TVD are three main objective functions optimized individually and simultaneously;

• the proposed IAEO validated on two standard electric systems (IEEE-30-Bus and IEEE-57-Bus) and an effective comparative study and critical review with many methods have been elaborated to demonstrate the efficiency of the proposed IAEO.

Power management optimization. The task of power management optimization known also as OPF is to minimize one or multi objective functions. The equality $H(X, U) = 0$ and the inequality constraints $G(X, U) \le 0$ related to operation security of electric systems [5] must be satisfied. The mathematical formulation of the multi objective power management optimization is expressed as follow:

$$Min\ \{obj\_F_i\} = \\ = Min\ \{obj\_F_1, obj\_F_2, obj\_F_3, ..., obj\_F_{nobj}\}. \quad (1)$$

Subject to:

Power balance constraints: represents the balance of active and reactive power between production and demand

$$H(X,U)=0 \Leftrightarrow \begin{bmatrix} P_{gi} - P_{di} - V_i \sum_{j=1}^{N} V_j \left(g_{ij} \cos\delta_{ij} + b_{ij} \sin\delta_{ij}\right) = 0 \\ Q_{gi} - Q_{di} - V_i \sum_{j=1}^{N} V_j \left(g_{ij} \sin\delta_{ij} - b_{ij} \cos\delta_{ij}\right) = 0 \end{bmatrix} \quad (2)$$

Operation constraints: reflects technical admissible operation limits of various elements of electric networks

$$G(X,U) \le 0 \Leftrightarrow \begin{bmatrix} V_{gi}^{\min} \le V_{gi} \le V_{gi}^{\max} \\ P_{gi}^{\min} \le P_{gi} \le P_{gi}^{\max} \\ Q_{gi}^{\min} \le Q_{gi} \le Q_{gi}^{\max} \\ T_i^{\min} \le T_i \le T_i^{\max} \\ Q_{svci}^{\min} \le Q_{svci} \le Q_{svci}^{\max} \\ \\ V_{Li}^{\min} \le V_{Li} \le V_{Li}^{\max} \\ S_{li} \le S_{li}^{\max} \end{bmatrix}. \quad (3)$$

The vectors X and U are expressed as:

$$X^T = \left[\delta, V_L(1...N_{PQ}), P_{gs}, Q_g(1...N_{PV})\right]; \quad (4)$$

$$U^T = \left[P_g(1...N_{PV}), V_g(1...N_{PV}), Q_{svc}(1...N_{svc}), T(1...N_T)\right]. \quad (5)$$

Various objective functions.

TFC minimization. The objective function associated to the TFC is expressed as follows.

$$OBJ_1(X,U) = \min(TFC) = \min\left(\sum_{i=1}^{NG}\left(a_i + b_i P_{gi} + c_i P_{gi}^2\right)\right), \quad (6)$$

where NG is the number of thermal generating units; P_{gi} is the real power of the ith generator; a_i, b_i, and c_i are the cost coefficients of the ith generator.

TVD minimization. The objective function associated to the TVD is expressed as:

$$OBJ_2(X,U) = \min(TVD) = \min\left(\sum_{i\in NL} |V_i - V_{des}|\right), \quad (7)$$

where V_{des} is the desired voltage magnitudes at all load buses.

TPL minimization. The objective function associated to the TPL is formulated as follow:

$$OBJ_3(X,U) = \min(TPL) = \\ = \min\left(\sum_{k=1}^{N_l} g_k \left[(t_k V_i)^2 + V_j^2 - 2 t_k V_i V_j \cos\delta_{ij}\right]\right). \quad (8)$$

TFC minimization in coordination with TVD. The objective function based on combining the TFC and the TVD is modelled using the following equation.

$$OBJ_4(X,U) = Min\left(\left(\sum_{i=1}^{NG}\left(a_i + b_i P_{gi} + c_i P_{gi}^2\right)\right) + \beta.(TVD)\right), \quad (9)$$

where β is a balancing factor.

Constraints management. Modified objective function is formulated using the following expression [18]:

$$OBJ_{\text{mod}}(X,U) = OBJ_i(X,U) + Pen; \quad (10)$$

$$Pen = \gamma_v \times \sum_{i=1}^{N_{PQ}} \left(V_{Li} - V_{Li}^{\lim}\right)^2 + \gamma_Q \times \sum_{i=1}^{N_{PV}} \left(Q_{gi} - Q_{gi}^{\lim}\right)^2 + \\ + \gamma_{Ps} \times \left(P_{gs} - P_{gs}^{\lim}\right)^2 + \gamma_{br} \times \sum_{i=1}^{Nl} \left(S_{bri} - S_{bri}^{\lim}\right)^2, \quad (11)$$

where γ_v, γ_Q, γ_{Ps} and γ_{br} are the penalty coefficients related to state variables [5].

Static Var Compensator (SVC) model. The SVC device is one of shunt compensators from the family of FACTS. As well shown in Fig. 1, the principle of SVC device consists in controlling the voltage magnitude at specified bus absorbing or injecting reactive power. The expression of reactive power Q_i^{SVC} controlled by the SVC device is given as follow:

$$Q_i^{SVC} = -B_{SVC} \cdot V_i^2. \quad (12)$$

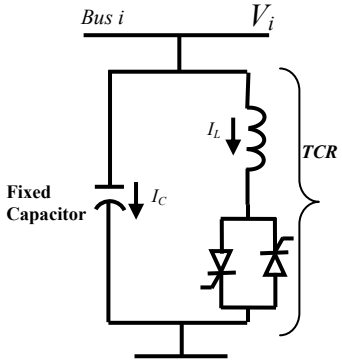

Fig. 1. Basic structure of the SVC

Basic structure of AEO. Recently in [29], authors developed a new optimizer tool based on ecosystem concept namely AEO. The standard AEO mimics the behavior of energy flow in an ecosystem. The basic architecture of the standard AEO is shown in Fig. 2, and the key steps of the AEO are described in the following:

• the main structure of AEO consists of three interactive operators organized based on their energy level;

• in the population, there is only one operator named the Producer which represents the plants in nature. Only one decomposer operator which is known as bacteria and fungi, and the remaining of individuals in the population are designed as consumers known in nature as animals selected as carnivores, herbivores or omnivores;

- the fitness function designed to evaluate all individuals is based on the level of their energy. High level of energy indicates that the selected individual will be the best candidate solution;
- the main task of the producer operator is dedicated to create balance between exploration and exploitation; however the consumer operators are oriented to execute intensification in coordination with the decomposer operator at specified iterations.

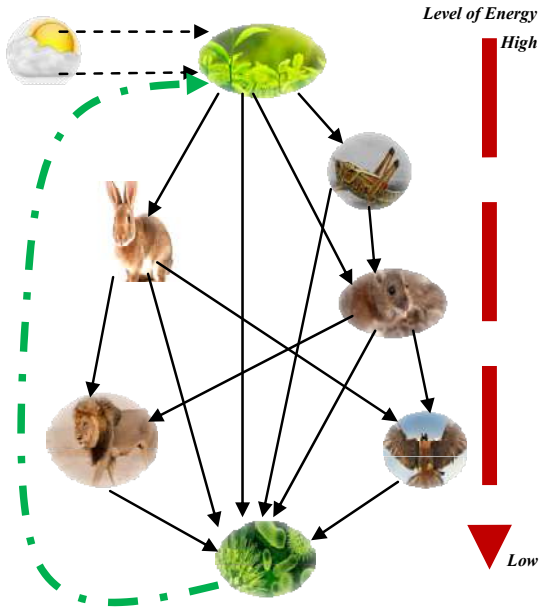

Fig. 2. Basic structure of an ecosystem

Mathematical modeling of AEO. Based on the flowchart shown in Fig. 3, the operators of the standard AEO are described as follows.

Production operator: based on the original AEO [29], the task of the producer operator in an ecosystem is to generate food energy. The evolution of production operator is modeled using the following mathematical expressions:

$$X_1(it+1) = (1-a)\times X_n(it) + a \times X_{rand}(it); \quad (13)$$

$$a = (1 - it/T_{\max}) \cdot r_1; \quad (14)$$

$$X_{rand} = r \cdot (U_{\max} - U_{\min}) + U_{\min}, \quad (15)$$

where it is the current iteration; X_n is the better candidate found so far; $T_{\max}$ is the maximum number of iterations; $U_{\max}$ and $U_{\min}$ are the maximum and the minimum limits of control variables, respectively; r_1 and r are two random number within the limits [0, 1]; a is the linear weight factor; X_{rand} is the random position of an individual.

Consumer operator: The consumers operations are modeled as follows.

For herbivore individuals, the evolution of a random consumer in the search space is modeled using the following equation:

$$X_i(it+1) = X_i(it) + CF \times (X_i(it) - X_1(it)), \quad i \in \{2,.....,n\}, \quad (16)$$

where CF is a consumption factor defined as follows:

$$CF = \frac{1}{2} \cdot \frac{v_1}{|v_2|}; \quad (17)$$

$$v_1 \sim N(0,1), \; v_2 \sim N(0,1). \quad (18)$$

For carnivore individuals, mathematically, the behavior of the evolution of carnivores on the search space is modeled as follows:

$$\begin{cases} X_i(it+1) = X_i(it) + CF \times (X_i(it) - X_j(it)), & i \in \{3,.....,n\}; \\ j = RANDi \;\; ([2i-1]). \end{cases} \quad (19)$$

For omnivore individuals, it is can each both randomly a consumer with the higher energy level and a producer. The behavior of an omnivore consumer is modeled as follows:

$$\begin{cases} X_i(it+1) = X_i(it) + CF \times (r_2 \times (X_i(it) - X_1(it))); \\ + (1-r_2) \times (X_i(it) - X_j(it)), \;\; i = 3,...,n; \\ j = RANDi \;\; ([2\,i-1]). \end{cases} \quad (20)$$

Decomposer operator: The equation describing the decomposition behavior is expressed as follows:

$$\begin{cases} X_i(it+1) = X_n(it) + D \times (E \times X_n(it) - H \times X_i(it)), \\ i = 1,\ldots,n; \end{cases} \quad (21)$$

$$D = 3 \times u, \quad u \sim N(0,1); \quad (22)$$

$$E = r_3 \times RANDi \;\; ([1 \quad 2]) - 1; \quad (23)$$

$$H = 2 \times r_3 - 1, \quad (24)$$

where D is the decomposition factor; E and H are the weight coefficients; u is the normal distribution with the mean = 0 and the standard deviation = 1.

Algorithm 1: Pseudo code of the standard AEO [29]

1 Input setting variables of AEO: Pop_size, Iter_max, Trial_max, Dim, ub, lb
2 Generating a population randomly X_i (solutions), evaluate the fitness Fit_i, and select the best solution found so far X_{best}
3 **While** Iter_max and Trial_max not reached do
//Production operator //
4 **For** individual X1, update its solution using eq. **13**
//Consumption operator //
5 **For** each individual Xi (i=2,...,n),
// Herbivore operator//
6 **If** rand<1/3 then update its solution using eq.**16**,
// Omnivore operator //
7 **Else If** 1/3< rand< 2/3 then update its solution using eq.**19**,
// Carnivore operator //
8 ***Else*** update its solution using eq. **20**,
9 ***End If***.
10 ***End If***.
11 Evaluate the fitness of each individual.
12 Update the best solution achieved so far X_{best}.
// Decomposition operator//
13 Update the position of each individual using equation (**21**).
14 Calculate the fitness of each individual.
15 Update the best solution found so far X_{best}.
16 ***End*** While
17 ***Return*** X_{best}

Strategy of the proposed IAEO based optimal power management. The strategy of the proposed IAEO designed for solving various OPF managements is focused to create interactive equilibrium between diversification and intensification.

Exploration phase. Three coordinated subsystems are designed to accomplish the exploration phase. The first subsystem consists of active powers of generating units, the second subsystem consists of voltage magnitudes of generators and the third subsystems contains the decision variables associated to tap transformers. Figure 3 shows the three decision variables associated to the exploration phase.

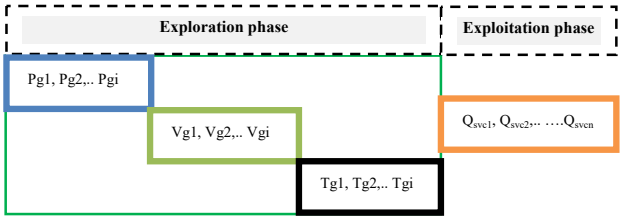

Fig. 3. Decision variables designed for exploration and exploitation phases

The steps of the diversification phase are described as follows.

Stage 1: the task of the first subsystem is designed to optimize only the decision variables associated to active power of generators. The first optimized decision variables achieved during the first stage is identified as Sub1_PG.

Stage 2: the task of the second subsystem is focused to optimize the decision variables related to the voltage magnitudes of thermal generators by considering the Sub1_PG as an initial solution. The second optimized control variables achieved during this stage is named Sub2_VG.

Stage 3: the task of the third subsystem to be optimized is oriented to optimize the decision variables associated to tap transformers by considering Sub1_PG and Sub2_VG as an initial solution. The third optimized control variables found during this third stage is identified as Sub3_T.

Exploitation phase. The task of the intensification phase is to optimize the decision variables associated to reactive power of multi SVC devices by considering the three optimized sub systems such as: Sub1_PG, Sub2_VG, and Sub3_T achieved during the diversification phase.

In this paper, the maximum number of generation and the population size related to this stage are taken 150 and 20 respectively, these values chosen carefully by experience and in general depend on the type of the test system to be solved.

Proposed interactive search process. In the proposed new variant named IAEO, an interactive search process is introduced to improve the solution quality, two modifications are proposed.

The first modification is related to the dynamic evolution of the weight coefficient during search task. The weight factor is controlled during the search process using the following expression:

$$a = \left(1 - \sin(it/T_{\max})\right) \times rand_{\,1}. \qquad (25)$$

The evolution of the weight coefficient for one run is shown in Fig. 4.

The second modification introduced focused on updating the evolution of production operator during search process using the following mathematical expressions:

$$X_1(it+1) = (1-a) \times X_n(it) + a \times X_{rand}(it); \qquad (26)$$

$$\begin{aligned} &\text{If } It < It_c \quad X_{rand} = r \times (U_{\max} - U_{\min}) + U_{\min}; \\ &\text{if } It > Itc \quad X_{rand} = r \times (best\_Pop\_Sol - U_{\min}) + U_{\min}, \end{aligned} \qquad (27)$$

where It_c is the critical iteration chosen by experience, it depends on the problem to be solved, in this study, It_c is taken between 10 to 20; *best_Pop_Sol* is the best solution found so far.

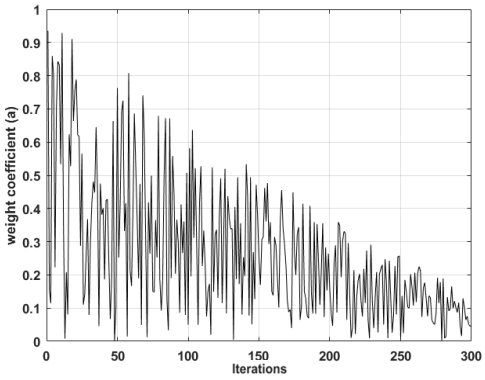

Fig. 4. Evolution of weight coefficient *a* during search process

Solution steps of the proposed IAEO strategy.

Based on the interactive of the proposed IAEO presented in Fig. 4, the following steps are required to apply the proposed IAEO to solve the OPF with various objective functions:

Step 1: Introduce the data related to eclectic network such as, fuel cost coefficients of generating units, lines and buses technical characteristics, load parameters, and all security and operation limits such as, permissible limits of voltages of generators and PQ-buses, permissible limits of tap transformers, and limits of reactive power of multi SVC.

Step 2: Identify the dimension of all subsystems to be optimized, the sub system for active power generation (Sub1_PG), the sub system for voltage magnitudes of PV bus (Sub2_VG), the sub system for tap transformers (Sub3_TP), and the sub system for reactive power of shunt SVC devices (Sub4_Qsvc).

Step 3: Define parameters of IAEO algorithm associated to each sub system.

Step 4: Execute the exploration phase based IAEO for solving the three subsystems: [Sub1_PG Sub2_VG Sub3_T].

Step 5: Define parameters of the algorithm for the forth subsystem Sub4_QSVC designed to elaborate the exploitation phase.

Step 6: Elaborate the exploitation phase, and save the new updated global decision variables: [Sub1_PG Sub2_VG Sub3_T Sub4_Qsvc]

Step 7: Repeat all steps until $Trial_{\max}$ is achieved

Cases studies. This section is focused in applying the proposed new variant namely IAEO to optimize various objective functions based OPF management. Two practical test systems are considered to validate the efficiency of the proposed variant. The IEEE-30-bus, and the IEEE-57-bus electric systems. In this study, and for fair comparison with other methods, the initial security limits of SVC devices for the test system IEEE 30-Bus is taken in the limits [–5, 5] MVAr, and for IEEE 57-Bus is taken in the limits [–20, 20] MVAr. Various objective functions such as, TFC, the TPL and the TVD have been optimized individually and in coordination.

Test-1: IEEE-30-Bus. The standard electric IEEE-30-Bus test system consists of 30 bus and 41 lines, the total load demand to satisfy at normal exploitation is (283.4+j126) MVA. The admissible limits of PQ-buses and PV-buses are in the limits [0.95, 1.1] p.u. The admissible limits of the four tap transformers are in the limits [0.9, 1.1] p.u., nine SVC have been integrated on buses (10, 12, 15, 17, 20, 21, 23, 24, 29), details technical data can be verified in [32]. For this electric network, six

cases have been elaborated to validate the efficacy of the proposed power management optimization based IAEO.

Case-1: TFC improvement.
Case-2: TPL improvement.
Case-3: TVD improvement.
Case-4: TFC and TPL improvement.
Case-5: TPL and TVD improvement.
Case-6: TFC and TVD improvement.

Case-1: TFC improvement. In this case, the proposed algorithm namely IAEO is applied to find the best fuel cost. Four vectors of control variables such as real power and voltages of thermal generators, tap transformers, and shunt compensators based SVC devices have been optimized. In order to create diversity in search space, four vector of decision variables (PG, VG, TP and Qsvc) are optimized based on interactive mechanism search. Figures 5,*a-c* show the convergence characteristics related to the three stages, it is found that the best cost is improved from stage to stage.

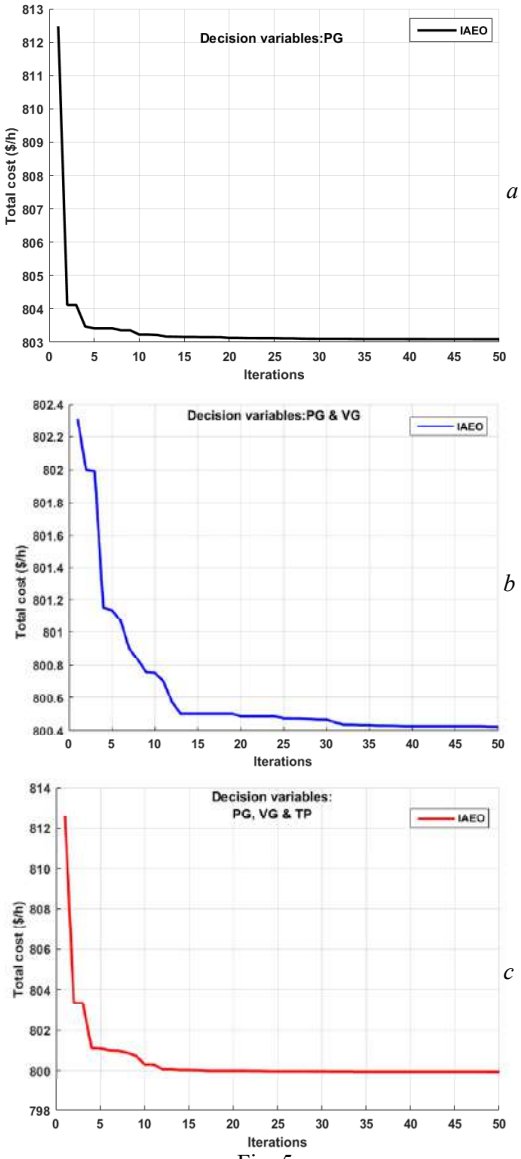

Fig. 5.
a – convergence behavior of TFC minimization using IAEO at stage 1 (decision variables PG) for IEEE-30-Bus;
b – convergence behavior of TFC minimization using IAEO at stage 2 (decision variables PG and VG) for IEEE-30-Bus;
c – convergence behavior of TFC minimization using IAEO at stage 3(decision variables PG, VG and TP) for IEEE-30-Bus

For this first case, and as well depicted in Table 1, the optimized TFC achieved at the final phase is 798.9457 $/h, which is better compared to the results found using various recent methods. The convergence behavior of the TFC minimization at the final stage is shown in Fig. 6. The profiles of voltages are shown in Fig. 11. As well shown in Table 2, the proposed IAEO variant outperforms many optimization techniques.

Table 1
The main optimized decision variables for IEEE-30-bus test system

Decision variables	Case-1	Case-2	Case-3	Case-4	Case-5	Case-6
P_{g1}	176.9702	51.2353	143.6338	150.9415	54.1571	165.6028
P_{g2}	48.3087	80.0000	29.6343	53.4670	79.8185	51.4071
P_{g5}	21.2048	50.0000	46.2980	26.2350	49.9782	24.8121
P_{g8}	21.5845	35.0000	27.6480	25.9711	34.5076	23.5360
P_{g11}	11.8614	30.0000	26.4342	16.8140	29.6331	12.3987
P_{g13}	12.0379	40.0000	16.3812	16.8992	38.9481	15.2052
V_{g1}	1.1000	1.0999	1.0125	1.1000	1.0127	1.0127
V_{g2}	1.0876	1.0976	1.0038	1.0876	1.0040	1.0040
V_{g5}	1.0612	1.0799	1.0135	1.0612	1.0137	1.0137
V_{g8}	1.0690	1.0871	1.0020	1.0690	1.0022	1.0022
V_{g11}	1.1000	1.0999	1.0515	1.1000	1.0517	1.0517
V_{g13}	1.1000	1.0999	1.0137	1.1000	1.0139	1.0139
T_{11}	1.0380	1.0438	1.0701	1.0405	1.0729	1.0692
T_{12}	0.9069	0.9142	0.9013	0.9094	0.9041	0.9004
T_{15}	0.9748	0.9813	0.9777	0.9773	0.9805	0.9768
T_{36}	0.9653	0.9707	0.9717	0.9678	0.9745	0.9708
Q_{svc10}	4.8612	4.8518	3.1553	4.5818	3.1955	2.8531
Q_{svc12}	4.7156	3.1956	4.1130	4.2198	4.5578	4.3988
Q_{svc15}	4.9608	2.9111	2.4363	4.9965	2.4236	2.3942
Q_{svc17}	4.8951	4.8909	4.1329	4.0765	4.1939	3.8261
Q_{svc20}	4.2697	3.7933	4.0801	4.3004	4.0587	4.0095
Q_{svc21}	4.9608	4.9008	4.6292	4.9965	4.6050	4.5491
Q_{svc23}	4.1186	2.6759	4.6118	4.1482	4.5876	4.5320
Q_{svc24}	4.5288	4.9008	4.4672	4.2328	4.3305	3.8259
Q_{svc29}	2.7809	2.5299	4.0889	1.8013	4.0675	3.0218
TPL, MW	8.5675	**2.835300**	6.6294	**6.9278**	**3.6426**	9. 5619
TFC, $/h	**798.9457**	967.0310	860.9828	**805.5460**	964.2807	**807.0926**
TVD, p.u.	1.9582	2.0747	**0.1098**	1.8877	**0.1204**	**0.1348**

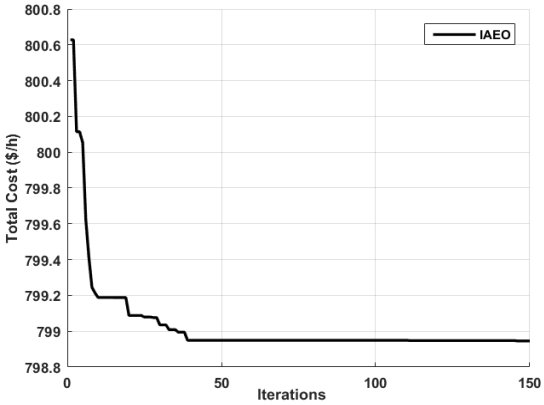

Fig. 6. Convergence behavior for TFC minimization using IAEO at the final stage for IEEE-30-Bus

Table 2

Comparison results of TFC minimization: test system IEEE-30-Bus: Voltage of PQ bus limits [0.95, 1.1] (p.u.)

Methods referenced in: [4, 5, 18]	TFC, $/h	TPL, MW	TVD, p.u.
TLBO	799.0715	–	–
GSA	798.6751*	–	–
DSA	799.0943	–	–
BBO	799.1116	–	–
DE	799.2891	–	–
SA	799.4500	–	–
AGAPOP	799.8441	–	–
BHBO	799.9217	–	–
EM	800.0780	–	–
EADHDE	800.1579	–	–
EADDE	800.2041	–	–
PSO	800.4100	–	–
FPSO	800.7200	–	–
IGA	800.8050	–	–
PSO	800.9600	–	–
GAF	801.2100	–	–
ICA	801.8430	–	–
EGA	802.0600	–	–
TS	802.2900	–	–
MDE	802.3760	–	–
IEP	802.4650	–	–
EP	802.6200	–	–
RGA	804.0200	–	–
GM	804.8530	–	–
GA	805.9400	–	–
GWO	–	2.9377	–
ABC	–	3.0410	–
ICEFO	799.0343	–	–
Proposed IAEO	**798.9457**	**2.8353**	**0.1098**

Case-2: TPL improvement. In this second case, the TPL is considered for optimization. Also, four control decision variables have been optimized in coordination. The TPL has an economic and technical aspect. Network with high losses in lines will affect the reliability of electric system in particular at critical situation. Figures 7,*a-c* show the convergence behavior related to TPL minimization for the three stages. It is found that the best TPL is improved from stage to stage. For this second case, and as well shown in Table 1, the TPL is optimized at a competitive value 2.8353 MW which is better than the result found using standard AEO and also compared to several recent methods. As well depicted in Table 1, and by optimizing the TPL, the corresponding TFC is increased to 967.031 $/h, and the TVD takes the value 2.0747 p.u., this clearly proves the conflict aspect between the three objective functions.

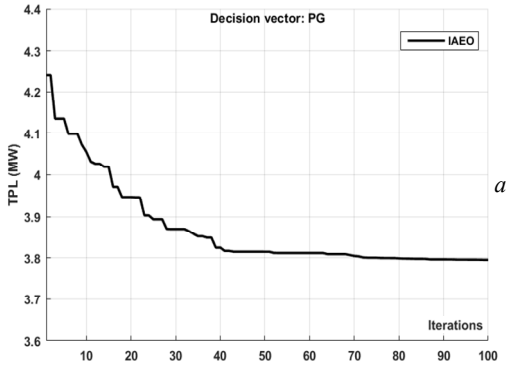

a

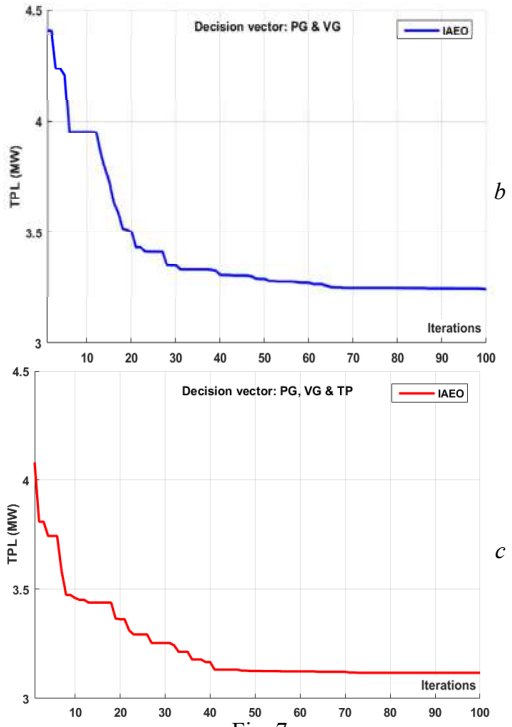

b

c

Fig. 7.
a – convergence behavior of TFC minimization using IAEO at stage 1 (decision variables PG) for IEEE-30-Bus;
b – convergence behavior of TFC minimization using IAEO at stage 2 (decision variables PG and VG) for IEEE-30-Bus;
c – convergence behavior of TFC minimization using IAEO at stage 3(decision variables PG, VG and TP) for IEEE-30-Bus

The convergence behavior of the TPL minimization at the final stage is shown in Fig. 8. The profile of voltage magnitudes obtained after optimization is shown in Fig. 11. It is clear that all the voltages at all PV and PQ-buses are within their permissible limits.

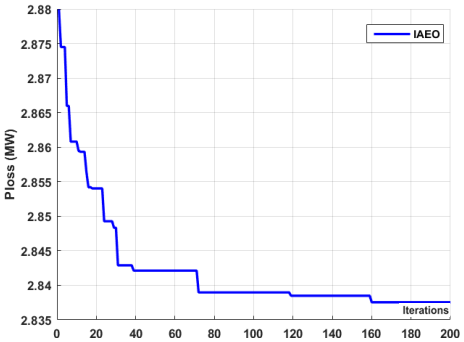

Fig. 8. Convergence behavior of TPL minimization using IAEO at the final stage for IEEE-30-Bus

Case-3: TVD improvement. The TVD is also an important index of power quality to evaluate the reliability of electric system. In this third case, the best TVD optimized at the final stage is improved to 0.1098 p.u., as a consequence the TFC is increased to 860.9828 $/h, and the TPL is also increased to 6.9278 MW. This proves the conflict aspect between TVD minimization and other objective functions. The convergence characteristics of TVD improvement during the three successive stages are shown in Fig. 9,*a-c*.

The convergence behavior at the final stage is shown in Fig. 10. It is important to confirm that, all optimized results are found at a reduced number of iteration and trials.

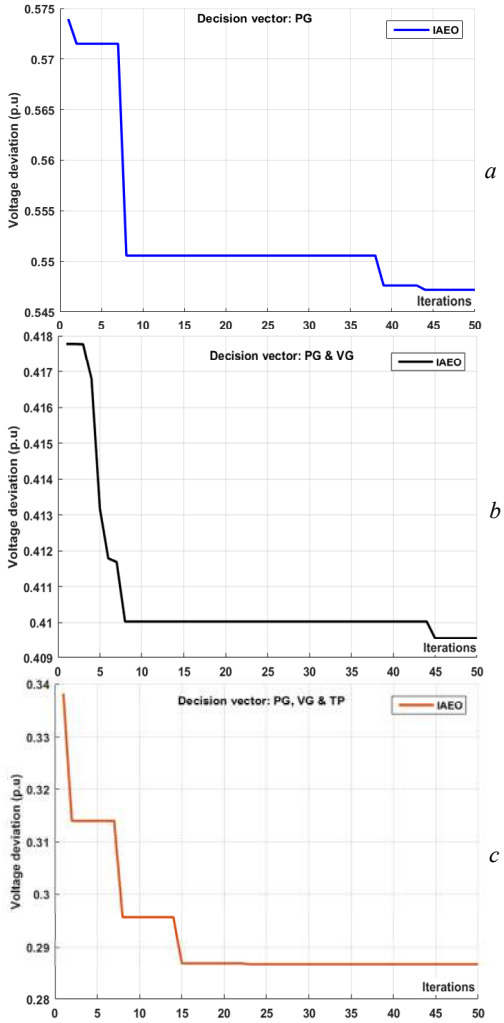

Fig. 9.
a – convergence behavior of TVD minimization using IAEO at stage 1 (decision variables PG) for IEEE-30-Bus;
b – convergence behavior of TVD minimization using IAEO at stage 2 (decision variables PG and VG) for IEEE-30-Bus;
c – convergence behavior of TVD minimization using IAEO at stage 3 (decision variables PG, VG and TP) for IEEE-30-Bus

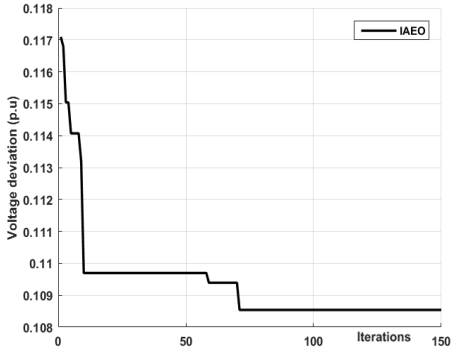

Fig. 10. Convergence behavior of TVD minimization using IAEO at the final stage for IEEE-30-Bus

The profiles of voltage magnitudes obtained after optimization are shown in Fig. 11.

Case-4: TFC and TPL improvement. Based on detailed results depicted in Table 1, it is confirmed that when optimizing individually each objective function, the optimized primary objective function will affect the quality of other objective functions. For this pertinent reason, and in this case, the TFC is improved in coordination with the TPL, this allows expert to identify an adequate compromise solution based on specified technical and economic aspects. For this fourth case, the optimized TFC in coordination with TPL are 805.546 $/h, and 6.9278 MW and consequently the TVD takes the value 1.8877 p.u.

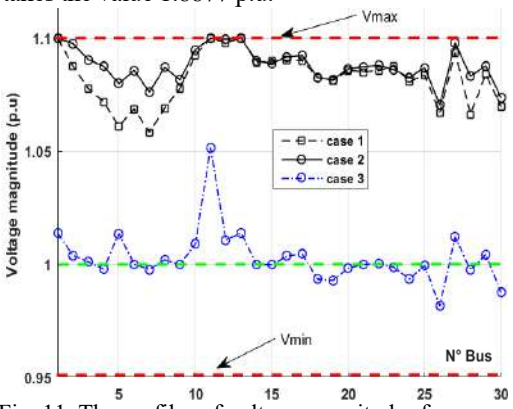

Fig. 11. The profiles of voltage magnitudes for cases: 1-2-3 for IEEE-30-Bus

Case-5: TPL and TVD improvement. One might think that improving the voltage magnitude will reduce the total power loss; this conclusion is relatively true when considering radial distribution system. However, in a meshed high transmission system, the improvement of TVD and TPL may be conflict. Also, it is important to optimize the TPL in coordination with TVD. For this case, the optimized values of TPL and TVD become 3.6426 MW and 0.1204 p.u., respectively, as a consequence the TFC achieves the value 964.2807 $/h. As well shown in Table 3, it is important to confirm that there is no violation of constraints of reactive power associated to all generating units.

Case-6: TFC and TVD improvement. As well demonstrated in case 1 when the TFC is optimized at a competitive value (798.9457 $/h), as a consequence the TVD takes high value (1.9582 p.u.). In this case, the main objective is to find a compromise solution between the TFC and the TVD which may be considered as an important issue for decision maker to ensure right equilibrium between economic and technical constraints imposed to utilities. Ensuring efficient TVD without affecting greatly the TFC has a positive impact on power quality. In this case, the optimized TVD is obtained by efficient coordination between the three suboptimal solutions found during the three stages associated to three decision variables. The best optimized TFC and TVD achieved at the last stage are 807.0926 $/h and 0.1348 p.u., respectively. As well shown in Table 3, there is no violation of security limits associated to reactive power of thermal generating units.

Test-2: IEEE-57-bus. The efficiency and particularity of the proposed OPF management based IAEO is also validated on the IEEE-57-bus. Details technical data of the IEEE-57-bus in terms of cost coefficients, lines and buses data can be retrieved from [34]. The total apparent power to satisfy is (1250.8 + j336.4) MVA, the maximum and minimum limits of tap setting transformers are in the limits [0.90, 1.1] in p.u., the permissible voltage limits of generating units are in the limits [0.95, 1.1] p.u., and the minimum and maximum bounds of PQ buses are taken in the limits [0.95, 1.1] p.u., however for fair comparison with other techniques, the security limits of voltage magnitudes at PQ buses are also considered to be in the limits [0.95, 1.05]. The IEEE-57-bus electric network consists of a

total of 34 decision variables, including 14 variables related to PV buses, 17 tap transformers, and 3 capacitor banks. In this study three SVC devices are used. To improve the solution quality of the various OPF problems, three objective functions have been optimized such as the TFC, the TPL and the TVD.

Table 3

Values of reactive power of generating units after optimization: cases 1 to 6

State variables, MVAr	Q_{Gmin}, MVAr	Q_{Gmax}, MVAr	Case-1	Case-2	Case-3	Case-4	Case-5	Case-6
Q_{G1}	–20	200	–16.4008	–10.0181	–20.0000	–10.5765	–3.0497	–20.0000
Q_{G2}	–20	100	21.7922	8.3262	–3.5263	16.4079	–20.0000	–6.5415
Q_{G5}	–15	80	26.6227	21.9110	49.0411	24.4629	45.8506	57.9317
Q_{G8}	–15	60	31.5658	31.0241	35.4018	28.4477	27.4492	41.6220
Q_{G11}	–10	50	11.8436	10.5031	26.7630	12.9860	27.4764	26.9296
Q_{G13}	–15	60	1.6210	1.1132	2.3241	2.9223	1.9628	2.7053

Case-7: TFC improvement. For this case, two scenarios are considered. In the first scenario, the security limits of voltages of generators are taken in the limits [0.95, 1.1], the optimized TFC achieved is 41638.6742 ($/h) which is better compared to the results found from other recent methods such as: Improved Chaotic Electromagnetic Field optimization (ICEFO), Electromagnetic Field Optimization (EFO), PSO, BBO, DE, and ABC. In the second scenario and for fair comparison with other techniques, the TFC is optimized by considering the voltage magnitudes limits in the limits [0.95, 1.05]. For this second scenario the optimized TFC is increased to 41684.00 $/h due to the new voltage constraints associated to PQ buses. Table 4 shows the optimized control variables using the proposed IAEO approach. Figure 12 shows the convergence of TFC minimization using IAEO at the final stage. The distributions of voltage magnitudes of TFC minimization for two scenarios are shown in Fig. 13. It is also important to confirm that all security constraints are satisfied.

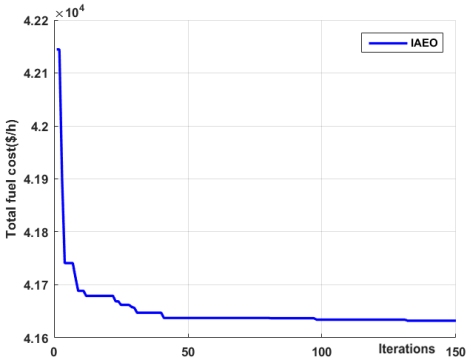

Fig. 12. Convergence behavior of TFC improvement using IAEO at the final stage for IEEE-57-bus electric system

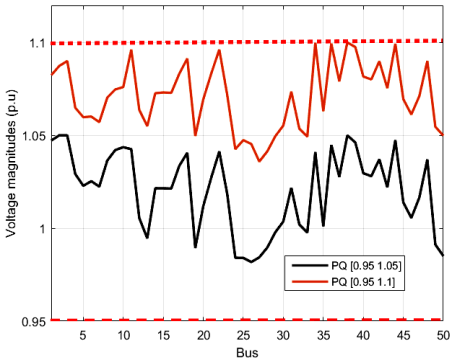

Fig. 13. The voltage profiles of IEEE-57-bus for TFC improvement

Table 4

Optimized decision variables for TFC minimization: Test-system-2: IEEE-57-bus: case-7

Control variables	Min	Scenario 1	Scenario 2	Max	Control variables	Min	Scenario 1	Scenario 2	Max
Pg1	0	142.4616	142.8434	575.88	T24-25	0.9	1.0926	1.0947	1.1
Pg2	0	87.8254	90.4059	100.00	T24-26	0.9	1.0229	1.0432	1.1
Pg3	0	44.7744	45.0471	140.00	T7-29	0.9	0.9837	1.0042	1.1
Pg6	0	72.1854	71.4206	100.00	T34-32	0.9	0.9598	0.9805	1.1
Pg8	0	461.9187	459.2815	550.00	T11-41	0.9	0.9072	0.9182	1.1
Pg9	0	96.5357	96.4080	100.00	T15-45	0.9	0.9621	0.9828	1.1
Pg12	0	359.3850	360.6297	410.00	T14-46	0.9	0.9481	0.9688	1.1
Vg1	0.95	1.0742	1.0588	1.1	T10-51	0.9	0.9567	0.9774	1.1
Vg2	0.95	1.0708	1.0566	1.1	T13-49	0.9	0.9207	0.9416	1.1
Vg3	0.95	1.0600	1.0496	1.1	T11-43	0.9	0.9549	0.9756	1.1
Vg6	0.95	1.0821	1.0565	1.1	T40-56	0.9	0.9910	1.0115	1.1
Vg8	0.95	1.1000	1.0600	1.1	T39-57	0.9	0.9607	0.9814	1.1
Vg9	0.95	1.0696	1.0373	1.1	T9-55	0.9	0.9744	0.9950	1.1
Vg12	0.95	1.0650	1.0429	1.1	Q_{SVC18} (MVAr)	0	6.0099	5.2929	20
T4-18	0.9	0.9530	0.9737	1.1	Q_{SVC25} (MVAr)	0	14.3869	15.7339	20
T4-18	0.9	0.9792	0.9998	1.1	Q_{SVC53} (MVAr)	0	11.7961	12.5047	20
T21-20	0.9	1.0094	1.0298	1.1					
T24-25	0.9	0.9628	0.9835	1.1					
TFC, $/h		**41638.6742**	**41684.00**						
TPL, MW		14.2861	15.2362						
TVD, p.u.		3.3403	1.2506						
Voltage of PQ bus limits, p.u.		**[0.95, 1.1]**	**[0.95, 1.05]**				**[0.95, 1.1]**	**[0.95, 1.05]**	

Case-8: TPL improvement. Two scenarios are considered to improve the TPL. In the first scenario and by considering the limits of voltages of PQ buses in the limits [0.95, 1.1] p.u., the best TPL found using IAEO is 9.288 MW which is better compared to results found from others techniques [18]. However, in the second scenario, when the margin security of voltages of PQ buses are [0.95 1.05] p.u., the TPL achieved becomes 10.1677 MW. The values of optimized decision variables such as real power and voltage magnitudes of generators, tap transformers, and reactive power of SVC devices installed at buses (18, 25, and 53) are depicted in Table 5.

The convergence behavior of TPL improvement in the last stage for scenario 1 is shown in Fig. 14. The profile of voltages at all PQ-buses for the two permissible voltage magnitude limits [0.95, 1.1] p.u. and [0.95, 1.05] p.u. are shown in Fig 15. It is clear that the proposed IAEO gives better results in terms of solution quality and also convergence behaviours.

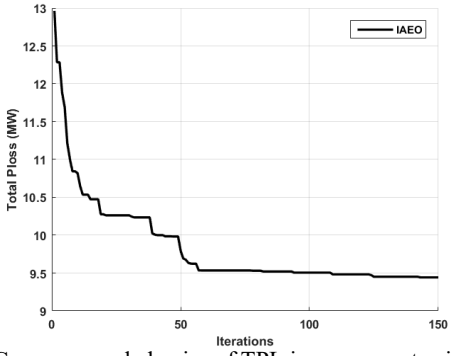

Fig. 14. Convergence behavior of TPL improvement using IAEO at the final stage for IEEE-57-bus electric system

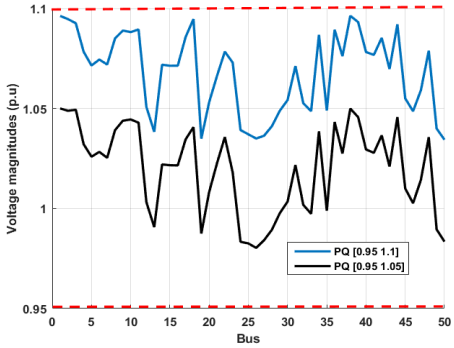

Fig. 15. The profile of voltages for IEEE-57-bus for TPL minimization

Table 5

Optimized decision variables for Test-system-2: IEEE-57-bus: case-8

Decision variables	Min	Scenario 1	Scenario 2	Max	Control variables	Min	Scenario 1	Scenario 2	Max
Pg1	0	199.0713	200.5999	575.88	T24-25	0.9	1.1000	1.0988	1.1
Pg2	0	4.236000	2.5244	100.00	T24-26	0.9	1.0485	1.0473	1.1
Pg3	0	139.3166	139.2099	140.00	T7-29	0.9	1.0095	1.0083	1.1
Pg6	0	99.99220	99.9989	100.00	T34-32	0.9	0.9858	0.9846	1.1
Pg8	0	307.4738	308.6348	550.00	T11-41	0.9	0.9235	0.9223	1.1
Pg9	0	99.99910	99.9998	100.00	T15-45	0.9	0.9881	0.9869	1.1
Pg12	0	409.9993	409.9999	410.00	T14-46	0.9	0.9741	0.9729	1.1
Vg1	0.95	1.1000	1.0587	1.1	T10-51	0.9	0.9827	0.9815	1.1
Vg2	0.95	1.0953	1.0523	1.1	T13-49	0.9	0.9469	0.9457	1.1
Vg3	0.95	1.1000	1.0539	1.1	T11-43	0.9	0.9809	0.9797	1.1
Vg6	0.95	1.0985	1.0532	1.1	T40-56	0.9	1.0168	1.0156	1.1
Vg8	0.95	1.1000	1.0600	1.1	T39-57	0.9	0.9867	0.9855	1.1
Vg9	0.95	1.0836	1.0397	1.1	T9-55	0.9	1.0003	0.9991	1.1
Vg12	0.95	1.0913	1.0454	1.1	Q_{SVC18}(MVAr)	0	5.8044	6.0732	20
T4-18	0.9	0.9790	0.9778	1.1	Q_{SVC25}(MVAr)	0	16.2454	16.5142	20
T4-18	0.9	1.0051	1.0039	1.1	Q_{SVC53}(MVAr)	0	13.0162	13.2850	20
T21-20	0.9	1.0351	1.0339	1.1					
T24-25	0.9	0.9888	0.9876	1.1					
TFC, $/h		44936.637	44976.00						
TPL, MW		**9.2880**	**10.1677**						
TVD, p.u.		3.3893	1.2496						
Voltage of PQ bus limits, p.u.		**[0.95, 1.1]**	**[0.95, 1.05]**				**[0.95, 1.1]**	**[0.95, 1.05]**	

Case-9: TVD improvement. As well shown in results found for TFC minimization, the TVD increases to a high value p.u., this confirms the conflict behaviour between TFC and TVD. For this case, the TVD is optimized individually, the optimized value of TVD achieved is 0.7613 p.u., as a consequence, the TFC and the TPL become, 43637.599 $/h, 12.6659 MW respectively. The convergence behavior of TVD minimization is shown in Fig. 16. The optimized decision variables are shown in Table 6. All security constraints are in their admissible bounds.

Table 7 shows detailed results related for generated reactive power for cases 7, 8, 9.

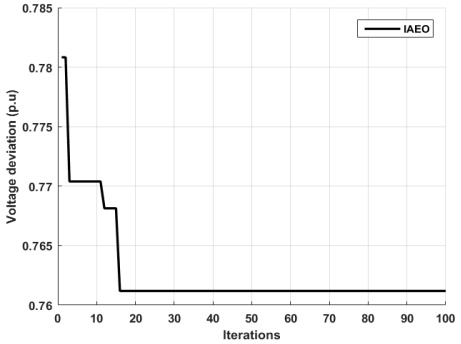

Fig. 16. Convergence behavior of TVD improvement using IAEO at the final stage for IEEE-57-bus electric network

Table 6

Optimized decision variables for Test-system 2: IEEE-57-bus: case-9

Decision variables	Min	Optimized	Max	Decision variables	Min	Optimized	Max
Pg1	0	253.2690	575.88	T24-25	0.9	1.0802	1.1
Pg2	0	35.1258	100.00	T24-26	0.9	1.0223	1.1
Pg3	0	84.8772	140.00	T7-29	0.9	0.9833	1.1
Pg6	0	69.7737	100.00	T34-32	0.9	0.9596	1.1
Pg8	0	333.2967	550.00	T11-41	0.9	0.9173	1.1
Pg9	0	91.3378	100.00	T15-45	0.9	0.9619	1.1
Pg12	0	395.7857	410.00	T14-46	0.9	0.9479	1.1
Vg1	0.95	1.0266	1.1	T10-51	0.9	0.9565	1.1
Vg2	0.95	1.0148	1.1	T13-49	0.9	0.9207	1.1
Vg3	0.95	1.0095	1.1	T11-43	0.9	0.9547	1.1
Vg6	0.95	1.0061	1.1	T40-56	0.9	0.9906	1.1
Vg8	0.95	1.0079	1.1	T39-57	0.9	0.9605	1.1
Vg9	0.95	0.9920	1.1	T9-55	0.9	0.9741	1.1
Vg12	0.95	1.0111	1.1	Q_{SVC18} (MVAr)	0	8.6025	20
T4-18	0.9	0.9528	1.1	Q_{SVC25} (MVAr)	0	19.2413	20
T4-18	0.9	0.9789	1.1	Q_{SVC53} (MVAr)	0	15.9510	20
T21-20	0.9	1.0089	1.1		-		
T24-25	0.9	0.9626	1.1				
TFC, $/h	43637.599						
TPL, MW	12.6659						
TVD, p.u.	**0.7613**						
Voltage of PQ bus limits, p.u.	**[0.95, 1.1]**						

Table 7

Values of reactive power of generating units after optimization: cases 7, 8, 9, for IEEE-57-bus electric system

State variables, MVAr	Q_{Gmin}, MVAr	Q_{Gmax}, MVAr	Case-7	Case-8	Case-9
Q_{G1}	–140	200	41.2497	25.1539	63.2333
Q_{G2}	–17	50	50.0000	50.0000	29.6884
Q_{G3}	–10	60	33.7970	30.6423	29.1474
Q_{G6}	–8	25	11.9570	–0.0081	5.3507
Q_{G8}	–140	200	31.8761	34.7790	27.0905
Q_{G9}	–3	9	8.7930	9.0000	3.8068
Q_{G12}	–150	155	55.4596	52.0659	73.4293

Comparative study and robustness evaluation. A comparative analysis is introduced to validate the performances and particularity of the proposed approach based IAEO designed to solve multi objective OPF. In the recent literature many several metaheuristic methods have been proposed to improve the solution quality of various OPF problems. It is found that some comparative studies are not adequate for one reason; the security limits associated to voltage of PQ-buses are not similar. In order to relieve conflicts about this subject, in this study, the OPF problem with various objective functions have been solved considering three types of constraints related to the voltage magnitudes of PQ-buses. In the first scenario, the security limits of voltage magnitudes of PQ-buses are taken in the limits [0.95, 1.1] p.u., in the second scenario, the admissible bounds of voltage magnitudes of PQ-buses are considered in the limits [0.95, 1.05] p.u., and in the third scenario the limits of voltage magnitudes of PQ-buses are taken in the limits [0.94, 1.06] p.u.. Table 8 shows a comparative analysis of statistical results for TFC, TPL and TVD minimization using the proposed method and other recent methods. The optimized results related to the first scenario are depicted in Table 6. These values are achieved by considering the voltage magnitudes of PQ buses in the limits [0.95, 1.1]. It is well demonstrated, that the proposed IAEO converges to a competitive value of TFC (41,638.6742 $/h) compared to other methods, expect the value of TFC achieved using the APFPA [18], otherwise, the TPL and TVD are also improved to a completive values, 9.28 MW, 0.7613 p.u., respectively.

Table 8

Comparative study: best results for TFC, TPL and TVD improvement for test system IEEE-57-bus: voltage magnitude at PQ-buses is in the limits [0.95, 1.1] p.u.

Methods: [6, 18, 20]	TFC, $/h	TPL, MW	TVD, p.u.
ICEFO	41,706.1117	–	–
EFO	41,706.3467	–	–
PSO	42,386.3675	–	–
BBO	41,698.9307	–	–
DE	41,689.7303	–	–
ABC	41,715.7607	–	–
APFPA	41,628.7520	9.3151	0.8909
CSSO	41,666.6620	–	–
Proposed method IAEO	**41,638.6742**	**9.2800**	**0.7613**

The results of the OPF for the second and third scenario are depicted in Table 9.

Table 9

Comparative study: best results for TFC, TPL and TVD improvement for electric system IEEE-57-bus: voltage magnitude at PQ-buses is in the limits [0.95, 1.05] p.u.

Methods [14, 21]	TFC, $/h	TPL, MW	TVD, p.u.	Observations
TLBO	41,688.7431	–	–	[0.95 1.05]
MTLBO	41,638.3822*	–	–	[0.95 1.05]
SKH	41,676.9152	10.6877	–	[0.94 1.06]
KH	41,681.3521	11.2158	–	[0.94 1.06]
Proposed method IAEO	**41,684.0000** **41,668.3663**	**10.1677** **9.9827**	**0.7613** –	[0.95 1.05] [0.94 1.06]

* Infeasible solution

The best TFC achieved using the proposed IAEO is compared to the results achieved using TLBO [14], MTLBO

[14], stud krill herd (SKH) algorithm [21], and the standard krill herd (KH) algorithm [21]. It is observed that the proposed IAEO algorithm achieves better optimal values compared to other methods, except the TFC achieved using MTLBO (41,638.3822 $/h), however, after verification by using the power flow tool, it is found that the obtained results are not feasible, violations of constraints in term of voltage magnitudes in several PQ buses. The proposed method named IAEO achieves better optimal TFC (41,668.3663 $/h) by considering the voltage magnitudes of PQ buses in the limits [0.94, 1.06] p.u., and by considering the voltage magnitudes of PQ buses in the limits [0.95, 1.05], the new optimized TFC values becomes 41,686.00 $/h. Tables 10, 11 show the optimal settings of decision variables achieved for TFC minimization and TPL improvement using the proposed IAEO method and the SKH method [14, 21].

Table 10

Optimal settings of decision variables of TFC minimization for Test-system-2: IEEE-57-bus: PQ-buses [0.94, 1.06] p.u.

Control variables	Min	IAEO	SKH [21]	Max	Control variables	Min	IAEO	SKH [21]	Max
Pg1	0	142.6746	142.8235	575.88	T24-25	0.9	1.0816	1.0782	1.1
Pg2	0	89.32490	90.4827	100.00	T24-26	0.9	1.0345	1.0257	1.1
Pg3	0	44.99740	45.1846	140.00	T7-29	0.9	0.9953	0.9895	1.1
Pg6	0	71.49150	71.8808	100.00	T34-32	0.9	0.9714	0.9691	1.1
Pg8	0	460.6816	459.2338	550.00	T11-41	0.9	0.9088	0.9008	1.1
Pg9	0	96.39720	96.1160	100.00	T15-45	0.9	0.9737	0.9740	1.1
Pg12	0	360.1558	360.1577	410.00	T14-46	0.9	0.9597	0.9591	1.1
Vg1	0.95	1.0570	1.0593	1.1	T10-51	0.9	0.9683	0.9649	1.1
Vg2	0.95	1.0551	1.0575	1.1	T13-49	0.9	0.9323	0.9310	1.1
Vg3	0.95	1.0489	1.0512	1.1	T11-43	0.9	0.9665	0.9657	1.1
Vg6	0.95	1.0595	1.0594	1.1	T40-56	0.9	1.0026	0.9937	1.1
Vg8	0.95	1.0747	1.0599	1.1	T39-57	0.9	0.9723	0.9629	1.1
Vg9	0.95	1.0451	1.0373	1.1	T9-55	0.9	0.9860	0.9846	1.1
Vg12	0.95	1.0414	1.0416	1.1	Q_{SVC18}, MVAr	0	5.6309	0.1580	20
T4-18	0.9	0.9646	0.9062	1.1	Q_{SVC25}, MVAr	0	14.0079	0.1563	20
T4-18	0.9	0.9908	1.0955	1.1	Q_{SVC53}, MVAr	0	11.4171	0.1380	20
T21-20	0.9	1.0210	1.0106	1.1					
T24-25	0.9	0.9744	0.9815	1.1					
TFC, $/h		**41,668.391696**	**41,676.9152**						
TPL, MW		14.923	15.0795						
TVD, p.u.		1.5901	–						
Voltage of PQ buses limits, p.u.	**[0.94, 1.06]**								

Table 11

Optimal settings of decision variables of TPL minimization for Test-system-2: IEEE-57-bus: PQ-buses [0.94, 1.06] p.u.

Control variables	Min	IAEO	SKH [21]	Max	Control variables	Min	IAEO	SKH [21]	Max
Pg1	0	203.4968	200.9220	575.88	T24-25	0.9	1.0823	1.0312	1.1
Pg2	0	2.282400	3.3270	100.00	T24-26	0.9	1.0508	1.0021	1.1
Pg3	0	137.2892	139.9317	140.00	T7-29	0.9	1.0118	0.9327	1.1
Pg6	0	99.99880	99.9470	100.00	T34-32	0.9	0.9881	0.9493	1.1
Pg8	0	307.7157	307.3602	550.00	T11-41	0.9	0.9258	0.9004	1.1
Pg9	0	99.99990	100.0000	100.00	T15-45	0.9	0.9904	0.9176	1.1
Pg12	0	409.9999	409.9996	410.00	T14-46	0.9	0.9764	0.9059	1.1
Vg1	0.95	1.0732	1.0023	1.1	T10-51	0.9	0.9850	0.9172	1.1
Vg2	0.95	1.0658	0.9957	1.1	T13-49	0.9	0.9492	0.9001	1.1
Vg3	0.95	1.0642	0.9987	1.1	T11-43	0.9	0.9832	0.9026	1.1
Vg6	0.95	1.0623	0.9983	1.1	T40-56	0.9	1.0191	1.0000	1.1
Vg8	0.95	1.0713	1.0012	1.1	T39-57	0.9	0.9890	0.9776	1.1
Vg9	0.95	1.0528	0.9795	1.1	T9-55	0.9	1.0026	0.9263	1.1
Vg12	0.95	1.0610	0.9855	1.1	Q_{SVC18}, MVAr	0	5.9720	0.0605	20
T4-18	0.9	0.9813	0.9643	1.1	Q_{SVC25}, MVAr	0	16.4130	0.1399	20
T4-18	0.9	1.0074	0.9004	1.1	Q_{SVC53}, MVAr	0	13.1838	0.1262	20
T21-20	0.9	1.0374	1.0096	1.1					
T24-25	0.9	0.9911	0.9759	1.1					
TFC, $/h		44,912.826117	45,044.2407						
TPL, MW		**9.9827**	10.6877						
TVD, p.u.		1.6011	–						
Voltage of PQ bus limits, p.u.	**[0.94, 1.06]**								

Robustness evaluation. The efficiency of the proposed variant namely IAEO has been validated on two practical electric systems, the IEEE-30-bus, and the IEEE-57-bus considering various objective functions. Compared to the standard algorithm (AEO), the proposed variant needs a reduced number of generations and trials

to converge to the best solution (100 to 150 generations, and between 5 to 10 trials). Also, due to the interactive decomposed concept based on optimizing a reduced number of decision variables, the proposed variant needs a small number of population and a reduced number of trials to explore the global search space. As well demonstrated on results given, the maximum number of iteration and population required to optimize all subsystems are 50 and 10, respectively. However in the last stage and to ensure fine intensification around the near optimal solution, the number of iteration required is relatively increased to 150.

Conclusion. This paper is elaborated to apply an efficient Interactive Artificial Ecosystem Algorithm (IAEO) to improve the solution quality of the multi objective OPF problem. Three objective functions such as the TFC, TPL and TVD have been optimized individually and simultaneously to improve the performances of practical power systems considering the integration of multi SVC based FACTS devices. For the IEEE 30-Bus test system, the optimized values for TFC, TPL and TVD are 798.9457 $/h, 2.83530 MW and 0.10980 p.u., respectively, and for the test system IEEE 57-Bus, the best values achieved for TFC, TPL and TVD are 41,638.6742 $/h, 9.28 MW and 0.7613 p.u., respectively. The mechanism search of the standard AEO is improved by creating flexible interactivity during search process between intensification and diversification. Initially, a specified number of sub systems have been created based on the types of decision variables. This first stage allows creating diversity in search space, and then at the final stages, the search process is guided to achieve an efficient local search around the best updated solution. The performances of the proposed optimization technique have been validated on two practical IEEE test systems. The obtained results using the proposed IAEO compared to many recent methods demonstrate its efficiency and competitive aspect in solving power management optimization.

Conflict of interest. The authors declare no conflict of interest.

REFERENCES

1. Carpentier J. Contribution á l'étude du dispatching économique. *Bulletin de la Société Francaise des électriciens*, 1962, vol. 3, pp. 431-447. (Fra).

2. Ullah Z., Elkadeem M.R., Wang S., Azam M., Shaheen K., Hussain M., Rizwan M. A Mini-review: Conventional and Metaheuristic Optimization Methods for the Solution of Optimal Power Flow (OPF) Problem. In: Barolli, L., Amato, F., Moscato, F., Enokido, T., Takizawa, M. (eds) *Advanced Information Networking and Applications. AINA 2020. Advances in Intelligent Systems and Computing*, 2020, vol. 1151. Springer, Cham. doi: https://doi.org/10.1007/978-3-030-44041-1_29.

3. Frank S., Steponavice I., Rebennack S. Optimal power flow: a bibliographic survey II. *Energy Systems*, 2012, vol. 3, no. 3, pp. 259-289. doi: https://doi.org/10.1007/s12667-012-0057-x.

4. Mahdad B., Srairi K. A new interactive sine cosine algorithm for loading margin stability improvement under contingency. *Electrical Engineering*, 2018, vol. 100, no. 2, pp. 913-933. doi: https://doi.org/10.1007/s00202-017-0539-x.

5. Mahdad B. Improvement optimal power flow solution under loading margin stability using new partitioning whale algorithm. *International Journal of Management Science and Engineering Management*, 2019, vol. 14, no. 1, pp. 64-77. doi: https://doi.org/10.1080/17509653.2018.1488225.

6. Bouchekara H. Solution of the optimal power flow problem considering security constraints using an improved chaotic electromagnetic field optimization algorithm. *Neural Computing and Applications*, 2020, vol. 32, no. 7, pp. 2683-2703. doi: https://doi.org/10.1007/s00521-019-04298-3.

7. Kotb M.F., El-Fergany A.A. Optimal Power Flow Solution Using Moth Swarm Optimizer Considering Generating Units Prohibited Zones and Valve Ripples. *Journal of Electrical Engineering & Technology*. 2019, vol. 15, pp. 179-192. doi: https://doi.org/10.1007/s42835-019-00144-7.

8. Taher M.A., Kamel S., Jurado F., Ebeed M. Modified grasshopper optimization framework for optimal power flow solution. *Electrical Engineering*, 2019, vol. 101, no. 1, pp. 121-148. doi: https://doi.org/10.1007/s00202-019-00762-4.

9. Warid W. Optimal power flow using the AMTPG-Jaya algorithm. *Applied Soft Computing*, 2020, vol. 91, art. no. 106252. doi: https://doi.org/10.1016/j.asoc.2020.106252.

10. El-Fergany A.A., Hasanien H.M. Tree-seed algorithm for solving optimal power flow problem in large-scale power systems incorporating validations and comparisons. *Applied Soft Computing*, 2018, vol. 64, pp. 307-316. doi: https://doi.org/10.1016/j.asoc.2017.12.026.

11. Radosavljević J., Klimenta D., Jevtić M., Arsić N. Optimal Power Flow Using a Hybrid Optimization Algorithm of Particle Swarm Optimization and Gravitational Search Algorithm. *Electric Power Components and Systems*, 2015, vol. 43, no. 17, pp. 1958-1970. doi: https://doi.org/10.1080/15325008.2015.1061620.

12. Youssef H., Kamel S., Ebeed, M. Optimal Power Flow Considering Loading Margin Stability Using Lightning Attachment Optimization Technique. *2018 Twentieth International Middle East Power Systems Conference (MEPCON)*, 2018, pp. 1053-1058. doi: https://doi.org/10.1109/MEPCON.2018.8635110.

13. Berrouk F., Bounaya K. Optimal Power Flow For Multi-FACTS Power System Using Hybrid PSO-PS Algorithms. *Journal of Control, Automation and Electrical Systems*, 2018, vol. 29, no. 2, pp. 177-191. doi: https://doi.org/10.1007/s40313-017-0362-7.

14. Shabanpour-Haghighi A., Seifi A.R., Niknam T. A modified teaching–learning based optimization for multi-objective optimal power flow problem. *Energy Conversion and Management*, 2014, vol. 77, pp. 597-607. doi: https://doi.org/10.1016/j.enconman.2013.09.028.

15. Mugemanyi S., Qu Z., Rugema F.X., Dong Y., Bananeza C., Wang L. Optimal Reactive Power Dispatch Using Chaotic Bat Algorithm. *IEEE Access*, 2020, vol. 8, pp. 65830-65867. doi: https://doi.org/10.1109/ACCESS.2020.2982988.

16. Nguyen T.T. A high performance social spider optimization algorithm for optimal power flow solution with single objective optimization. *Energy*, 2019, vol. 171, pp. 218-240. doi: https://doi.org/10.1016/j.energy.2019.01.021.

17. Kahourzade S., Mahmoudi A., Mokhlis H. Bin. A comparative study of multi-objective optimal power flow based on particle swarm, evolutionary programming, and genetic algorithm. *Electrical Engineering*, 2015, vol. 97, no. 1, pp. 1-12. doi: https://doi.org/10.1007/s00202-014-0307-0.

18. Mahdad B., Srairi K. Security constrained optimal power flow solution using new adaptive partitioning flower pollination algorithm. *Applied Soft Computing*, 2016, vol. 46, pp. 501-522. doi: https://doi.org/10.1016/j.asoc.2016.05.027.

19. Mahdad B., Kamel S. New strategy based modified Salp swarm algorithm for optimal reactive power planning: a case study of the Algerian electrical system (114 bus). *IET Generation, Transmission & Distribution*, 2019, vol. 13, no. 20, pp. 4523-4540. doi: https://doi.org/10.1049/iet-gtd.2018.5772.

20. Bentouati B., Javaid M.S., Bouchekara H.R.E.H., El-Fergany A.A. Optimizing performance attributes of electric power systems using chaotic Salp swarm optimizer. *International Journal of Management Science and Engineering*

Management, 2020, vol. 15, no. 3, pp. 165-175. doi: https://doi.org/10.1080/17509653.2019.1677197.
21. Pulluri H., Naresh R., Sharma V. A solution network based on stud krill herd algorithm for optimal power flow problems. *Soft Computing*, 2018, vol. 22, no. 1, pp. 159-176. doi: https://doi.org/10.1007/s00500-016-2319-3.
22. Li S., Gong W., Wang L., Yan X., Hu C. Optimal power flow by means of improved adaptive differential evolution. *Energy*, 2020, vol. 198, art. no. 117314. doi: https://doi.org/10.1016/j.energy.2020.117314.
23. El-Fergany A.A., Hasanien H.M. Salp swarm optimizer to solve optimal power flow comprising voltage stability analysis. *Neural Computing and Applications*, 2020, vol. 32, no. 9, pp. 5267-5283. doi: https://doi.org/10.1007/s00521-019-04029-8.
24. Sakthivel V.P., Suman M., Sathya P.D. Squirrel search algorithm for economic dispatch with valve-point effects and multiple fuels. *Energy Sources, Part B: Economics, Planning, and Policy*, 2020, vol. 15, no. 6, pp. 351-382. doi: https://doi.org/10.1080/15567249.2020.1803451.
25. Meng A., Zeng C., Wang P., Chen D., Zhou T., Zheng X., Yin H. A high-performance crisscross search based grey wolf optimizer for solving optimal power flow problem. *Energy*, 2021, vol. 225, art. no. 120211. doi: https://doi.org/10.1016/j.energy.2021.120211.
26. Mehdi M.F., Ahmad A., Ul Haq S.S., Saqib M., Ullah M.F. Dynamic economic emission dispatch using whale optimization algorithm for multi-objective function. *Electrical Engineering & Electromechanics*, 2021, no. 2, pp. 64-69. doi: https://doi.org/10.20998/2074-272X.2021.2.09.
27. Kouadri R., Slimani L., Bouktir T. Slime mould algorithm for practical optimal power flow solutions incorporating stochastic wind power and static var compensator device. *Electrical Engineering & Electromechanics*, 2020, no. 6, pp. 45-54. doi: https://doi.org/10.20998/2074-272X.2020.6.07.
28. Djabali C., Bouktir T. Simultaneous allocation of multiple distributed generation and capacitors in radial network using genetic-salp swarm algorithm. *Electrical Engineering & Electromechanics*, 2020, no. 4, pp. 59-66. doi: https://doi.org/10.20998/2074-272X.2020.4.08.
29. Zhao W., Wang L., Zhang Z. Artificial ecosystem-based optimization: a novel nature-inspired meta-heuristic algorithm. *Neural Computing and Applications*, 2020, vol. 32, no. 13, pp. 9383-9425. doi: https://doi.org/10.1007/s00521-019-04452-x.
30. Mouassa S., Jurado F., Bouktir T., Raja M.A.Z. Novel design of artificial ecosystem optimizer for large-scale optimal reactive power dispatch problem with application to Algerian electricity grid. *Neural Computing and Applications*, 2021, vol. 33, no. 13, pp. 7467-7490. doi: https://doi.org/10.1007/s00521-020-05496-0.
31. Shaheen A., Elsayed A., Ginidi A., El-Sehiemy R., Elattar E. Reconfiguration of electrical distribution network-based DG and capacitors allocations using artificial ecosystem optimizer: Practical case study. *Alexandria Engineering Journal*, 2022, vol. 61, no. 8, pp. 6105-6118. doi: https://doi.org/10.1016/j.aej.2021.11.035.
32. Khasanov M., Kamel S., Tostado-Veliz M., Jurado F. Allocation of Photovoltaic and Wind Turbine Based DG Units Using Artificial Ecosystem-based Optimization. *2020 IEEE International Conference on Environment and Electrical Engineering and 2020 IEEE Industrial and Commercial Power Systems Europe (EEEIC / I&CPS Europe)*, 2020, pp. 1-5. doi: https://doi.org/10.1109/EEEIC/ICPSEurope49358.2020.9160696.
33. Eid A., Kamel S., Korashy A., Khurshaid T. An Enhanced Artificial Ecosystem-Based Optimization for Optimal Allocation of Multiple Distributed Generations. *IEEE Access*, 2020, vol. 8, pp. 178493-178513. doi: https://doi.org/10.1109/ACCESS.2020.3027654.
34. Zimmerman R.D., Murillo-Sanchez C.E., Thomas R.J. MATPOWER: Steady-State Operations, Planning, and Analysis Tools for Power Systems Research and Education. *IEEE Transactions on Power Systems*, 2011, vol. 26, no. 1, pp. 12-19. doi: https://doi.org/10.1109/TPWRS.2010.2051168.

Received 30.04.2022
Accepted 14.08.2022
Published 06.11.2022

Belkacem Mahdad [1], *PhD,*
Kamel Srairi[1], *PhD,*
[1] University of Biskra, Algeria,
e-mail: Belkacem.mahdad@univ-biskra.dz (Corresponding Author);
k.srairi@univ-biskra.dz

How to cite this article:
Mahdad B., Srairi K. Interactive artificial ecosystem algorithm for solving power management optimizations. *Electrical Engineering & Electromechanics*, 2022, no. 6, pp. 53-66. doi: https://doi.org/10.20998/2074-272X.2022.6.09

UDC 621.3 https://doi.org/10.20998/2074-272X.2022.6.10

R. Shweta, S. Sivagnanam, K.A. Kumar

Fault detection and monitoring of solar photovoltaic panels using internet of things technology with fuzzy logic controller

Purpose. *This article proposes a new control monitoring grid connected hybrid system. The proposed system, automatic detection or monitoring of fault occurrence in the photovoltaic application is extremely mandatory in the recent days since the system gets severely damaged by the occurrence of different faults, which in turn results in performance degradation and malfunctioning of the system.* ***The novelty*** *of the proposed work consists in presenting solar power monitoring and power control based Internet of things algorithm. In consideration to this viewpoint, the present study proposes the Internet of Things (IoT) based automatic fault detection approach, which is highly beneficial in preventing the system damage since it is capable enough to identify the emergence of fault on time without any complexities to generate Dc voltage and maintain the constant voltage for grid connected hybrid system.* ***Methods.*** *The proposed DC-DC Boost converter is employed in this system to maximize the photovoltaic output in an efficient manner whereas the Perturb and Observe algorithm is implemented to accomplish the process of maximum power point tracking irrespective of the changes in the climatic conditions and then the Arduino microcontroller is employed to analyse the faults in the system through different sensors. Eventually, the IoT based monitoring using fuzzy nonlinear autoregressive exogenous approach is implemented for classifying the faults in an efficient manner to provide accurate solution of fault occurrence for preventing the system from failure or damage.* ***Results.*** *The results obtained clearly show that the power quality issue, the proposed system to overcome through monitoring of fault solar panel and improving of power quality. The obtained output from the hybrid system is fed to the grid through a 3ϕ voltage source inverter is more reliable and maintained power quality. The power obtained from the entire hybrid setup is measured by the sensor present in the IoT based module. The experimental validation is carried out in ATmega328P based Arduino UNO for validating the present system in an efficient manner.* ***Originality.*** *The automatic Fault detection and monitoring of solar photovoltaic system and compensation of grid stability in distribution network based IoT approach is utilized along with sensor controller.* ***Practical value****. The work concerns a network comprising of electronic embedded devices, physical objects, network connections, and sensors enabling the sensing, analysis, and exchange of data. It tracks and manages network statistics for safe and efficient power delivery. The study is validated by the simulation results based on real interfacing and real time implementation.* References 22, tables 2, figures 8.

Key words: **photovoltaic system, automatic fault detection, DC-DC boost converter, perturb and observe algorithm, fuzzy nonlinear autoregressive exogenous approach, renewable energy source.**

Мета*. У цій статті пропонується нова гібридна система керування моніторингу підключення до мережі. Пропонована система автоматичного виявлення або моніторингу виникнення несправностей у фотогальванічному обладнанні наразі вкрай необхідна, оскільки система серйозно ушкоджується при виникненні різних несправностей, що, у свою чергу, призводить до погіршення показників і некоректної роботи системи.* ***Новизна*** *запропонованої роботи полягає у поданні алгоритму моніторингу сонячної енергетики та управління потужністю на основі Інтернету речей. Зважаючи на цю точку зору, у цьому дослідженні пропонується підхід автоматичного виявлення несправностей на основі Інтернету речей (IoT), який дуже корисний для запобігання пошкодженню системи, оскільки вона достатньо здатна вчасно ідентифікувати виникнення несправності без будь-яких складнощів, щоб генерувати постійну напругу. та підтримувати постійну напругу для гібридної системи, підключеної до мережі.* ***Методи****. Пропонований перетворювач постійного струму, що підвищує, використовується в цій системі для максимізації фотоелектричної потужності ефективним чином, тоді як алгоритм збурення та спостереження реалізований для виконання процесу відстеження точки максимальної потужності незалежно від змін кліматичних умов, а потім мікроконтролер Arduino використовується для аналізу несправностей у системі за допомогою різних датчиків. Зрештою, моніторинг на основі IoT з використанням нечіткого нелінійного авторегресійного екзогенного підходу реалізований для ефективної класифікації несправностей, щоб забезпечити точне вирішення несправності, що виникла, для запобігання відмови або пошкодженню системи.* ***Результати****. Отримані результати показують, що запропонована система вирішує проблему якості електроенергії за рахунок моніторингу несправності сонячної панелі та покращення якості електроенергії. Отримана з гібридної системи енергія подається в мережу через інвертор джерела напруги 3ϕ, що є більш надійним і підтримує якість електроенергії. Потужність, отримана від усієї гібридної установки, вимірюється датчиком, присутнім у модулі на основі IoT. Експериментальна перевірка проводиться у Arduino UNO на базі ATmega328P для ефективної перевірки цієї системи.* ***Оригінальність****. Автоматичне виявлення несправностей та моніторинг сонячної фотоелектричної системи і компенсація стабільності мережі у підході IoT на основі розподільчої мережі використовуються разом із контролером датчиків.* ***Практична цінність****. Робота стосується мережі, що складається з вбудованих електронних пристроїв, фізичних об'єктів, мережевих підключень і датчиків, що дозволяють сприймати, аналізувати і обмінюватися даними. Вона відстежує та керує мережевою статистикою для безпечної та ефективної подачі енергії. Дослідження підтверджено результатами моделювання, що базуються на реальному інтерфейсі та реалізації в реальному часі.* Бібл. 22, табл. 2, рис. 8.

Ключові слова: **фотогальванічна система, автоматичне виявлення несправностей, перетворювач постійного струму, що підвищує, алгоритм збурення та спостереження, нечіткий нелінійний авторегресійний екзогенний підхід, відновлюване джерело енергії.**

Introduction. In the process of power generation, the demand of renewable energy (RE) sources is extremely high for compensating the power requirement of people and overcoming the exhaustion of fossil fuels in an efficient manner. The usage of RE sources has gained huge attention in different industrial or domestic applications as it aids in generating electricity with plenty of beneficial impacts like zero CO_2 emission, trouble free maintenance, easy installation and less expenditure. The increasing cost of conventional fossil fuels in the recent days causes the people to switch to the usage of RE sources as these sources are easily available and cost effective. Moreover, the usage of these sources has widely influenced the economic growth of the nation as it contributes enough in maximizing the uninterrupted

generation and transmission of electricity without requiring any expensive processes [1-4].

The solar energy is one of the significant RE sources that is comparatively better than the other sources like tidal, biomass, geothermal and wind energy since the profitability of this photovoltaic (PV) source is extremely higher than the others. The usage of PV system in the process of electricity generation is extremely advantageous as it is capable enough to be installed even in the rural places without any complexities. Furthermore, the environmental friendly features of this PV system are highly preferable for the future projects in multiple sectors since the government has aimed to make the green society with pollution free applications [5, 6]. In spite of having all these advantageous measures, the PV owns the limitation of delivering low voltage as output and so it is highly mandatory to maximize the PV output in an optimal manner [7]. Therefore, the usage of DC-DC converters are emerged in the process of maximizing the PV output voltage to compensate the voltage requirement of load in an optimal way and so this present study proposes the boost converter for improving the PV output as it elevates the voltage with less components without affecting the efficiency or reliability of the system.

Due to the intermittent nature or non-linear features of solar energy, the PV delivers the output with extensive oscillations and so the process of tracking maximum power from PV is extremely mandatory for the complete use of PV output irrespective of the varying weather condition. Various maximum power point tracking (MPPT) algorithms are used for the extraction of maximum available power from PV panel and all these approaches have involved in finding the operating point of PV in an efficient manner [8-11]. Hence, this present study employs the Perturb and Observe (P&O) approach to effectively track the maximum power from PV by accurately identifying its operating point in an optimal way because this approach owns the beneficial measure of high tracking efficiency with lesser complexity.

The operating condition of PV system gets affected by the occurrence of different faults that initiate potential energy loss, which in turn influence the safety of the system in a wider range and these faults affect the efficiency of the system in delivering the desired outcomes. It is thus extremely mandatory to monitor the entire system to protect it from being affected by the faults in order to maximize safety and productivity of the system [12, 13]. The timely detection of fault occurrence for the purpose of enhancing the system performance with high efficiency is extremely crucial because it assists in preventing the panel damage or output current disruptions and hence various fault detection approaches are employed in the past decades to obtain fault free operation [14]. Though multiple approaches with different conceptual variations are used in the process of identifying the emergence of fault in PV system, the ultimate motive of achieving fault detection on time is not effectively accomplished as all these approaches have only given temporary solution. Thus, the detection capability of the conventional strategies are not sufficient enough to prevent the system free from damages or malfunctioning and hence the Internet of Things (IoT) based detection approaches are introduced in the field for identifying the fault occurrence [15, 16].

The implementation of IoT based approach in the process of automatically identifying the faults in the system is highly advantageous since it is wrapped with plenty of beneficial measures like cost minimization, anytime-anywhere device control and real-time data assess, which makes is highly preferable for the applications that require automatic detection. In addition, it effectively involves in lessening the limitation of distance range, which is regarded as one of the significant features of this approach [17-19]. Various intelligent based optimization approaches are involved in the IoT based operation but all these methods are not capable enough in delivering optimal outcomes and so the present study prefers the implementation of Fuzzy system for acquiring optimal results in the process of identifying the system faults in an efficient manner [20-22].

In all the previously used methods for monitoring of solar power plant was discussed in brief. First, we had discussed on traditional approaches like Zigbee, Bluetooth and WSN, and then moved concentration on the PLC and SCADA system, which are most widely used methods nowadays from last 2 decades. After the review on traditional methods for remote monitoring and control for solar power plant, we have turned our focus on recent trends like IoT.

The purpose of the work is some of the drawbacks of previous methods are reduced by the use of new innovative techniques like Internet of Things. IoT allows us to remote monitoring and control the energy parameters but traditional systems can't allow us to remotely access energy parameters.

Proposed control system. The process of detecting the fault occurrence in the power generation system using IoT application is significantly introduced in this present study, which indulges in enhancing the overall performance of the system by preventing the output current from being affected by different faults that occurs in the system. As it is a sensor based system of automatic fault identification, the real time status of the power system is observed in an optimal manner and so the reliability of this system is extremely higher than the conventional fault tracking systems. The operation of this system is remarkably illustrated through the block representation in Fig. 1 for validating the proposed methodology.

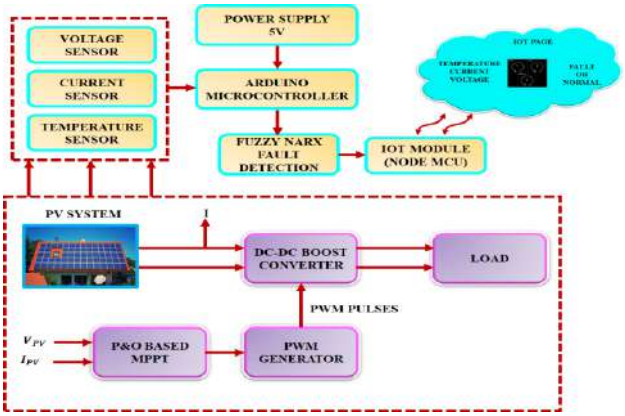

Fig. 1. Block representation of the proposed methodology

As the obtained voltage of PV is low in nature, it is not sufficient enough in compensating the voltage requirement of load in an efficient manner and so the boost converter is employed in this study to maximize the output voltage of PV in a wider range. Due to the intermittent nature of PV, the output gets fluctuated or becomes inconstant, which hurdles the overall operation of the system and hence the P&O algorithm is implemented to extract the maximum power from PV by comparing the current and voltage of PV module.

The duty cycle command of this MPPT controller is fed to the pulse-width modulation (PWM) generator that generates the pulses and delivers it to the converter for delivering the constant output voltage without any oscillation. The obtained output voltage is then given to the load and the load requirement is thus effectively compensated.

The occurrence of any fault in this system causes panel damage or interruption in current flow and so it is highly mandatory to monitor the fault occurrence for the disruption free operation of the system.

Therefore, the current, voltage and temperature of the entire system are sensed by 3 different sensors and the outputs of these sensors are fed to the Arduino microcontroller that gets operated through the supply of. The output of this controller is then given to the fuzzy nonlinear autoregressive exogenous (NARX) system that effectively detects the faults and the identified faults are evidently displayed by using the IoT module (Node MCU ESP8266) in an efficient manner. Thus, this system maximizes the overall performance of the system by effectively detecting the fault occurrence along with the observation of variations in temperature, current and voltage.

System modelling. The detailed analysis and modelling of the employed approaches are significantly provided in the subsequent section.

1. PV system. Because of providing an ideal balance between precision and simplicity, the present study uses the single diode model of PV system. Its equivalent circuit representation is significantly, which includes a series resistance R_s, a parallel resistance indicating the leakage current R_p, a diode I_D and a photocurrent I_{ph}. By applying Kirchhoff's law, the current is generated through the subsequent equation as:

$$I = I_{ph} - I_D - I_p, \tag{1}$$

where I_{ph} is the photocurrent; I_p is the current flows through the parallel resistor.

The I_p is computed as

$$I_p = \frac{V + R_s \cdot I}{R_p}, \tag{2}$$

where I_D is the diode current that is equal to the saturation current, which is expressed as:

$$I_D = I_{sd} \cdot \left(\exp\left(\frac{q \cdot (V + R_s \cdot I)}{n \cdot K \cdot T} \right) - 1 \right), \tag{3}$$

where q is the electron charge; K is the Boltzmann constant; n is the ideal factor; T is the cell temperature; I_{sd} is the reverse saturation current.

Equation (1) is thus replaced as:

$$I = I_{ph} - I_{sd} \cdot \left(\exp\left(\frac{q \cdot (V + R_s \cdot I)}{n \cdot K \cdot T} \right) - 1 \right) - \frac{V + R_s \cdot I}{R_p}, \tag{4}$$

As solar irradiation and temperature influence the photocurrent, it is expressed as:

$$I_{ph} = \left[I_{sc} + K_i \cdot (T - T_{ref}) \right] \cdot \frac{G}{G_{ref}}, \tag{5}$$

where G is the solar irradiance; K_i is the temperature coefficient; G_{ref} is the reference insolation of the cell; T_{ref} is the reference temperature; I_{sc} is the short circuit current.

As the temperature is varies, the saturation current gets fluctuated, which is expressed as:

$$I_{sd} = I_{rs} \cdot \left(\frac{T}{T_{ref}} \right)^3 \cdot \exp\left(\frac{q \cdot E_g \cdot \left(\frac{1}{T_{ref}} - \frac{1}{T} \right)}{K \cdot n} \right), \tag{6}$$

where E_g is the semiconductor's gap energy; I_{rs} is the PV cell's reverse saturation current; n is the ideal factor relies on PV.

The reverse saturation current is thus expressed as:

$$I_{rs} = \frac{I_{sc}}{\exp\left(\frac{q \cdot V_{oc}}{N_s \cdot n \cdot K \cdot T} \right) - 1}. \tag{7}$$

The output of this PV system is then given to the boost converter as the input and the converter involves in maximizing the voltage in an optimal manner.

2. Boost converter. One of the simplest kind of switch mode converter is known as boost converter, which has the elements like a capacitor C, an inductor L, a diode D, a load resistor R_L, a semiconductor switch s as involves in significantly maximizing the low output voltage of PV in an optimal way.

By modifying the switch ON time, the converter output voltage gets varied since it highly depends on the duty cycle of the switch and hence the average output voltage for duty cycle «D» is computed as:

$$\frac{V_o}{V_{in}} = \frac{1}{(1 - D)}, \tag{8}$$

where V_o and V_{in} are the output and input voltages of the converter are respectively specified.

The input and output power of converter are proportional to each other in an ideal circuit, which is expressed as:

$$P_o = P_{in} \Rightarrow V_o \cdot I_o = V_{in} \cdot I_{in}, \tag{9}$$

The boost converter's inductor value is computed by:

$$L = \frac{V_{in}}{(f_s \cdot \Delta I_L)} \cdot D, \tag{10}$$

where ΔI_L is the input current ripple; f_s is the switching frequency.

For the accurate estimation of inductor value, the current ripple factor that is the ratio among output current and input current ripple has to be ranges within 30 %, which is expressed as:

$$\Delta I_L / I_o = 30\ \%. \tag{11}$$

The capacitor value of the converter is obtained by:

$$C = \frac{I_{out}}{(f_s \cdot \Delta V_o)} \cdot D, \tag{12}$$

where ΔV_o is the output voltage ripple that is actually regarded as the 5 % of output voltage, which is expressed as:

$$\Delta V_o / V_o = 5\ \%. \tag{13}$$

Thus, the contribution of this converter is extremely high in the process of maximizing the output voltage of PV in a wider range.

For the disruption free operation of the PV system, the maximum power has to be extracted from the PV system and so the P&O algorithm is employed in this present study.

3. P&O algorithm. As the necessity of tracking the maximum power from PV is enormously high in the process of enhancing the system operation without any fluctuation, the P&O algorithm is employed in this study for extracting the maximum power from PV irrespective of the changes in the climatic conditions. Few measured parameters and a straightforward feedback ground work are utilized by this algorithm in the initial stage for effectively tracking the MPP whereas the system gets operated at the obtained MPP for acquiring optimal efficiency along with the disruption free outputs. The functioning measures of this algorithm are evidently explained through the steps.

The power from the PV panel gets constantly fluctuated by the slight perturbation initiated by this algorithm. The direction of the perturbation remains the same when the power gets increased by the initiated perturbation whereas the direction is reversed when the power gets decreased after reaching the peak point. For lessening the power variation, the perturbation size is fixed as small and the algorithms gets fluctuated around the peak point when it reaches the steady state. Initially, it involves in estimating the current and voltage of PV for measuring the actual power and then the condition $\Delta P = 0$ is tested. If this condition is compensated, the operating point is obtained or else the condition of $\Delta P > 0$ is tested. The operating point relies on the left part of MPP when $\Delta P > 0$ is satisfied and so the condition of $\Delta V > 0$ is performed whereas the operating point relies on the left part of MPP when $\Delta P > 0$ is not compensated. This process gets repeated until the MPP is reached.

The acquired MPP is then given to the PWM generator for generating the required pulses of the boost converter in an efficient manner.

4. Algorithm:

Step-1: Input (number of strings, IoT granularity level, number of PV panel in one string)
Step-2: Test each string input for possible fault
Step-3: If faults identified then
Step-4: Issue command to IoT cloud to eliminate half of the existing nodes
Step-5: Do the step:2 again
Step-6: If (there is no further possible node elimination)
Step-7: Return the current node as the faulty node.
Step-8: No fault Exist
Step-9: Add a leaf node from the eliminated part
Step-10: Do the step:2 again
Step-11: Fault Exist
Step-12: Return the last added leaf node as faulty node
Step-13: output (the PV panel of group of PV panel causing the fault)

5. Fault analysis. The emergence of any fault in this system causes severe negative impacts like panel damage or interruption in current flow, which in turn lessens the cumulative performance of the system in a wider range and so in is extremely mandatory to identify these faults for preventing the system from being damaged. Therefore, the present study proposes the IoT based detection approach using fuzzy NARX algorithm, which contributes enough in monitoring the system and identifying the faults in an efficient manner. The working principles of this approach are evidently explained in the subsequent section with proper analysis and the flow chart of this fault detection approach is significantly illustrated in Fig. 2.

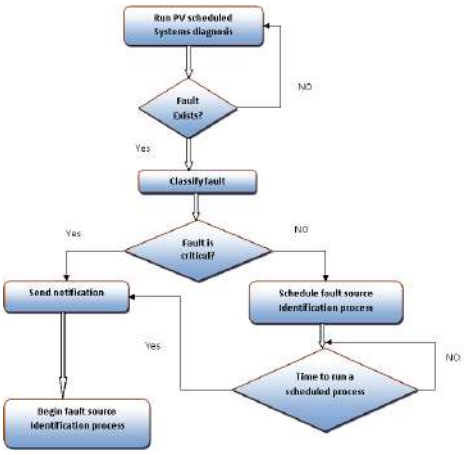

Fig. 2. Flow chart of detection algorithm

6. IoT based power monitoring. In general, the output power degradation in the power generation system occurs due to the occurrence of faults which in turn affects the overall current flow and this necessitates the continuous monitoring of various parameters. The voltage, current and the temperature obtained from the power generation system are monitored continuously by the IoT based power monitoring system. It comprises of a Node MCU ESP8266 controller along with INA219 sensor for voltage and current monitoring, DH11sensor for temperature. The obtained values of voltage, current and temperature are applied to the controller and from these values the presence and absence of faults are detected. In this work, the detection of faults is carried out by fuzzy NARX based fault detection approach as denoted in Fig. 3.

The expressions of power ratio PR and voltage ratio VR are given by:

$$VR = V_P / V_S; \quad (15)$$

$$PR = P_P / P_S; \quad (16)$$

where V_P is the maximum output voltage; P_P is the maximum output power obtained theoretically; V_S is the measured output voltage; P_S is the measured output power obtained practically.

The obtained values of VR and PR indicate the presence and absence of faults in the power generation system. The data thus monitored is stored in the IoT webpage through Node MCU.

Thus a wide analysis is performed with the usage of sensors and NARX model for fault detection in the power generation system. Depending on the obtained values of voltage, current and temperature, the effective functioning of the system is concluded which further indicates the presence and absence of faults. The NARX model effectively identifies and classifies faults generating improved fault detection outputs.

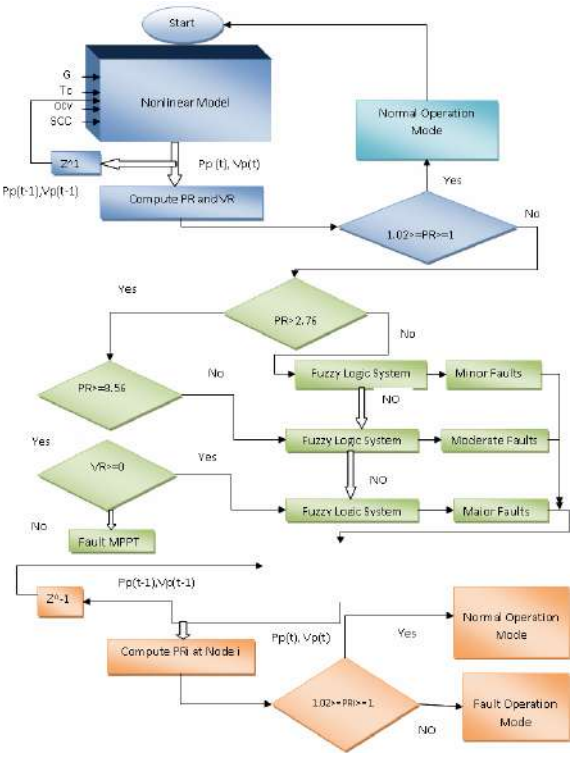

Fig. 3. Flow chart of fault detection

Results and discussions. The process of detecting the emergence faults that affect the output current of PV system is effectively performed in this study through the implementation of IoT based fault detection approach using fuzzy NARX algorithm. The experimental validation of the entire work is carried out using ATmega328P based Arduino UNO for authenticating the performance capability of this approach in the detection of fault current with optimal outcomes. After identifying the input variables VR and PR regions, the fuzzy sets and the membership functions for the three Sugeno fuzzy models are shown in Fig. 4. The waveform representing the output voltage of PV is significantly highlighted in Fig. 5, which illustrates that the output voltage gets varied from 180 V to 200 V but this obtained low DC output with oscillations is not sufficient enough to compensate the voltage requirement of load and so this obtained voltage of PV is fed to the boost converter as input for maximizing the voltage in a wider range.

After identifying the input variables VR and PR regions, the fuzzy sets and the membership functions for the three Sugeno fuzzy models are shown in Fig. 4.

The obtained PV voltage is significantly improved by the boost converter as represented in Fig. 5,*a-d*, which validates that the converter delivers the constant output voltage of 220 V without any fluctuations. Irrespective of the oscillations in the PV output, the converter delivers disruptions free output and hence the efficiency of this converter in the process of maximizing the low DC output of PV is remarkably high.

The waveform indicating the output current without fault is evidently illustrated in Fig. 6, which validates that the output current shows no oscillations during the no fault condition and the constant output current is obtained. In this fault free condition, the constant output current of 3 A is significantly obtained, which in turn improves the overall system performance in a wider range.

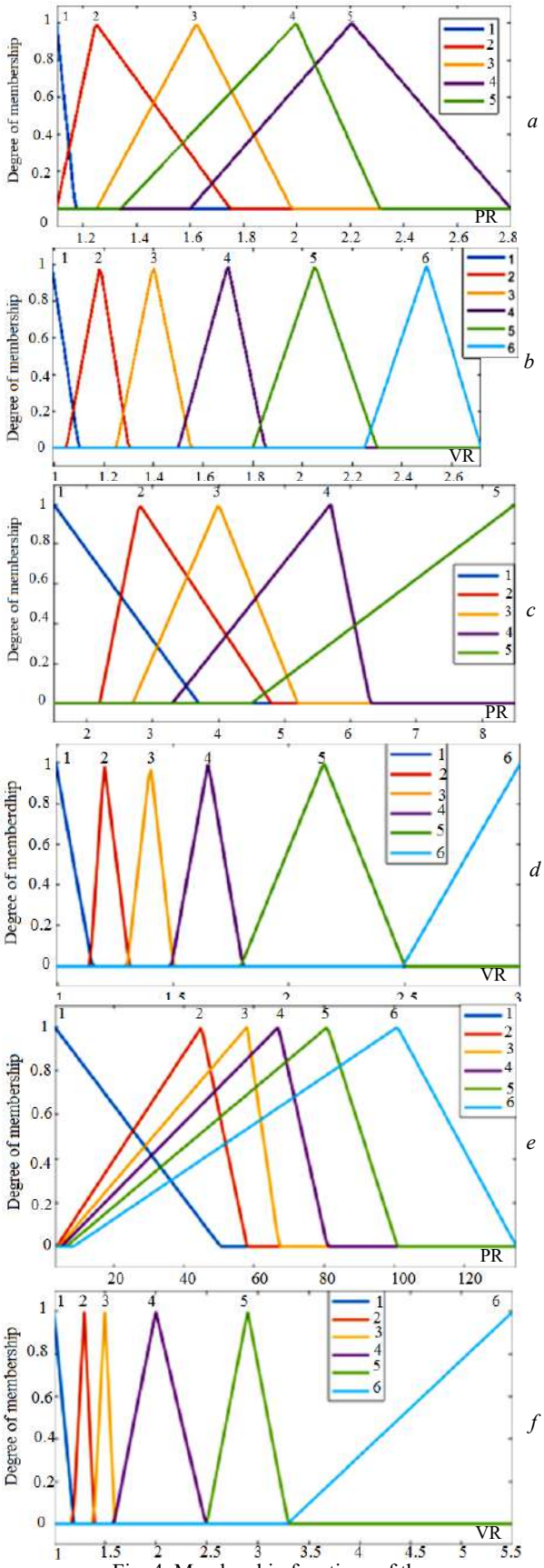

Fig. 4. Membership functions of the:
a – minor fault model power rate;
b – minor fault model voltage rate;
c – moderate fault model power rate;
d – moderate fault model voltage rate;
e – major fault model power rate;
f – major fault model voltage rate

The waveform representing the output voltage of PV is significantly highlighted in Fig. 5, which illustrates that the output voltage gets varied from 180 V to 200 V but this obtained low DC output with oscillations is not sufficient enough to compensate the voltage requirement of load and so this obtained voltage of PV is fed to the boost converter as input for maximizing the voltage in a wider range.

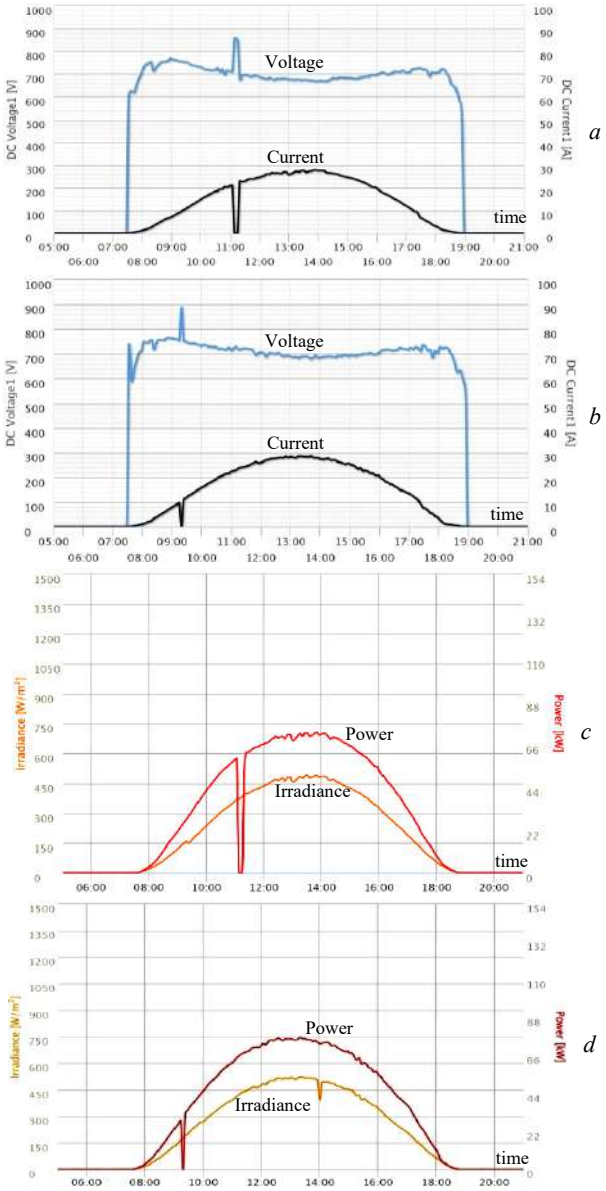

Fig. 5. *a* – fault current; *b* – fault cleared current; *c* – fault irradiation; *d* – fault cleared irradiation

When the fault is emerged in the system the output current gets extremely deviated as depicted in Fig. 7, which illustrates the fault current waveform in an efficient manner. The obtained waveform proves that the current is highly disrupted and varied up to 10.5 A, which severely affects the performance efficiency of the system or initiates the panel damage. To prevent these issues, the occurrence of fault is remarkably monitored through the IoT fault detection approach.

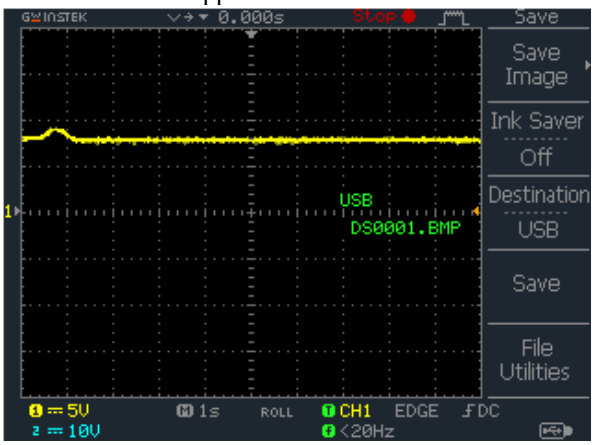

Fig. 6. Output current without fault

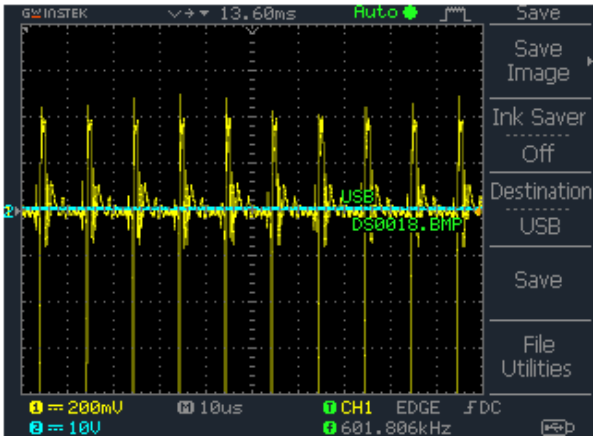

Fig. 7. Output current with fault

The hardware outcomes of the fuzzy fault classification along with the execution time and accuracy of proposed fuzzy NARX system are evidently listed out in Table 1 and Table 2, which proves that the accuracy of this proposed approach in the process of detecting the fault occurrence in the PV system is remarkably high. In addition, it consumes less time for the execution of fault analysis, which in turn makes the system free from unwanted delays.

Table 1

Test cases of fuzzy classification

No.	Power ratio	Voltage ratio	Fault mode	Fuzzy classification region	Diagnosis time, ms
1	1.8	2.0	Minor	4	4.02
2	1.4	1.1	Minor	9	4.03
3	5.3	2.7	Moderate	18	1.93
4	2.4	1.0	Moderate	7	3.04
5	116	4.5	Major	23	1.82
6	80.6	3.0	Major	22	2.01

Table 2

Accuracy and execution time using NARX

No.	Solar irradiation, W/m^2	Input temperature, °C	Open-circuit voltage, V	Short-circuit current, A	Hardware		Tracking time, ms
					I	V	
1	200	10	36.88	8.27	1.36	31.28	7.85
2	500	20	36.88	8.27	3.68	30.41	7.74
3	350	15	36.88	8.27	2.54	30.95	7.86
4	600	25	30	8.37	4.49	23.64	7.89
5	400	20	30	8.37	2.85	24.11	7.58
6	800	30	30	8.37	6.23	22.69	8.02

The hardware outcomes of the IoT based system monitoring are evidently illustrated in Fig. 8,*a*,*b*, which proves that fault current outcomes exhibits much variations.

The temperature, current and voltage values of the system are sensed through three various sensors to monitor the fault occurrence in an efficient manner. The sensed output is to the Arduino controller, which simultaneously fed the output to the Fuzzy NARX system to classify the faults in an optimal manner. The classified outputs are evidently displayed in the IoT webpage as represented in the subsequent figures.

Hence, the acquired outcomes have proved that the performance capability of the proposed methodology in the automatic monitoring and detection of fault occurrence in PV system is extremely high.

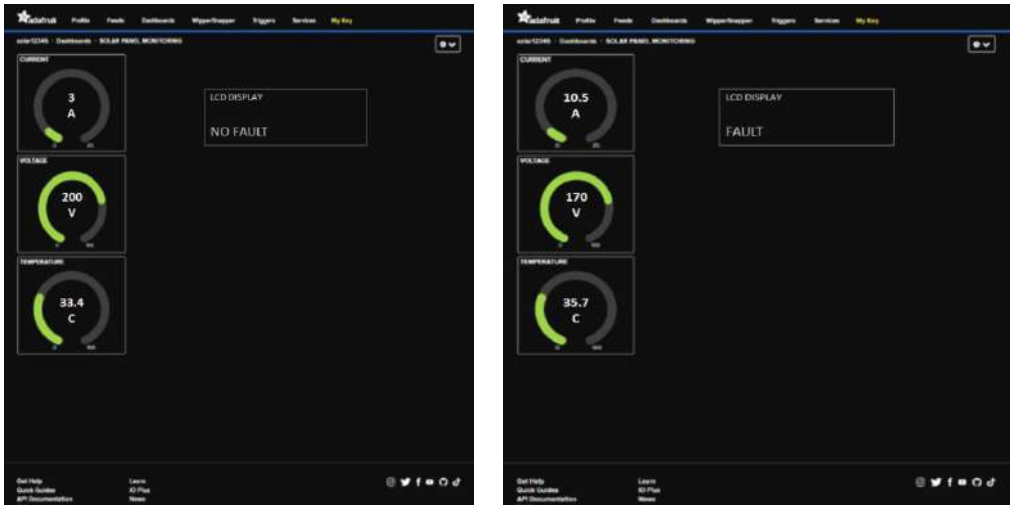

a *b*

Fig. 8. *a* – output of fault; *b* – no fault conditions

Conclusions. The present study describes the detailed analysis of implementing the Internet of Things based automatic fault identification in the photovoltaic application, which assists in rectifying the issues like panel damage, malfunctioning and system failure in an optimal manner. The low photovoltaic output voltage is effectively maximized through the implementation of boost converter and the maximum power from photovoltaic is remarkably extracted by the implementation of Perturb and Observe algorithm, which in turn efficiently compensated the load requirement without any disruptions. As the emergence of fault in the system affects the current flow in a wider range, the entire system is monitored through three different sensors whereas the sensed output is fed to the fuzzy nonlinear autoregressive exogenous system, which efficiently classifies the faults in the system and displays the occurred faults in the Internet of Things webpage through Node MCU. Thus, the proposed approach performs well in identifying whether the system has any faults or not and in effectively monitoring the changes in system parameters like voltage, current or temperature. The entire work is experimentally validated using ATmega328P based Arduino UNO and the obtained outcomes have proved that this approach is capable enough in automatically identifying the fault occurrence in an efficient manner without any complexities.

Conflict of interest. The authors declare no conflict of interest.

REFERENCES

1. Gu Y., Huang Y., Wu Q., Li C., Zhao H., Zhan Y. Isolation and Protection of the Motor-Generator Pair System for Fault Ride-Through of Renewable Energy Generation Systems. *IEEE Access*, 2020, vol. 8, pp. 13251-13258. doi: https://doi.org/10.1109/ACCESS.2020.2965773.

2. Kavin K.S., Subha Karuvelam P. PV-based Grid Interactive PMBLDC Electric Vehicle with High Gain Interleaved DC-DC SEPIC Converter. *IETE Journal of Research*, 2021, pp. 1-15. doi: https://doi.org/10.1080/03772063.2021.1958070.

3. Ma M., Zhang Z., Yun P., Xie Z., Wang H., Ma W. Photovoltaic Module Current Mismatch Fault Diagnosis Based on I-V Data. *IEEE Journal of Photovoltaics*, 2021, vol. 11, no. 3, pp. 779-788. doi: https://doi.org/10.1109/JPHOTOV.2021.3059425.

4. Jia K., Yang Z., Fang Y., Bi T., Sumner M. Influence of Inverter-Interfaced Renewable Energy Generators on Directional Relay and an Improved Scheme. *IEEE Transactions on Power Electronics*, 2019, vol. 34, no. 12, pp. 11843-11855. doi: https://doi.org/10.1109/TPEL.2019.2904715.

5. Elavarasan R.M., Shafiullah G.M., Padmanaban S., Kumar N.M., Annam A., Vetrichelvan A.M., Mihet-Popa L., Holm-Nielsen J.B. A Comprehensive Review on Renewable Energy Development, Challenges, and Policies of Leading Indian States With an International Perspective. *IEEE Access*, 2020, vol. 8, pp. 74432-74457. doi: https://doi.org/10.1109/ACCESS.2020.2988011.

6. Pradhan S., Hussain I., Singh B., Ketan Panigrahi B. Performance Improvement of Grid-Integrated Solar PV System Using DNLMS Control Algorithm. *IEEE Transactions on Industry Applications*, 2019, vol. 55, no. 1, pp. 78-91. doi: https://doi.org/10.1109/TIA.2018.2863652.

7. Karthikeyan V., Kumaravel S., Gurukumar G. High Step-Up Gain DC–DC Converter With Switched Capacitor and Regenerative Boost Configuration for Solar PV Applications. *IEEE Transactions on Circuits and Systems II: Express Briefs*, 2019, vol. 66, no. 12, pp. 2022-2026. doi: https://doi.org/10.1109/TCSII.2019.2892144.

8. Abdel-Rahim O. A New High Gain DC-DC Converter With Model-Predictive-Control Based MPPT Technique for Photovoltaic Systems. *CPSS Transactions on Power Electronics and Applications*, 2020, vol. 5, no. 2, pp. 191-200. doi: https://doi.org/10.24295/CPSSTPEA.2020.00016.

9. Ali A., Almutairi K., Padmanaban S., Tirth V., Algarni S., Irshad K., Islam S., Zahir M.H., Shafiullah M., Malik M.Z. Investigation of MPPT Techniques Under Uniform and Non-Uniform Solar Irradiation Condition–A Retrospection. *IEEE Access*, 2020, vol. 8, pp. 127368-127392. doi: https://doi.org/10.1109/ACCESS.2020.3007710.

10. Praveen Kumar T., Ganapathy S., Manikandan M. Improvement of voltage stability for grid connected solar photovoltaic systems using static synchronous compensator with recurrent neural network. *Electrical Engineering & Electromechanics*, 2022, no. 2, pp. 69-77. doi: https://doi.org/10.20998/2074-272X.2022.2.10.
11. Bhattacharyya S., Kumar P D.S., Samanta S., Mishra S. Steady Output and Fast Tracking MPPT (SOFT-MPPT) for P&O and InC Algorithms. *IEEE Transactions on Sustainable Energy*, 2021, vol. 12, no. 1, pp. 293-302. doi: https://doi.org/10.1109/TSTE.2020.2991768.
12. Samkria R., Abd-Elnaby M., Singh R., Gehlot A., Rashid M., H. Aly M., El-Shafai W. Automatic PV Grid Fault Detection System with IoT and LabVIEW as Data Logger. *Computers, Materials & Continua*, 2021, vol. 69, no. 2, pp. 1709-1723. doi: https://doi.org/10.32604/cmc.2021.018525.
13. Gopal Reddy S., Ganapathy S., Manikandan M. Power quality improvement in distribution system based on dynamic voltage restorer using PI tuned fuzzy logic controller. *Electrical Engineering & Electromechanics*, 2022, no. 1, pp. 44-50. doi: https://doi.org/10.20998/2074-272X.2022.1.06.
14. Harrou F., Taghezouit B., Sun Y. Robust and flexible strategy for fault detection in grid-connected photovoltaic systems. *Energy Conversion and Management*, 2019, vol. 180, pp. 1153-1166. doi: https://doi.org/10.1016/j.enconman.2018.11.022.
15. Mellit A., Tina G.M., Kalogirou S.A. Fault detection and diagnosis methods for photovoltaic systems: A review. *Renewable and Sustainable Energy Reviews*, 2018, vol. 91, pp. 1-17. doi: https://doi.org/10.1016/j.rser.2018.03.062.
16. Mansouri M., Hajji M., Trabelsi M., Harkat M.F., Al-khazraji A., Livera A., Nounou H., Nounou M. An effective statistical fault detection technique for grid connected photovoltaic systems based on an improved generalized likelihood ratio test. *Energy*, 2018, vol. 159, pp. 842-856. doi: https://doi.org/10.1016/j.energy.2018.06.194.
17. Pillai D.S., Blaabjerg F., Rajasekar N. A Comparative Evaluation of Advanced Fault Detection Approaches for PV Systems. *IEEE Journal of Photovoltaics*, 2019, vol. 9, no. 2, pp. 513-527. doi: https://doi.org/10.1109/JPHOTOV.2019.2892189.
18. de Melo G.C.G., Torres I.C., de Araújo Í.B.Q., Brito D.B., Barboza E. de A. A Low-Cost IoT System for Real-Time Monitoring of Climatic Variables and Photovoltaic Generation for Smart Grid Application. *Sensors*, 2021, vol. 21, no. 9, art. no. 3293. doi: https://doi.org/10.3390/s21093293.
19. Mellit A., Herrak O., Rus Casas C., Massi Pavan A. A Machine Learning and Internet of Things-Based Online Fault Diagnosis Method for Photovoltaic Arrays. *Sustainability*, 2021, vol. 13, no. 23, art. no. 13203. doi: https://doi.org/10.3390/su132313203.
20. Babu V., Ahmed K.S., Shuaib Y.M., Manikandan M. Power Quality Enhancement Using Dynamic Voltage Restorer (DVR)-Based Predictive Space Vector Transformation (PSVT) With Proportional Resonant (PR)-Controller. *IEEE Access*, 2021, vol. 9, pp. 155380-155392. doi: https://doi.org/10.1109/ACCESS.2021.3129096.
21. Babu V., Ahmed K.S., Shuaib Y.M., Mani M. A novel intrinsic space vector transformation based solar fed dynamic voltage restorer for power quality improvement in distribution system. *Journal of Ambient Intelligence and Humanized Computing*, 2021. doi: https://doi.org/10.1007/s12652-020-02831-0.
22. Manikandan M., Basha A.M. ODFF: Optimized Dual Fuzzy Flow Controller Based Voltage Sag Compensation for SMES-Based DVR in Power Quality Applications. *Circuits and Systems*, 2016, vol. 07, no. 10, pp. 2959-2974. doi: https://doi.org/10.4236/cs.2016.710254.

Received 26.05.2022
Accepted 07.06.2022
Published 06.11.2022

Raj Shweta [1], *Research Scholar,*
Sivaramalingam Sivagnanam[1], *Professor,*
Kevin Ark Kumar[2], *Manager,*
[1] Annamalai University,
Chidambaram, Tamil Nadu, 608002, India,
e-mail: er.shwetaraj@gmail.com (Corresponding Author),
sivadots@gmail.com
[2] Bharat Heavy Electricals Limited (BHEL),
Tiruchirappalli, Tamil Nadu, 620014 India,
e-mail: kevin@bhel.in

How to cite this article:
Shweta R., Sivagnanam S., Kumar K.A. Fault detection and monitoring of solar photovoltaic panels using internet of things technology with fuzzy logic controller. *Electrical Engineering & Electromechanics*, 2022, no. 6, pp. 67-74. doi: https://doi.org/10.20998/2074-272X.2022.6.10

UDC 621.3 https://doi.org/10.20998/2074-272X.2022.6.11

N. Tebbakh, D. Labed, M.A. Labed

Optimal size and location of distributed generations in distribution networks using bald eagle search algorithm

Introduction. *In the actual era, the integration of decentralized generation in radial distribution networks is becoming important for the reasons of their environmental and economic benefits.* ***Purpose.*** *This paper investigate the optimal size, location and kind of decentralized generation connected in radial distribution networks using a new optimization algorithm namely bald eagle search.* ***Methods.*** *The authors check the optimal allocation of two kinds of decentralized generation the first is operated at unity power factor and the second is operated at 0.95 power factor, a multi-objective functions are minimized based on reduction of voltage deviation index, active and reactive power losses, while taking into consideration several constraints.* ***Results.*** *Simulation results obtained on Standard IEEE-33 bus and IEEE-69 bus radial distribution networks demonstrate the performance and the efficiency of bald eagle search compared with the algorithms existing in literature and radial distribution networks performances are improved in terms of voltage profile and notably active and reactive power losses reduction, decentralized generation operated at 0.95 power factor are more perfect than those operated at unit power factor.* References 31, tables 4, figures 8.
Key words: **decentralized generation, radial distribution networks, bald eagle search algorithm, power losses, voltage profile.**

Вступ. *У сучасну епоху інтеграція децентралізованої генерації до радіальних розподільчих мереж стає важливою з причин їх екологічних та економічних переваг.* ***Мета.*** *У цій статті досліджується оптимальний розмір, розташування та тип децентралізованої генерації, підключеної до радіальних розподільних мереж, з використанням нового алгоритму оптимізації, а саме пошуку білоголового орла.* ***Методи.*** *Автори перевіряють оптимальне розподілення двох видів децентралізованої генерації, перший працює при коефіцієнті потужності, рівному одиниці, а другий працює при коефіцієнті потужності 0,95, мінімізується багатоцільова функція на основі зниження показника відхилення напруги, втрат активної та реактивної потужності, беручи до уваги кілька обмежень.* ***Результати.*** *Результати моделювання, отримані на радіальних розподільних мережах стандартної шини IEEE-33 та шині IEEE-69, демонструють продуктивність та ефективність пошуку білоголового орлана в порівнянні з існуючими в літературі алгоритмами, а характеристики радіальних розподільчих мереж покращуються з точки зору профілю напруги та помітного зниження втрат активної та реактивної потужності, децентралізована генерація з коефіцієнтом потужності 0,95 більш досконала, ніж з одиничним коефіцієнтом потужності.* Бібл. 31, табл. 4, рис. 8.
Ключові слова: **децентралізована генерація, радіальні розподільчі мережі, алгоритм пошуку білоголового орла, втрати потужності, профіль напруги.**

1. Introduction. Previously generation and transmission power systems were responsible for the power quality transmitted to customers, but nowadays the close attention is distribution networks which are an easy target for electrical breakdowns [1]. The insertion of distributed generation (DGs) called decentralized generation; embedded generation, dispersed generation or on-site generation [2] into the radial distribution networks (RDNs) has attracted the attention of many researchers cause of their efficiency in improving voltage profile and decreasing power losses [3, 4]. DGs units can be divided into 2 types according to their resources, conventional such as diesel engines and renewable energies such as photovoltaic and wind turbine [5], and they can be divided into 4 groups according to the type of power supplied to RDNs:

- Group 1: DGs supply only active power;
- Group 2: DGs supply active and reactive power;
- Group 3: DGs supply active power and absorb reactive power;
- Group 4: DGs supply only reactive power [6].

Several studies have been carried out in literature with the main objective being to take advantage of benefits from connecting DGs to RDNs, either by optimizing the combination site and size, their location with specific capacity, their size with a defined site, their optimal size and site or specifying the correct type of DGs to be connected [7], without neglecting the permissible voltage limits which are RDNs nominal voltage plus ±5 % [8], because the integration of DGs units at inappropriate location with aleatory size may have adverse effects on RDNs power losses and voltage profile [9, 10].

Various algorithms have been used to study the optimal size and location of DGs where we mention next: Bat Optimization Algorithm (BA) [11], Water Cycle Algorithm (WCA) [12], Optimal Power Flow Algorithm (OPFA) [13], Slime Mould Algorithm (SMA) [14], Teaching Learning Combined with Harmony Search Algorithm (TLCHS) [15], Dragonfly Algorithm (DA) [16], Hybrid (WOA – SSA) Algorithm [17], Salp Swarm Algorithm (SSA) [18], Exchange Market Algorithm (EMA) [19], Fuzzy Logic Controller (FLC) [20], Fast Voltage Stability Index (FVSI), Whale Optimization Algorithm (WOA) [21], Genetic Algorithm (GA) [22, 23], Harris Hawks Optimization Algorithm (HHO) [24], Genetic Salp Swarm Algorithm (GA-SSA) [25], and Hybrid Firefly and Particle Swarm Optimization Algorithm (HFPSO) to find the optimal size of distributed generation and D-STATCOM [26].

The goal of the paper is checking the performance and the efficiency of the proposed bald eagle search (BES) algorithm compared to other algorithms existing in literature and compare the simulation results obtained by connecting distributed generation to radial distribution networks operating firstly at unity power factor and secondly at 0.95 power factor, on network performances such as voltage profile and reduction of active and reactive power losses.

The results are carried out on standard IEEE-33 bus and IEEE-69 bus test systems by reducing active and reactive power losses and voltage profile enhancement.

2. Problem formulation.

2.1 Objective function. The aim of this work is adapted to study the impact of the integration of DGs in

RDNs on active and reactive power losses and the voltage profile; therefore, the objective function can be described as:

Minimization of:

$$(F) = TPL + TQL + VDI\,, \tag{1}$$

where *TPL*, *TQL* and *VDI* are the total active power losses, total reactive power losses and voltage deviation index respectively:

$$TPL = \sum_{i=1}^{Nl} P_{loss}\,; \tag{2}$$

$$P_{loss} = \left|I_{ij}\right|^2 \cdot R_{ij}\,; \tag{3}$$

$$TQL = \sum_{i=1}^{Nl} Q_{loss}\,; \tag{4}$$

$$Q_{loss} = \left|I_{ij}\right|^2 \cdot X_{ij}\,, \tag{5}$$

where *Nl* is the lines number; R_{ij} and X_{ij} are the resistance and reactance of *ij* line; I_{ij} is the current that flow from bus *i* to bus *j*;

$$VDI = \sum_{i=1}^{Nb} \left(1 - V_i\right)^2\,, \tag{6}$$

where V_i is the voltage magnitude at i^{th} bus in p.u.; *Nb* is the number of busses.

2.2 Constraints.

$$P_{DG\min} \le P_{DG} \le P_{DG\max}\,; \tag{7}$$

$$P_{DG\min} = 0 \text{ kW and } P_{DG\max} = 3000 \text{ kW};$$

$$Q_{DG\min} \le Q_{DG} \le Q_{DG\max}\,; \tag{8}$$

$$Q_{DG\min} = 0 \text{ kVAr and } Q_{DG\max} = 986 \text{ kVAr};$$

$$\max\left\{S_{ij} \text{ or } S_{ji}\right\} \le S_{ij\max}\,; \tag{9}$$

$$0.95 \le V_i \le 1.05\,; \tag{10}$$

$$(i = 1 \ldots Nb);$$

where $P_{DG\max}$, $P_{DG\min}$ are the DGs generation active power limits; $Q_{DG\max}$, $Q_{DG\min}$ are the DGs generation reactive power limits; P_{DG}, Q_{DG} are DGs active and reactive power; S_{ij} and S_{ji} are the apparent power that flow from bus *i* to bus *j* or from bus *j* to *i*; $S_{ij\max}$ is the maximum apparent power flow in ij^{th} branch; V_i is the voltage magnitude at the i^{th} bus.

DGs can be connected at all busses except the substation bus.

$$2 \le DG_{Location} \le Nb\,, \tag{11}$$

$DG_{Location}$ is the bus where the DG can be connected; N_{DG} is the number of DGs installed in RDN (= 3).

3. Bald Eagle Search Algorithm. In 2020 H.A. Alsattar et al [27] developed a novel meta-heuristic Bald Eagle Search (BES) optimization algorithm, which mimics the behaviour of bald eagles during the hunt, bald eagles often hunt from perches but they can also hunt in flight and they are able to locate fish at great distances because it is difficult to catch the fish in water.

When the bald eagles start searching for the prey on a water spot, these hunters fly off in a specific direction and select a certain space to start the hunt. Consequently, this algorithm was divided into 3 stages and Fig. 1 exhibits the main steps of BES.

3.1 Select stage. In the select stage, bald eagles select the favourable search space (in terms of food quantity) where they can hunt prey (Fig. 2).

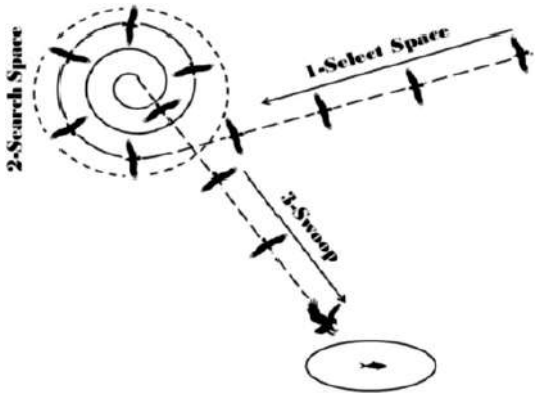

Fig. 1. Different steps of BES

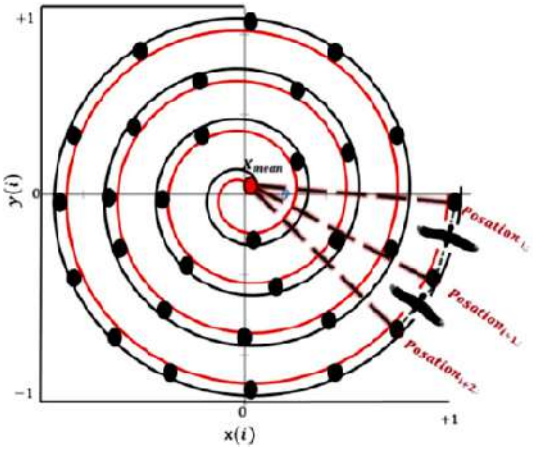

Fig. 2. Bald Eagles Searching within a spiral space

The bald eagles behaviour is presented in (12):

$$P_{new,i} = P_{best} + \alpha \cdot r\left(P_{mean} - P_i\right), \tag{12}$$

where α is the element that controls the position changes and it is in range of 1.5 to 2; *r* is the random number within [0, 1]; P_{best} is the best position identified by bald eagles during their previous search; P_{mean} indicates that the eagles have used all information from the previous points; P_i is the old eagle position and $P_{new,i}$ is the new position.

3.2 Search stage. In this stage, the eagles search for fish within the chosen search space and move within a spiral sense to accelerate their search.

The best position for the swoop is expressed by (13):

$$P_{new,i} = P_i + y(i) * \left(P_i - P_{i+1}\right) + x(i) * \left(P_i - P_{mean}\right)\,; \tag{13}$$

$$x(i) = \frac{xr(i)}{\left(\max\left|xr\right|\right)}\,; \tag{14}$$

$$y(i) = \frac{yr(i)}{\left(\max\left|yr\right|\right)}\,; \tag{15}$$

$$xr(i) = r(i) \cdot \sin(\theta(i))\,; \tag{16}$$

$$yr(i) = r(i) \cdot \cos(\theta(i))\,; \tag{17}$$

$$\theta(i) = \alpha \cdot \pi \cdot rand\,; \tag{18}$$

$$r(i) = \theta(i) + R \cdot rand\,, \tag{19}$$

where α is the parameter which is in range of 5 to 10 for determining the corner between point search in the central point, and *R* takes a value between 0.5 and 2 for defining the number of search cycles and rand is the number within [0, 1].

3.3 Swooping stage. The bald eagles swooping from the best position in the search space to their target fish, all points move towards the best point. This behaviour is illustrated in (20):

$$P_{new,i} = rand \cdot P_{best} + x1(i) \cdot (P_i - C1 \cdot P_{mean}) + \\ + y1(i) \cdot (P_i - C2 \cdot P_{best}); \quad (20)$$

$$x1(i) = \frac{xr(i)}{(\max|xr|)}; \quad (21)$$

$$y1(i) = \frac{yr(i)}{(\max|yr|)}; \quad (22)$$

$$xr(i) = r(i) \cdot \sinh(\theta(i)); \quad (23)$$

$$yr(i) = r(i) \cdot \cosh(\theta(i)); \quad (24)$$

$$\theta(i) = \alpha \cdot \pi \cdot rand; \quad (25)$$

$$r(i) = \theta(i), \quad (26)$$

where $C1$, $C2 \in [1, 2]$ and *rand* is the number within [0, 1].

3.4 BES pseudo code.

Algorithm 1 Pseudo-Code of BES algorithm
1: Randomly initialize point P_i for n point;
2: Calculate the fitness values of initial point: $f(P_i)$;
3: WHILE (the termination conditions are not met)
Select space
4: For (each point i in the population)
5: $P_{new} = P_{best} + \alpha \cdot \text{rand}(P_{mean} - P_i)$
6: if $f(P_{new}) < f(P_i)$
7: $P_i = P_{new}$
8: if $f(P_{new}) < f(P_{best})$
9: $P_{best} = P_{new}$
10: End If
11: End If
12: End For
Search in space
13: For (each point i in the population)
14: $P_{new} = P_i + y(i) \cdot (P_i - P_{i+1}) + x(i) \cdot P_i - P_{mean})$
15: if $f(P_{new}) < f(P_i)$
16: $P_i = P_{new}$
17: if $f(P_{new}) < f(P_{best})$
18: $P_{best} = P_{new}$
19: End If
20: End If
21: End For
Swoop
22: For (each point i in the population)
23: $P_{new} = \text{rand} \cdot P_{best} + x1(i) \cdot (P_i - \text{c1} \cdot P_{mean}) +$
$+ y1(i) \cdot (P_i - \text{c2} \cdot P_{best})$
24: if $f(P_{new}) < f(P_i)$
25: $P_i = P_{new}$
26: if $f(P_{new}) < f(P_{best})$
27: $P_{best} = P_{new}$
28: End If
29: End If
30: End For
31: Set $k = k+1$;
32:END WHILE

4. Results and discussion. In this section improvement of voltage profile and reducing power losses are the mains objectives of the integration of DGs in RDNs. Backward / forward sweep based load flow has been chosen for load flow studies.

BES algorithm bio inspired algorithm is used for the optimization of the chosen objective function, and it is developed using MATLAB.

The simulation study was performed on: a PC with Intel (R) Core (TM) 2 Duo CPU t6570, 2.10 GHz, and 3.00 GB RAM.

The first studied system is IEEE-33 bus radial distribution network which has 33 bus, and 32 lines with total load of 3715 kW and 2300 kVAr [28].

The second studied system is IEEE-69 bus radial system which contains 69 bus, and 68 branches with total load of 3801, 39 kW and 2693 kVAr [28].

To check if the BES algorithm had given a perfect solution or not, a comparative study has been made with other well-known optimization algorithms.

BES algorithm was set with 100 of the population and 150 of maximum iterations as parameters setting values.

Three cases have been considered in the systems which are:

1. Base case (without DG).
2. Injecting of 3 DGs with unity p.f.
3. Injecting of 3 DGs with 0.95 p.f.

The base values are taken as 100 MVA and 12, 66 kV.

4.1 IEEE-33 bus distribution system. The first test system is standard IEEE-33 bus, which is depicted in Fig. 3.

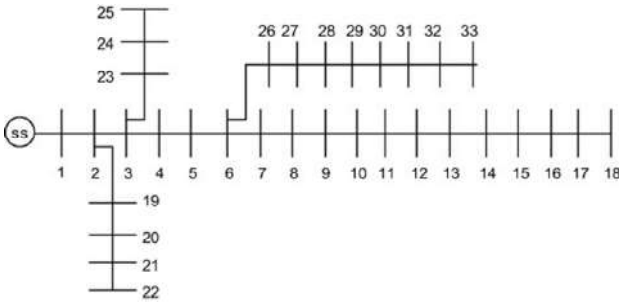

Fig. 3. IEEE-33 bus radial system single line diagram

In the base case the system fed only from the grid through the bus 1 (without DG) and the voltage profile curve per bus, displayed in Fig. 4 showed that the voltage magnitude at many busses is less than the minimum acceptable voltage (0.95 p.u.) and the lowest voltage is 0.9042 p.u. at bus 18, the simulation results indicate that the voltage deviation index is 3.2318 p.u., total active power losses 210.0534 kW and total reactive power losses 142.4354 kVAr.

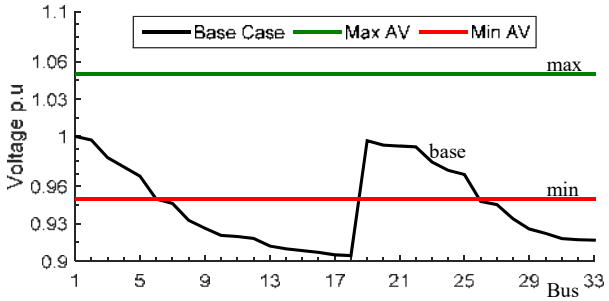

Fig. 4. Voltage profile IEEE-33 bus base case
max AV = 1.05 p.u. and min AV = 0.95 p.u.
are maximum and minimum acceptable voltages

The results at unity power factor presented in Table 1 and shows that the optimal locations and sizes obtained by BES algorithm reduces the active power losses to 70.64 kW, reactive power losses to 49.2659 kVAr and VDI to 0.2973 p.u.

Furthermore, the results at 0.95 power factor are performed and they are presented in Table 2, where the active power losses reach 27.859 kW, reactive power losses 20.7192 kVAr and VDI 0.0451 p.u.

Table 1

Optimal DG location for IEEE-33 bus test system at unity p.f.

Method	Optimal DG		TPL	VDI
	Bus	Size kW	kW	p.u.
MOHHO [5]	13 25 31	1207.0 763.0 1400.0	92.95	0.0020
MOIHHO [5]	14 24 31	1223.0 1144.0 1290.0	92.25	0.0019
GA [29]	11 29 30	1500.0 422.8 1071.4	106.30	0.0407
PSO [29]	08 13 32	1176.8 981.6 829.7	105.30	0.0335
GA/PSO [29]	11 16 32	925.0 863.0 1200.0	103.40	0.0124
TLBO [30]	12 28 30	1182.6 1191.3 1186.3	124.70	0.0011
QOTLBO [30]	13 26 33	1083.4 1187.6 1199.2	103.40	0.0011
BES	14 24 30	784.71 1053.8 1083.0	70.64	0.2973

Table 2

Optimal DG location for IEEE-33 bus test system at 0.95 p.f.

Method	Optimal DG			TPL	VDI
	Bus	Size		kW	p.u
		kW	kVAr		
MOHHO [5]	13 25 30	1008.0 910.0 1334.0	331.0 299.0 439.0	31.4	0.0005
MOIHHO [5]	13 24 30	924.0 1312.4 1356.0	304.0 431.0 446.0	30.6	0.0004
SIMBO-Q [31]	13 24 30	943.0 1327.0 1443.0	309.0 436.0 474.0	32.4	0.0003
QOSIMBO-Q [31]	13 24 30	898.0 1392.0 1419.0	295.0 458.0 467.0	31.7	0.0003
BES	13 24 30	840.41 1096.4 1234.1	276.23 360.38 405.63	27.6357	0.0445

From Fig. 5 it is clear that the voltage profile is improved at the 2 cases, but integration of DGs at 0.95 power factor is more convenient than at unity power factor.

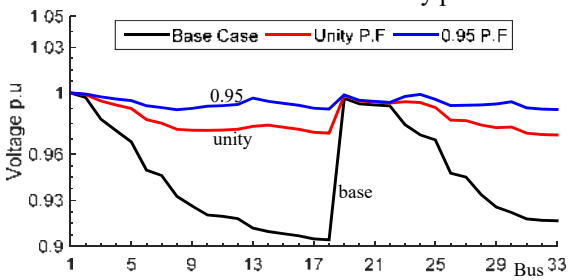

Fig. 5. Voltage profile curve IEEE 33 bus at the studied cases

Compared to other reviewed literatures this algorithm resulted a high reduction in terms of active and reactive power losses but not for the VDI.

4.2 IEEE-69 bus radial system. The second test system is IEEE-69 bus, which is presented in Fig. 6.

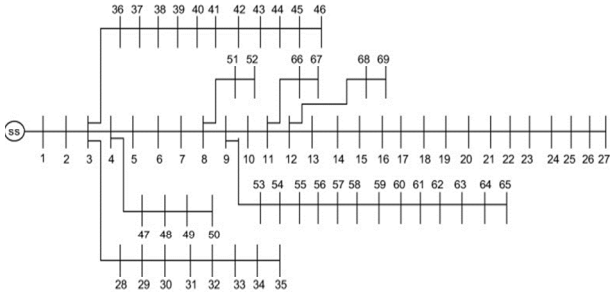

Fig. 6. IEEE-69 bus radial system single line diagram

In the base case the simulation results were carried out without DG and the voltage profile curve per bus figured in Fig. 7 showed that the magnitude voltage at many busses is less than the minimum acceptable voltage (0.95 p.u) and the lowest voltage is 0.9102 p.u. at bus 65.

The obtained results are as follows: voltage deviation index 3.3242 p.u., total active power losses 224.5533 kW and 101.9725 kVAr for the total reactive power losses.

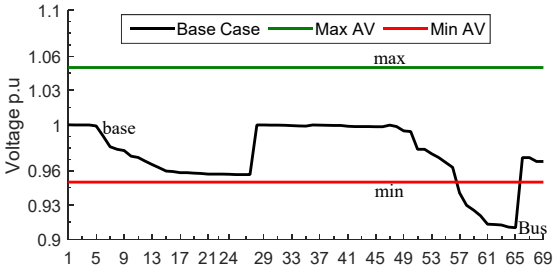

Fig. 7. Voltage profile IEEE-69 bus base case max AV = 1.05 p.u. and min AV = 0.95 p.u. are maximum and minimum acceptable voltages

Table 3 summarised the simulation results at unity power factor in this case the optimal locations and sizes obtained by BES algorithm reduced the active power losses to 68.9347 kW, reactive power losses to 31.6214 kVAr and VDI to 0.1689 p.u.

Table 3

Optimal DG location for IEEE-69 bus test system at unity p.f.

Method	Optimal DG		TPL	VDI
	Bus	Size kW	kW	p.u.
MOHHO [5]	20 60 61	643.6 763.4 1328.2	81.00	0.0008
MOIHHO [5]	18 61 64	796.2 1447.1 707.5	80.88	0.0007
GA [29]	21 62 64	929.7 1075.2 984.8	89.00	0.0012
PSO [29]	17 61 63	992.5 1199.8 795.6	83.20	0.0049
GA/PSO [29]	21 61 63	910.5 1192.6 1200.0	81.1	0.0031
TLBO [30]	13 61 62	1013.4 990.1 1160.1	82.2	0.0008
QOTLBO [30]	15 61 63	811.4 1147.0 1002.2	80.6	0.0007
BES	17 50 61	537.07 720.21 1805.6	68.94	0.1689

The results at 0.95 power factor presented in Table 4 were as follows the active power losses equal to 21.1609 kW, reactive power losses 9.8564 kVAr and VDI 0.0174 p.u.

Table 4

Optimal DG location for IEEE-69 bus test system at 0.95 p.f.

Method	Optimal DG			TPL	VDI
	Bus	Size		kW	p.u
		kW	kVAr		
MOHHO [5]	23	519.0	171.0	30.2	0.0010
	60	1176.0	387.0		
	62	1179.0	387.0		
MOIHHO[5]	13	1038.0	341.0	28.9	0.0003
	61	799.0	263.0		
	63	1229.0	404.0		
SIMBO-Q [31]	13	953.0	313.0	29.7	0.0003
	59	1002.0	329.0		
	62	1121.0	369.0		
QOSIMBO-Q [31]	17	487.0	160.0	31.4	0.0002
	56	1260.0	414.0		
	63	1500.0	493.0		
BES	17	586.64	192.82	21.16	0.0174
	50	802.38	263.72		
	61	1955.5	642.73		

From Fig. 8 it is clear that the voltage profile is improved at the 2 cases, but integration of DGs at 0.95 power factor is more efficient.

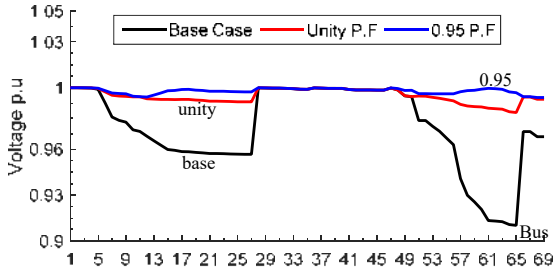

Fig. 8. Voltage profile curve IEEE-69 bus at the studied cases

Compared to other reviewed literatures this algorithm resulted a high effectiveness in terms of active and reactive power losses but not for the VDI.

Conclusions.

In this paper bald eagle search algorithm is used to investigate the optimal size and location of multiple decentralized generation with multi-objective functions (total active power losses, total reactive power losses and voltage deviation index). The bald eagle search algorithm has been assessed in standard IEEE-33 bus and 69 bus test systems.

The results obtained by bald eagle search algorithm showed a significant reduction of power losses as well as the improvement of voltage profile, and indicated that the case where distributed generation are operated at 0.95 power factor is more practical than the case where distributed generation are operated at unity power factor.

However, the comparison of simulation results with those existing in literature confirm the performance and the efficiency of this algorithm in terms of reducing power losses and little bit less concerning voltage deviation index.

Conflict of interest. The authors declare no conflict of interest.

REFERENCES

1. Gopal Reddy S., Ganapathy S., Manikandan M. Power quality improvement in distribution system based on dynamic voltage restorer using PI tuned fuzzy logic controller. *Electrical Engineering & Electromechanics*, 2022, no. 1, pp. 44-50. doi: https://doi.org/10.20998/2074-272X.2022.1.06.

2. Labed D. Production Decentralisée et Couplage au Réseau. *PhD Thesis. Department of Electrical Engineering University Frères Mentouri*, 2008, 173 p. (Fra).

3. M'hamdi B., Teguar M., Tahar B. Optimal DG Unit Placement and Sizing in Radial Distribution Network for Power Loss Minimization and Voltage Stability Enhancement. *Periodica Polytechnica Electrical Engineering and Computer Science*, 2020, vol. 64, no. 2, pp. 157-169. doi: https://doi.org/10.3311/PPee.15057.

4. Bouraghda S., Sebaa K., Bechouat M., Sedraoui M. An improved sliding mode control for reduction of harmonic currents in grid system connected with a wind turbine equipped by a doubly-fed induction generator. *Electrical Engineering & Electromechanics*, 2022, no. 2, pp. 47-55. doi: https://doi.org/10.20998/2074-272X.2022.2.08.

5. Selim A., Kamel S., Alghamdi A.S., Jurado F. Optimal Placement of DGs in Distribution System Using an Improved Harris Hawks Optimizer Based on Single- and Multi-Objective Approaches. *IEEE Access*, 2020, vol. 8, pp. 52815-52829. doi: https://doi.org/10.1109/ACCESS.2020.2980245.

6. Noureddine T., Djamel L. Load flow analysis using newton raphson method in presence of distributed generation. *International Journal of Power Electronics and Drive Systems (IJPEDS)*, 2021, vol. 12, no. 1, pp. 489-498. doi: https://doi.org/10.11591/ijpeds.v12.i1.pp489-498.

7. Ouali S., Cherkaoui A. Optimal Allocation of Combined Renewable Distributed Generation and Capacitor Units for Interconnection Cost Reduction. *Journal of Electrical and Computer Engineering*, 2020, pp. 1-11. doi: https://doi.org/10.1155/2020/5101387.

8. Raj A., Aziz N.F.A., Yasin Z.M., Salim N.A. Investigation of distributed generation units placement and sizing based on voltage stability condition indicator (VSCI). *International Journal of Power Electronics and Drive Systems (IJPEDS)*, 2019, vol. 10, no. 3, pp. 1317-1323. doi: https://doi.org/10.11591/ijpeds.v10.i3.pp1317-1323.

9. Sa'ed J.A., Quraan M., Samara Q., Favuzza S., Zizzo G. Impact of integrating photovoltaic based DG on distribution network harmonics. *2017 IEEE International Conference on Environment and Electrical Engineering and 2017 IEEE Industrial and Commercial Power Systems Europe (EEEIC / I&CPS Europe)*, 2017, pp. 1-5. doi: https://doi.org/10.1109/EEEIC.2017.7977786.

10. Kyryk V.V., Bohomolova O.S. Justification of optimal location of connection of the distributed generation source and value of its power. *Electrical Engineering & Electromechanics*, 2019, no. 2, pp. 55-60. doi: https://doi.org/10.20998/2074-272X.2019.2.08.

11. Yuvaraj T., Devabalaji K.R., Ravi K. Optimal Allocation of DG in the Radial Distribution Network Using Bat Optimization Algorithm. In: Garg, A., Bhoi, A., Sanjeevikumar, P., Kamani, K. (eds) *Advances in Power Systems and Energy Management. Lecture Notes in Electrical Engineering*, 2018, vol. 436. Springer, Singapore. doi: https://doi.org/10.1007/978-981-10-4394-9_55.

12. El-Ela A.A.A., El-Sehiemy R.A., Abbas A.S. Optimal Placement and Sizing of Distributed Generation and Capacitor Banks in Distribution Systems Using Water Cycle Algorithm. *IEEE Systems Journal*, 2018, vol. 12, no. 4, pp. 3629-3636. doi: https://doi.org/10.1109/JSYST.2018.2796847.

13. Singh B., Gyanish B.J. Impact assessment of DG in distribution systems from minimization of total real power loss viewpoint by using optimal power flow algorithms. *Energy Reports*, 2018, vol. 4, pp. 407-417. doi: https://doi.org/10.1016/j.egyr.2018.07.003.

14. Kouadri R., Slimani L., Bouktir T. Slime mould algorithm for practical optimal power flow solutions incorporating stochastic wind power and static var compensator device. *Electrical Engineering & Electromechanics*, 2020, no. 6, pp. 45-54. doi: https://doi.org/10.20998/2074-272X.2020.6.07.

15. Alam A., Zaheer B., Zaid M. Optimal Placement of DG in Distribution System for Power Loss Minimization and Voltage Profile Improvement. *2018 International Conference on Computing, Power and Communication Technologies (GUCON)*, 2018, pp. 837-842. doi: https://doi.org/10.1109/GUCON.2018.8674930.
16. Suresh M.C.V., Belwin E.J. Optimal DG placement for benefit maximization in distribution networks by using Dragonfly algorithm. *Renewables: Wind, Water, and Solar*, 2018, vol. 5, no. 1, art. no. 4. doi: https://doi.org/10.1186/s40807-018-0050-7.
17. Alzaidi K.M.S., Bayat O., Uçan O.N. Multiple DGs for Reducing Total Power Losses in Radial Distribution Systems Using Hybrid WOA-SSA Algorithm. *International Journal of Photoenergy*, 2019, pp. 1-20. doi: https://doi.org/10.1155/2019/2426538.
18. Sambaiah K.S., Jayabarathi T. Optimal Allocation of Renewable Distributed Generation and Capacitor Banks in Distribution Systems using Salp Swarm Algorithm. *International Journal of Renewable Energy Research*, 2019, vol. 9, no. 1, pp. 96-107. doi: https://doi.org/10.20508/ijrer.v9i1.8581.g7567.
19. Daneshvar M., Abapour M., Mohammadi-ivatloo B., Asadi S. Impact of Optimal DG Placement and Sizing on Power Reliability and Voltage Profile of Radial Distribution Networks. *Majlesi Journal of Electrical Engineering*, 2019, vol. 13, no. 2, pp. 91-102. Available at: http://mjee.iaumajlesi.ac.ir/index/index.php/ee/article/view/2782 (Accessed 10 May 2022).
20. Kumar Sharma S., K. Palwalia D., Shrivastava V. Distributed generation integration optimization using fuzzy logic controller. *AIMS Energy*, 2019, vol. 7, no. 3, pp. 337-348. doi: https://doi.org/10.3934/energy.2019.3.337.
21. Ang S., Leeton U. Optimal placement and size of distributed generation in radial distribution system using whale optimization algorithm. *Suranaree Journal of Science and Technology*, 2019, vol. 26, no. 1, pp. 1-12. Available at: https://ird.sut.ac.th/e-journal/Journal/pdf/180101220.pdf (Accessed 10 May 2022).
22. Bawa A., Uthman M., Shaibu F.E., Oyewale K.S. Optimal Sizing and Sitting of Distributed Generation for Power Quality Improvement of Distribution Network. *European Journal of Engineering and Technology Research*, 2019, vol. 4, no. 10, pp. 18-23. doi: https://doi.org/10.24018/ejeng.2019.4.10.1555.
23. Prakash S., Rangta V., Jayalakshmi N.S., Kumar Jadoun V. Optimal Location of DGs in a Distribution System for Maintaining Voltage Profile and Loss Reduction Using Genetic Algorithm. *2020 International Conference on Power Electronics & IoT Applications in Renewable Energy and Its Control (PARC)*, 2020, pp. 59-64. doi: https://doi.org/10.1109/PARC49193.2020.236558.
24. Islam M.Z., Wahab N.I.A., Veerasamy V., Hizam H., Mailah N.F., Guerrero J.M., Mohd Nasir M.N. A Harris Hawks Optimization Based Single- and Multi-Objective Optimal Power Flow Considering Environmental Emission. *Sustainability*, 2020, vol. 12, no. 13, art. no. 5248. doi: https://doi.org/10.3390/su12135248.
25. Djabali C., Bouktir T. Simultaneous allocation of multiple distributed generation and capacitors in radial network using genetic-salp swarm algorithm. *Electrical Engineering & Electromechanics*, 2020, no. 4, pp. 59-66. doi: https://doi.org/10.20998/2074-272X.2020.4.08.
26. Mohsin Al-Wazni H.S., Abdulla Al-Kubragyi S.S. A hybrid algorithm for voltage stability enhancement of distribution systems. *International Journal of Electrical and Computer Engineering (IJECE)*, 2022, vol. 12, no. 1, pp. 50-61. doi: https://doi.org/10.11591/ijece.v12i1.pp50-61.
27. Alsattar H.A., Zaidan A.A., Zaidan B.B. Novel meta-heuristic bald eagle search optimisation algorithm. *Artificial Intelligence Review*, 2020, vol. 53, no. 3, pp. 2237-2264. doi: https://doi.org/10.1007/s10462-019-09732-5.
28. Aguirre-Angulo B.E., Giraldo-Bello L.C., Montoya O.D., Moya F.D. Optimal Integration of Dispersed Generation in Medium-Voltage Distribution Networks for Voltage Stability Enhancement. *Algorithms*, 2022, vol. 15, no. 2, art. no. 37. doi: https://doi.org/10.3390/a15020037.
29. Moradi M.H., Abedini M. A combination of genetic algorithm and particle swarm optimization for optimal DG location and sizing in distribution systems. *International Journal of Electrical Power & Energy Systems*, 2012, vol. 34, no. 1, pp. 66-74. doi: https://doi.org/10.1016/j.ijepes.2011.08.023.
30. Sultana S., Roy P.K. Multi-objective quasi-oppositional teaching learning based optimization for optimal location of distributed generator in radial distribution systems. *International Journal of Electrical Power & Energy Systems*, 2014, vol. 63, pp. 534-545. doi: https://doi.org/10.1016/j.ijepes.2014.06.031.
31. Sharma S., Bhattacharjee S., Bhattacharya A. Quasi-Oppositional Swine Influenza Model Based Optimization with Quarantine for optimal allocation of DG in radial distribution network. *International Journal of Electrical Power & Energy Systems*, 2016, vol. 74, pp. 348-373. doi: https://doi.org/10.1016/j.ijepes.2015.07.034.

Received 15.05.2022
Accepted 27.07.2022
Published 06.11.2022

Noureddine Tebbakh[1]*, PhD Student,*
Djamel Labed[1]*, Professor,*
Mohamed Amir Labed[1]*, PhD Student,*
[1] Laboratory of Electrical Engineering,
Department of Electrical Engineering,
University of Constantine 1,
Constantine 25000, Algeria,
e-mail: tebbakh.noureddine@yahoo.com (Corresponding Author);
djamel_labed@yahoo.fr;
mohamedamir.labed@student.umc.edu.dz

How to cite this article:
Tebbakh N., Labed D., Labed M.A. Optimal size and location of distributed generations in distribution networks using bald eagle search algorithm. *Electrical Engineering & Electromechanics*, 2022, no. 6, pp. 75-80. doi: https://doi.org/10.20998/2074-272X.2022.6.11

Матеріали приймаються за адресою:
Кафедра "Електричні апарати", НТУ "ХПІ", вул. Кирпичева, 2, м. Харків, 61002, Україна
Електронні варіанти матеріалів по e-mail: a.m.grechko@gmail.com

Довідки за телефонами: +38 067 359 46 96 Гречко Олександр Михайлович

Передплатний індекс: 01216